The role of GBA2 in controlling locomotor activity

Dissertation

zur

Erlangung des Doktorgrades (Dr. rer. nat.)

der

Mathematisch-Naturwissenschaftlichen Fakultät

der

Rheinischen Friedrich-Wilhelms-Universität Bonn

vorgelegt von

Marina Amelie Woeste

aus

Borken (i. Westf.)

Bonn 2018

Angefertigt mit Genehmigung der Mathematisch-Naturwissenschaftlichen Fakultät der
Rheinischen Friedrich-Wilhelms-Universität Bonn

1. Gutachter: Prof. Dr. Dagmar Wachten
2. Gutachter: Prof. Dr. Christoph Thiele
3. Gutachter: Prof. Dr. Frank Bradke
4. Gutachter: Prof. Dr. Anton Bovier

Tag der Promotion: 11. Oktober 2018
Erscheinungsjahr: 2018

Abstract

Glycosphingolipids are major constituents of cellular membranes, fulfilling both structural and functional roles. Modifications of the basic glycosphingolipid glucosylceramide (GlcCer) result in numerous complex glycosylated and sialylated glycosphingolipids, which are highly abundant in the central nervous system (CNS). Glycosphingolipid homeostasis is tightly regulated and the non-lysosomal glucosylceramidase GBA2 plays a central role as it hydrolyzes GlcCer to glucose and ceramide. Recently, mutations in *GBA2* have been identified in human patients suffering from autosomal-recessive cerebellar ataxia (ARCA), hereditary spastic paraplegia (HSP), or Marinesco-Sjögren-like Syndrome (MSLS). How these mutations impair enzyme function and might cause locomotor dysfunction is not known. I could show that all these mutations – beside one – cause a complete loss of GBA2 activity, indicating that also the human patients potentially lack GBA2 activity. Detailed analysis of the structure-function properties of GBA2 revealed that its activity is encoded in the protein's tertiary structure, including the N-terminal domain, linker region, and C-terminal domain. GBA2 proteins interact and form oligomers, a characteristic that might also be crucial for enzyme function. However, *in vivo* experiments did not reveal severe locomotor dysfunction or morphological defects in the cerebellum in GBA2-knockout mice, pointing towards species-dependent differences in GBA2-regulated metabolism of GlcCer and GlcCer metabolites in the CNS. However, acute pharmacological inhibition of GBA2 in murine cerebellar neurons *in vitro* impairs neurite outgrowth, suggesting a potential mechanism how loss of GBA2 activity results in ataxia and spasticity in ARCA, HSP, and MSLS patients carrying mutations in *GBA2*. *In vivo* in the mouse, compensatory mechanisms might occur, preventing severe neurological manifestation after genetic loss of GBA2.

Zusammenfassung

Glycosphingolipide sind Hauptbestandteile zellulärer Membranen und erfüllen sowohl strukturelle als auch funktionelle Aufgaben. Modifizierungen des einfachen Glycosphingolipids Glucosylceramid (GlcCer) bringen zahlreiche komplexe glycosylierte und sialylierte Glycosphingolipide hervor, die besonders im zentralen Nervensystem (ZNS) vorkommen. Die Glycosphingolipid-Homöostase unterliegt einer starken Regulation, wobei die nicht-lysosomale Glucosylceramidase GBA2 eine zentrale Rolle spielt, da sie GlcCer zu Glucose und Ceramid hydrolysiert. Kürzlich wurden Mutationen im *GBA2*-Gen in Patienten identifiziert, die an autosomal-rezessiver cerebellärer Ataxie (ARCA), hereditärer spastischer Paraplegie (HSP) oder dem Marinesco-Sjögren-ähnlichen Syndrom (MSLS) leiden. Ob und wie diese Mutationen die Funktion des Enzyms beeinträchtigen und möglicherweise die lokomotorische Dysfunktion in ARCA, HSP und MSLS verursachen, ist nicht bekannt. Ich konnte zeigen, dass, bis auf eine, all diese Mutationen zu einem kompletten Funktionsverlust von GBA2 führen, was darauf hinweist, dass auch in den Patienten ein Verlust der GBA2-Aktivität zu verzeichnen ist. Eine detaillierte Analyse der strukturellen und funktionellen Eigenschaften von GBA2 zeigte, dass die Aktivität in der tertiären Proteinstruktur, einschließlich der N-terminalen Domäne, der Linker-Region und der C-terminalen Domäne, kodiert ist. GBA2-Proteine interagieren miteinander und bilden oligomere Komplexe, eine charakteristische Eigenschaft, die auch für die Funktion des Enzyms wichtig sein könnte. *In vivo* Experimente, zeigten jedoch keinen eindeutigen Defekt in der lokomotorischen Funktion oder morphologische Veränderungen des Cerebellums in GBA2-knockout Mäusen, was womöglich auf spezies-spezifische Unterschiede im GBA2-regulierten Metabolismus von GlcCer und GlcCer-Metaboliten im ZNS zurückzuführen ist. Ein akuter pharmakologischer Block der GBA2-Aktivität in murinen cerebellären Neuronen *in vitro* inhibierte jedoch das Neuritenwachstum, was darauf hindeutet, dass ein solcher Effekt auch die Grundlage für die Entwicklung von Ataxie und Spastik in ARCA, HSP und MSLS-Patienten sein könnte. *In vivo* in der Maus scheinen hingegen kompensatorische Mechanismen zu greifen, die eine schwere neurologische Manifestation durch den Verlust von GBA2 verhindern.

Table of contents

List of figures

List of tables

Abbreviations

>	Substitution
Å	Ångström
AMP-DNM	*N*-(5′-adamantane-1′-yl-methoxy)-pentyl-1-deoxynojirimycin
ANOVA	Analysis of variance
APS	Ammonium persulfate
ARCA	Autosomal-recessive cerebellar ataxia
Arp2/3	Actin-related protein 2/3
ATP	Adenosine 5′-triphosphate
AU	Arbitrary units
BCA	Bicinchoninic acid
bp	Base pair
bPAC	Photoactivated adenylyl cyclase from *Beggiatoa sp*.
BSA	Bovine serum albumin
°C	Degree Celsius
c.	Coding DNA
$CaCl_2$	Calcium chloride
CBE	Conduritol B epoxide
Cer	Ceramide
CerS	Ceramide synthase
CERT	Ceramide transport protein
CHO	Chinese hamster ovary cell line
CM	Calcium chloride/magnesium chloride buffer
CMF	Calcium and magnesium free
CNS	Central nervous system
CO_2	Carbon dioxide
coA	Coenzyme A
COS-7	Fibroblast-like cell line (origin: kidney of the African green monkey)
CV	Column volume
Da	Dalton
DAG	Diacylglycerol
DAPI	4′,6-diamidin-2-phenylindol
dbSNP	Single Nucleotide Polymorphism database
ddH_2O	Double-destilled water
DEAE	Diethylaminoethyl

DES	Ceramide desaturase
del	Deletion
dk	Donkey (*Equus asinus*)
DMEM	Dulbecco's Modified Eagle Medium
DMF	Dimethylformamide
DMSO	Dimethylsulfoxide
DNA	Deoxyribonucleic acid
dNTP	Deoxynucleoside tripshophate
DSS	Disuccinimidyl suberate
DTT	Dithiothreitol
dup	Duplication
E	Eluate
E.coli	*Escherichia coli*
ECL	Enhanced chemiluminescence
EDTA	Ethylenediaminetetraacetic acid
e.g.	Exempli gratia, for example
EGF	Epidermal growth factor
ER	Endoplasmic reticulum
ERT	Enzyme replacement therapy
et al.	Et alii
EU	EUCOMM
F12	Ham's F-12 Nutrient Mixture
FAS receptor	First apoptosis signal receptor
FCS	Fetal calf serum
fuc	Fucosylated
g	Gram
x g	x times gravitational force (9.81 m/sec^2)
G418	Geneticin
GalC	Galactosylceramidase
GalCer	Galactosylceramide
GalNAc	*N*-acetylgalactosamine
Gb3	Globotriaosylceramide
Gb4	Globotetraosylceramide
Gb5	Globopentaosylceramide
GBA1	Lysosomal glucosylceramidase
GBA2	Non-lysosomal glucosylceramidase
GBA3	Cytosolic glucosylceramidase

GD1/ GD2/ GD3	Disialogangliosides
GDP	Guanosine 5′-diphosphate
GF	Gel filtration (size-exclusion chromatography) fraction
GH	Glycoside hydrolase
GlcCer	Glucosylceramide
GlcChol	Glucosylcholesterol
GM1/ GM2/ GM3	Monosialogangliosides
GP1	Pentasialoganglioside
GPI	Glycosylphospatidylinositol
GQ1	Tetrasialoganglioside
GST	Glutathione S-transferase
GT1/ GT2/ GT3	Trisialogangliosides
GTP	Guanosine-5'-triphosphate
h	Hour(s)
h	Human
H_3PO_4	Phosphoric acid
HA	Hemagglutinin
HBSS	Hank's Balanced Salt Solution
HeLa	Immortalized cervical cancer cell line (origin: cervical tumor of the patient Henrietta Lacks)
HEPES	4-(2-hydroxyethyl)-1-piperazineethanesulfonic acid
het	Heterozygous
HexCer	Hexosylceramide
HCl	Hydrochloric acid
HGDP	Human Genome Diversity Project
HP(-TLC)	High-performance (thin layer chromatography)
HRP	Horseradish peroxidase
HSP	Hereditary spastic paraplegia
IC_{50}	Half maximal inhibitory concentration
ICC	Immunocytochemistry
In	Input
IPTG	Isopropyl-β-D-thiogalactopyranoside
IR	Infrared
k	Kilo
K_{av}	Available value of the distribution coefficient
KCl	Potassium chloride
kDa	Kilodalton

$K_3[Fe(CN)_6]$	Potassium hexacyanoferrate(III), red prussiate
$K_4[Fe(CN)_6]$	Potassium hexacyanoferrate(II), yellow prussiate
KH_2PO_4	Dipotassium hydrogen phosphate
3-KS	3-ketosphinganine
KO	Global GBA2-knockout (Yildiz et al., 2006)
KO^{EU}	Global GBA2-knockout (EUCOMM)
KOD	*Thermococcus kodakaraensis*
KOH	Potassium hydroxide
KO^{Myf}	Muscle-specific GBA2-knockout
KO^{Syn}	Neuron-specific GBA2-knockout
l	Liter
LacCer	Lactosylceramide
LB	Lysogeny broth
LC	Liquid Chromatography
LCB	Long-chain bases
LED	Light-emitting diode
LIM kinase	Lin-11/Isl-1/Mec-3 kinase
LIMP-2	Lysosomal integral membrane protein-2
µ	Micro
M	Molar
m	Milli
m	Mouse
mA	Milliampere
mAb	Monoclonal antibody
MAG	Myelin-associated protein
MAP-2	Microtubule-associated protein 2
MBP	Maltose binding protein
min	Minute(s)
$MgCl_2$	Magnesium chloride
$MgSO_4$	Magnesium sulfate
mol	Mole
MPa	Megapascal
mPIC	Mammalian protease inhibitor cocktail
MRI	Magnetic resonance imaging
mRNA	Messenger ribonucleic acid
ms	Mouse (*Mus musculus*)
MSLS	Marinesco-Sjögren-like Syndrome

MS/MS	Tandem Mass Spectrometry
MW	Molecular weight
Myf5	Myogenic factor 5
4-MU	4-methylumbelliferone
4-MUG	4-methylumbelliferyl-ß-D-glucopyranoside
n	Nano
NB	Non-Bound
NaCl	Sodium chloride
NADPH	Nicotinamide adenine dinucleotide phosphate (reduced)
$NaHCO_3$	Sodium bicarbonate
NaH_2PO_4	Sodium dihydrogen phosphate
Na_2HPO_4	Disodium hydrogen phosphate
NaOH	Sodium hydroxide
NB-DNJ	*N*-butyldeoxynojirimycin
NeuAc	*N*-acetylneuroaminic acid
NH_4Cl	Ammonium chloride
NJ	Nojirimycin
NPC	Niemann-Pick type C
N-WASP	Neural Wiskott-Aldrich syndrome protein
OD	Optical density
OptiMEM	Reduced Serum Medium
p	Pico
P	Postnatal day
PA	Phosphatidic acid
pAb	Polyclonal antibody
PAGE	Polyacrylamide gel electrophoresis
PAK	p21-activated kinase
PBGG	Porcine brain gangliosides
PBD	p21-activated kinase binding domain
PBS	Phosphate-buffered saline
PBS-T	Phosphate-buffered saline with Tween 20
PCR	Polymerase chain reaction
PEI	Polyethylenimine
PenStrep	Penicillin/ Streptomycin
PFA	Paraformaldehyde
pH	p[H+]
PH domain	Pleckstrin homology domain

PIP_2	Phosphatidylinositol-(4,5)-bisphosphate
PIP_3	Phosphatidylinositol-(3,4,5)-trisphosphate
PIP_4	Phosphatidylinositol 4-phosphate
PLL	Poly-L-lysine
PNS	Postnuclear supernatant
PVDF	Polyvinylidene difluoride
Q-TOF	Quadrupole time-of-flight
R^2	Correlation coefficient
rpm	Rounds per minute
rfu	Relative fluorescence units
rsu	Relative muscle strength unit
rt	Rat (*Rattus norvegicus*)
SD	Standard deviation
SDS	Sodium dodecyl sulfate
sec	Second(s)
sh	Sheep (O*vis aries*)
Skel.Mus.	Skeletal muscle
Sp.C.	Spinal cord
SphMy	Sphingomyelin
SPT	Serine palmitoyl-transferase
Syn	Synapsin
t	Time
T_A	Annealing temperature
t_e	Elongation time
TE	Tris-EDTA
TEMED	Tetramethylethylendiamine
Tet	Tetracycline
tev protease	Tobacco Etch Virus protease
TLC	Thin layer chromatography
T_m	Melting temperature
TNE	Tris/ NaCl/ EDTA buffer
TRE	Tetracycline-responsive promotor element
Tris	Tris(hydroxymethyl)aminomethane
tTA	Tetracycline-controlled transactivator protein
Tx	*Thermoanaerobacterium xylolyticum*
UDP	Uridine diphosphate
UV	Ultraviolet

V	Volume
V	Volt
V_0	Void volume
V_b	Bead volume
V_e	Elution volume
V_t	Total volume
v/v	Volume per volume
WASP	Wiskott-Aldrich syndrome protein
WAVE	WASP family Verprolin-homologous protein
WB	Western blot
w/v	Weight per volume
WT	Wild-type
X-gal	5-Bromo-4-chloro-3-indolyl-β-D-galactopyranoside
ZNS	Zentrales Nervensystem

Decimal (sub-)multiples of the base units are designated according to the international unit system “Système International d’Unités”.

Nucleotides are abbreviated by the initial letter of their bases (A: adenine, C: cyanine, G: guanine and T: thymine).

Amino acids (aa) are referred to using the one letter code:

Alanine	A	Leucine	L
Arginine	R	Lysine	K
Asparagine	N	Methionine	M
Aspartate	D	Phenylalanine	F
Cysteine	C	Proline	P
Glutamate	E	Serine	S
Glutamine	Q	Threonine	T
Glycine	G	Tryptophan	W
Histidine	H	Tyrosine	Y
Isoleucine	I	Valine	V

1 Introduction

1.1 Glycosphingolipids

Major constituents of cellular membranes comprise glycerophospholipids, cholesterol, and sphingolipids (van Meer et al., 2008). Glycerophospholipids consist of a diacylglycerol (DAG) backbone modified by different alcohol head groups, with choline being the most abundant one in eukaryotes (Holub and Kuksis, 1978; van Meer et al., 2008). Cholesterol accounts for about 20% of the total lipid species in eukaryotic plasma membranes and is an important regulator of membrane fluidity and permeability (Cooper, 1978; Raffy and Teissie, 1999). The four-ring steroid is built from the hydrocarbon precursor squalene in complex modification and cyclization steps (Bloch, 1992). Sphingolipids are structurally based on ceramide, which can be synthesized in three distinct metabolic pathways: 1.) in the *de novo* synthesis, 2.) by sphingomyelin hydrolysis, or 3.) in the salvage pathway of complex glycosphingolipids.

In the *de novo* synthesis of ceramide in the endoplasmic reticulum (ER), palmitoyl-coenzyme A (CoA) and serine are condensated by the serine palmitoyl-transferase (SPT) to form 3-ketosphinganine (3-KS) (**Figure 1**) (Mandon et al., 1992). Reduction of 3-KS in a NAPDH-dependent manner by the 3-KS reductase results in sphinganine (Stoffel et al., 1968), which is subsequently acylated by ceramide synthases to dihydroceramide (Rother et al., 1992). Acyl chains of different length can be attached to sphinganine; this reaction is catalyzed by one of the six identified ceramide synthases (CerS), which use a fatty acyl-coA of a certain chain length as a donor (Levy and Futerman, 2010). Thus, ceramides vary in the length, hydroxylation, and saturation state of the fatty acid attached to the sphingoid base (Stults et al., 1989). The synthesis of ceramide is finalized by the ceramide desaturase (DES), which introduces a *trans* double bond between C4 and C5 of the sphingoid base (Geeraert et al., 1997). In distinct metabolic pathways at the ER and Golgi, ceramide is further modified to form sphingomyelin and glycosphingolipids, which contain hydrophilic sugar moieties (Stults et al., 1989). At the luminal side of the ER, ceramide is galactosylated at the C1-hydroxyl group by the galactosylceramide synthase (Schulte and Stoffel, 1993; Sprong et al., 1998). Galactosylceramide (GalCer) is used as a building block for the synthesis of sulfatides, which are important structural components of myelin sheaths (Cuzner and Davison, 1968; Thudichum et al., 1884). Moreover, GalCer is highly abundant in epithelial cells, e.g in the kidney (Simons and van Meer, 1988). For the synthesis of sphingomyelin and the glycosphingolipid glucosylceramide (GlcCer), ceramide is transported from its site of synthesis at the ER to the Golgi. The transport of ceramide to the Golgi for sphingomyelin synthesis is mediated by the ceramide transport protein (CERT), which binds ceramide and via its pleckstrin homology (PH) domain recruits the lipid to the phosphatidylinositol 4-phosphate (PIP_4)-rich *trans* Golgi membrane (Hanada et al., 2003; Sugiki et al., 2012). In the Golgi lumen, sphingomyelin is synthesized by addition of phosphocholine to the C1-hydroxyl group of

ceramide (Futerman et al., 1990) and, thus, shares both phospho- and sphingolipid characteristics. The hydrolysis of sphingomyelin by sphingomyelinases allows recycling of ceramide (Okazaki et al., 1989), which can be further degraded to sphingosine or re-used for the synthesis of various sphingolipids. At the cytoplasmic side of the *cis* and *medial* Golgi (Futerman and Pagano, 1991; Schweizer et al., 1994), the glucosylceramide synthase glycosylates ceramide at the C1-hydroxyl group to GlcCer (Basu et al., 1968; Morell and Radin, 1969), the precursor for all complex glycosphingolipids of the ganglio and globo series. These glycosphingolipids themselves serve as a ceramide source and can be re-used after their hydrolysis in the salvage pathway for the synthesis of different glycosphingolipid species (Tettamanti et al., 2003).

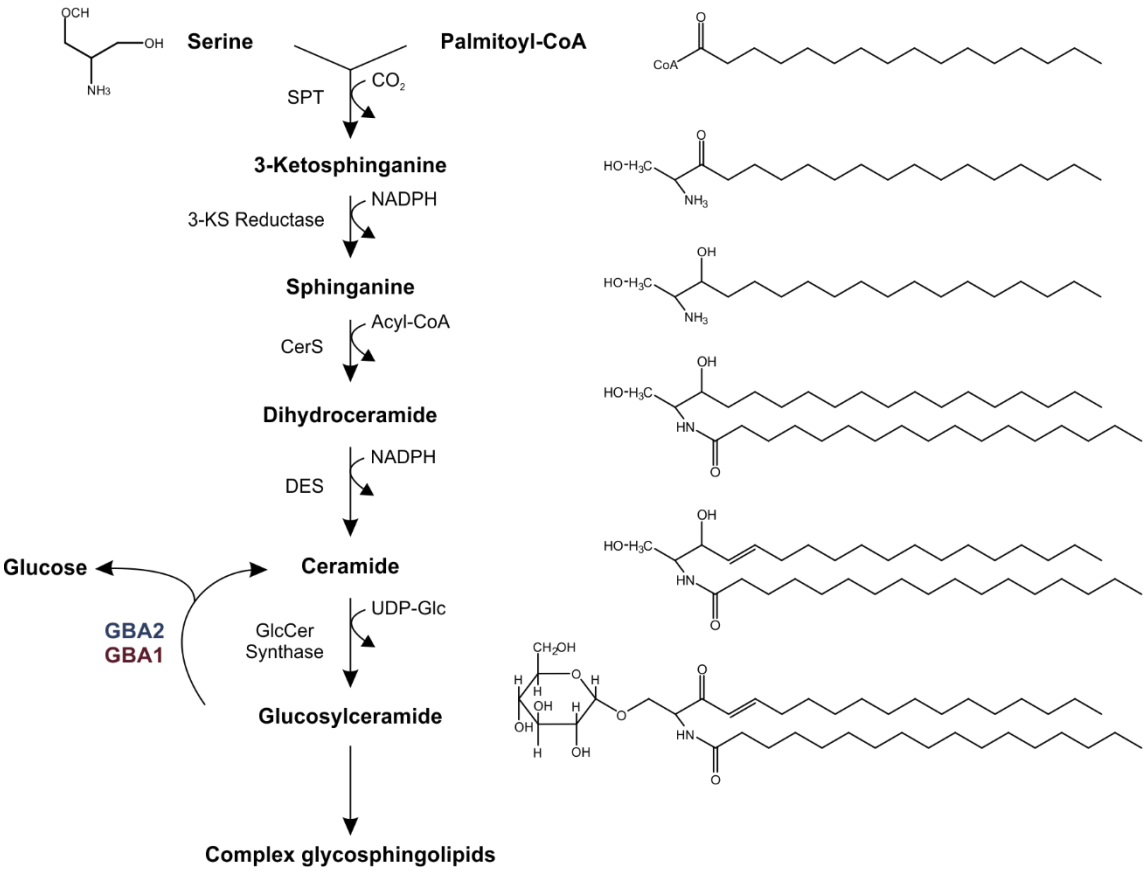

Figure 1: Synthesis of glucosylceramide as the precursor for complex glycosphingolipids. In the *de novo* pathway, serine palmitoyl-transferase (SPT) condensates serine and palmitoyl-coenzyme A (CoA) to 3-ketosphinganine (3-KS), which is subsequently reduced by the 3-ketosphinganine reductase (3-KS Reductase) to sphinganine. Ceramide synthases (CerS) acylate sphinganine to form dihydroceramide. Desaturation of dihydroceramide by the ceramide desaturase (DES) gives rise to ceramide. The glucosylceramide synthase (GlcCer Synthase) glycosylates ceramide to glucosylceramide (GlcCer) using uridine diphosphate glucose (UDP-Glc) as a donor. GlcCer is then used as a building block for the synthesis of complex glycosphingolipids. GlcCer is hydrolyzed by the β-glucosidases GBA2 and GBA1 to glucose and ceramide. Figure modified from Woeste and Wachten, 2017.

1.2 Glucosylceramide: key lipid in glycosphingolipid metabolism

For the synthesis of all complex glycosphingolipids of the ganglio and globo series, GlcCer is translocated from the cytoplasmic to the luminal side of the Golgi (Brade et al., 2000) by a yet

unidentified flippase at the ER (Chalat et al., 2012) or at the Golgi (D'Angelo et al., 2007). In a first step, galactose is attached to GlcCer by the lactosylceramide synthase (LacCer Synthase) to form lactosylceramide (LacCer) (Lannert et al., 1994; Takizawa et al., 1999). Addition of one (mono, "**M**"), two (di, "**D**"), or three (tri, "**T**") *N*-acetylneuroaminic acid (NeuAc) moieties generates the gangliosides (Klenk, 1951) of the a-, b-, and c-series with G**M**3, G**D**3, and G**T**3 being the most basic lipids, respectively (**Figure 2**) (Svennerholm, 1956; 1963; 1980). In the globo series, LacCer is further galactosylated to Gb3 (Hildebrand and Hauser, 1969). Sequential addition of *N*-acetylgalactosamine (GalNAc), galactose (Gal), and NeuAc moieties, catalyzed by specific transferases residing in the Golgi cisternae and the *trans* Golgi network (Schwarzmann and Sandhoff, 1990), forms various glycosylated and sialyated glycosphingolipids (**Figure 2**) .

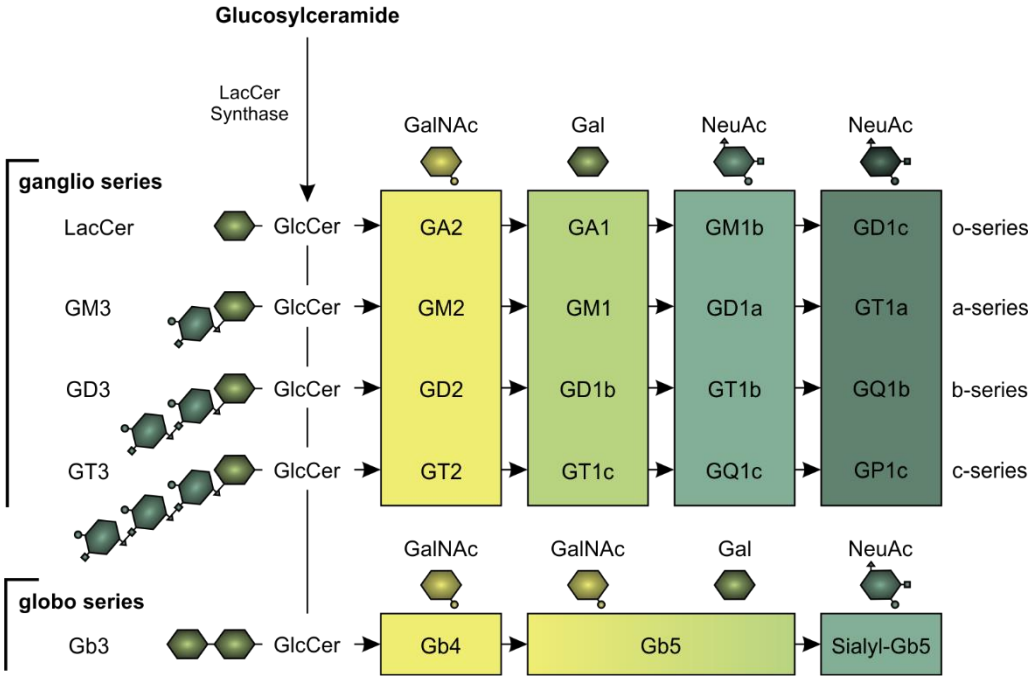

Figure 2: Synthesis of glycosphingolipids of the ganglio and globo series. In a first step, glucosylceramide is galactosylated by the lactosylceramide synthase (LacCer) to lactosylceramide (LacCer) and then gives rise to more complex glycosphingolipids of the ganglio and globo series. Sequential addition of one, two, or three N-acetylneuraminic acid residues (NeuAc) yields gangliosides of the a-, b-, or c-series, respectively. Galactosylation of LacCer is performed to build lipids of the globo series. For both ganglio and globo series, consecutive addition of N-acetylgalactosamine (GalNAc), Gal, and NeuAc by specific transferases results in glycosphingolipids of different structural complexity and function. Modified from Woeste and Wachten, 2017.

With their hydrophobic ceramide anchored in the external leaflet of the plasma membrane and their complex hydrophilic sugar and sialic acid head groups, glycosphingolipids induce a spatial segregation of incorporated lipids and shape a positive membrane curvature (Brocca and Sonnino, 1997). Moreover, these lipids together with cholesterol and sphingomyelin cluster in specific microdomains, so called *lipid rafts* (Simons and Ikonen, 1997). In lipid rafts, glycosphingolipids and cholesterol reside in the external leaflet, whereas glycerophospholipids are especially localized in the internal leaflet of the plasma membrane (Simons and Toomre,

2000). Cholesterol was shown to be required for the formation of these membrane domains, as depletion of cholesterol from the membrane using cyclodextrin disrupted lipid raft formation resulting in release of raft-associated proteins (Ilangumaran and Hoessli, 1998; Sheets et al., 1999). Interaction of cholesterol with phospho- and sphingolipids, in particular with species that contain saturated acyl chains, is thought to be involved in lipid raft formation (Ali et al., 2007; Samsonov et al., 2001; Slotte, 1999). Resistance of the membrane to detergents is proposed to be attributable to lipid rafts (Brown and Rose, 1992). However, it is still debated whether detergent-resistant membranes, indeed, resemble the lipid rafts or whether these are different entities (Lichtenberg et al., 2005). Nonetheless, glycosphingolipid-rich membrane domains play an important role in signaling as they harbor a variety of proteins, including transmembrane receptors (Bethani et al., 2010), palmitoylated proteins (Levental et al., 2010), and glycosylphospatidylinositol (GPI)-anchored proteins (Sargiacomo et al., 1993). Moreover, proteins can be selectively excluded from these domains, e.g. prenylated proteins or proteins modified by multiple unsaturated acyl chains are barely incorporated into lipid rafts (Wang et al., 2001).

Rearrangement of the membrane induced by changes in glycosphingolipid metabolism perturbs the function of membrane-associated proteins. Gangliosides modify the activity of receptors: GM3 inhibits phosphorylation of the epidermal growth factor (EGF) receptor, thereby impairing receptor dimerization and EGF signaling (Zurita et al., 2001). A similar effect was observed for the insulin receptor in adipocytes: Addition of the glycosphingolipid GM3 to cultured adipocytes negatively affected insulin signaling by impairing tyrosine phosphorylation of the insulin receptor (Tagami et al., 2002). Interestingly, obese mice that are insulin resistant reveal increased GM3 synthase mRNA levels in adipose tissue (Tagami et al., 2002). Insulin resistance in cultured adipocytes, induced by the tumor necrosis factor-alpha (TNF-α), was also accompanied by increased GM3 synthase activity. Apart from GM3, Gb3 and LacCer were shown to regulate receptor signaling: The first apoptosis signal (Fas) receptor contains a glycosphingolipid-binding domain and binds Gb3 and LacCer (Chakrabandhu et al., 2008). Disturbing the interaction by mutating the binding domain, impaired clathrin-mediated endocytosis of the receptor, but promoted an alternative internalization that finally induced a non-death signal (Chakrabandhu et al., 2008).

The oligosaccharide chains, emanating from the plasma membrane, make glycosphingolipids accessible to toxins and non-enveloped viruses: Shigatoxin and choleratoxin bind to Gb3 and GM3, respectively (Jacewicz et al., 1986; Kuziemko et al., 1996); the human rotavirus contains a sialic-acid binding site (Delorme et al., 2001) and binds to GM1, promoting internalization via the endocytic pathway (Taube et al., 2010).

Massive remodeling of glycosphingolipid species is observed during development, especially during neurodevelopment: Simple gangliosides (e.g. GD3) are predominantly generated during

embryonic brain development, whereas complex gangliosides (e.g. GD1a and sulfatides) are synthesized in later developmental stages (Ngamukote et al., 2007; Yu et al., 1988). This remodeling relies on a tight regulation of transferase and hydrolase expression and activity, and the transport of the glycosphingolipids and their precursors to the synthesis and degradation machinery residing in different cellular compartments.

1.2.1 Degradation of glycosphingolipids

Glycosphingolipids are degraded in a sequential manner by specific hydrolases that remove the sugar and sialic acid moieties from the ceramide backbone (Schwarzmann and Sandhoff, 1990). These hydrolytic pathways not necessarily implement complete elimination of glycosphingolipid metabolites, but rather serve as a huge source of sphingoid bases and sugar residues that can be re-used for the synthesis of new glycosphingolipids (Tettamanti et al., 2003). This salvage pathway is especially dominant in slowly dividing cell types (Gillard et al., 1998).

The majority of the glycosphingolipid hydrolases reside in the endosomal and lysosomal compartment, implicating that lipids need to be internalized, e.g. via the endocytic pathway (Kolter and Sandhoff, 2010). Plasma membrane lipids are majorly engulfed in endocytic vesicles into the cytosol, which fuse with early endosomes (Pryor and Luzio, 2009). During maturation, this compartment acidifies and forms the late endosome (Grabe and Oster, 2001; Maxfield and Yamashiro, 1987), which finally fuses with the even more acidic lysosome. The former plasma membrane lipids are accessible to the glycosphingolipid hydrolases on intra-endosomal and -lysosomal vesicles (Furst and Sandhoff, 1992). Finally, the β-glycosidic linkage of GlcCer is cleaved by β-glucosidases and releases glucose and ceramide, which can be further degraded to the sphingoid base and fatty acid. GBA1 and GBA2 that are also termed lysosomal and non-lysosomal glucosylceramidase (**Figure 3**), respectively, catalyze the hydrolysis of GlcCer (**Figure 1**). Moreover, a third cytosolic β-glucosidase GBA3 (**Figure 3**) has been identified (Hayashi et al., 2007); however, its natural substrate to date is unknown.

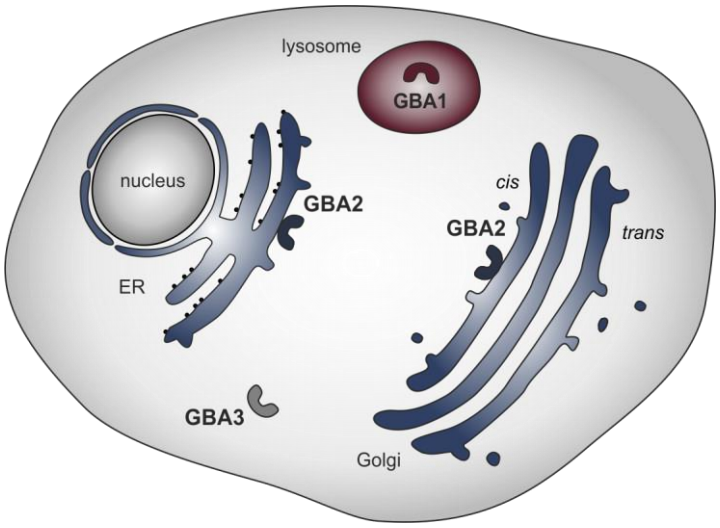

Figure 3: Cellular localization of glucosylceramidases. GBA2 is associated with the membrane of the ER and *cis* Golgi, facing the cytosol, whereas GBA1 is located in the lysosome. GBA3 is present in the cytosol. GBA1: lysosomal glucosylceramidase, GBA2: non-lysosomal glucosylceramidase, GBA3: cytosolic glucosylceramidase.

1.2.1.1 The lysosomal glucosylceramidase GBA1

Human GBA1 is encoded by the *GBA1* gene (NM_000157) on chromosome 1. The enzyme is synthesized at the ER and undergoes several posttranslational modifications, the first one being N-linked glycosylation at distinct asparagine residues (N19, N59, N146, and N270) in the ER lumen (Berg-Fussman et al., 1993). However, solely glycosylation at N19 is required for GBA1 function, whereas mutating the other asparagine residues did not affect enzyme activity (Berg-Fussman et al., 1993). GBA1 binds to hydrophobic helices in the luminal domain of the lysosomal integral membrane protein (LIMP)-2 for transport to the Golgi (Reczek et al., 2007; Zunke et al., 2016). At the Golgi, GBA1 is further modified by high-mannose oligosaccharides and sialic acid residues, resulting in the 69-kDa mature GBA1 protein (Bergmann and Grabowski, 1989). In a complex with LIMP-2, GBA1 is translocated to the *trans* Golgi network, where the proteins bud off the membrane by a clathrin-mediated vesiculation and shuttle to the lysosome (Fujita et al., 1999; Reczek et al., 2007). The GBA1/LIMP-2 interaction is highly pH dependent: Acidification, resembling the pH in the late endosomal/lysosomal compartment, was shown to induce dissociation of the complex (Zachos et al., 2012). However, the nature of the pH sensing moiety is still unclear. In the lysosome, the catalytic activity of GBA1 is dependent on its interaction with the activator protein saposin C (Berent and Radin, 1981; Ho et al., 1973). GBA1 exhibits optimal activity at pH 4 (Körschen et al., 2013) and can be inhibited by conduritol B epoxide (CBE), which irreversibly binds to the active site of the enzyme (Grabowski et al., 1986).

1.2.1.2 The non-lysosomal glucosylceramidase GBA2

Human GBA2 (hGBA2) is encoded by the *GBA2* gene (NM_020944.2) on chromosome 9 and comprises 927 amino acids with a calculated molecular mass of 104.6 kDa (Matern et al.,

2001). GBA1 and GBA2 do not share any primary or tertiary structural similarities. To date, the structure of mammalian GBA2 is unknown. According to domain predictions using InterPro (Finn et al., 2017), hGBA2 bears an N-terminal domain, spanning amino acid 151 to 455, and a catalytic glucosylceramidase domain at the C terminus, spanning amino acid 521 to 886 (**Figure 4**). Moreover, the amino acid sequences aa453-890 and aa562-877 reveal high homology to the 6-hairpin glucosidase-domain and 6-hairpin glucosidase-like domain, respectively, which are present e.g. in glucoamylases and endo- and exocellulases in homology superfamilies of GBA2 (Finn et al., 2017). The two domains differ in the number of circular arranged hairpins, with up to 6 or up to 7 hairpins for the 6-hairpin glucosidase-domain and 6-hairpin glucosidase-like domains, respectively (Finn et al., 2017). A similar domain topology is predicted for mouse GBA2 (mGBA2) (**Figure 4**). Of note, hGBA2 and mGBA2 are highly conserved, sharing 87% sequence identity (supplementary information: **Figure 79**) (Finn et al., 2017).

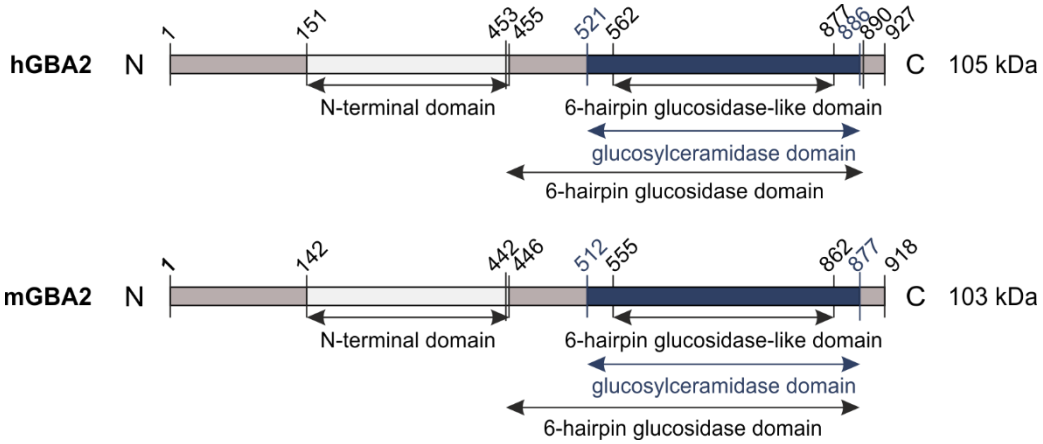

Figure 4: Postulated domain structure of human and mouse GBA2. Human GBA2 (hGBA2; 105 kDa) bears an N-terminal domain (aa151-455), a predicted catalytic glucosyceramidase domain (aa521-886), 6-hairpin glucosidase domain (aa453-890), and 6-hairpin glucosidase-like domain (aa562-877). Accordingly, postulated domains in mouse GBA2 (mGBA2; 103 kDa) include an N-terminal domain (aa142-446), a predicted catalytic glucosyceramidase domain (aa512-877), 6-hairpin glucosidase domain (aa442-877), and 6-hairpin glucosidase-like domain (aa555-862). Functional domains assigned according to InterPro (Finn et al., 2017) and protein sizes are indicated. Modified from Woeste, Master thesis, 2015.

GBA2 is ubiquitously expressed with highest expression levels in brain, liver, and testis in mice (Yildiz et al., 2006). GBA2 was identified as a β-glucosidase in human liver, hydrolyzing bile acid 3-O-glucosides (Matern et al., 1992; Matern et al., 1997). However, the enzyme was later identified as a non-lysosomal glucosylceramidase that hydrolyzes GlcCer to D-glucose and ceramide (Boot et al., 2007; van Weely et al., 1993). Initially, GBA2 was supposed to be a single transmembrane protein localized at the plasma membrane (Boot et al., 2007) or ER (Matern et al., 2001). However, we could show that GBA2 is a membrane-associated protein, located at the cytosolic side of the Golgi and the ER (**Figure 3**) (Körschen et al., 2013). Several activity studies demonstrated that GBA2 – in contrast to GBA1 – is active at a less acidic pH (Körschen et al., 2013; Matern et al., 1997; van Weely et al., 1993), depends on the presence

of phospholipids (Matern et al., 1997), and is easily disturbed by the presence of detergents (Körschen et al., 2013). Membrane solubilization or the absence of membranes was shown to be crucial for GBA2 function (Boot et al., 2007; Körschen et al., 2013). GBA2 is not inhibited by 1 mM CBE, which blocks GBA1 activity, but rather by the iminosugar *N*-butyl-deoxynojirimycin (NB-DNJ) (Overkleeft et al., 1998; van Weely et al., 1993). The IC_{50} of NB-DNJ towards GBA2 in murine liver, brain, and testis accounts for 20.9 ± 1.3 nM, 18.2 ± 0.3 nM, and 19.2 ± 0.4 nM, respectively (Körschen et al., 2013).

1.3 Glycosphingolipid-associated disorders

1.3.1 Lysosomal storage disorders

Deficiency in acid hydrolases, which degrade sphingolipids in the lysosome, or lack of glycosphingolipid transport proteins results in severe lysosomal storage disorders (Platt et al., 2012). To date, more than 50 different diseases have been identified that are mostly inherited as an autosomal-recessive trait (Filocamo and Morrone, 2011). Disease symptoms are very heterogeneous, however, patients often reveal neuropathological defects (Hoffmann and Mayatepek, 2005). Lack of the galactosylceramidase caused by mutations in the *GALC* gene in Krabbe's disease leads to muscle weakness and motor defects due to demylination and degeneration of neurons induced by the accumulation of GalCer metabolites (Suzuki, 2003). Tay-Sachs disease patients, suffering from impaired GM2 degradation (Hoffman et al., 1976; Kolodny et al., 1969), exhibit neuronal loss in the central nervous system (Huang et al., 1997). Mutations in the *GBA1* gene underlie Gaucher disease, a lysosomal storage disorder characterized by an accumulation of GlcCer (Grace et al., 1994; Scriver, 1995). A common symptom seen in Gaucher patients is organ enlargement of liver and spleen caused by excessive storage of GlcCer in resident tissue macrophages (Cox, 2001; Pennelli et al., 1969). Gaucher patients suffering from the neuronopathic form also exhibit severe neurological defects and die early during childhood (Brady et al., 1993; Scriver, 1995). Recently, both heterozygous and homozygous carriers of *GBA1* mutations were shown to have an increased risk to develop Parkinson's disease (Migdalska-Richards and Schapira, 2016), a synucleinopathy evoked by an accumulation of misfolded α-synuclein, predominantly in neurons (Breydo et al., 2012). Different models propose that either mutant GBA1 directly interacts with α-synuclein causing its aggregation (Sidransky and Lopez, 2012) or that the accumulated GlcCer and GlcCer metabolites promote α-synuclein aggregation (Blanz and Saftig, 2016; Migdalska-Richards and Schapira, 2016; Sidransky and Lopez, 2012).

To date, enzyme replacement therapy (ERT) is a commonly used therapeutic approach to ameliorate lipid accumulation in these lysosomal storage disorders (Rohrbach and Clarke, 2007).

1.3.2 GBA2-associated disorders

1.3.2.1 Male subfertility in GBA2-knockout mice

Loss of GBA2 in mice causes an accumulation of GlcCer, especially in brain, liver, and testis – the tissues with highest GBA2 expression levels (Yildiz et al., 2006). The main phenotype is male subfertility due to morphological defects that occur during sperm development, resulting in a round, globozoospermic rather than sickle-shaped sperm morphology (**Figure 5**) (Yildiz et al., 2006). Moreover, the acrosome, which contains hydrolytic enzymes packed in secretory vesicles, was completely disordered (Yildiz et al., 2006). Mitochondria that are normally tightly aligned within the sperm's head and sheath along the tail, were also misaligned (Yildiz et al., 2006).

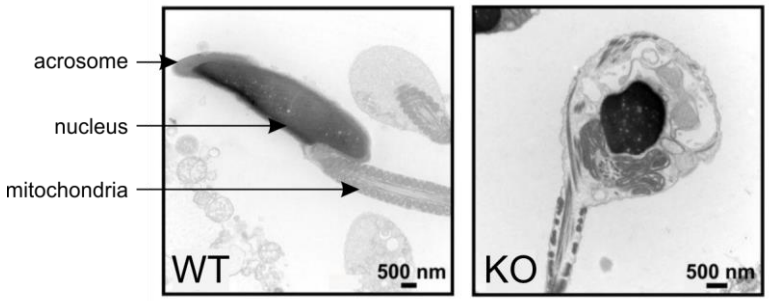

Figure 5: Impaired sperm morphology in GBA2-knockout mice. Electron micrograph of a sperm from a wild-type (WT) mouse displaying a normal sickle-shaped head (left panel), and a GBA2-knockout (KO) mouse displaying a round-shaped (globozoospermic) head (right panel). Localization of the acrosome, nucleus, and mitochondria along the tail are labelled exemplarily in the WT sperm. Scale bars are indicated. Modified from Yildiz et al., 2006.

A similar phenotype was evoked by pharmacological inhibition of GBA2 in wild-type mice (van der Spoel et al., 2002). In this study, a three-week oral administration with a daily dose of 2,400 mg/kg of NB-DNJ, resulting in a blood serum concentration of 57 µM NB-DNJ (Platt et al., 1997), inhibited GBA2 activity and caused an impaired spermatogenesis accompanied by GlcCer accumulation. This effect could be reversed after withdrawal of the inhibitor for at least 3 weeks (van der Spoel et al., 2002).

Recently, we identified the mechanism underlying impaired spermatogenesis in GBA2-knockout mice and revealed that GlcCer accumulation in sperm and Sertoli cells alters the lipid stacking of the plasma membrane (Raju et al., 2015; Yildiz et al., 2006). More precisely, the lipid organization of the plasma membranes shifts to a more ordered state, which in turn dysregulates the cytoskeletal dynamics: Microtubules persisted longer and, in particular, actin dynamics were altered (Raju et al., 2015). Using fibroblasts as a model system, we could show that actin polarization is augmented in GBA2-knockout (KO) cells. When fibroblasts were seeded on CYTOO chips that force cells to grow on a certain shape, GBA2-KO fibroblasts failed to follow this shape and exhibited extended actin protrusions, namely filopodia and lamellipodia (**Figure 6**) (Raju et al., 2015).

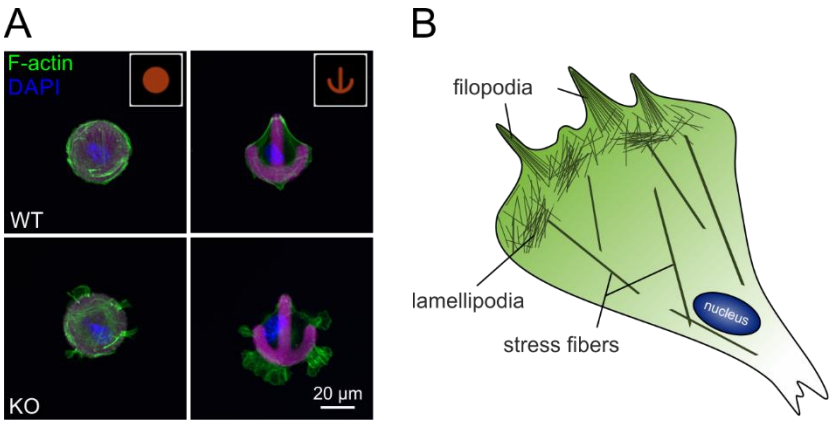

Figure 6: Analysis of the actin cytoskeleton in GBA2-knockout mouse dermal fibroblasts. A) Representative images of fibroblasts isolated from wild-type (WT) and GBA2-knockout (KO) mice were seeded on CYTOO chips with fluorescently labeled fibronectin patterns (purple) and F-actin and nuclei were stained using Alexa Fluor Phalloidin 488 (green) and DAPI (blue), respectively. Scale bar is indicated. Modified from Raju et al., 2015. **B)** Illustration of the cellular actin cytoskeleton, including filopodia (spike-like actin protrusions), lamellipodia (actin mesh at the periphery), and stress fibers (actin bundles).

We hypothesized that these changes in the actin dynamics are evoked by a change in the activity of the small Rho GTPases Cdc42 and Rac1 (Raju et al., 2015). Filopodia formation is regulated by the Cdc42, whereas lamellipodia formation is regulated by Rac1 (Hall, 1998; Nobes and Hall, 1995; Ridley et al., 1992). Both Rho GTPases are active in a GTP-bound state at the plasma membrane (Boivin and Beliveau, 1995; Fleming et al., 1996). Accumulation of GlcCer, resulting in an altered lipid stacking of the membrane, might affect their recruitment to the plasma membrane and, thereby, their activity.

1.3.2.2 Mutations in *GBA2* in neurological disorders

GBA2 not only plays a pivotal role during sperm development in the testis, it is also prominently expressed in the brain (Yildiz et al., 2006). However, so far, studies shedding light on the role of GBA2 in the brain, are lacking. Recently, several mutations in *GBA2* in human patients suffering from autosomal-recessive cerebellar ataxia (ARCA), hereditary spastic paraplegia (HSP), or Marinesco-Sjögren-like Syndrome (MSLS) have been identified (Citterio et al., 2014; Hammer et al., 2013; Haugarvoll et al., 2017; Martin et al., 2013; Votsi et al., 2014).

Homozygosity mapping and whole-exome sequencing of three Tunisian families with seven patients suffering from ARCA of unknown genetic origin, unveiled a mutation in exon 5 of the *GBA2* gene (c.1017C>T) in two families (Hammer et al., 2013). According to protein domain predictions using InterPro, this mutation results in the truncated protein R340*, lacking the C-terminal catalytic domain (**Figure 7**). Moreover, a mutation in exon 17 (c.2618G>A), resulting in the amino-acid substitution R873H (**Figure 7**) and in exon 2 (c.363C>A), resulting in the truncating Y121* (**Figure 7**) were identified in the third family and three siblings in a cohort of 21 Tunisian individuals, respectively (Hammer et al., 2013). None of the three mutations was present in 50 healthy control Tunisian families nor 330 controls of the Human Genome

Diversity Project (HGDP) (Hammer et al., 2013). Furthermore, three ARCA patients in a Cypriot family have been identified using homozygosity mapping and exome sequencing of chromosome 9 to carry a GBA2 mutation in exon 11 (c.1780G>C) or 15 (c.2201G>A) (Votsi et al., 2014). These mutations result in the amino-acid substitutions D594H and R734H (**Figure 7**), respectively, and co-segregated in the three affected patients (Votsi et al., 2014). The D594H mutation was absent in 264 Cypriot controls, R734H was found in four individuals of 52 controls and in five of 4300 control genomes of the Single Nucleotide Polymorphism database (dbSNP) and Ensemble database (Votsi et al., 2014). However, in all these individuals the R725H was solely present in a heterozygous state.

Interestingly, GBA2 mutations were also identified in HSP patients (Citterio et al., 2014; Martin et al., 2013; Sultana et al., 2015). A mutation in exon 13 (c.2048G>C) was identified by screening of 46 Italian and African families with cases of complicated HSP (Citterio et al., 2014). This mutation, resulting in the amino-acid substitution G683R, was not observed in any of the 600 controls of Italian origin nor the genome databases dbSNP or 1,000 Genomes (Citterio et al., 2014). Moreover, studies of Martin and colleagues revealed four GBA2 mutations in HSP patients with additional ataxic symptoms (Martin et al., 2013). In two families, six individuals carried the mutation c.700C>T in exon 4, resulting in the truncated protein R234*, missing the C-terminal catalytic and parts of the N-terminal domain (**Figure 7**) (Martin et al., 2013). In another family, GBA2 mutations in exon 3 (c.518G>A) and 9 (c.1471_1474dupGGCA) were identified (Martin et al., 2013). Also these mutation result in a C-terminal truncation to W173* and T492R*9, respectively (**Figure 7**).

Recently, a mutation in *GBA2* was also identified in two Norwegian families and one unrelated individual suffering from MSLS (Haugarvoll et al., 2017). Using whole-exome sequencing, Haugarvoll and colleagues identified the mutation c.1528_1529del, leading to the amino-acid substitution M510V*16 (**Figure 7**) (Haugarvoll et al., 2017). This mutations was absent in 500 control exomes and 195 control blood samples (Haugarvoll et al., 2017).

Of note, besides the mutations F419V and R870* (Sultana et al., 2015), and T492R*9 and W173* (Martin et al., 2013), which co-segregated in affected patients in a heterozygous state, all other mutations were only pathogenic in a homozygous state (Citterio et al., 2014; Hammer et al., 2013; Haugarvoll et al., 2017; Martin et al., 2013; Votsi et al., 2014).

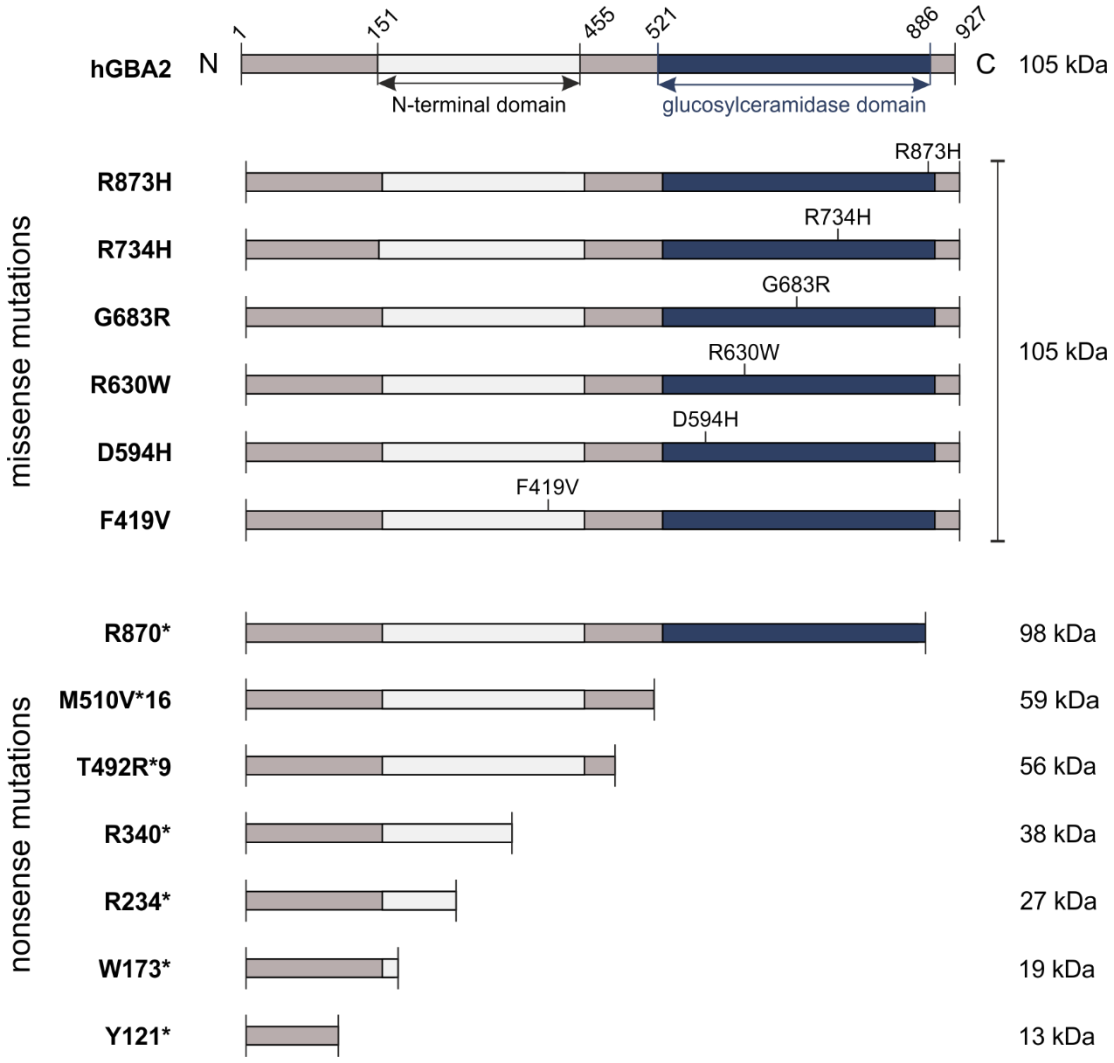

Figure 7: Mutations in hGBA2 identified in human patients. Wild-type hGBA2 (top) and the hGBA2 variants with a missense mutation R873H, R734H, G683R, R630W, D594H, and F419V, and the nonsense mutations R870*, M510V*16, T492R*9, R340*, R234*, W173*, and Y121* are depicted. Functional domains were assigned according to InterPro (Finn et al., 2017) and protein sizes are indicated. Modified from Woeste and Wachten, 2017.

Although patients carrying mutations in the *GBA2* gene were diagnosed with different neurological disorders, they all shared spastic and ataxic symptoms with an onset in childhood or early adulthood (7 ± 5 years) and slow disease progression (Citterio et al., 2014; Hammer et al., 2013; Haugarvoll et al., 2017; Martin et al., 2013; Votsi et al., 2014). In addition, more than half of the patients displayed peripheral neuropathy impairing sensory or motor functions caused by axonal damage or demyelination (Hammer et al., 2013; Haugarvoll et al., 2017; Martin et al., 2013; Votsi et al., 2014). Magnetic resonance imaging (MRI) of the brain revealed atrophy in the cerebellum, cerebrum, and/or the corpus callosum in several patients. Furthermore, reflex tests at the lower or upper limbs provoked brisk reflexes in the patients, in some cases a Babinski or Hoffman sign was observed, indicating defects in the corticospinal tracts (Citterio et al., 2014; Hammer et al., 2013; Martin et al., 2013; Votsi et al., 2014). Less common symptoms included amyotrophy, dysathria, and tremor of the upper limbs or head (Citterio et al., 2014; Hammer et al., 2013; Haugarvoll et al., 2017; Martin et al., 2013). Taken

together, patients developed quite diverse symptoms during disease progression with predominant ataxia and spasticity.

So far, first attempts to decode the role of GBA2 in locomotion have only been performed in a zebrafish model (Martin et al., 2013). When injecting antisense *zGba2* mRNA into larvae to depress GBA2 expression, malformation of the tail and motor coordination defects was observed in 12.5% of the animals (Martin et al., 2013). Detailed analyses of the motor neurons in the zebrafish spinal cord revealed defective axon growth that could be rescued by injection of wild-type, but not R630W hGBA2 mRNA (Martin et al., 2013). Moreover, lymphocytes or leukocytes isolated from three human patients carrying the R630W mutation, did not show any GBA2 activity, at least in the experimental set-up used (Martin et al., 2013). A first functional study of the GBA2 mutations using a luciferase-based activity assay revealed that the hGBA2 variants Y121*, W173*, R234*, R340*, F419V, D594H, R630W, G683R, R870*, and R873H are devoid of GBA2 activity (Sultana et al., 2015). However, also the expression levels of the mutant proteins in transfected COS-7 and HeLa cells were decreased compared to wild-type hGBA2 (Sultana et al., 2015).

1.4 Aim of this thesis

A variety of mutations in the *GBA2* gene of ARCA, HSP, and MSLS patients have been identified. In my thesis, I analyzed whether these mutations in GBA2 result in a loss of function of the enzyme, leading to defects in the central nervous system and, in turn, locomotor dysfunction. Two studies have already shown that 1.) some GBA2 mutations identified in ARCA and HSP patients result in a loss of function of the enzyme (Sultana et al., 2015) and 2.) zebrafish lacking GBA2 display motor coordination defects and impaired axon outgrowth in the spine (Martin et al., 2013). However, a direct link between a defect in GBA2 function and locomotor dysfunction in mammals, to date, has not been described and the underlying mechanisms remain enigmatic. Moreover, a structure-function relationship for GBA2 has not been precisely defined. Using mice as a model system, I aimed to 1.) characterize the GBA2 mutations identified in human patients, 2.) analyze the structural and functional properties of GBA2, and 3.) define the role of GBA2 in controlling locomotor activity *in vivo*.

2 Material and methods

2.1 Chemicals

Chemicals in *pro analysis* quality were purchased from AppliChem (Darmstadt), BioRad (Munich), Eppendorf (Hamburg), GE Healthcare Life Sciences (Munich), Invitrogen (Karlsruhe), Merck (Darmstadt), Piramal Healthcare (Bethlehem, USA), Polysciences Inc. (Pennsylvania, USA), Quiagen (Hilden), Roth (Karlsruhe), Sigma (Steinheim), and Thermo Scientific (Waltham, USA). Oligonucleotides were generated and ordered from Eurofins MWG Operon (Ebersberg). Enzymes and corresponding buffers were purchased from Cell systems (Troisdorf), Novagen (Darmstadt), New England Biolabs (Frankfurt), Sigma (Steinheim), and Roche (Mannheim). Primary and secondary antibodies were purchased from Abcam (Cambridge, UK), Cell Signaling (Massachusetts, USA), Cytoskeleton Inc. (Denver, USA), Dianova (Hamburg), BioLegend (San Diego, USA), LI-COR Biosciences (Nebraska, USA), Sigma (Steinheim), and Thermo Scientific (Waltham, USA). PVDF-membrane Immobilon-P for protein transfer via Western blotting was purchased from Merck Millipore (Darmstadt).

All buffers and solutions were prepared using double-distilled water (ddH_2O). Autoclaving for sterilization was performed at 121°C for 20 min, if necessary. Sterile-filtering of buffers was achieved using 0.45 µm or 0.22 µm pore filter membranes (Millipore) in a vacuum filtration.

2.2 Cell culture material

The CHO K1 cell line was purchased from European Collection of Cell Cultures (ECACC). Cryo tubes were purchased from Thermo Scientific (Waltham, USA), media and buffers were purchased from Thermo Scientific (Waltham, USA), cell culture supplements were purchased from Biochrome (Berlin), Pan Biotech (Aidenbach), Sigma (Steinheim), and Thermo Scientific (Waltham, USA).

2.3 Antibodies

2.3.1 Primary antibodies

Commercially available primary antibodies from Abcam (Cambridge, UK), BioLegends (San Diego, USA), Cell Signaling (Massachusetts, USA), Cytoskeleton Inc. (Denver, USA), and Sigma (Steinheim) were used for immunocytochemical (ICC) stainings and Western blot analysis (WB) (**Table 1**). The monoclonal rat antibodies against GBA2 were generated as described in Körschen et al., 2013. The polyclonal rabbit antibodies against GBA2 were generated as described in Schonauer et al., 2017.

Table 1: Primary antibodies used for immunocytochemistry and Western blot analysis

Antibody	kDa	Species	Type	Dilution		Producer	Catalog #
				ICC	WB		
β-Actin	42	ms		-	1:5000	abcam	ab8224
β-Actin AC-15	42	ms	mAb	-	1:10,000	abcam	ab6276
Calnexin	90	rb	pAb	-	1:1000/ 1:5000/ 1:10,000	Sigma	C4731
Caveolin-1	21	rb	pAb	-	1:1000	Cell Signaling	3238
Cdc42	21	ms	pAb	-	1:1000	Abcam	ab64533
Desmin	50-55	ms	mAb	-	1:500	Sigma	D1033
Flag M2	-	ms	mAb	-	1:1000/ 1:2000	Sigma	F1804
HA (R001 3F10)	-	rt	mAb	1:1000	1:5000	EKr	n.a.
HA-7	-	ms	mAb	1:500	-	Sigma	H9658
GAPDH-71.1	37	ms	mAb	-	1:30,000	Sigma	G9295
GBA2-5kb	103	rb	pAb	-	1:500/ 1:1000/ 1:5000	HGKö	n.a.
GBA2-4kb/5kb	103	rb	pAb	-	1:2000/ 1:5000	HGKö	n.a.
GBA2-2F8	103	rt	mAb	-	1:10	EKr	n.a.
MBP-7G4	-	rt	mAb	-	1:1000/ 1:3000/ 1:10,000	EKr	n.a.
Rac1	21	ms	mAb	-	1:1000	Abcam	ab33186
Rac1	21	ms	mAb	-	1:1000	Cytoskeleton Inc.	ARC03
α-Tubulin B-5-2-1	55	ms	mAb	-	1:5000	Sigma	T5168

Antibody	kDa	Species	Type	Dilution		Producer	Catalog #
				ICC	WB		
β-Tubulin 2.1	55	ms	mAb	-	1:1000/ 1:10,000	Sigma	T4026
β-Tubulin III, neuronal (TUJ1)	50	ms	mAb	1:500	-	BioLegends	MMS-435P

EKr: E. Kremmer (HZ München), HGKö: Dr. Heinz Gerd Körschen, ICC: Immunocytochemistry, WB: Western blot, MW: molecular weight, kDa: kilo Dalton, mAb: monoclonal antibody, ms: mouse, pAb: polyclonal antibody, rt: rat, rb: rabbit, kb: Körschen, Bonn

2.3.2 Secondary antibodies

Secondary antibodies used for immunocytochemical stainings (ICC) and Western blot analysis (WB) were purchased from Dianova (Hamburg), LI-COR Biosciences (Nebraska, USA), and Thermo Scientific (Waltham, USA) (**Table 2**).

Table 2: Secondary antibodies used for immunocytochemistry and Western blot analysis

Antigen	Antibody	Species	Type	Dilution		Producer	Catalog #
				ICC	WB		
ms	ms Alexa 488	gt	pAb	1:400	-	Thermo Scientific	A11029
ms	IRDye 680RD	dk	pAb	-	1:20,000	LI-COR Biosc.	926-68072
ms	IRDye 800CW	dk	pAb	-	1:20,000	LI-COR Biosc.	926-32212
ms	ms HRP	sh	pAb	-	1:5000	Dianova	515-035-062
rb	IRDye 680RD	dk	pAb	-	1:20,000	LI-COR Biosc.	926-32223
rb	IRDye 800CW	dk	pAb	-	1:20,000	LI-COR Biosc.	926-32213
rb	rb HRP	dk	pAb	-	1:5000	Dianova	711-035-152
rt	rt Alexa 488	dk	pAb	1:500	-	Dianova	712-545-153

Antigen	Antibody	Species	Type	Dilution		Producer	Catalog #
				ICC	WB		
rt	IRDye 680LT	gt	pAb	-	1:20,000	LI-COR Biosc.	926-32229
rt	IRDye 800CW	gt	pAb	-	1:20,000	LI-COR Biosc.	926-32219
rt	rt HRP	gt	pAb	-	1:5,000	Dianova	112-035-068

ICC: Immunocytochemistry, IRDye: infrared dye, kDa: kilo Dalton, mAb: monoclonal antibody, ms: mouse, MW: molecular weight, pAb: polyclonal antibody, rt: rat, rb: rabbit, gt: goat, dk: donkey, sh: sheep, WB: Western blot

2.3.3 Dyes

Table 3: Dyes used for immunocytochemistry

Dye	Dilution ICC	Producer	Catalog #
Rhodamine-conjugated Phalloidin	1:500	Life Technologies	R415
Alexa Fluor™ 488-conjugated Phalloidin	1:500	Life Technologies	A12379
4',6-Diamidino-2-Phenylindole (DAPI)	1:10,000	Life Technologies	D1306

2.4 Molecular biology

2.4.1 Cloning of wild-type and mutant mGBA2 proteins

2.4.1.1 Vectors

The vectors pcDNA3.1(+) (Invitrogen; pcDNA3), pET21a (Novagen; pET21), and pET28 MBP-tev (provided by Prof. Dr. Matthias Geyer) were used to generate plasmids for the expression of wild-type and mutant mGBA2 proteins in mammalian cells and bacteria.

2.4.1.2 Primers

Primers were synthesized by Eurofins MWG Operon (Ebersberg; **Table 38**). The lyophilisate was dissolved in TE buffer to a final concentration of 100 µM and stored at -20°C. The pcDNA6 mGBA2-Flag (Dr. W. Bönigk, 2014; pcDNA6/V5-HisA, Invitrogen) and pcDNA3 mGBA2-HA (Dr. W. Bönigk, 2012) plasmids were used as a template DNA. Mutant mGBA2-x-HA plasmids (listed in **Table 4**) served as a template to generate mGBA2 2A peptide constructs (**Table 4**).

Table 4: Primers used to generated mGBA2 constructs

Internal construct #	Vector	Expresses	Internal primer #	Producer
371	pcDNA3	mGBA2-R864H-HA	C1067/C2068; C2069/C0609; C1067/C0609	CMa
365	pcDNA3	mGBA2-R864K-HA	C1054/C2444; C2445/C1997; C1054/C0609	WBö
364	pcDNA3	mGBA2-R864Q-HA	C1054/C2446; C2447/C1997; C1054/C0609	WBö
388	pcDNA3	mGBA2-R725H-HA	C1054/C2477; C2478/C0609; C1054/C0609	WBö
372	pcDNA3	mGBA2-R621W-HA	C1067/C2066; C2067/C0609; C1067/C0609	CMa
363	pcDNA3	mGBA2-R621K-HA	C1054/C2440; C2441/C1997; C1054/C0609	WBö
362	pcDNA3	mGBA2-R621Q-HA	C1054/C2442; C2443/C1997; C1054/C0609	WBö
386	pcDNA3	mGBA2-G674R-HA	C1054/C2475; C2476/C0609; C1054/C0609	WBö
387	pcDNA3	mGBA2-D585H-HA	C1054/C2473; C2474/C0609; C1054/C0609	WBö
597	pcDNA3	mGBA2-F410V-HA	C1054/C3635; C3636/C1055; C1054/C1055	MWo
370	pcDNA3	mGBA2-T483R*9-HA	C1054/C2070; C1054/C2071; C1054/C0609	CMa
369	pcDNA3	mGBA2-R331*-HA	C1054/C2065; C1054/C0609	CMa
368	pcDNA3	mGBA2-R225*-HA	C1054/C2064; C1054/C0609	CMa
367	pcDNA3	mGBA2-W164*-HA	C1054/C2063; C1054/C0609	CMa
366	pcDNA3	mGBA2-Y112*-HA	C1054/C2062; C1054/C0609	CMa
406	pcDNA3	mGBA2-Q882*-HA	C2474/C2665; C2474/C0609	WBö
396	pcDNA3	mGBA2-aa442/918-HA	C2609/C0609	MWo
397	pcDNA3	mGBA2-aa512/918-HA	C2610/C0609	MWo
404	pcDNA3	mGBA2-aa126/918-HA	C2663/C0609	MWo

Internal construct #	Vector	Expresses	Internal primer #	Producer
405	pcDNA3	mGBA2-aa136/918-HA	C2664/C0609	MWo
567	pcDNA3	mGBA2-WT-Flag-2A	C3462/C1055; C1056/C3463; C3464/C3476; C1056/C3477; C3464/3478; C3464/C3479; C3462/C3480	WBö
573	pcDNA3	mGBA2-WT-Flag-2A-mGBA2-WT-HA	Ligation of restricted #567/ #373	WBö
615	pcDNA3	mGBA2-WT-Flag-2A-mGBA2-R864H-HA	Ligation of restricted #567/ #371	WBö
696	pcDNA3	mGBA2-R864H-Flag-2A-mGBA2-R864H-HA	C3462/C3463; C3464/C2436, C3464/C3476; C3464/C3477; C3464/C3478; C3464/C3479; C3462/C3480	WBö
617	pcDNA3	mGBA2-WT-Flag-2A-mGBA2-R725H-HA	Ligation of restricted #567/ #388	WBö
693	pcDNA3	mGBA2-R725H-Flag-2A-mGBA2-R725H-HA	C3462/C3463; C3464/C2436, C3464/C3476; C3464/C3477; C3464/C3478; C3464/C3479; C3462/C3480	WBö
613	pcDNA3	mGBA2-WT-Flag-2A-mGBA2-R621W-HA	Ligation of restricted #567/ #372	WBö
675	pcDNA3	mGBA2-R621W-Flag-2A-mGBA2-R621W-HA	C3462/C3463; C3464/C3480 C3462/C3480	WBö
634	pcDNA3	mGBA2-WT-Flag-2A-mGBA2-G674R-HA	Ligation of restricted #567/ #386	WBö
676	pcDNA3	mGBA2-G674R-Flag-2A-mGBA2-G674R-HA	C3462/C3463; C3464/C3480 C3462/C3480	WBö

Internal construct #	Vector	Expresses	Internal primer #	Producer
619	pcDNA3	mGBA2-WT-Flag-2A-mGBA2-D585H-HA	Ligation of restricted #567/ #387	WBö
674	pcDNA3	mGBA2-D585H-Flag-2A-mGBA2-D585H-HA	C3462/C3463; C3464/C3480 C3462/C3480	WBö
636	pcDNA3	mGBA2-WT-Flag-2A-mGBA2-F410V-HA	Ligation of restricted #567/ #597	WBö
672	pcDNA3	mGBA2-F410V-Flag-2A-mGBA2-F410V-HA	C3462/C3463; C3464/C3480 C3462/C3480	WBö
609	pcDNA3	mGBA2-WT-Flag-2A-mGBA2-T483R*9-HA	Ligation of restricted #567/ #370	WBö
673	pcDNA3	mGBA2-T483R*9-Flag-2A-mGBA2-T483R*9-HA	C3462/C3800; C3462/C3801; C3462/C3477; C3462/C3478; C3462/C3479; C3462/C3480	WBö
609	pcDNA3	mGBA2-WT-Flag-2A-mGBA2-R331*-HA	Ligation of restricted #567/ #369	WBö
671	pcDNA3	mGBA2-R331*-Flag-2A-mGBA2-R331*-HA	C3462/C3804; C3462/C3805; C3462/C3477; C3462/C3478; C3462/C3479; C3462/C3480	WBö
623	pcDNA3	mGBA2-WT-Flag-2A-mGBA2-R225*-HA	Ligation of restricted #567/ #368	WBö
670	pcDNA3	mGBA2-R225*-Flag-2A-mGBA2-R225*-HA	C3462/C3866; C3462/C3867; C3462/C3477; C3462/C3478; C3462/C3479; C3462/C3480	WBö
611	pcDNA3	mGBA2-WT-Flag-2A-mGBA2-W164*-HA	Ligation of restricted #567/ #367	WBö

Internal construct #	Vector	Expresses	Internal primer #	Producer
669	pcDNA3	mGBA2-W164*-Flag-2A-mGBA2-W164*-HA	C3462/C3802; C3462/C3803; C3462/C3477; C3462/C3478; C3462/C3479; C3462/C3480	WBö
625	pcDNA3	mGBA2-WT-Flag-2A-mGBA2-Y112*-HA	Ligation of restricted #567/ #366	WBö
668	pcDNA3	mGBA2-Y112*-Flag-2A-mGBA2-Y112*-HA	C3462/C3802; C3462/C3803; C3462/C3477; C3462/C3478; C3462/C3479; C3462/C3480	WBö
n.a.	pET21	mGBA2-His	C1061/C1055; C1056/C1216; C1056/C1217	WBö
417	pET28	MBP-tev-mGBA2-126/882	C2793/C2794; C2795/C2796; C2793/C2796	WBö

CMa: Carina E. Marx, HA: hemagglutinin, pcDNA3: pcDNA3.1(+), pcDNA6: pcDNA6/V5-HisA, pET21: pET21a, MWo: Marina A. Woeste, WBö: Dr. Wolfgang Bönigk, WT: wild-type

2.4.1.3 Polymerase Chain Reaction (PCR)

Polymerase chain reaction (PCR) was performed to amplify DNA fragments of interest using sequence-specific primers (**Table 4**). The reactions were performed in a Thermocycler (Labcycler, SensoQuest) using the KOD Hot Start DNA Polymerase (Novagen) and the corresponding buffer and kit components in a 50 µl approach as listed in **Table 5**. Prior to amplification in repetitive cycles, the DNA was initially denatured at 94°C for 2 min. During the repetitive cycles (35 to 40), denaturation was accomplished at 94°C in 45 sec. Annealing of the primers was allowed for 45 sec at a temperature closest to the lowest melting temperature (T_m) of the two primers, which is calculated as follows:

$$T_m = \left(\frac{G}{C}\right) \text{x } 4°\text{C} + \left(\frac{A}{T}\right) \text{x } 2°\text{C} - (basepair\ mismatches) \text{ x } 4°\text{C} - 4°\text{C}$$

Elongation of the DNA was performed at 72°C for 1 min per 1000 bp, before cycles were repeated starting with DNA denaturation. A final extension was allowed at 70°C for 2 min, then PCR mixture was cooled to 8°C. To validate DNA amplification, 5 µl of the PCR product was subjected to agarose gel electrophoresis (2.4.1.4).

Table 5: Pipetting scheme for PCR reactions

PCR master mix
50 ng plasmid DNA
5 µl KOD Hot Start DNA Polymerase buffer (10 x; Novagen)
5 µl dNTP (2 mM; Novagen)
2 µl $MgSO_4$ (25 mM; Novagen)
3 µl forward primer (5 pmol/µl)
3 µl reverse primer (5 pmol/µl)
1 µl KOD HOT Start DNA Polymerase (1 U/µl; Novagen)
fill up with ddH_2O to 50 µl

2.4.1.4 Agarose gel electrophoresis for detection of nucleic acids

DNA fragments were separated according to their size in an agarose gel electrophoresis. 1% (w/v) agarose gels were prepared for analyzing 500- to 10,000-bp DNA fragments. Agarose was dissolved in 1 x TAE buffer by heating in a micro wave. After cooling down to approximately 60°C, ethidium bromide was added to a final concentration of 1 µg/ml and the gel was poured into a gel chamber with inserted comb. The samples were prepared with 10 x loading buffer (final 1x; **Table 6**). Lambda DNA/EcoRI+HindIII Marker (Thermo Scientific) or GeneRuler 1 kb DNA ladder (Thermo Scientific) served as a size standard (10 µl loaded per lane; **Figure 8**). 1 x TAE buffer served as a running buffer for gel electrophoresis, which was performed at 120 V for 20 to 25 min. Finally, DNA fragments were visualized with UV light using a gel documentation system (Vilber Lourmat).

Table 6: Buffers used for agarose gel electrophoresis

TAE buffer (50 x)	Loading buffer (10 x)
2 M tris/acetate pH 7.5	10 x TAE buffer
50 mM EDTA	50% (v/v) glycerol
	0.25% (v/v) xylene cyanol

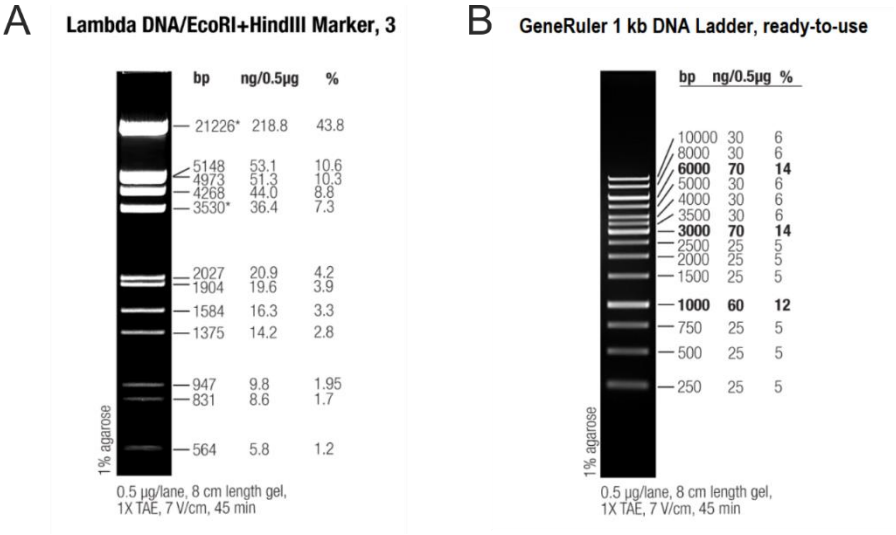

Figure 8: DNA standards used for agarose gel electrophoresis. A) Lambda DNA/EcoRI+HindIII Marker (Thermo Scientific) and **B)** GeneRuler 1 kb DNA Ladder (Thermo Scientific).

2.4.1.5 DNA purification using Sure Clean

DNA was purified for subsequent cloning procedures using the Sure Clean Plus Pink reagent (Bioline) according to the manufacturer's protocol at room temperature. An equal volume of the reagent was added to the DNA sample, mixed thoroughly, and incubated for 10 min. The DNA was pelleted at 14,000 x g for 10 min and washed with 2 x DNA sample volume of 70% ethanol. The mix was vortexed for 10 sec, then ethanol was removed in a subsequent centrifugation (14,000 x g, 10 min). The DNA pellet was air-dried and finally dissolved in an appropriate volume of TE buffer (**Table 7**) or ddH_2O.

Table 7: TE buffer used to dissolve DNA

TE buffer
10 mM Tris/HCl pH 8.0
1 mM EDTA

2.4.1.6 Restriction digest of plasmid DNA

To enable subcloning of generated plasmid DNA into the vector of interest, both had to be digested by restriction endonucleases. 1 to 3 U/ µg DNA of restriction enzyme, purchased from New England Biolabs (Frankfurt) or Roche (Mannheim), was used for the digestion. Buffers were used according to the manufacturer's protocol and digestion with two or more enzymes at once was only performed if the enzymes were compatible with one and the same buffer. If an enzyme was known to lose its activity using another enzyme's buffer, restriction digest was performed in a two-step approach including a DNA fragment purification via agarose gel electrophoresis after the first restriction digestion. Restriction digest was performed at 37°C (if

not stated otherwise in the enzyme's data sheet) for 1 to 1.5 h. The entire volume of the restriction digest was loaded for agarose gel electrophoresis (2.4.1.4) and the DNA fragments of interest were extracted (2.4.1.7).

2.4.1.7 Extraction of DNA from agarose gels

DNA was extracted from agarose gel using the NucleoSpin Kit (Macherey-Nagel) according to the manufacturer's protocol. In short, gel slices containing DNA fragments of interest were dissolved in 200 µl NTI buffer per 100 mg gel at 50°C for up to 10 min. The sample was loaded onto a filter column, centrifuged for 30 sec at 11,000 x g and washed twice with NT3 buffer. An additional centrifugation allowed the column to dry and remove residual washing buffer. Finally, column-bound DNA was eluted in 30 µl TE buffer in a 1-min incubation at room temperature and subsequent centrifugation at 11,000 x g for 1 min.

2.4.1.8 Ligation of DNA fragments with vector

DNA fragments were ligated with the pcDNA3.1(+) (Invitrogen), pcDNA6/V5-HisA (Invitrogen), or pET28 MBP-tev vector (Prof. Dr. Matthias Geyer) using the T4-DNA ligase (Roche) in an 1- to 2-h incubation at 37°C. To do so, 0.5 µl T4-DNA ligase (Roche), 1x ligation buffer (Roche), 1 µl 25 mM $MgCl_2$ (Thermo Scientific), 50 ng digested vector, and 2 x to 5 x molar excess of insert DNA (determined by agarose gel electrophoresis of digested vector and insert in comparison to a standard with known DNA quantity) was prepared in a total volume of 10 µl.

2.4.1.9 Determining nucleic acid concentrations by spectrophotometry

Using a spectrophotometer (Hitachi U-1900), the DNA concentration was determined in DNA diluted in TE buffer at OD_{260} in comparison to a blank sample. 50 µg/ml DNA result in an OD_{260} of 1, according to this, the DNA concentration in the measured sample can be calculated. As a read-out for the purity of the DNA sample, the OD_{280} was determined additionally. A 260/280 ratio smaller than 1.8 indicates low purity of the DNA but high contamination with e.g. proteins. Similarly, the DNA concentration was determined using 1.5 µl of the DNA sample in the NanoDrop ND-1000 spectrophotometer (NanoDrop Products).

2.5 *Escherichia coli* culture

2.5.1 Bacterial strains

The *Escherichia coli* (*E.coli*) strain XL1-Blue (#200249, Stratagene, California, USA) and One Shot™ TOP10 (#C404010, Invitrogen, California, USA) was used to amplify plasmid DNA. The *E.coli* strain BL21 (DE3) pLysE (#69389-3, Novagen, California, USA) and BL21 CodonPlus (DE3) RIPL (#230280, Stratagene, California, USA) was used for the expression of MBP-tev-mGBA2-126/882 and wild-type mGBA2, respectively.

2.5.2 Culture medium

E.coli bacteria were grown at high density in liquid culture using lysogeny broth (LB)-medium (Roth; **Table 8**) or isolated as individual colonies on solid LB-agar plates. LB-agar plates were prepared by addition of 15 g/l agar (Sigma) to the LB-medium. Both LB-containing media were autoclaved at 121°C for 20 min to prevent bacterial contamination. After cooling down to 50°C, antibiotics were added to the LB-agar suspension to a final concentration of 100 µg/ml (ampicillin) or 30 µg/ml (kanamycin). LB-agar plates were stored at 4°C, LB-medium at room temperature until further use.

Table 8: *E.coli* culture medium

Lysogeny broth (LB)-medium (Roth)
10 g/l Tryptone
5 g/l Yeast extract
5 g/l NaCl
pH 7.0 ± 0.2

2.5.3 Generation of competent *E.coli*

$CaCl_2$ transformation of *E.coli* was performed to enable incorporation of plasmid DNA and was performed according to a modified protocol based on the technique established elsewhere (Mandel and Higa, 1970). 50 ml bacterial culture was grown to an OD_{600} of 0.4 resembling a cell density of approximately 2 x 10^8 cells/ ml. Cells were allowed to acclimate on ice for 30 min before they were pelleted at 5,000 x g for 10 min at 4°C. The pellet was resuspended in 1 ml ice-cold 0.1 M $CaCl_2$ and filled up to a final volume of 25 ml. Cells were incubated with $CaCl_2$ for 20 min on ice, pelleted again as described before, resuspended in 1 ml ice-cold 0.1 M $CaCl_2$ containing 25% glycerol. Finally, the stock of competent cells was brought to a volume of 5 ml, incubated for 2 more h on ice, and aliquoted to be stored at -80°C (after snap-freezing in liquid nitrogen) until further use.

2.5.4 DNA amplification in *E.coli*

2.5.4.1 Transformation of competent bacteria

50 µl competent bacteria were transformed with 1 µl plasmid DNA or 5 µl ligation mix precooled with 5 µl CM buffer (100 mM $CaCl_2$/ 400 mM $MgCl_2$) in ddH_2O to make a final volume of 100 µl. DNA/*E.coli* mix was incubated on ice for 20 min prior to a heat shock at 42°C for 1 min. 200 µl prewarmed LB medium was added and bacterial suspension was incubated at 37°C for 30-45 min. Transformed bacteria (50 to 100 µl) were plated on LB agar plates containing antibiotic (100 µg/ml ampicillin or 30 µg/ml kanamycin) and grown overnight at 37°C. Colonies

were then picked to finally inoculate 250 ml or 500 ml LB after growing a preculture in 5 ml LB overnight at 37°C on an orbital shaker. Transformed bacteria were used to isolate amplified plasmids (2.5.4.2, 2.5.4.3) or express recombinant protein (2.11.5, 2.11.5.2).

2.5.4.2 Small-scale (Mini) plasmid preparation via alkaline lysis

Plasmid DNA was extracted from 5 ml overnight cultures via alkaline lysis in a Mini prep (Birnboim and Doly, 1979). All steps were performed at room temperature with centrifugations at 20,000 x g. Bacteria grown in 2 ml of the overnight culture were pelleted by centrifugation for 1 min and resuspended in 150 µl solution I by vortexing (**Table 9**). Subsequently, 180 µl solution II was added and gently mixed by inverting the tube to lyse the cells (**Table 9**). Immediately, proteins were denatured by addition of 225 µl solution III (**Table 9**). The sample was then centrifuged for 5 min and the supernatant was transferred to a fresh reaction tube to precipitate the plasmid DNA by addition of 1.5 ml 100% ethanol. The solution was centrifuged for 5 min and the pellet was washed with 1 ml 75% ethanol. The final DNA pellet was allowed to dry at 37°C and dissolved in 20 µl TE buffer containing 8 µg/ml RNase Cocktail (Ambion) at 37°C for 15 min. A test digest was performed to verify amplification of subcloned plasmid DNA via agarose gel electrophoresis.

Table 9: Solution used for alkaline lysis of bacteria to isolate plasmid DNA

Solution I	Solution II	Solution III
25 mM Tris/HCl pH 8.0 10 mM EDTA 50 mM glucose	0.2 M NaOH 1% (w/v) SDS	3 M CH_3CO_2K pH 4.8

2.5.4.3 Sequencing of amplified plasmid DNA

Sequencing was performed at Eurofins Genomics (Ebersberg) and 7.5 µl plasmid DNA diluted in ddH_2O to a total volume of 15 µl was sent. If needed, primers for sequencing were added in 15 µl aliquots of a 2 pmol/µl dilution prepared in ddH_2O. Sequences of all DNA constructs used for this study were validated (data not shown).

2.5.4.4 Large-scale (Midi/Maxi) plasmid preparation

Large-scale amplification of plasmid DNA was performed in 250 ml or 500 ml overnight cultures of bacteria (2.5.4.1). DNA isolation from the bacterial cultures was performed using the NucleoBond Xtra Midi or Maxi Kit (Macherey-Nagel) according to the manufacturer's protocol. For Midi preparation from a 250 ml culture, bacteria were first pelleted by centrifugation at 6,000 x g for 15 min (4°C) and resuspended in 20 ml resuspension buffer supplemented with RNase A prior to use. Cells were lysed by addition of 20 ml lysis buffer by gently inverting the

tube and incubating for 5 min at room temperature. Solution was neutralized with 20 ml neutralization buffer and subsequently loaded onto the equilibrated filter column. The column was washed with 25 ml equilibration buffer and 25 ml washing buffer after sample has run through via gravity flow. The plasmid DNA was eluted with 15 ml elution buffer and precipitated by addition of 10.5 ml isopropanol by inverting the tube. Finally, DNA was pelleted by centrifugation at 15,000 x g for 45 min (4°C), washed once with 5 ml 70% ethanol, air-dried, and finally dissolved in 200 to 300 µl TE buffer.

2.6 Mice

All experiments were performed in agreement with the German law of animal protection and local institutional animal care committees (Landesamt für Natur, Umwelt und Verbraucherschutz, LANUV; Az 84-02.04.2014.A194). Mice were maintained in individually ventilated cages in the mouse facility of the Center of Advanced European Studies and Research (caesar), Bonn. Animals were given water and complete diet (sniff Spezialdiäten) ad libitum. Perfusion of mice was approved by LANUV Az 84-02.04.2017.A246.

2.6.1 Isolation of genomic DNA from mouse tails

Tail tips from mice were taken to isolate genomic DNA for genotyping polymerase chain reaction (PCR). 250 µl or 500 tail lysis buffer (**Table 10**) was added to tail tips from early postnatal or adult mice, respectively, and lysis was performed at 56°C for 4 h or overnight. Lysed tissue was then centrifuged at 14,000 x g for 5 min at room temperature and supernatant was transferred to the same volume of isopropanol. Inverting the tubes enabled precipitation of the DNA, which was subsequently pelleted by centrifugation for at least 30 min at 14,000 x g at 4°C. Next, pellets were washed in 70% ethanol followed by a 10-min centrifugation at 14,000 x g at 4°C. At 37°C DNA pellets were dried for maximum 15 min, DNA was resuspended in 30 to 100 µl TE buffer (**Table 10**), and dissolved for 1 h at 37°C. Isolated genomic DNA was stored at room temperature until further use.

Table 10: Buffers used for genomic DNA isolation

Tail lysis buffer	TE buffer
10 mM Tris/HCl pH 8.0	10 mM Tris/HCl pH 8.0
100 mM EDTA	1 mM EDTA
0.5% (w/v) SDS	

2.6.2 Genotyping of mice by PCR

Genotyping of mice was performed by polymerase chain reaction (PCR) with 1 µl genomic DNA using the DreamTaq™ Hot Start Green DNA polymerase and the DreamTaq™ Green buffer (Thermo Scientific). Annealing temperature ($T_{A;}$ °C) and elongation time (t_E; sec) were adjusted as listed in **Table 11** and implemented in the PCR program depicted in **Table 12**.

Table 11: Primers used for genotyping of mice

Mouse line	PCR	Primer #	T_A (°C)	t_E (sec)
GBA2-KO	GBA2	C0895/ C0896/ C0897	60	60
GBA2-EUCOMM	GBA2-EU WT	C2152/ C2153	62	40
	GBA2-EU lacZ	C2154/ C2155	60	30
Neuron-specific GBA2-KO	GBA2-EU WT	C2152/ C2153	62	40
	Cre-deleter	C0098/ C0099	51	60
Muscle-specific GBA2-KO	GBA2-EU WT	C2152/ C2153	62	40
	Cre-deleter	C0098/ C0099	51	60

EU: EUCOMM, KO: knockout, T_A: annealing temperature, t_E: elongation time

Table 12: Pipetting scheme for PCR reactions and PCR programs

		PCR program		
DreamTaq™ Master Mix	PCR mix	Step	Temp. (°C)	Time (sec)
300 µl DreamTaq™ 10x buffer	1 µl DNA	Initial denaturation	95	300
32 µl DreamTaq™ Polymerase (5 U/µl)	1 µl of each primer (10 mM)	Denaturation	94	45
50 µl 100 µM dNTPs	8.3 µl DreamTaq™ Master Mix	35x Annealing	x	45
868 µl H_2O	ad 20 µl with H_2O	Elongation	72	x
		Final elongation	72	600
		Cooling down	8	∞

dNTPs: deoxynucleoside tripshophates, Temp.: temperature, U/µl: Units/µl

2.7 Mammalian cell culture

2.7.1 Buffers and media used for cell culture

Cultured cells were washed with phosphate buffered saline (PBS; **Table 13**) and maintained in DMEM (Gibco) or F12 medium (Gibco) with 10% FCS (Biochrome). Neurobasal-based medium (Gibco) with 2% horse serum (Pan Biotech) was used for culturing cerebellar neurons (see 2.7.5). All cell lines were kept in an incubator (SanyO) at 37°C in the presence of 5% CO_2 at 95% humidity. For maintenance and transfection procedures cells were handled under safety work benches (Herasafe, Thermo Scientific) using gloves.

Table 13: Phosphate buffered saline (PBS) used for cell culture

1 x PBS
137 mM NaCl
2.7 mM KCl
6.5 mM Na_2HPO_4
1.5 mM KH_2PO_4
adjust to pH 7.4, autoclave

2.7.1 Cell line

Chinese Hamster Ovary (CHO) K1 cells were used to express mGBA2 proteins (**Table 14**).

Table 14: CHO cell line.

Cell line	Producer	Catalog #	Growth medium
CHO K1	European Collection of Cell Cultures (ECACC)	85051005	F12 + 10% FCS

2.7.1 Preparing back-ups of cultured cells

For long-term storage, cultured cells were cryopreserved in cell culture medium containing 10% DMSO. Therefore, CHO cells were washed in PBS, trypsinized, and pelleted by centrifugation at 200 x g for 5 min at room temperature. Pellet was resuspended in DMSO-containing cell culture medium as mentioned before and at least $1x10^6$ cells were transferred to cryogenic vials (Thermo Scientific). Cells were frozen in a freezing container (Mr. Frosty™, Thermo Scientific) at -80°C overnight and then transferred to liquid nitrogen for long-term storage.

2.7.1 Re-culturing of cells frozen as back-ups

1 ml cell suspension frozen as a back-up was thawed at 37°C in a water bath and directly substituted to 20 ml pre-warmed cell culture medium. To remove residual DMSO, the cells were centrifuged at 200 x g for 5 min at room temperature. The pellet was resuspended in cell culture medium and seeded on cell culture dishes for maintenance.

2.7.1 Poly-L-lysine (PLL) coating of glass coverslips

13 mm glass coverslips prepared in 4-well dishes were coated with poly-L-lysine (PLL; Sigma) for 30 to 60 min in 500 µl of 0.1 mg/ml PLL. After incubation, the coverslips were washed twice in PBS and directly used or stored at 4°C in PBS until further use.

2.7.2 Transient transfection using PEI

8 x 10^4 and 1.5-2.5 x 10^6 cells were seeded on a 4-well plate or 9 cm plate, respectively, one day prior to transfection to reach 90-95% confluency. Plasmid DNA, polyethylenamine (PEI; Sigma), and OptiMEM (Gibco) were prepared in a sterile Eppendorf tube as depicted in **Table 15** and incubated for 10 min at room temperature. Cell culture medium was replaced by starvation medium containing only 2% FCS. The DNA/PEI mix was added to the cells drop-wise and cells were kept at 37°C/5% CO_2 overnight.

Table 15: Pipetting scheme for transient transfection using polyethylenamine (PEI)

Dish	DNA (µg)	PEI (µg)	OptiMEM (µl)	Starvation medium (µl)
4-well plate	0.7	1	50	200
9 cm plate	13.16	20	940	4000

2.7.3 Stable cell line expressing mGBA2

Stable cell lines were generated by Dr. Heinz Gerd Körschen via electroporation (Neon™ Transfection System 100 µl Kit, Invitrogen) using the pc3.1-mGBA2-HA plasmid (**Table 16**). The detailed protocol is described elsewhere (Körschen et al., 2013). 1.5-2.5 x 10^6 were seeded on a 9 cm plate one day prior to the experiment.

Table 16: Stable cells line expressing mGBA2

Clone #	Cell type	Expressed protein	Producer	antibiotic resistance
G4A11	CHO	mGBA2-HA	H. G. Körschen	G418 (geneticin)

2.7.4 Isolation of murine dermal fibroblasts

Isolation of dermal fibroblasts from mouse tails has been performed by Dr. Diana N. Raju according to an earlier published protocol (Raju et al., 2015). Tail was thoroughly sterilized with 70% ethanol and cut into three pieces of similar size. Lysis of the tissue was allowed in 3 ml fibroblast growth medium containing 1 mg/ml collagenase (Sigma) in a 3-h incubation at 37°C/ 5% CO_2. Afterwards, the supernatant was pelleted in a 5-min centrifugation at 600 x g (room temperature). Resuspension of the cell pellet was performed using fibroblast growth medium (**Table 17**) and suspension was plated on cell culture plates. 24 h later, medium was changed and fibroblasts were grown to 70% confluency before splitting. Depending on the growth rate, 6 to 8 x 10^5 cells were seeded on a 9 cm plate for maintenance. For the experiments, cells were grown for 24 h after seeding.

Table 17: Fibroblasts cell culture growth medium

Fibroblast growth medium
DMEM/GlutaMax (Gibco)
10% FCS
1 mM sodium pyruvate (Gibco)
2 mM L-glutamine (Gibco)
100 U/ml penicillin (Gibco)
100 µg/ml streptomycin (Gibco)

2.7.4.1 Transient transfection of murine fibroblasts via electroporation

1 x 10^6 murine fibroblasts were resuspended in 100 µl transfection buffer (Neon transfection system, Life technologies) and transfected with 4 µg plasmid DNA using a microporator mini (Digital Bio Technology, MP-100). 10 µl cell suspension was electroporated in two pulses (20 sec each) of 1000 V and seeded on PLL-coated glass coverslips or on CYTOO chips (CYTOO Cell Architects, #10-900-13-06) in a 35 mm cell culture plate.

2.7.5 Isolation of murine cerebellar neurons

Isolation of neurons from mouse cerebella was performed by Dr. Sina Stern in the research group of Prof. Dr. Frank Bradke (DZNE, Bonn). Cerebellum was dissected at postnatal day P7-P9 and directly placed in sterile HBSS supplemented with 7 mM HEPES. Meninges were carefully removed using fine forceps and the cerebellum was mince into small pieces. Tissue was dissociated in 1 ml Trypsin/DNase solution (**Table 18**) and incubated for 10 min at room temperature. Trypsin was inactivated by addition of 5 ml DMEM/GlutaMax/ 5% heat-inactivated horse serum (Pan Biotech). Afterwards, the tissue was washed thrice with HBSS in the

presence of 0.005 µg/ml DNase (Roche). Next, cells were dissociated using 4% BSA (Sigma)-coated glass Pasteur pipettes, centrifuged at 800 x g for 5 min at 4°C, and washed twice with HBSS supplemented with 7 mM HEPES. Finally, cell pellet was resuspended in 5 ml complete Neurobasal Medium (**Table 18**) and seeded on PLL-coated coverslips at a density of 30,000 cells per 13 mm coverslip, which were provided per well on a 4-well plate. The cells were kept at 37°C/ 5% CO_2.

Table 18: Buffers and medium used for isolation of murine cerebellar neurons

Calcium- and magnesium-free (CMF-) PBS	Trypsin/DNase solution	Complete Neurobasal Medium
137 mM NaCl	CMF-PBS	Neurobasal Medium (Gibco)
4 mM KCl	1% (w/v) Trypsin (Cell Systems)	2% (v/v) B-27 supplement (Gibco)
11 mM glucose	1 mg/ml DNase (Roche)	2 mM L-glutamine (Gibco)
4.2 µM Na_2HPO_4	0.9 mM $MgSO_4$	1% PenStrep (Gibco)
1.8 mM K_2HPO_4	0.6% (v/v) 1 N NaOH	2% heat-inactivated horse serum (Pan Biotech)
0.004% (w/v) $NaHCO_3$		
pH 7.4		

2.7.5.1 Treatment of cultured cerebellar neurons with NB-DNJ or AMP-DNM

When the isolated cerebellar neurons adhered to the coverslips they were seeded on, medium was exchanged and 5 µM NB-DNJ (stock: 5 mM in PBS; Sigma-Aldrich) or 30 µM AMP-DNM (stock: 50 mM in DMSO; kindly provided by Prof. Dr. Johannes Aerts, Leiden University) (Overkleeft et al., 1998) was added. Cells were incubated for 48 h with the GBA2 inhibitors and incubated at 37°C in the presence of 5% CO_2. Control cells were treated with PBS or DMSO at the same concentrations.

2.8 Immunocytochemistry

2.8.1 Fixation of cells

One day after transfection, cells were washed once in PBS and fixed in fresh-prepared 4% paraformaldehyde (PFA) in PBS for 10 min at room temperature. Fixed cells were washed thrice in PBS and used directly for immunocytochemical staining or stored at 4°C in PBS until further usage.

Isolated cerebellar neurons were seeded (30,000 cells per 13 mm coverslip) on PLL-coated coverslips and cultured for 48 h in absence of presence of NB-DNJ or AMP-DNM (see 2.7.5.1).

Cells were fixed in 4% PFA in PBS for 15 min at room temperature, then washed thrice in PBS. Residual PFA was quenched in a 10-min incubation with 50 mM NH_4Cl followed by three PBS-washing steps. For X-gal staining, cerebellar neurons were fixed in 0.2% glutaraldehyde in PBS for 5 min at room temperature.

2.8.2 Immunocytochemical (ICC) staining

All steps were performed at room temperature. Cells were blocked in 5% Chemieblocker (Millipore)/ 0.5% TritonX-100 in PBS for 30 min and then stained with the primary antibody prepared in blocking solution for 60 min. Antibody was removed and cells were washed thrice in PBS. Secondary antibody incubation in blocking solution followed in the presence of DAPI (1:10,000 of 5 µg/µl stock in H_2O) for 45 min in the dark. Finally, cells were washed thrice in PBS prior to mounting in Aqua Poly/Mount (Polysciences Inc.). Mounting medium was allowed to harden overnight and slides were stored at 4°C until imaging was performed using a confocal laser scanning microscope (Olympus FV1000).

Murine dermal fibroblasts were stained with Alexa Fluor™ 488-conjugated Phalloidin (1:500; Life Technologies) and DAPI for 1 h after 30-minute blocking as decribed before.

In collaboration with Prof. Dr. Frank Bradke (DNZE, Bonn), cerebellar neurons were permeabilized in 0.1% TritonX-100 (in PBS) for 3 min, then blocked with blocking solution containing 2% FCS/ 2% BSA/ 0.2% fish gelatin (in PBS). Cells were incubated with primary and secondary antibody in 10% blocking solution for 1 h or 30 min, respectively, with three PBS-washing steps in between. F-actin was stained using Rhodamine-conjugated Phalloidin (Life Technologies, 1:500). Afterwards, cells were washed thrice in PBS and finally mounted using Fluoromount (Sigma). Confocal imaging was performed using the fluorescent microscope (Zeiss Observer D1) or confocal laser scanning microscope (Olympus FV1000). Neurite length was measured based on the neuronal β-Tubulin III-positive protrusions.

2.9 Isolation of murine tissue

2.9.1 Dissection of mice

Mice were anesthetized using isoflurane (Piramal Healthcare) followed by a cervical dislocation. Thoracic cavity was opened by an abdominal incision to extract testis, liver, and spleen. Brain, was carefully dissected and freed from the skull by cutting the cranial nerves. For separate studies of the cerebellum, this brain region was removed along the colliculus inferior and separated from the underlying pons and medulla. Isolation of the cerebellum of early postnatal mice for the isolation of cerebellar neurons is more precisely described in 2.7.5. Starting from the skull base, a dorsal laminectomy was performed to carefully isolate the spinal cord. Skeletal muscle was isolated from the hind limbs and fat and connective tissue were thoroughly removed. All tissues were snap-frozen in liquid nitrogen and kept at -80°C for long-

term storage. In contrast, for histological analysis tissue was fixed and cryopreserved as described in 2.9.2 and 2.9.3.

2.9.2 Fixation of tissue in glutaraldehyde

For X-gal staining tissue was fixed in 0.2% glutaraldehyde (without perfusion of the animal) in PBS for 7 days at 4°C. Fixed tissue was washed in PBS for 10 min at room temperature while shaking. Cryopreservation of the tissue was performed in a sucrose gradient including a 1-h incubation in 10% sucrose in PBS at room temperature on a shaker and an overnight-incubation in 30% sucrose in PBS at 4°C. Afterwards, brain was snap-frozen without embedding, whereas spinal cord was embedded in Tissue Tek (Sacura). All tissues were kept at -80°C for long-term storage.

2.9.3 Perfusion of mice with paraformaldehyde (PFA)

Mice were anesthetized by intraperitoneal injection of 100 mg/kg body weight ketamin (Medistar) and 10 mg/kg body weight xylazin (Ceva). A thoracotomy of the anesthetized animal was performed and the left ventricle was cut carefully to insert a perfusion needle to the ascending aorta. Next, the right atrium was incised and the circulatory system was washed with saline solution until the liver has destained using a peristaltic pump (MINIPULS® 3, Gilson). Fixation was performed with 4% paraformaldehyde (PFA) in PBS for 5 to 10 min at a flow rate of 10 ml/min. Finally, brain and spinal cord were dissected as described earlier (2.9.1).

2.9.4 Cryopreservation in sucrose gradient

After dissection of the tissue, post-fixation in fresh-prepared 4% paraformaldehyde (PFA) in PBS was performed overnight at 4°C. The following washing step in PBS for 10 min and incubation in 10% sucrose (in PBS) for 1 h were performed at room temperature on a shaker. Cryopreservation was finalized by an incubation in 30% sucrose (in PBS) overnight at 4°C. Afterwards, brain was snap-frozen on dry-ice without embedding, whereas spinal cord was embedded in Tissue Tek (Sacura). All tissues were kept at -80°C for long-term storage.

2.9.5 Cryosectioning of murine brain and spinal cord

16 µm sagittal and coronal sections of the brain (caudal region including cerebellum and brainstem) and 16 µm transverse sections of the spinal cord (cervical region) were prepared using the cryostat (Mikrom HM560, Thermo Scientific) and mounted on SuperFrost® Plus glass slides (Thermo Scientific). Sections were stored at -20°C for long-term storage. Before staining, slides were thawed at room temperature and sections were surrounded using a hydrophobic barrier pen (ImmEdge Pen; Vector Laboraties).

2.10 Histochemical stainings

2.10.1 Detection of β-galactosidase expression using X-gal

All steps were performed at room temperature if not stated otherwise. lacZ basis buffer was prepared for long-term storage at room temperature (**Table 19**), whereas all other buffers were prepared fresh before usage. Cyrosections of murine cerebellum and spinal cord or cells fixed with glutaraldehyde (see 2.8.1, 2.9.2) were washed thrice for 5 min with lacZ washing buffer (**Table 19**). lacZ substrate solution was prepared and prewarmed at 37°C, 5-bromo-4-chloro-3-indolyl-β-D-galactopyranoside (X-gal; Roth) was dissolved in dimethylformamide (DMF) and added to a final concentration of 0.01% or 0.05% (**Table 19**). Subsequently, 200 µl to 250 µl substrate solution was added to the sections/ cells and incubated in a humidified chamber at 37°C (in an incubator without controlled CO_2 supply) overnight. On control sections/ cells, lacZ substrate solution without X-gal was added. Afterwards, sections/cells were washed twice shortly with ddH_2O and mounted using Aqua Poly/Mount (Polysciences Inc.). Stained tissue sections/ cells were imaged using the Nikon Eclipse Ti microscope (stitching mode for tissue sections).

Table 19: Buffers used for X-gal staining

lacZ basis buffer	lacZ washing buffer	lacZ substrate solution
77 mM Na_2HPO_4	lacZ basis buffer	lacZ basis buffer
23 mM NaH_2PO_4	0.1% (w/v) sodium deoxycholate	5 mM $K_3[Fe(CN)_6]$
1.25 mM $MgCl_2$	0.2% (v/v) Ipegal-CA630	5 mM $K_4[Fe(CN)_6]$
2 mM EGTA pH 8.0		0.01% or 0.05% X-gal (in DMF)

2.10.2 Nissl body staining

All steps were performed at room temperature under the hood. Murine brain and spinal cord was demyelinated in a graded alcohol series (70%, 95%, and 100% ethanol; 5 min each) and subsequently rehydrated (95%, 70%, and 50% ethanol; 5 min each). The tissue was rinsed shortly in ddH_2O and stained with sterile-filtered 1% cresyl violet acetate (Sigma) in 1% acetic acid for 4 min. Afterwards, sections were washed in ddH_2O thrice (30 sec each) to remove excess stain and shortly washed in 70% and 95% ethanol. Differentiation of the staining was performed in 95% ethanol/ 1% acetic acid followed by a dehydration in 95% and 100% ethanol. Excessive destaining was prevented by constantly monitoring the sections and adjusting incubation times accordingly. Prior to mounting the sections in Entellan (Merck), sections were

shortly cleared in xylol (Isomere, Roth). Stained sections were stored at 4°C until being imaged using the Nikon Eclipse Ti microscope (stitching mode).

2.11 Protein biochemistry

2.11.1 Preparation of proteins

2.11.1.1 Protein lysates of cultured cells

Transfected cells were washed thrice with 5 ml PBS. Cells were scratched from a 9 cm plate in 1 ml of 0.5 g/l EDTA in PBS or from a 6-well plate in 0.5 ml of 0.5 g/l EDTA in PBS using a cell scraper. Harvested cells were pelleted at 500 x g for 5 min at 4°C. All subsequent steps were performed at 4°C or on ice in the presence of a mammalian protease inhibitor cocktail (mPIC; Sigma Aldrich). Pelleted cells were resuspended in total lysis buffer or hypotonic lysis buffer (9 cm plate: 200 µl; 6-well plate: 50 µl; **Table 20**). Lysis of the cells in total lysis buffer was allowed by incubation for 30 min. Finally, cell debris was removed by centrifugation at 10,000 x g for 10 min and supernatant was used in further steps. Lysis in hypotonic buffer was performed by sonication in three pulses à 20 sec (Branson sonicator). Protein concentration was determined in a Bradford assay (2.11.2.1) or bicinchoninic acid (BCA) test (2.11.2.2).

Table 20: Total and hypotonic buffer used for cell lysis

Total lysis buffer	Hypotonic lysis buffer
10 mM Tris/HCl pH 7.6	10 mM HEPES/NaOH pH 7.4
140 mM NaCl	0.5 mM EDTA
1 mM EDTA	1:500 mPIC
1% (v/v) TritonX-100	
1:500 mPIC	

2.11.1.2 Protein lysates of murine tissue

All steps were performed at 4°C or on ice in the presence of mPIC (Sigma Aldrich). Brain, skeletal muscle, liver, spleen, was homogenized in total lysis buffer or hypotonic lysis buffer (**Table 20**) in the presence of a mammalian protease inhibitor using a tissue douncer (IKA® ULTRA-TURRAX® T18 basic disperser, Sigma-Aldrich). Testis, cerebellum, spinal cord was homogenized mechanically using a pistil (Wheaton, USA). 2 to 10 ml buffer per g wet weight of the tissue was used for lysis using either of the above mentioned buffers. Homogenate prepared with total lysis buffer was incubated for 30 min and centrifuged at 10,000 x g for 10 min and supernatant was used in further steps. Homogenates prepared with hypotonic buffer were sonicated in three pulses (20 sec each; Sonics Vibra-Cell sonicator) and subjected to low-speed centrifugation at 1,000 x g for 20 min to remove cell debris. The post-nuclear

supernatant (PNS) was used for further experiments. Protein concentration was determined in a Bradford assay (2.11.2.1) or bicinchoninic (BCA) test (2.11.2.2).

2.11.2 Protein concentration determination

2.11.2.1 Bradford assay

The Bradford assay, which is based on a reaction of the Coomassie dye with proteins (Bradford, 1976), was performed to determine the protein concentration in prepared lysates. The Coomassie Brilliant Blue G-250 provided in the acidic Bradford reagent (Biorad) is protonated and, under these conditions, appears red. When protein is added, the dye reacts with charged groups on the protein and destabilizes the protein. Hydrophobic pockets get exposed at the protein surface and can also be bound by Coomassie. In this unprotonated, protein-bound form, the dye becomes blue and its absorption shifts from 470 nm (red dye) to 595 nm (blue dye). An increase in absorption at 595 nm is thus directly proportional to the amount of protein present in the sample. To determine the protein concentration in lysates prepared of cells or tissues, the lysate was diluted 1:5, 1:10, 1:20, or 1:50 in lysis buffer. The Bradford reagent (Biorad) was diluted 1:5 in ddH_2O and 1 ml diluted reagent was used to determine a shift in absorption upon addition of 5 µl diluted protein lysate compared to a blank sample. Samples were prepared in disposable plastic cuvettes (Brand) and absorption was measured at 595 nm in a spectrophotometer (Hitachi U-1900). Only for samples with an absorption in the linear range from 0.005 to 0.15 the protein concentration was calculated as follows:

$$c\ [\mu g/\mu l] = \frac{Abs_{595}}{5\ \mu l\ x\ 0.06}\ \mathrm{x}\ x$$

whereby c refers to the protein concentration in µg/µl, Abs_{595} to the absorption measured at 595 nm, 5 µl to the volume of diluted lysate added to the Bradford reagent, 0.06 to the absorption corresponding to a protein concentration of 1 µg/µl, and x describes the dilution factor of the added lysate. Measurements below or above the aforementioned linear range were repeated with lower or higher diluted protein lysate.

2.11.2.2 Bicinchoninic (BCA) test

The Pierce® bicinchoninic (BCA) Protein Assay Kit (Thermo Scientific) allows to determined protein concentrations based on the protein-dependent reduction of Cu^{2+} to Cu^{+} in the provided alkaline solution. Bicinchoninic acid complexes in the presence of Cu^{+} and exhibits an absorption maximum of 562 nm. For the BCA test, protein lysate was diluted in lysis buffer 1:5, 1:10, 1:20, or 1:50. Measurements for each sample were performed in duplicates in a 96-well plate and 10 µl of the diluted lysates was provided per well. As a protein standard, a bovine albumin standard series ranging from 25 µg/ml to 2000 µg/ml protein (Thermo Scientific) was

included. The BSA reagent B was diluted 1:50 in reagent A (Thermo Fisher) and 190 µl diluted BCA solution was added per well. The plate was incubated at 37°C for 30 min and the absorption at 570 nm was measured in a plate reader (Fusion Microplate Reader; Perkin Elmer). Linear regression of the BSA standard allowed to calculate the protein concentrations.

2.11.3 Sodium dodecyl sulfate polyacrylamide gel electrophoresis (SDS-PAGE)

2.11.3.1 Self-casted SDS gels

Denaturing sodium dodecyl sulfate polyacrylamide gel electrophoresis (SDS-PAGE) was performed to separate proteins according to Laemmli (Laemmli, 1970). Discontinuous gels were prepared with a 5% stacking gel and 7.5% to 12.5% separating gel for larger or smaller proteins of interest, respectively (**Table 21**). Protein samples were prepared in SDS sample buffer (diluted to 1 x; **Table 22**) and boiled for 5 min at 95°C before loading if not stated otherwise. Electrophoretic separation was performed in SDS running buffer (diluted to 1 x; **Table 22**) in a minigel chamber (Biometra) and initiated at a current of 15 mA per gel in the stacking gel phase, whereas for the separating gel phase current was increased to maximum 25 mA per gel.

Table 21: Pipetting scheme to cast polyacrylamide gels for SDS-PAGE

Component	Stacking gel (5%)	Separating gel (7.5% - 10% - 12.5%)
1.5 M Tris/HCl pH 6.8 or 8.8	0.5 ml (pH 6.8)	1.5 ml (pH 8.8)
10% (w/v) SDS	20 µl	60 µl
10% (w/v) APS	40 µl	40 µl
TEMED	3.5 µl	3 µl
Acrylamide/Bis-acrylamide 30% solution (37.5:1)	340 µl	1.5 ml - 2 ml - 2.5 ml
ddH_2O	1.12 ml	2.92 ml - 2.42 ml - 1.92 ml

Table 22: SDS sample buffer used to prepare samples for SDS-PAGE

SDS sample buffer (4 x)	SDS running buffer (20 x)
200 mM Tris/HCl pH 6.8	250 mM Tris
8% (w/v) SDS	1% (w/v) SDS
5% (v/v) β-mercaptoethanol	1.92 M gylcine
50% (v/v) glycerol	
0.04% (w/v) bromophenol blue	

2.11.3.2 Protein marker

As a protein standard the prestained AppliChem VI (11-245 kDa), Biomol BLUEplus-wide (3.5-245 kDa), and HiMark™ (Invitrogen; 31-460 kDa) protein ladder was used (**Figure 9**). 5-10 µl protein ladder was loaded per lane.

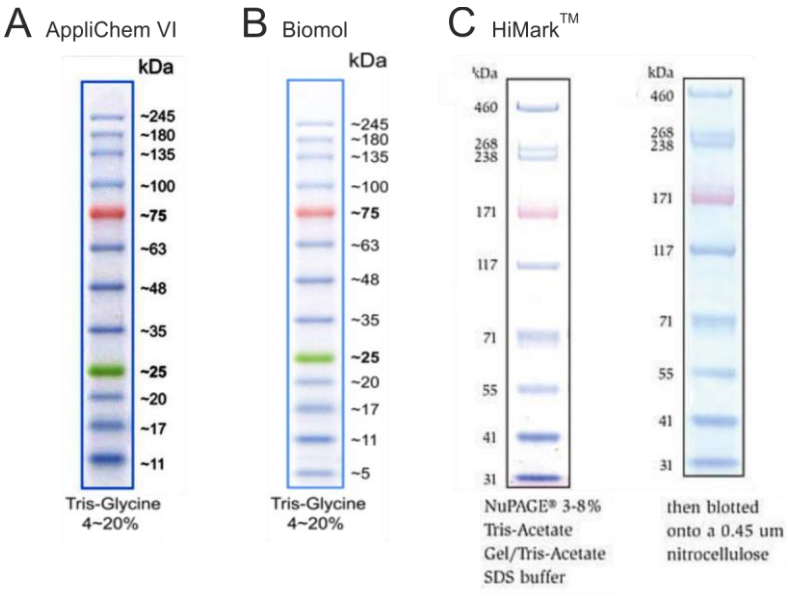

Figure 9: Protein standards used for SDS-PAGE. Images were taken and modified from **A)** #A8889 data sheet (AppliChem Panreac), **B)** #10009 data sheet (Biomol), and **C)** #LC5699 data sheet (Invitrogen).

2.11.3.3 Coomassie staining to detect proteins on polyacrylamide gels

The polyacrylamide gel was shortly rinsed in H_2O to remove excess SDS running buffer and subsequently stained in Coomassie staining solution (**Table 23**) overnight at room temperature whilst shaking. Destaining was performed in Coomassie destaining solution for at least 1 h (changing the solution periodically) until background staining was sufficiently minimized (**Table 23**). Afterwards, the gel was rinsed in H_2O and imaged using the image analyzer LAS-3000 (Fujifilm Life Science).

Table 23: Coomassie staining and destaining solutions

Coomassie staining solution	Coomassie destaining solution
50% (v/v) ethanol 7% (v/v) acetic acid 0.2% Coomassie Brilliant Blue R250 (Sigma-Aldrich)	25% (v/v) ethanol 5% (v/v) acetic acid

2.11.4 Western blot analysis

For immunostainings, proteins separated by SDS-PAGE were transferred onto a polyvinylidene difluoride (PVDF; Immobilon FL, Millipore) membrane by performing discontinuous semi-dry Western blotting. Membrane was activated in methanol, gel and membrane were then set up in blotting chamber (Roth) as depicted in **Figure 10**. A current of 2.4 mA/cm^2 was applied per 8 x 9 cm PVDF membrane and transfer time was set to 35-42 min, 50 min, or 65 min for small (< 30 kDa), medium-sized (30 to 110 kDa), or large (> 110 kDa) proteins of interest, respectively.

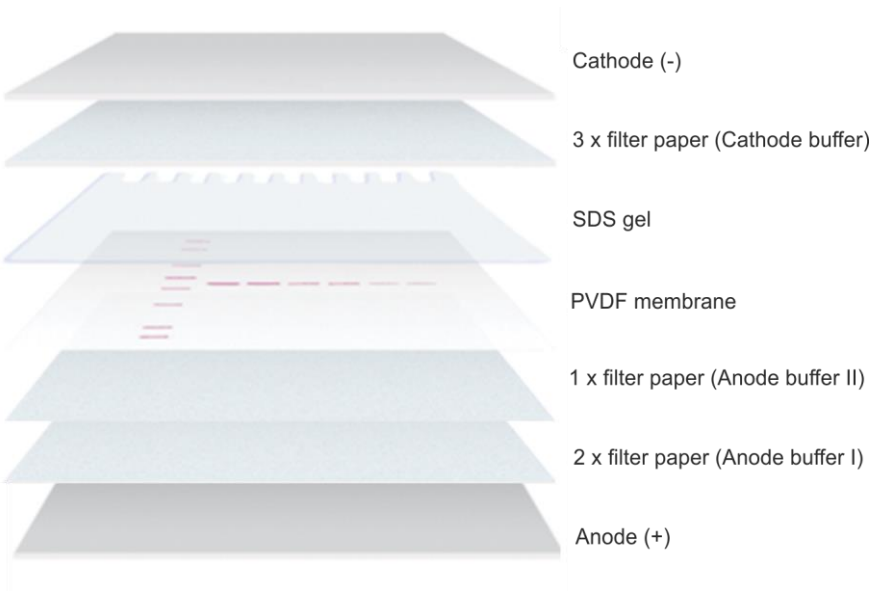

Figure 10: Gel and membrane setup for discontinuous semi-dry protein transfer. Image modified from: BioRad Protein Blotting Methods – Electrophoretic Transfer Setup

Table 24: Buffers used for protein transfer onto PVDF membranes

Anode buffer I	Anode buffer II	Cathode buffer
0.3 M Tris/HCl pH 10.4 20% methanol	25 mM Tris/HCl pH 10.4 20% methanol	25 mM Tris/HCl pH 9.4 20% methanol 40 mM glycine

2.11.4.1 Immunostaining of immobilized proteins

After blotting, the membrane was shortly washed in PBS (**Table 25**), then blocking of unspecific binding sites was performed by incubation with blocking buffer (**Table 25**) for 30 min at room temperature. Next, the membrane was probed with a primary antibody against the protein of interest prepared in blocking buffer overnight at 4°C. The next day, non-bound antibody was washed off from the membrane in three 20-min washing steps with PBS-T (**Table 25**) at room temperature. Finally, the secondary antibody raised against the species the primary antibody

was produced in was prepared in blocking buffer and added to the membrane for a 1 h-incubation at room temperature. Non-bound antibody was removed in three washing steps with PBS-T for 20 min each and the membrane was finally transferred to PBS. The use of fluorescently-labeled secondary antibodies IRDye680 and IRDye800 (0) allowed me to visualize expression of the protein of interest using the Odyssey Imaging detection system (LI-COR Biosciences) and excite the infrared fluorophores at 680 nm and 778 nm to emit fluorescence at 694 nm and 794 nm, respectively (LI-COR Biosciences). Horseradish peroxidase (HRP)-coupled secondary antibodies were detected by addition of luminol, which in the presence of peroxide is oxidized by the HRP-catalyst and then luminesces (enhanced chemiluminescence (ECL) detection reagent; Sigma-Aldrich). The luminescent image analyzer LAS-3000 (Fujifilm Life Science) was used to detect the emitted light at 425 nm.

Table 25: Buffers used for immunostaining of immobilized proteins

PBS washing buffer	PBS-T washing buffer	Blocking buffer
130 mM NaCl 7 mM Na_2HPO_4 3 mM NaH_2PO_4 adjust to pH 7.4 to 7.5 autoclave	PBS washing buffer 0.05% (v/v) Tween 20	PBS-T washing buffer 50% (v/v) Bløk (Millipore)

2.11.5 Protein expression in *E.coli*

2.11.5.1 Test expression of recombinant protein

To find optimal conditions for the expression of MBP-tev-mGBA2-126/882 in *E.coli*, a 10 ml preculture inoculated with transformed *E.coli* of the pLysE strain (see 2.5.1) was grown at 37°C on an orbital shaker to reach an OD_{600} of 0.4 to 0.6. Protein expression was then induced by addition of 1 mM Isopropyl-β-D-thiogalactopyranoside (IPTG) and culture was incubated at 18°C for 1 h, 3 h, 5 h, or overnight on an orbital shaker. All subsequent steps were performed at 4°C or on ice. Bacterial culture was pelleted at 14,000 x rpm for 2 min, frozen at -20°C until further use, or directly resuspended in 140 µl PBS with 140 mM NaCl, 1 mM dithiothreitol (DTT), and a spatula tip of DNase (AppliChem) in the presence of mPIC (Sigma Aldrich). Bacterial lysate was sonicated (Sonics Vibra-Cell sonicator) with three pulses (20 sec each) and centrifuged at 14,000 x g for 30 min. For Western blot analysis, 15 µl of the bacterial lysate prior to centrifugation, 15 µl of the supernatant, and 15 µl of the pellet resuspended in 75 µl resuspension buffer were loaded as total, soluble, and insoluble fraction on a SDS gel, respectively.

2.11.5.2 Large-scale expression of recombinant mGBA2 protein

500 ml LB was inoculated 1:50 with bacterial pre-culture, which has been generated from BL21 CodonPlus (DE3) RIPL *E.coli* transformed with the pET21 mGBA2-His plasmid or One Shot™ TOP10 *E.coli* transformed with pET28 MBP-tev-mGBA2-126/882 plasmid, respectively (see 2.5.1). Bacterial culture was grown at 37°C on an orbital shaker to an OD_{600} of 0.4 to 0.6. Protein expression was then induced by addition of 1 mM IPTG and the culture was incubated at 18°C overnight or at 37°C for 3 h on an orbital shaker to an OD_{600} of ~2.0. Bacterial cells were pelleted at 6,000 x g for 15 min at 4°C and frozen at -20°C until further use.

2.11.5.3 Activity measurements of recombinant mGBA2

Protein expression of MBP-tev-mGBA2-126/882 (pET28 MBP-tev-mGBA2-126/882 plasmid) and wild-type mGBA2-His (pET21 mGBA2-His plasmid) in *E.coli* was performed on a large scale as described before (2.11.5.2). All subsequent steps were performed at 4°C or on ice. 30 ml bacterial culture was taken and pelleted by centrifugation at 11,000 x g for 10 min. Pellet was resuspended in 4.8 ml hypotonic buffer and sonicated in three pulses 20 sec each (total fraction). 2.4 ml of the lysate were taken and separated into soluble fraction (supernatant) and insoluble membrane fraction (pellet) by centrifugation at 14,000 x rpm for 30 min. Pellet was then resuspended in 2.8 ml hypotonic buffer. Both total and soluble fraction were subjected to a β-glucosidase activity assay to measure GBA2 activity (see 2.11.9). 15 µl of the total, soluble, and insoluble fraction was prepared in 4 x SDS sample buffer and analyzed by Western blot analysis.

2.11.6 Purification of recombinant protein

Expression of MBP-tev-mGBA2-126/882 in *E.coli* was performed at 18°C overnight as described before (2.11.5.2). All subsequent steps were performed at 4°C or on ice. Two 500 ml-culture pellets were resuspended in 25 ml resuspension buffer each (**Table 26**). Cells were broken up by sonication with four pulses 40 sec each (Sonics Vibra-Cell sonicator) and incubated for 10 min on a tube roller. Centrifugation for 20 min at 11,000 x g followed and supernatants were combined. 1 mM EDTA and 1 mM dithiothreitol (DTT) was added and the solution was sterile filtered through a 0.22 µm syringe filter.

Table 26: Resuspension buffer used for purification of recombinant protein

Resuspension buffer
20 mM Tris/HCl
200 mM NaCl
adjusted to pH 7.4

25 ml buffer per 500 ml *E.coli* culture with:
1 mg DNase (AppliChem)
5 mg Lysozyme (Sigma)
added after *E.coli* lysis:
1 mM EDTA
1 mM DTT
sterile filtered

2.11.6.1 Affinity chromatography to purify recombinant mGBA2

For the purification of MBP-tev-mGBA2 (aa126-882) I performed an affinity chromatography in a liquid chromatography system (ÄKTA; GE Healthcare) using a commercial MBPTrap™ HP column (GE Healthcare) which contains cross-linked agarose coated with dextrin (Dextrin Sepharose™; column volume: 1 ml). The complete ÄKTA system was washed with H_2O before the MBPTrap™ column was inserted, which was also rinsed with 5 x column volumes (CV) H_2O with a flow rate of 1 ml/min never exceeding a pressure of 0.3 MPa. According to the manufacturer's protocol, I used a Tris-based binding buffer and performed the purification under physiological conditions at pH 7.4 (**Table 27**). The column was equilibrated with 5 x CV binding buffer with a flow rate of 1 ml/min (≤ 0.3 MPa). Next, 50 ml supernatant (prepared as described in 2.11.6) was loaded on the column with a flow rate of 0.5 ml/min (≤ 0.3 MPa). 1 ml of the flow-through (Non-Bound) was collected for Western blot analysis. After removing unbound proteins by washing the column with 20 x CV binding buffer (flow rate: 1 ml/min; ≤ 0.3 MPa), elution of bound protein was performed with buffer containing 10 mM maltose (**Table 27**) at a flow rate of 0.5 ml/min (≤ 0.3 MPa; no gradient). Protein elution was monitored at 280 nm and the eluate was collected in fractions of 500 µl. The fractions with the highest amount of protein according to the absorbance detection were used for further purification experiments (see 2.11.6.5, 0) or Western blot analysis.

For regeneration, the column was washed in 3 x CV H_2O, 3 x CV 0.5 M NaOH, then 3 x CV H_2O at a flow rate of 0.5 ml/min or 1 ml/min never exceeding a pressure of 0.3 MPa. Column was stored in 20% ethanol at 4°C until further use.

Table 27: Binding and elution buffer used for affinity chromatography.

Binding buffer	Elution buffer
20 mM Tris/HCl	20 mM Tris/HCl
200 mM NaCl	200 mM NaCl
1 mM EDTA	1 mM EDTA
1 mM DTT	1 mM DTT

adjust to pH 7.4	10 mM Maltose
sterile filtered	adjusted to pH 7.4, sterile filtered

2.11.6.2 Tobacco Etch Virus (tev) protease cleavage

The tev protease is found in the Tobacco Etch Virus (tev) and recognizes the amino-acid sequence ENLYFQG, which we introduced into the pET28 MBP-tev-mGBA2-126/-882 plasmid between the MBP and mGBA2 protein. Cleavage will occur between the Q and G residue resulting in MBP protein (41.57 kDa) and mGBA2 (aa126-882) (85.47 kDa). The tev protease (His-tagged) for my experiments was kindly provided as a 3.92 µg/µl stock in 50 mM Tris pH 8.0/ 300 mM NaCl/ 2 mM β-mercaptoethanol/ 10% (v/v) glycerol by Prof. Dr. Matthias Geyer (Institute of Innate Immunity, Bonn; 25.06.2015). Eluate obtained from purification of MBP-tev-mGBA2-126/882 via MBPTrap™ (2.11.6.1) was incubated with 1 µg tev protease per 100 µg protein (= 1:100), per 50 µg protein (= 1:50), or per 10 µg protein (= 1:10) at 4°C in 1 x tev buffer (**Table 28**) diluted in elution buffer.

Table 28: Buffer used for tev protease-mediated cleavage of MBP-tev-mGBA2-126/882

Tev buffer (10 x)
500 mM Tris/HCl pH 7.6
1.5 M NaCl
5 mM EDTA

2.11.6.3 Buffer exchange using NaP™-5 columns

A buffer exchange of the elution fractions for subsequent experiments was performing using Illustra NaP™-5 columns (GE Healhcare) to remove maltose. Column was equilibrated with 10 ml binding buffer after excess storage buffer was allowed to flow through the column. 500 µl elution fraction after MBPTrap™ was loaded and finally eluted with 1 ml binding buffer (see 3.4.2).

2.11.6.4 Calibration of the Superdex™ 200 Increase 10/300 column

For size-exclusion chromatography, a Superdex™ 200 Increase 10/300 GL column (GE Healthcare) containing cross-linked agarose coated with dextran (Superdex™; column volume: 24 ml; bed diameter: 10 mm, bed height 300 mm) was used. The complete ÄKTA system was washed with H_2O before the Superdex™ column was inserted, which was also rinsed with 2 x column volumes (CV) H_2O and 2 x CV binding buffer (see 2.11.6.1) with a flow rate of 0.5 ml/min never exceeding a pressure of 1.5 MPa. Proteins of known sizes provided in the Gel Filtration Calibration LMW and HMW Kit (GE Healthcare) were used as standards. Protein solutions were prepared as depicted in **Table 29** containing ribonuclease A (3 µg/µl),

conalbumin (3 µg/µl), and ferritin (0.3 µg/µl), or ovalbumin (4 µg/µl), aldolase (4 µg/µl), thyroglobulin (5 µg/µl), or blue dextran 2000 (1 µg/µl). Protein mix was centrifuged at 10,000 x g for 10 min prior to injection into the ÄKTA system. 150 µl of each protein mix was loaded one after the other onto the Superdex™ column at a flow rate of 0.5 ml/min never exceeding a pressure of 1.5 MPa. Protein elution was monitored at 280 nm. In between, the column was washed with binding buffer (see 2.11.6.1) until absorption reached baseline. Based on the elution peaks corresponding to the standard proteins a standard curve was compiled.

Table 29: Protein mix prepared for calibration of Superdex™ 200 Increase 10/300 GL column

Mix	Protein	Final concentration of prepared stock	Protein in 150 µl subjected to column
A	Ribonuclease A	3 µg/µl	450 µg
	Conalbumin	3 µg/µl	450 µg
	Ferritin	0.3 µg/µl	45 µg
B	Ovalbumin	4 µg/µl	600 µg
	Aldolase	4 µg/µl	600 µg
	Thyroglobulin	5 µg/µl	750 µg
Dextran	Blue dextran 2000	1 µg/µl	150 µg

2.11.6.5 Size-exclusion chromatography

Size-exclusion chromatography was performed using the calibrated Superdex™ 200 Increase 10/300 GL column (GE Healthcare; see 2.11.6.3). The column was equilibrated with 2 x column volume (CV) eluent buffer at a flow rate of 0.5 ml/min never exceeding a pressure of 3 MPa. 180 µl eluate obtained by purification of MBP-tev-mGBA2-126/882 via MBPTrap™ (incubated with tev protease or left untreated) was loaded onto the column. Protein elution was monitored at 280 nm and the eluate was collected in fractions of 750 µl. The fractions with the highest amount of protein according to the absorbance detection were used for Western blot analysis. For regeneration, the column was washed in 1 x CV H_2O, 1 x CV 0.5 M NaOH, then 2 x CV H_2O at a flow rate of 0.5 ml/min never exceeding a pressure of 1.5 MPa. Column was stored in 20% ethanol at 4°C until further use.

2.11.7 Co-immunoprecipitation using magnetic beads

Cells seeded on a 9 cm plate expressing mGBA2-Flag, mGBA2-HA, mGBA2-Flag and mutant or wild-type mGBA2-HA, or bPAC-HA (pcDNA3.1(+) bPAC-HA) were washed twice with 5 ml PBS and harvested in 1 ml of 0.5 g/l EDTA in PBS. The subsequent steps were performed at

4°C or on ice if not stated otherwise. Cells were pelleted by centrifugation at 250 x g for 5 min and resuspended in 200 µl lysis buffer (**Table 30**) in the presence of mPIC (Sigma Aldrich). Vigorous pipetting during the 30-min incubation time allowed proper lysis of the cells. Cell debris was removed by centrifugation at 10,000 x g for 5 min and protein concentration in the supernatant (total lysate) was determined in a BCA test (2.11.2.2). 20 µl were taken as an input (Input 1) for Western blot analysis. For pre-clearing on underivatized agarose matrix, cyanogen-bromide activated agarose (Sigma) was prepared in 50% (w/v) suspension with 50% (v/v) glycerol in 10 mM sodium phosphate buffer (pH 7.4)/ 150 mM NaCl/ 0.02% (w/v) sodium azid. 50 µl underivatized agarose matrix suspension was centrifuged at 14,000 x g to remove the buffer. Next, matrix was equilibrated in 5 x column volume (CV; 250 µl) equilibration buffer, then 5 x CV (250 µl) lysis buffer. 250 µg protein in a total volume of 500 µl was added to the matrix and incubated for 5 to 6 h end-over-end. Agarose matrix was then pelleted at 14,000 x g, 20 µl were taken as input (Input 2) for Western blot analysis, and the remaining supernatant was loaded on anti-Flag magnetic beads (Sigma) which have been prepared as follows: 50 µl bead slurry was equilibrated in 5 x CV (250 µl) equilibration buffer (**Table 30**), then 5 x CV (250 µl) lysis buffer (**Table 30**). Beads were incubated with the lysate overnight end-over-end. The next day, suspension was magnetically separated and supernatant was taken as Non-Bound for Western blot analysis. Magnetic particles were washed four times with 300 µl washing buffer (supernatant taken as washing fractions for Western blot analysis; **Table 30**). Finally, bound protein was eluted in 2 x CV (100 µl) 0.1 M glycine (pH 3.0) during incubation at room temperature end-over-end. Supernatant after magnetic separation was immediately transferred to 16.67 µl 1 M Tris/HCl (pH 8.0) for neutralization and subjected to Western blot as the eluate.

Optimization experiments were performed with cells expressing mGBA2-Flag without pre-clearing on agarose matrix but overnight incubation of 250 µg protein in 500 µl total volume on 75 µl anti-Flag magnetic bead slurry, and included different lysis and washing buffer conditions with 500 mM NaCl (“high NaCl”), with 10 mM NaCl (“low NaCl”), without EDTA (“w/o EDTA”), or with CHAPS instead of TritonX-100 in the same concentrations (“CHAPS”). The corresponding washing buffers contained a reduced Triton X-100 or CHAPS concentration of 0.2%. Buffer volumes used for equilibration, elution, and neutralization were adjusted accordingly. To analyze unspecific binding of mGBA2-Flag or mGBA2-HA during precipitation, lysate of cells expressing either of the proteins was loaded overnight on either 50 µl anti-Flag magnetic bead slurry or 50 µl agarose matrix suspension after equilibration (250 µg protein in 500 µl total volume). Finally, the different fractions were subjected to Western blot analysis.

Table 30: Buffers used for co-immunoprecipitation of mGBA2

Equilibration buffer	Lysis buffer	Washing buffer
10 mM Tris/HCl pH 7.4	10 mM Tris/HCl pH 7.5	10 mM Tris/HCl pH 7.5
150 mM NaCl	150 mM NaCl	150 mM NaCl
	0.5 mM EDTA	0.5 mM EDTA
	1% (v/v) TritonX-100	0.2% (v/v) TritonX-100
	1:500 mPIC	1:500 mPIC

2.11.8 Chemical protein cross-linking using disuccinimidyl suberate (DSS)

Cells seeded on a 9 cm plate expressing mGBA2-Flag and mutant or wild-type mGBA2-HA were washed twice in 5 ml PBS, harvested in 1 ml of 0.5 g/l EDTA in PBS, and then lysed in hypotonic buffer in the presence of mammalian protease inhibitor cocktail and sonicated on ice thrice 30 sec each. The homo-bifunctional disuccinimicyl suberate (DSS; Thermo Scientific) with a linker arm length of 11.4 Å was used as a cross-linking reagent. In a first set of experiments, cells were lysed in either 10 mM HEPES/NaOH (pH 7.4) or 25 mM HEPES/NaOH (pH 7.4)/ 100 mM NaCl. DSS added to 40 µg protein in a total volume of 40 µl was used at a final concentration of 0.77 mM, 1.48 mM, 2.14 mM, or 2.76 mM DSS and incubated either at room temperature for 20 min or at 4°C for 20 min, 60 min, 120 min, or 180 min end-over-end. For all conditions, reaction was quenched by addition of 12 µl 1 M Tris-(hydroxymethyl)-aminomethane (Tris) pH 7.5. A control sample with no addition of DSS and Tris was run in parallel. Western blot analysis was performed and the total volume of the samples was loaded with cross-linked samples either being boiled or not boiled for 5 min at 95°C. Optimal cross-linking conditions used for all subsequent experiments included lysis in 10 mM HEPES/NaOH (pH 7.4), 0.77 mM DSS, incubation at 4°C for 2 h, and finally loading non-boiled samples for Western blot analysis.

2.11.9 Fluorescence-based β-glucosidase activity assay

2.11.9.1 Setup of the β-glucosidase activity assay

A fluorescence-based activity assay was performed as described previously to determine β-glucosidase activity *in vitro* (Körschen et al., 2013). Protein lysates of cultured cells or tissue were prepared in hypotonic buffer as described earlier (2.11.1.1, 2.11.1.2). Measurements were performed in McIlvaine buffer at pH 4 and pH 6 to distinguish GBA1 and GBA2 activity, respectively. Therefore, 20 µl protein lysate was diluted in 90 µl McIlvaine buffer per well on a 96-well plate (**Table 31**). Moreover, the GBA1 inhibitor CBE (conduritol B epoxide, Sigma Aldrich) and the GBA2 inhibitor NB-DNJ (*N*-butyl-deoxynojirimycin, Sigma Aldrich) were prepared as a 390 µM and 130 µM stock, respectively, of which 10 µl (each or both blockers)

was added per well (**Table 31**). If necessary, the final volume of 130 µl per well was adjusted with hypotonic buffer. This suspension prepared on the 96-well plate was transferred to a 384-well plate as quadruplicates à 25 µl (**Table 31**). Each well of the 384-well plate contained 4-34 µg of total protein. Finally, 5 µl 4-methylumbelliferyl-β-D-glucopyranoside (4-MUG; 10 mM) was added, resulting in a final concentration of 4-MUG accounting for 1.67 mM, of CBE accounting for 25 µM, and of NB-DNJ accounting for 8.3 µM (**Table 31**). 4-MUG is cleaved by the β-glucosidases and emits fluorescence at 460 nm when being excited at 355 nm.

Table 31: Pipetting scheme for β-glucosidase activity assay

<table>
<tr><td>McIlvaine buffer</td><td colspan="4">96-well plate assay approach</td><td>384-well plate assay approach</td></tr>
<tr><td rowspan="3">0.1 M citric acid
0.2 M Na_2HPO_4</td><td>1</td><td>2</td><td>3</td><td>4</td><td rowspan="3">25 µl of 96-well plate assay approach
5 µl 10 mM 4-MUG</td></tr>
<tr><td colspan="4">90 µl McIlvaine buffer (pH 4 or pH 6)</td></tr>
<tr><td colspan="4">20 µl protein lysate</td></tr>
<tr><td rowspan="2"></td><td>-</td><td>10 µl
390 µM CBE</td><td>10 µl
130 µM NB-DNJ</td><td>10 µl
390 µM CBE
and
130 µM NB-DNJ</td><td rowspan="2">25 µM final CBE concentration
and
8.3 µM final NB-DNJ concentration</td></tr>
<tr><td>20 µl</td><td>10 µl</td><td>10 µl</td><td>-</td></tr>
<tr><td colspan="5">hypotonic buffer</td></tr>
</table>

2.11.9.2 Fluorometric measurement using Fluostar plate reader

Emitted fluorescence was measured at 29°C or 37°C in individual wells of a black 384-well plate (Greiner) from the top view using a 355 nm (excitation)/ 460 nm (emission) filter in a fluorescence plate reader (Fluostar OMEGA reader, BMG Labtech). Gain was adjusted to 800 and prior to addition of 4-MUG, a basal fluorescence of the cell suspension was determined in 5 cycles. In total, fluorescence was measured over 150 cycles, whereas in later cycles the number of flashes per well was increased according to **Table 32**.

Table 32: Kinetic windows set for fluorescence measurements using the Fluostar plate reader

	Kinetic window 1	Kinetic window 2
Number of cycles	50	100
Cycle time (sec)	50	80
Number of flashes per well	2	10

2.11.9.3 Dose-response analysis of AMP-DNM

A 50 mM stock of AMP-DNM (molecular weight of 397.6 g/mol), which was kindly provided by Prof. Dr. Johannes Aerts (Leiden University), was prepared in pure DMSO and stored at -20°C until further use. For dose-response analyses utilizing the β-glucosidase activity assay, AMP-DNM diluted in hypotonic buffer (10 mM HEPES/NaOH, 0.5 mM EDTA, 1:500 mPIC) in a serial manner to yield final concentrations of 0.0083 pM up to 25 µM AMP-DNM.

2.11.10 Rho GTPase pull-down activation assay

All steps were performed on ice in the presence of mPIC (Sigma Aldrich). Murine dermal fibroblasts were harvested from three confluent 9 cm plates and lysed in 750 µl lysis buffer (**Table 33**) by passing through a 24G needle connected to a 1 ml syringe (20 strokes) within 5 min. An aliquot was taken to determine the protein concentration (see 2.11.2.2) and the remaining sample was directly snap frozen to prevent Rho GTPase degradation. For the assay, 400 µg protein and 300 µg protein was used to measure the amount of Rac1-GTP and Cdc42-GTP, respectively, and diluted with lysis buffer to 0.5 µg/µl. 10 µg glutathione S-transferase (GST)-tagged PAK-PBD protein (PAK: p21-activated kinase, PBD: p21-activated kinase binding domain; Cytoskeleton Inc., PAK01-A) was added to each of the samples and incubated for 30 min end-over-end. 25 µl Glutathione Sepharose® beads (GE Healthcare, 17-0756-05), which have been equilibrated with lysis buffer, were added. The samples were incubated for 30 min end-over-end. Next, beads were pelleted by centrifugation at 8000 x g for 1 min and washed once with 500 µl washing buffer (**Table 33**). After a 3-minute centrifugation at 8000 x g, the pellet was resuspended in 25 µl 2 x SDS sample buffer and analyzed by Western blot. 10 µg protein of the original lysate was taken as an input for Western blot analysis. As positive and negative controls, protein lysates loaded with 200 µM guanosine-5'-triphosphate (GTP) or guanosine 5′-diphosphate (GDP) (Cytoskeleton Inc., BK035), respectively, were prepared in parallel. To allow nucleotide exchange, samples were treated with 15 mM EDTA prior to incubation with PAK-PBD protein. The reaction was quenched by addition of 60 mM $MgCl_2$.

Table 33: Buffers used for Rho GTPase pull-down activation assay

Lysis buffer	Washing buffer
50 mM Tris/HCl pH 7.5	25 mM Tris/HCl pH 7.5
10 mM $MgCl_2$	30 mM $MgCl_2$
0.5 M NaCl	40 mM NaCl
2% Ipegal-CA630	1:500 mPIC
1:500 mPIC	

2.12 Lipid analyses

Mass spectrometry and thin layer chromatography (TLC) analysis of GlcCer and complex glycosphingolipids were performed in collaboration with Prof. Dr. Peter Dörmann (Institute of Molecular Physiology and Biotechnology of Plants, Bonn) and Prof. Dr. Roger Sandhoff (DKFZ, Heidelberg), respectively.

2.12.1 Isolation of lipids from murine cerebellum

Cerebellum of 10- to 13-week old mice was dissected and lysed in 800 µl hypotonic buffer (10 mM HEPES, 0.5 mM EDTA, 1:500 mPIC). In addition, cerebellum of early postnatal mice (P10) was isolated and homogenized in 600 µl hypotonic buffer (see 2.11.1.2). Protein concentration was determined in a Bradford test (2.11.2.1). Samples were stored at -80°C until further use and sent on dry ice for measurements in the collaborating labs.

2.12.2 Lipid extraction for mass spectrometry

Lipid extraction for mass spectrometry was performed as described in Schonauer et al., 2017 by Dr. Katharina Gutbrod (Institute of Molecular Physiology and Biotechnology of Plants, Bonn). 500 µl chloroform/ methanol/ formic acid (ratio 1:1:0.1) was added per sample and mixed thoroughly. As a control, 50 µl of an internal standard lipid mix was added. Phase separation was obtained by centrifugation at 5,000 x rpm for 3 min after 250 µl 1 M KCl/ 0.2 M H_3PO_4 has been added and mixed by vortexing. The lower lipid-containing phase was transferred to a fresh glass vial and addition of chloroform/methanol (ratio 2:1) was performed to re-extract lipids from the remaining sample. Samples were vortexed and centrifuged at 5,000 x rpm for 3 min. The lower phase was combined with the lipid extract obtained before. Solvents were evaporated under a gentle nitrogen flow and the fraction was finally dissolved in 500 µl chloroform.

Lipids were purified using small silica columns (Strata-1-Silica) which have been equilibrated with pure chloroform before. Lipid extracts dissolved in chloroform were loaded and non-polar lipids, medium-polar sphingolipids (long chain bases, ceramides, hexosylceramides), and very

polar sphingolipids (e.g. sphingomyelin) were eluted in 3 x column volume (CV) of chloroform, acetone/ isopropanol (ratio 1:1), and methanol, respectively. Solvents were evaporated under a gentle nitrogen flow and the fraction was finally dissolved in 100 µl methanol. Half of the sample was dried once more to be dissolved in 100 µl chloroform/ methanol/ 300 mM ammonium acetate (ratio 300:665:35) and used for mass spectrometry analysis by nanospray direct infusion Q-TOF MS/MS as described previously in Ginkel et al. (Ginkel et al., 2012) and Raju et al. (Raju et al., 2015). The remaining 50 µl sample, dissolved in methanol, was used for LC-MS/MS measurements to analyze contents of glycosylated long chain bases (LCBs) according to Scherer et al. (Scherer et al., 2010).

2.12.3 Lipid extraction for thin layer chromatography (TLC)

For thin layer chromatography (TLC), 2 to 3 mg protein were transferred into 2 ml Eppendorf tubes, lyophilized, and directly suspended in 1 ml methanol in a TissueLyser using metal beads. Samples were supplemented with 1 ml chloroform and incubated for 15 min at 37°C in an ultrasonic bath. Centrifugation at 12,000 x g for 5 min followed and the pellet was re-extracted with 2 ml chloroform/ methanol/ water (ratio 10:10:1) and 2 ml chloroform/ methanol/ water (ratio 30:60:8). Supernatant in the first, second, and third phase was combined (raw extract) and acidic lipids were separated from neutral lipids by performing anion-exchange chromatography on DEAE Sephadex® A-25 columns (100 µl column volume). Finally, acidic fraction was desalted by reversed-phase chromatography. Mild alkaline treatment for 2 h at 37°C using 0.1 M KOH in methanol was performed to enrich gangliosides. Afterwards, acetic acid was used for neutralization and samples were desalted by reversed-phase chromatography. Solvents in the ganglioside fraction were evaporated under a gentle nitrogen flow at 37°C and the fraction was dissolved in chloroform/ methanol/ water (ratio 10:10:1) yielding a concentration of 1 mg protein per 100 µl. Finally, 1 mg of total protein was subjected to high-performance thin layer chromatography (HP-TLC) developed with the solvent chloroform/ methanol/ 0.2% aqueous $CaCl_2$ (ratio 45:45:10) and stained for glycolipids using the orcinol colorimetric detection reagent (Sigma). Porcine brain gangliosides (PBGG) and the gangliosides GM3, GM2, GM1a, and GD3 were run in parallel as standards.

2.12.4 Isolation of detergent-resistant (DRM) membranes

Separation of detergent-resistant membrane fractions was adapted from a study published by Lingwood & Simons (Lingwood and Simons, 2007). All steps were performed at 4°C or on ice in the presence of mPIC (Sigma Aldrich). 3 x 10^6 murine dermal fibroblasts were pelleted and lysed in 0.7 ml 1x TNE buffer (**Table 34**) by passing through a 24G needle connected to a 1 ml syringe (25 strokes). Cerebellum and spinal cord was lysed in 0.8 ml and 1 ml 1x TNE buffer, respectively. Tissue was homogenized using a pistil and passed through a 24G needle

connected to a 1 ml syringe (25 strokes). Cell debris of the tissue lysates was pelleted by centrifugation at 10,000 x g for 1 min and small portions of the supernatant (10-50 µg) were taken as input samples for Western blot analysis after protein concentration has been determined in a BCA test (2.11.2.2). 315 µl of the supernatant was transferred to a new Eppendorf tube, gently mixed with 35 µl 10% (v/v) TritonX-100 prepared in 1x TNE buffer, and incubated for 30 min. 700 µl of 60% iodoxanol (Optiprep, Sigma, D1556) was added and mixed well resulting in a final concentration of 40% iodoxanol. The sample (1050 µl) was then transferred to an ultracentrifuge tube and overlaid with 2.1 ml of 30% iodoxanol (Optiprep diluted in 2x TNE buffer in a ratio of 1:1). Finally, 350 µl TNE buffer was pipetted on top without disturbing the gradient. Ultracentrifugation at 260,000 x g for 2 h was performed in a SW-55 Ti rotor (Beckman Coulter, 342196). After centrifugation, three equal fractions à 1167 µl were taken as top, middle, and bottom fraction and 15 µl samples were prepared in 4x SDS sample buffer to be loaded onto a 12.5% SDS gel for subsequent Western blot analysis.

Table 34: TNE buffer for detergent-resistant membrane isolation

TNE buffer (1 x)
5 mM Tris/HCl pH 7.4
150 mM NaCl
2 mM EDTA
1:500 mPIC

2.13 Behavioral tests

2.13.1 Weight Test

The weight test was performed to determine the forepaw muscle strength of mice (Deacon, 2013) that had to grasp a steel chain consisting of different weights: 1) 21 g, 2), 34.8 g, 3) 48.6 g, 4) 62.4 g, 5) 75.5 g, 6) 89 g, and 7) 103.3 g. When the mouse grasped the steel wool attached to the chain solely with its forepaws, it was lifted by its tail. If the animal held the weight for 3 sec it was tested on the next heavier weight. If the mouse failed to hold the weight for 3 sec, it was tested on the same weight again after a resting phase of at least 10 sec. The trial was terminated when the animal failed thrice to hold a weight for 3 sec and the time (0 to 2 sec) it was able to hold this weight was noted. Finally, the relative muscle strength unit (rsu) was calculated as follows:

$$x\ [rsu] = n \text{ x } 3\ [\text{sec}] + t\ [\text{sec}]$$

whereby *n* refers to the weight (0 to 7) the mouse could lift for 3 sec and *t* is defined by the time the animal could hold the next heavier weight (1 to 7).

The weight test was performed on 3 individual days after the animals habituated to the experiment setup one day before and an average rsu value was calculated for each mouse. (Khrameeva et al., 2018)

2.13.2 Catwalk

In collaboration with Prof. Dr. Frank Bradke (DZNE, Bonn) and PD Dr. Heike Endepols (Institute of Radiochemistry and Experimental Molecular Imaging, Cologne) locomotion of GBA2-knockout mice was analyzed. The CatWalk™ XT system (Noldus Information Technology, The Netherlands) was used to study the gait of freely moving mice passing a walkway. The CatWalk™ consists of a glass plate that is illuminated with green light. Upon placement of a paw, the light is scattered, which is detected by a camera positioned underneath the glass plate. The detection sensitivity is enhanced by complementary red light illuminating the walkway from the ceiling. Thus, the experiments have to be performed in darkness.

Prior to the experiment, the distance of the camera to the glass plate was set to 40 cm and the software was calibrated using a 20 cm x 10 cm calibration sheet to provide a distance scale for subsequent analyses. The width of the corridor the mice have to pass was set to 5.5 cm and its dimensions were defined in the live view of the software. By performing test runs with mice, the optimal detection settings were determined: The camera gain was set to 20.00 db (Catwalk XT 10.6) or 30.00 dB (CatWalk XT 9.0) and the green intensity threshold to 0.1 to define the maximum and minimum green intensity for paw detection, respectively. In addition, the Catwalk XT 10.6 software allowed to adjust the intensity of the red ceiling and green walkway LED lights and was set to 17.7 V and 16.0 V, respectively. Overall, the experiment was performed on three consecutive days at the same time in the morning after the animals could habituate to the setup one day before. Prior to each run, the walkway was cleaned and the background was snapped in the software's live view. Two runs per animal (with a maximum speed variation of 60%) from each of the three experimental days were classified for the analysis, including four consecutive steps of each paw. Since both the CatWalk XT 9.0 and 10.6 software were used, data of GBA2-knockout mice was analyzed relative to the corresponding wild-type (WT) mice tested with the same software (% relative to WT). The interpaw coordination parameter step sequence and Phase Dispersion, which are based on the temporal relationship of consecutive placement of the different paws, were compiled as averaged values for WT and GBA2-knockout over all experiments or as individual values for each animal, respectively.

2.14 Validation of mouse genotypes

After the behavior tests, genotypes of all tested mice were verified in a β-glucosidase activity assay (see 2.11.1.2, 2.11.9) using hypotonic brain lysates or in addition hypotonic skeletal muscle lysates to validate the muscle-specific GBA2-knockout.

2.15 Software applications

In addition to the aforementioned device-specific software applications, Origin Pro (version 9.0), CorelDRAW (version X7), ImageJ (version 1.51w, Wayne Rasband, National Institutes of Health, USA), ChemDraw (version 16), Olympus FV10-ASW viewer (version 03.00.01.15), NIS elements viewer (version 4.20), Microsoft Excel 2013, Microsoft Word 2013, and EndNote (version X7.2) were utilized to analyze and visualize the experimental data and compile this thesis.

2.16 Statistics

Data represent mean values with standard deviation (+ S.D.) from independent experiments (n numbers are indicated) if not stated otherwise. Statistical analysis was performed with Origin Pro (version 9.0) using one-sample t-test or one-way analysis of variance (ANOVA).

3 Results

3.1 Do mutations in GBA2 affect enzyme function?

3.1.1 Cloning of mGBA2 mutants

The open reading frame of mouse GBA2 (NM_172692) was amplified from cDNA using primers containing restriction sites and a Kozak sequence in front of the start codon (**Table 4**, 2.4.1). The sequence encoding a hemagglutinin (HA) tag was added by PCR at the 3'-end. PCR products were subcloned into pcDNA3.1(+) and their sequence was verified.

3.1.2 Heterologous expression of mGBA2 mutants

To study the effect of mutations on GBA2 function, I heterologously expressed mGBA2 mutants in CHO cells (Woeste, Master thesis, 2015). First, the expression of wild-type GBA2 and GBA2 mutants was analyzed by immunocytochemistry (**Figure 11**; experiments were performed by Dominik Dittmann based on Woeste, Master thesis, 2015). All mutants were expressed and the subcellular localization was similar to wild-type GBA2.

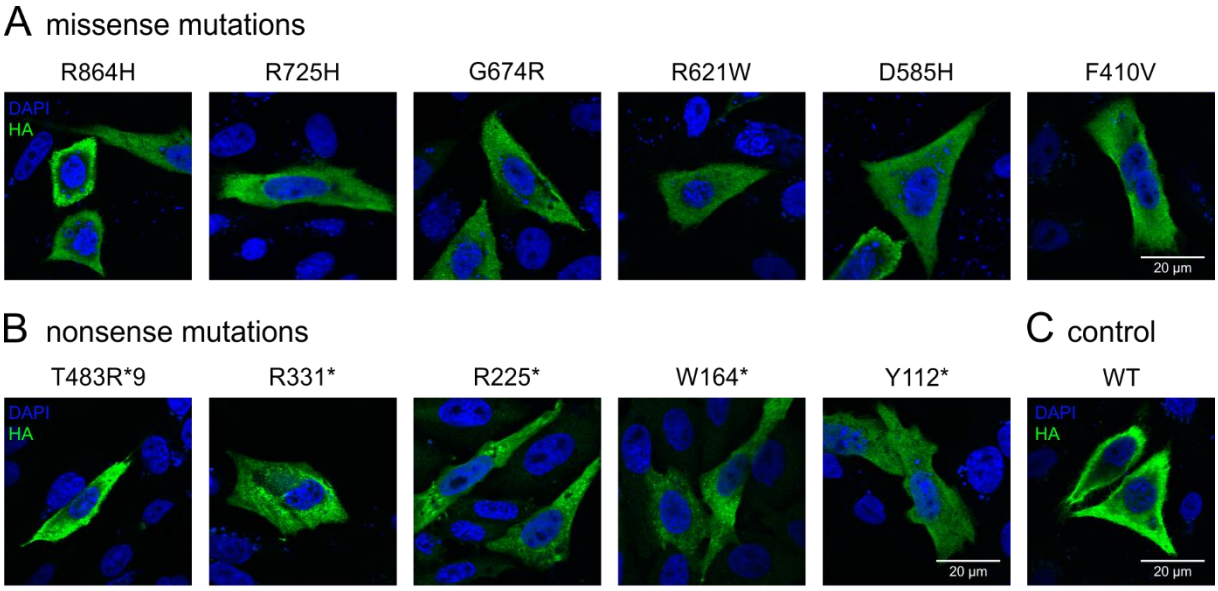

Figure 11: Immunocytochemical staining of CHO cells expressing mGBA2 mutants. Expression of **A)** mGBA2 missense mutations, **B)** nonsense mutations, and **C)** wild-type mGBA2 in CHO cells. The HA-tagged mGBA2 proteins were stained using an HA-specific antibody (green). Nuclei were stained using DAPI (blue). Scale bars are indicated. Experiments were performed by Dominik Dittmann.

3.1.3 β-Glucosidase activity assay

The activity of GBA2 was analyzed by using a β-glucosidase activity assay established in our lab (Körschen et al., 2013). In this assay, the artificial, water-soluble substrate 4-methylumbelliferyl-β-D-glucopyranoside (4-MUG) is hydrolyzed by β-glucosidases to 4-methylumbelliferone (4-MU) (**Figure 12 A**). Since 4-MU emits fluorescence at 460 nm when being excited at 355 nm, an increase in fluorescence, proportional to the amount of cleaved substrate, is measured in a Fluostar plate reader. The slope over the linear range (cycle 50 to 100) is calculated, which resembles the activity of GBA2 in rfu/min (**Figure 12 B**).

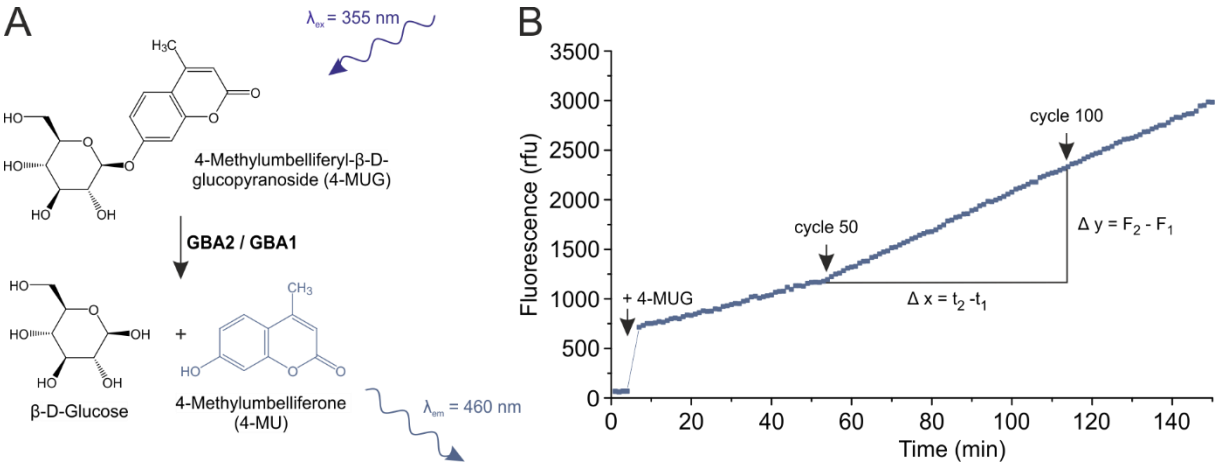

Figure 12: Fluorescence-based measurement of GBA2 and GBA1 activity. A) 4-Methylumbelliferyl-β-D-glucopyranoside (4-MUG) is used as an artificial, water-soluble substrate in the β-glucosidase activity assay. GBA2 and GBA1 cleave 4-MUG to β-D-glucose and 4-Methylumbelliferone (4-MU). The sample is excited at 355 nm and fluorescence emission is measured at 460 nm. **B)** The increase in fluorescence (rfu) over time (min) upon cleavage of 4-MUG to 4-MU is monitored in a Fluostar fluorescence plate reader. For each sample (measured as quadruplicates), the slope (per min) is calculated over the linear range (cycle 50 to 100). λ_{ex}: excitation wavelength; λ_{em}: emission wavelength; rfu: relative fluorescence units; min: minutes; t: time; F: fluorescence.

Importantly, the assay allows to distinguish between the activities of the lysosomal glucosylceramidase GBA1 and the non-lysosomal glucosylceramidase GBA2 using the specific inhibitors conduritol B epoxide (CBE, GBA1-specific) and *N*-butyl-deoxynojirimycin (NB-DNJ, GBA2-specific), and their different pH optima (**Figure 13**) (Körschen et al., 2013). The pH optimum for GBA1 is at pH 4, whereas GBA2 activity is highest at pH 6 (**Figure 13**). However, both enzymes display residual activity at pH 6 and pH 4. Addition of CBE and NB-DNJ allows to determine GBA1 (CBE-blockable; pH 4) and GBA2 activity (NB-DNJ-blockable; pH 6) (**Figure 13**).

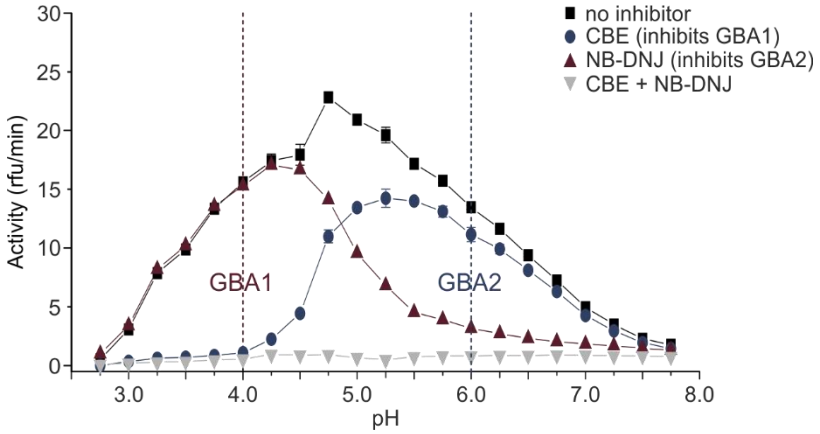

Figure 13: pH dependence of GBA1 and GBA2 activity. Fluorescence-based activity assay was performed at different pH with hypotonic liver lysates by adding 1.67 mM 4-MUG. Without any blocker (black squares), GBA1 and GBA2 activity cannot be distinguished, whereas addition of 30 µM CBE (blue circles) or 10 µM NB-DNJ (red triangles) reveals GBA1 and GBA2 activity at pH 4 and pH 6, respectively. Presence of both blockers (grey triangles) completely diminished any β-glucosidase activity in liver lysates. CBE: Conduritol B epoxide; NB-DNJ: *N*-butyl-deoxynojirimycin. Modified from: Körschen et al., 2013.

3.1.4 Mutations in GBA2 cause a loss of function of the enzyme

The GBA2 proteins with a missense or nonsense mutation were heterologously expressed in CHO cells (Woeste, Master thesis, 2015). Western blot analysis revealed that the missense mutations are all expressed at similar levels and migrated on a SDS-PAGE according to their calculated molecular weight (**Figure 14 A**). The nonsense mutations T483R*9 and R331* also revealed comparable expression levels, whereas the expression of R225*, W164*, and Y112* was low (**Figure 14 A**). Of note, the mutants T483R*9, R331*, R225*, W164*, and Y112* ran at slightly higher molecular weight than their calculated molecular weight of 55 kDa, 37 kDa, 26 kDa, 18 kDa, and 12 kDa, respectively. Next, GBA2 activity was determined in hypotonic lysates from transfected cells and compared to the activity of cells stably expressing wild-type GBA2 (Woeste, Master thesis, 2015). My results show that all mutations besides R725H caused a complete loss of function of the enzyme (**Figure 14 B**; Woeste, Master thesis, 2015). The activity of the R725H mutant accounted for 30.28 ± 9.32 % compared to wild-type GBA2. Interestingly, although, a similar amino-acid substitution to histidine (H) affected the arginine (R) at position 864, phenotypes of the R725H and R864H mutant differed, resulting in a dead mutant.

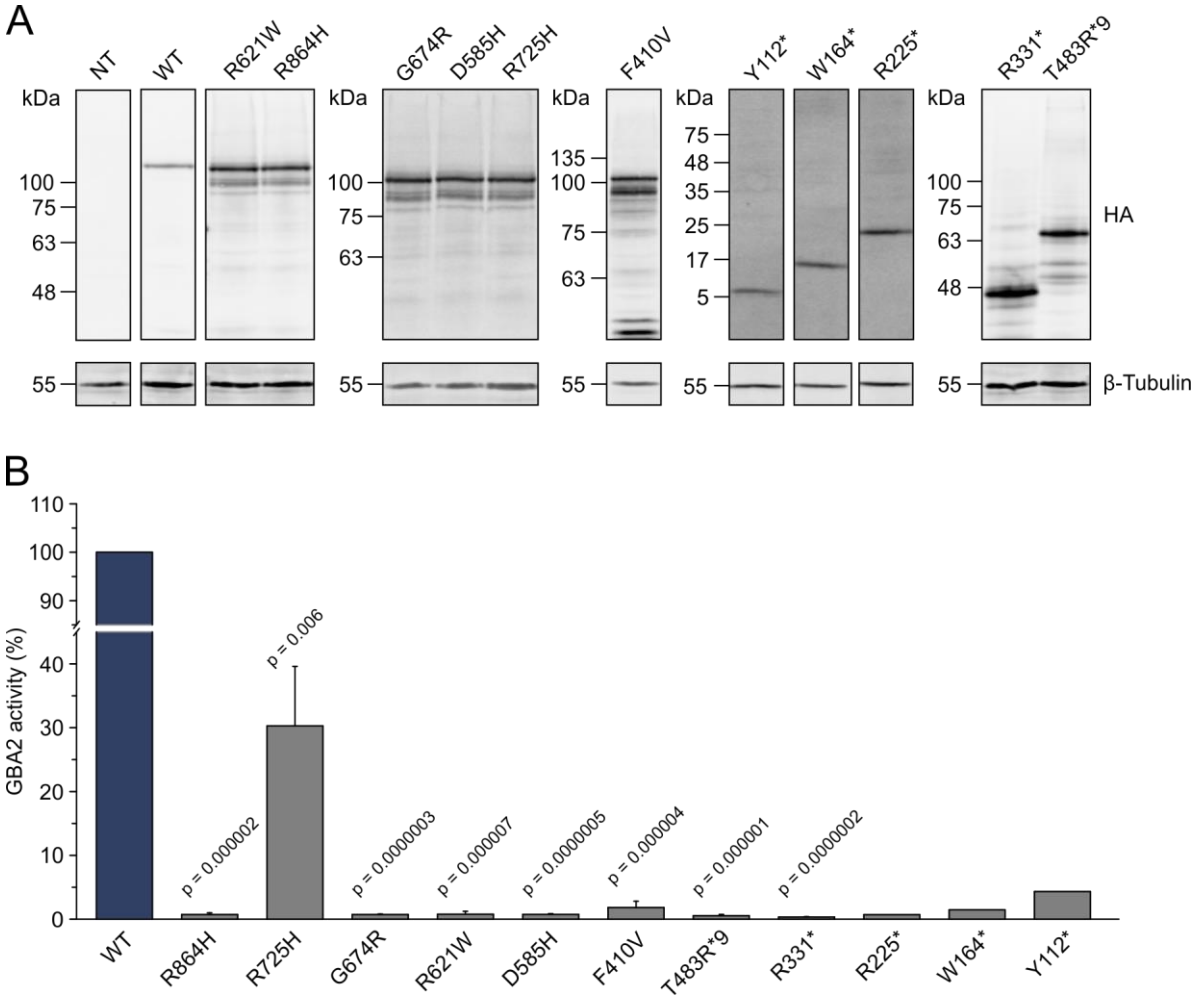

Figure 14: Heterologous expression and activity of mGBA2 mutants in CHO cells. A) Western blot analysis of hypotonic lysates from non-transfected CHO cells (NT), CHO cells stably expressing wild-type mGBA2-HA (WT), or CHO cells expressing the different mGBA2 mutants. mGBA2 was detected using an HA-specific antibody. B-Tubulin served as a loading control. 10-20 µg protein was loaded per lane. **B)** Analysis of the GBA2 activity in hypotonic lysates of CHO cells heterologously expressing wild-type mGBA2 (WT) or mutant mGBA2. Columns represent mean values of three independent experiments (besides R225*, W164*, Y112*: n = 1) + SD. Statistical analysis was performed using one-sample t-test (p values are indicated). Modified and expanded by the analysis of the F410V mGBA2 mutant from Woeste, Master thesis, 2015.

3.2 Structure-function analysis of GBA2

Enzyme function depends on electrostatic interaction with the substrate (Graf et al., 1988; Wade et al., 1998). Several GBA2 mutations exchange an uncharged to a charged amino acid, or vice versa, suggesting that loss of activity is caused by impaired electrostatic interactions with the substrate. This applies to the mutations R864H, R725H, R621W, G674R, and D585H, where a positively charged arginine (R) was exchanged to a polar, uncharged histidine (H) or tryptophan (W), an uncharged, hydrophobic glycine (P) to a positively charged arginine (R), or the negatively charged aspartate (D) to a polar uncharged histidine (H). The charged residues arginine and aspartate might be involved in the formation of salt bridges (Barlow and Thornton, 1983). Thus, loss or introduction of a charge might destabilize the GBA2 protein, leading to impaired enzyme function.

To test whether the charge is indeed important for protein function, I exchanged R864 or R621 to another positively charged amino acid (lysine: K) or to an amino acid that is not charged (glutamine: Q) (Woeste, Master thesis, 2015). Mutants were expressed in CHO cells and their activity was determined (**Figure 15**). However, all mutants showed a significant decrease in GBA2 activity compared to wild-type GBA2 (**Figure 15 B**), demonstrating that both arginines at position 864 and 621 are required for GBA2 activity (Woeste, Master thesis, 2015). In contrast to lysine with its single terminal ammonium moiety, arginine bears three asymmetric nitrogens in the guanidinium moiety and, thereby, carries multiple sites to form electrostatic interactions within a protein (Borders et al., 1994). Moreover, arginine residues (aqueous pK_a: 13.8) stay protonated even when buried inside proteins or facing lipid membranes (Fitch et al., 2015; Harms et al., 2011; Li et al., 2013), whereas lysine (aqueous pK_a: 10.4) easily deprotonates and exhibits large pK_a shifts in different environments (Isom et al., 2011; Li et al., 2013). These properties of arginine might be indispensable to form a stable and functional GBA2 protein.

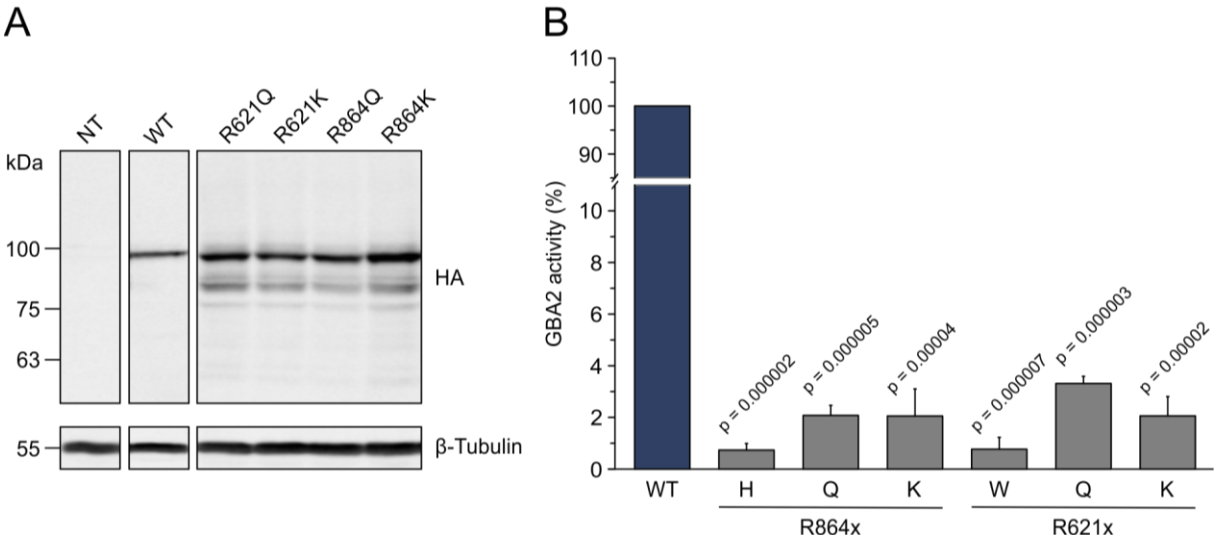

Figure 15: Heterologous expression and activity of mGBA2 mutants. A) Western blot analysis and **B)** analysis of the GBA2 activity of hypotonic cell lysates from non-transfected cells (NT), cells heterologously expressing wild-type mGBA2-HA (WT), or cells expressing the different mGBA2 mutants. mGBA2 was detected using an HA-specific antibody. β-Tubulin served as a loading control. 10-20 µg protein was loaded per lane. Columns represent mean values of three independent experiments + SD. Statistical analysis was performed using one-sample t-test (p values are indicated). Modified from Woeste, Master thesis, 2015.

Next, I wondered whether there is a “minimal” GBA2 protein that conveys β-glucosidase activity (Woeste, Master thesis, 2015). I tested different constructs that include 1.) the catalytic 6-hairpin glucosidase domain (aa 442-918), 2.) the glucosylceramidase domain (aa 512-918), or lack 3.) the N-terminal aa1-125 (Δ126), 4.) the N-terminal aa1-135 (Δ136), or 5.) the C-terminal aa883-918 (Q882*) (**Figure 16**). The last three constructs have been generated according to RaptorX modelling of mGBA2, which postulated protein domain boundaries

starting from amino acid 126 or 136 and ending at amino acid 882 (**Figure 16**; Prof. Dr. Matthias Geyer, unpublished data).

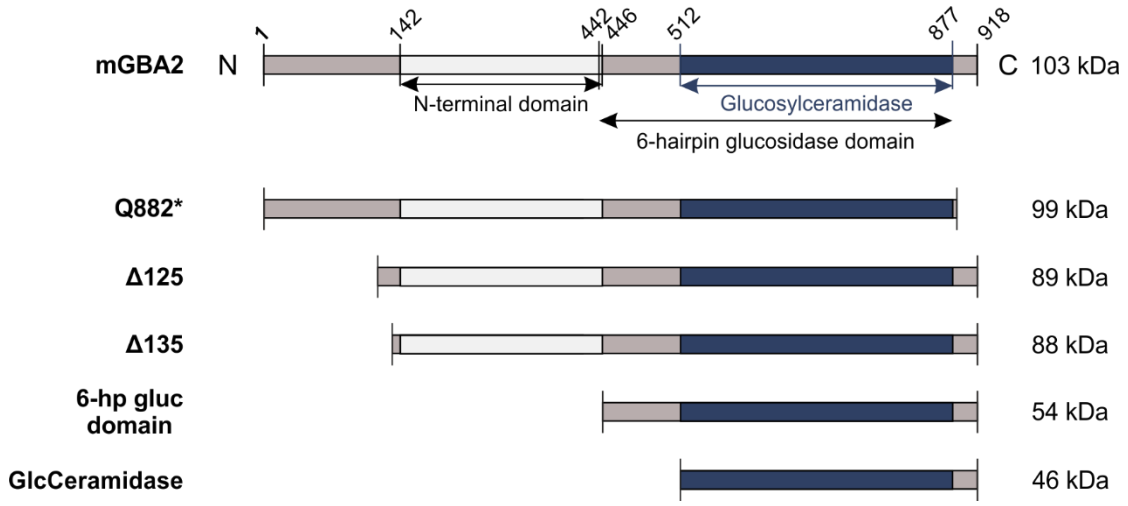

Figure 16: Mutations introduced into the *mGBA2* gene for structure-function studies. Wild-type mGBA2 (top) and the mGBA2 variants with a C- or N-terminal deletion are depicted. Functional domains were assigned according to InterPro (Finn et al., 2017) and protein sizes are indicated. 6-hp gluc domain: 6-hairpin glucosidase domain; GlcCeramidase: glucosylceramidase domain.

Western blot analysis revealed that the truncated GBA2 variants were expressed at equal levels (**Figure 17 A**). However, GBA2 activity of these mutants was significantly decreased compared to wild-type GBA2 (**Figure 17 B**). Thus, neither the 6-hairpin glucosidase nor the glucosylceramidase domain are sufficient for GBA2 function (**Figure 17 B**). Additional N-terminal amino-acids (Δ125, Δ135) did not recover enzyme activity (**Figure 17 B**). Even the sequence containing the complete N-terminal part and the C-terminal part up to aa 882 did not display significant GBA2 activity (**Figure 17 B**). In summary, my results reveal that the catalytic activity of GBA2 seems to be encoded by its tertiary structure rather than a defined amino-acid sequence (Woeste, Master thesis, 2015).

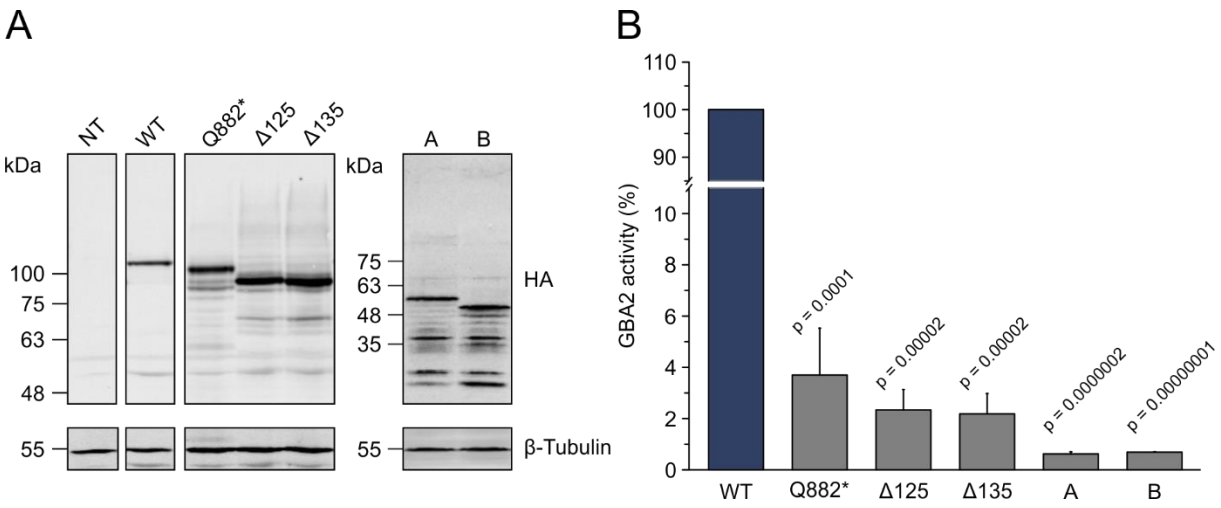

Figure 17: Expression and activity of mGBA2 mutants generated for structure-function studies. A) Western blot analysis and **B)** analysis of the GBA2 activity of hypotonic cell lysates from non-transfected cells (NT), cells heterologously expressing wild-type mGBA2-HA (WT), or cells expressing the different mGBA2 mutants. mGBA2 was detected using an HA-specific antibody. β-Tubulin served as a loading control. 10-20 µg protein was loaded per lane. Columns represent mean values of three independent experiments + SD. Statistical analysis was performed using one-sample t-test (p values are indicated). A: 6-hairpin glucosidase domain, B: glucosylceramidase domain. Modified from Woeste, Master thesis, 2015.

3.3 Structural modelling of GBA2

Recently, the crystal structure of the β-glucosidase *Tx*GH116 from *Thermoanaerobacterium xylolyticum* was solved (Charoenwattanasatien et al., 2016). *Tx*GH116 belongs to the same glycoside hydrolase family GH116 as GBA2 and bears 40% sequence identity over the catalytic domain (Charoenwattanasatien et al., 2016). Structural modelling of hGBA2 based on the crystal structure of *Tx*GH116 revealed that the missense mutations R873H, R734H, G683R, R630W, and D594H assemble in the catalytic domain at the C terminus, while F419V and M510V locate to the linker region preceding the C-terminal domain (**Figure 18 B**; Prof. Dr. Matthias Geyer, unpublished data). According to the studies of Charoenwattanasatien and colleagues, the amino-acid residues D508 and R786 in *Tx*GH116, corresponding to D594 and R873 in hGBA2, respectively, face the catalytic cleft and might be involved in hydrogen bond formation to the hydroxyl groups of glucose (Charoenwattanasatien et al., 2016). The amino acid G683 in hGBA2 is located in a loop involved in the acid/base reaction and sugar binding, whereas R630 might electrostatically interact with the anionic carboxylates E555 and D631 in close proximity (Charoenwattanasatien et al., 2016). Mutating the amino acids D594 and R873, G683, or R630 could therefore impair hydrogen-bond formation with the substrate, perturb proper formation of the loop including the acid/base and sugar-binding residue, or disturb amino-acid interactions important to stabilize GBA2 (Charoenwattanasatien et al., 2016). However, the amino acid R734 is not conserved in *Tx*GH116 and, according to our structural model, faces the surface of the protein rather than the catalytic site (**Figure 18**). Mutations at this position might therefore not directly affect the catalytic function of GBA2. Solving the crystal

structure of a mammalian GBA2 is needed to validate whether the homology modelling reliably predicted the protein structure. Thus, I aimed to purify mGBA2 for crystallization.

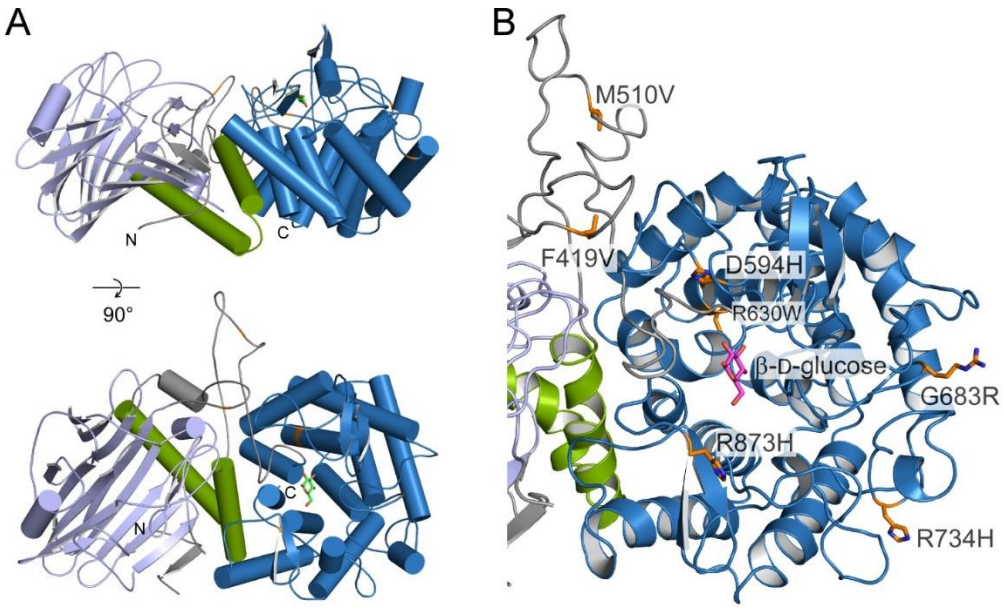

Figure 18: Structural modelling of hGBA2. A) Structural modelling of hGBA2 based on the crystal structure of the bacterial β-glucosidase from *Thermoanaerobacterium xylolyticum Tx*GH116 (Charoenwattanasatien et al., 2016). **B)** Detailed view of the missense disease-associated mutations found in GBA2 in the structural model of the human isoform. The missense mutations R873H, R734H, G683R, R630W, and D594H assemble in the catalytic domain (dark blue), whereas F419V and M510V align to the linker region preceding the C-terminal domain. The mutations are shown in stick representations. N-terminal domain: light blue; linker domain: green; β-D-glucose is depicted in light green **(A)** or pink **(B)**. Modelling was performed by Prof. Dr. Matthias Geyer (unpublished data).

3.4 Purification of mGBA2

Before the structure of the *Tx*GH116 protein has been solved, we performed RaptorX modelling of mGBA2, which proposed protein domains spanning amino-acid sequence 126-882. This sequence was required for proper folding of mGBA2 *in silico*, whereas additional N- or C-terminal amino acids disturbed homology modelling (Prof. Dr. Matthias Geyer, unpublished data). According to this model, we generated a construct to express mGBA2-126/882 in bacteria and purify the protein for structural analysis.

Previous studies in our lab revealed that wild-type mGBA2 cannot be purified in a soluble state (Dr. Heinz Gerd Körschen, unpublished data). To allow purification by affinity chromatography, mGBA2-126/882 was fused to MBP (maltose binding protein), which is supposed to provide more stability and solubility (Fox and Waugh, 2003; Kapust and Waugh, 1999). The open reading frame of mouse GBA2 (NM_172692) from amino acid 126 to 882 was amplified from cDNA using primers containing restriction sites (**Table 4**). PCR product was subcloned into pET28 MBP-tev (kindly provided by Prof. Dr. Matthias Geyer), which bears a tev (Tobacco Etch Virus) protease cleavage site following the coding sequence for the MBP protein, and the sequence was verified.

3.4.1 Expression of mGBA2 in *E.coli*

To express mGBA2 in *E.coli*, bacteria of the strain pLysE were transformed with pET28 MBP-tev-mGBA2-126/882 and the expression was induced by addition of 1 mM Isopropyl-β-D-thiogalactopyranoside (IPTG). Protein expression was analyzed at different time points after induction (1 h, 3 h, 5 h, and overnight at 18°C) by Western blot (**Figure 19**). To reveal whether MBP-tev-mGBA2-126/882 is soluble, total lysates (T) were separated into supernatant and pellet after centrifugation at 15,300 rpm, resulting in the soluble (S) and insoluble membrane (M) fraction. At all tested conditions, MBP-tev-mGBA2-126/882 (127.02 kDa) was predominantly localized in the membrane fraction, but also to a lesser extend in the soluble fraction.

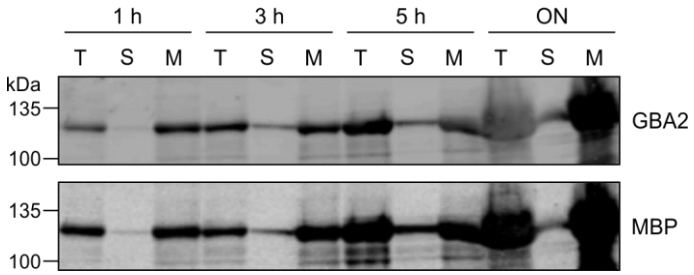

Figure 19: Expression of MBP-tev-mGBA2-126/882 in *E.coli*. Bacteria of the *E.coli* strain pLysE were transformed with a pET28 vector containing the coding sequence for MBP-tev-mGBA2-126/882. Expression was induced by addition of 1 mM Isopropyl β-D-1-thiogalactopyranoside (IPTG) and bacteria were grown for 1 h, 3 h, 5 h, or overnight (ON) at 18°C. 15 µl of the total fraction (T), soluble fraction (S), and membrane fraction (M) was loaded after resuspending the bacterial pellet in resuspension buffer and separating the fractions by centrifugation. MBP-tev-mGBA2-126/882 was detected using a GBA2- and MBP-specific antibody.

MBP-tev-mGBA2-126/882 expression levels was highest after overnight expression and the ratio of protein localization in the soluble compared to the membrane fraction was best under this condition (**Figure 19**). Thus, this condition was chosen for further experiments.

3.4.2 Affinity chromatography of MBP-tagged mGBA2 via MBPTrap™

To purify MBP-tev-mGBA2-126/882, I performed an affinity chromatography in a liquid chromatography system (ÄKTA; GE Healthcare) using a commercial MBPTrap™ column (GE Healthcare) containing cross-linked agarose (Sepharose) coated with dextrin. The eluted protein was collected and the input (In), non-bound (NB), washing fraction (Wash), and eluate (E) were analyzed by Western blot (**Figure 20 A, B**). Indeed, the MBP-tev-mGBA2-126/882 protein, with a calculated size of 127 kDa, could be purified and eluted from the column by addition of maltose (**Figure 20 A, B**).

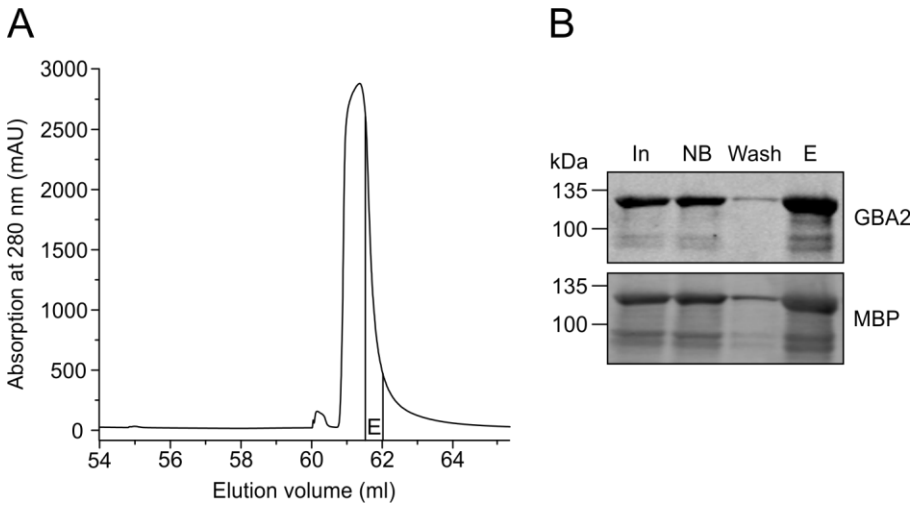

Figure 20: Affinity chromatography of MBP-tev-mGBA2-126/882. A) MBP-tev-mGBA2-126/882 was loaded onto an MBPTrap™ column (GE Healthcare) and eluted with 10 mM maltose. mAU: milli arbitrary units. **B)** Western blot analysis of the input (In, 1:10), non-bound (NB, 1:10), washing fraction (Wash, 1:10), and eluate (E, 1:10) obtained from the affinity chromatography depicted in **(A)**. 10 µl diluted sample was loaded per lane. MBP-tev-mGBA2-126/882 was detected using a GBA2- and MBP-specific antibody.

3.4.3 Separation of mGBA2-126/882 from MBP-tev-mGBA2-126/882 via MBPTrap™

The MBP-tag was used to increase the solubility of mGBA2 and enhance its stability during purification (Fox and Waugh, 2003; Kapust and Waugh, 1999), but the protein tag should be removed for crystallization. To this end, purified MBP-tev-mGBA2-126/882 (MBP-Trap; **Figure 21 A**) was incubated with tev protease. 500 µl of eluate obtained after purification was incubated with 1 µg tev protease per 100 µg MBP-tev-mGBA2-126/882 protein (= 1:100) overnight at 4°C. The tev protease recognizes the amino-acid sequence ENLYFQG, which we introduced into pET28-MBP-tev-mGBA2-126/882 between the MBP and mGBA2 protein. Cleavage will occur between the Q and G residue, separating MBP (41.57 kDa) and mGBA2-126/882 (85.47 kDa). Indeed, Western blot analysis revealed that MBP-tev-mGBA2-126/882 was cleaved by the tev protease, yielding mGBA2-126/882 with a size of 85.47 kDa (E^{tev}, E^{tev*}: after buffer exchange; **Figure 21 D**).

To separate MBP and mGBA2-126/882, I performed an affinity chromatography (MBPTrap™) of the protein sample, which was incubated with the tev protease (**Figure 21 B**). Prior to loading on the MBPTrap™ column, the buffer of the protein sample was exchanged to remove excess maltose and allow binding (E^{tev*}; **Figure 21 B**). The flow-through after binding will contain mGBA2-126/882 and the tev protease. However, Western blot analysis revealed that only a small portion of mGBA2-126/882 is found in the Non-Bound (NB^2; **Figure 21 D**). Most of the mGBA2-126/882 protein was present in the elution fraction (E^2) together with non-cleaved MBP-tev-mGBA2-126/882. Thus, affinity chromatography could not sufficiently separate cleaved and non-cleaved mGBA2-126/882 protein.

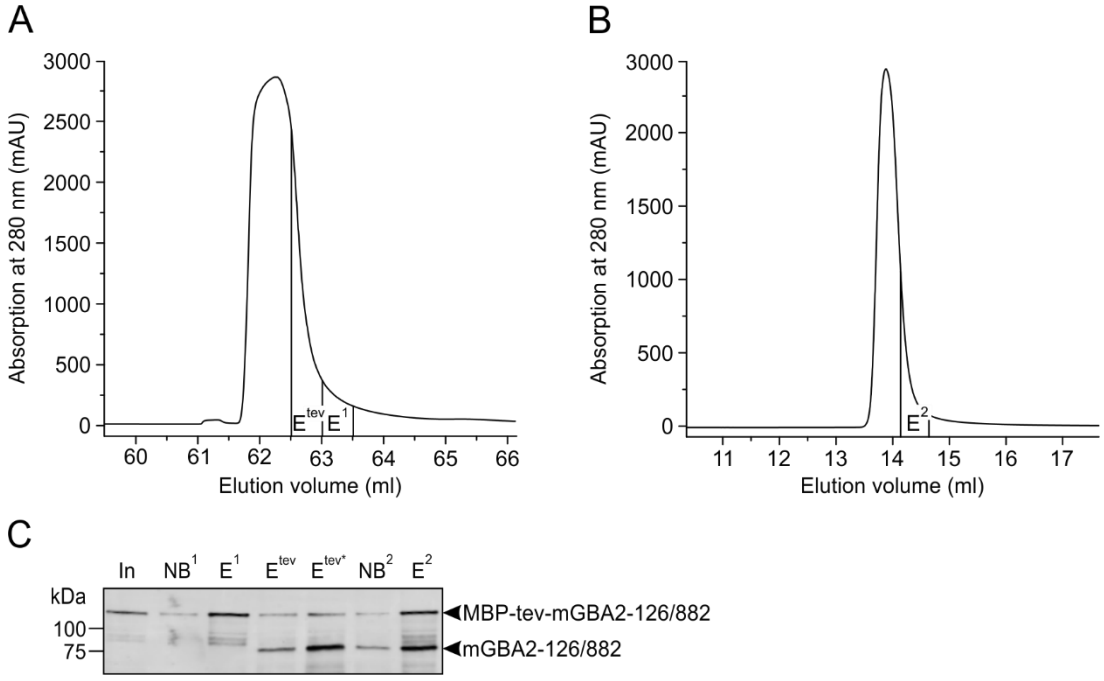

Figure 21: Size-exclusion chromatography of purified MBP-tev-mGBA2-126/-882 after tev protease incubation. A) Affinity chromatography of MBP-tev-mGBA2-126/882 loaded onto an MBPTrap™ column (GE Healthcare) and eluted with 10 mM maltose. **B)** The purified sample (E^{tev}) was incubated with tev protease overnight at 4°C and subjected to affinity chromatography to separate mGBA2-126/882 and MBP-tev-mGBA2-126/882. 500 µl eluate (E^{tev}) containing 2975 µg protein was incubated with 29.75 µg (= 1:100) tev protease in a total volume of 600 µl. 500 µl sample after incubation was subjected to the MBPTrap™ column after a buffer exchange in 1 ml binding buffer. mAU: milli arbitrary units. **C)** Western blot analysis of the input (In, 1:500), non-bound (NB^1, 1:500), and eluate (E^1, 1:300) obtained from the affinity chromatography depicted in **(A)**, the purified sample incubated with tev protease (E^{tev}, 1:500; E^{tev*}: E^{tev} after buffer exchange, 1:170) and subjected to the MBPTrap™ column depicted in **(B)**, and the corresponding non-bound (NB^2, 1:22) and eluate (E^2, 1:170) of **(B).** 10 µl diluted sample was loaded per lane. MBP-tev-mGBA2-126/882 and mGBA2-126/882 was detected using a GBA2-specific antibody.

3.4.4 Calibration of the size-exclusion chromatography column

Since affinity chromatography was inefficient to separate mGBA2-126/882 from MBP-tev-mGBA2-126/882 after tev protease incubation, I performed size-exclusion chromatography. The Superdex™ 200 Increase 10/300 GL column (bed diameter: 10 mm, bed height 300 mm) allows to separate globular proteins with a molecular weight of 10 to 600 kDa (Manual GE Healthcare). Calibration of the Superdex™ column was performed using standard proteins of known size. A protein mix containing thyroglobulin (669 kDa), aldolase (158 kDa), and ovalbumin (43 kDa) (Mix A; **Figure 22 A**) or ferritin (440 kDa), conalbumin (75 kDa), and ribonuclease (13.7 kDa) (Mix B; **Figure 22 B**) was injected and the elution was monitored at 280 nm. Due to their different sizes, the proteins enter the porous beads of the Superdex™ column accordingly and will eluted at different volumes. Proteins which are smaller than the average bead size of the column (8.6 µm) enter the pores of the beads and migrate slowly to the column, whereas large proteins are excluded from the beads and elute fast. To determine the void volume of the column, blue dextran (2000 kDa) was used because it is completely excluded from the column pores (**Figure 22 C**).

Protein size and elution volume are proportional and can be plotted as a standard curve. Elution peaks were integrated to calculate the elution volume.

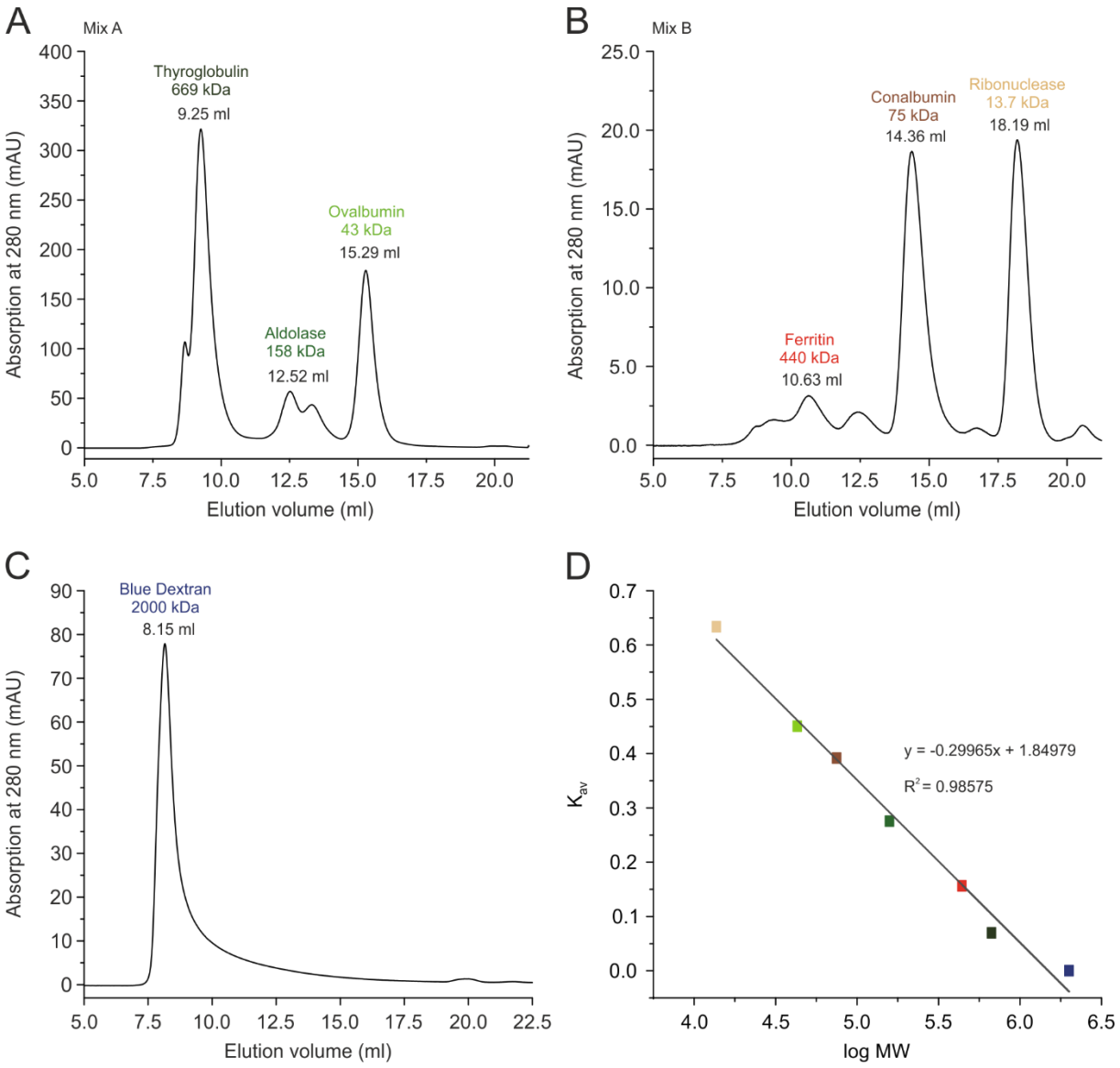

Figure 22: Size-exclusion chromatography of standard proteins using a Superdex^{TM} 200 Increase 10/300 GL column. 150 µl of **A)** protein mix A containing 750 µg thyroglobulin (669 kDa), 600 µg aldolase (158 kDa), and 600 µg ovalbumin (43 kDa), **B)** of protein mix B containing 45 µg ferritin (440 kDa), 450 µg conalbumin (75 kDa), and 450 µg ribonuclease (13.7 kDa), and **C)** 150 µg blue dextran (2000 kDa) was subjected to size-exclusion chromatography. Peak integration was performed using the UNICORN software (GE Healthcare) to calculate the elution volume for the different standard proteins as indicated. mAU: milli arbitrary units. **D)** Standard curve of the available value of the distribution coefficient (K_{av}) plotted against the logarithm of the molecular weight (log MW) for the different standard proteins. The K_{av} was calculated as described in the text. R^2: correlation coefficient.

The total volume of the Superdex^{TM} column is defined as

$$Vt = \mathrm{Vb} + \mathrm{Vo} \quad \text{(I)}$$

with V_t as the total volume of column, V_b as volume of the beads, and V_o as the void volume of the column. V_t of the Superdex^{TM} column is 24 ml (V_t) as stated in the manufacturer's data sheet, V_o is defined as the elution volume of blue dextran (8.15 ml), which is completely excluded from the column beads. According to equation (I), V_b equals 15.85 ml.
Depending on the protein size, a small or large proportion of the bead pores is accessible to the protein. This proportion is defined by the available value of the distribution coefficient K_{av} and equals 0 for proteins, which are completely excluded from the beads, and 1 for proteins, which are completely included.

$$Kav = \frac{Ve - Vo}{\mathrm{Vb}} \quad \text{(II)}$$

V_o and V_b I already determined, can be substituted as follows

$$Kav = \frac{Ve - 8.15\ ml}{15.85\ \mathrm{ml}} \quad \text{(III)}$$

Based on the chromatograms of the eluted standard proteins (**Figure 22 A-C**), V_e was determined by peak integration, and the K_{av} was calculated (using equation III) for the standard proteins ribonuclease, ovalbumin, conalbumin, aldolase, ferritin, thyroglobulin, and blue dextran (**Table 35**).

Table 35: Standard proteins used for calibration of the Superdex^{TM} 200 Increase 10/300 GL column

Standard protein	MW (Da)	log (MW)	V_e (ml)	K_{av}
Ribonuclease	13,700	4.14	18.19	0.63
Ovalbumin	43,000	4.63	15.29	0.45
Conalbumin	75,000	4.88	14.36	0.39
Aldolase	158,000	5.20	12.52	0.28
Ferritin	440,000	5.64	10.63	0.16
Thyroglobulin	669,000	5.82	9.25	0.07
Blue dextran	2,000,000	6.30	8.15	0

Da: Dalton, log: logarithm, K_{av}: available value of the distribution coefficient, MW: molecular weight, V_e: elution volume

Based on these data, a standard curve with K_{av} *versus* the molecular weight of the standard proteins (on a logarithmic scale) was plotted, indicating a linear correlation with a correlation coefficient (R^2) of 0.98575 (**Figure 22 D**). Thus, the following equation can be used to determine the K_{av} of any protein loaded on the size-exclusion chromatography column:

$$Kav = -0.29965x + 1.84979 \quad \text{(IV)}$$

whereby x is the logarithm of the molecular weight. V_e can be calculated using the transposed equation (according to III)

$$Ve = 8.15\ ml + Kav\ x\ 15.85\ ml \quad \text{(V)}$$

According to this equation, MBP-tev-mGBA2-126/882, mGBA2-126/882, MBP, and the tev protease should elute at the following V_e:

Table 36: Calculated elution volumes of MBP and mGBA2-126/882 during size-exclusion chromatography

Protein	MW (Da)	log (MW)	K_{av}	V_e (ml)
MBP-tev-mGBA2-126/882	127,022	5.10	0.32	13.23
mGBA2-126/882	85,472	4.93	0.37	14.05
MBP	41,568	4.62	0.47	15.53
tev protease	28,617	4.46	0.51	16.30

Da: Dalton, log: logarithm, K_{av}: available value of the distribution coefficient, MW: molecular weight, V_e: elution volume

3.4.5 Size-exclusion chromatography of mGBA2-126/882

After calibration of the Superdex™ column, I subjected purified MBP-tev-mGBA2-126/882 to size-exclusion chromatography. Here, 100 µl eluate after affinity-chromatography (**Figure 23Table 23 A**) was incubated with 1 µg tev protease per 100 µg MBP-tev-mGBA2-126/882 protein (= 1:100) overnight at 4°C or, in a control experiment, left untreated (- tev protease), and subsequently loaded onto the Superdex™ column. Immediately after injection of the untreated sample (set to 0 ml), a large protein fraction eluted at 8.25 ml corresponding to the void volume of the column (see **Figure 22 C**). Western blot analysis revealed that this fraction (GF^1) contains high amounts of MBP-tev-mGBA2-126/882 (**Figure 23 C**), thus, it is this protein that formed aggregates. Moreover, the chromatogram reveals a prominent protein peak at 15.82 ml (36.16 kDa) after injection of the sample (**Figure 23Table 23 B**). The size of the eluted protein was calculated using equation III and IV. This elution peak most probably refers to MBP (41.57 kDa; **Table 36**), which, due to the labile tev cleavage site, detached from mGBA2-126/882 already in the absence of tev protease (GF^1, - tev protease; **Figure 23 D**). Coomassie staining of the SDS-gel after blotting revealed a prominent protein band in the GF^1 sample at the expected size of MBP, but could not be detected by the MBP-specific antibody due to an insufficient protein transfer onto the PVDF membrane (**Figure 23 D**). Also, unspecific

binding of the MBP-specific antibody to blotted proteins (e.g. mGBA2-126/882) requires an optimization of Western blotting and antibody staining conditions.

Size-exclusion chromatography of the tev protease incubated sample revealed no difference in elution peaks compared to the non-treated sample with most protein being eluted in the void volume at 8.25 ml after sample injection (**Figure 23 C**), indicating that also mGBA2-126/882 formed aggregates. Western blot analysis confirmed the presence of mGBA2-126/882 in the elution fraction at 8.25 ml after incubation with tev protease; however, a high proportion of non-cleaved MBP-tev-mGBA2-126/882 is present (GF^1, 1:100 tev protease; **Figure 23 D**). The elution peak at 15.89 ml (34.95 kDa) likely refers to MBP, as seen in the Coomassie-stained SDS-gel, representing a prominent band at ~42 kDa (GF^2, 1:100 tev protease; **Figure 23 D**). However, the fact that the elution peaks and the protein bands on the SDS-gel and Western blot did not clearly differ between the tev protease incubated and non-incubated sample, implies that the cleavage needs to be optimized. Using 1:100 tev protease was not efficient to cleave MBP-tev-mGBA2-126/882. Thus, I tested different tev protease concentrations and incubation times. Western blot analysis revealed that incubation with 1 µg tev protease per 10 µg MBP-tev-mGBA2-126/882 protein (= 1:10; E^{tev}) yielded highest mGBA2-126/882 levels for both 24-h (ON) and 48-h (2xON) incubation at 4°C (**Figure 23 D**). Further experiments should be performed using this higher tev protease concentration.

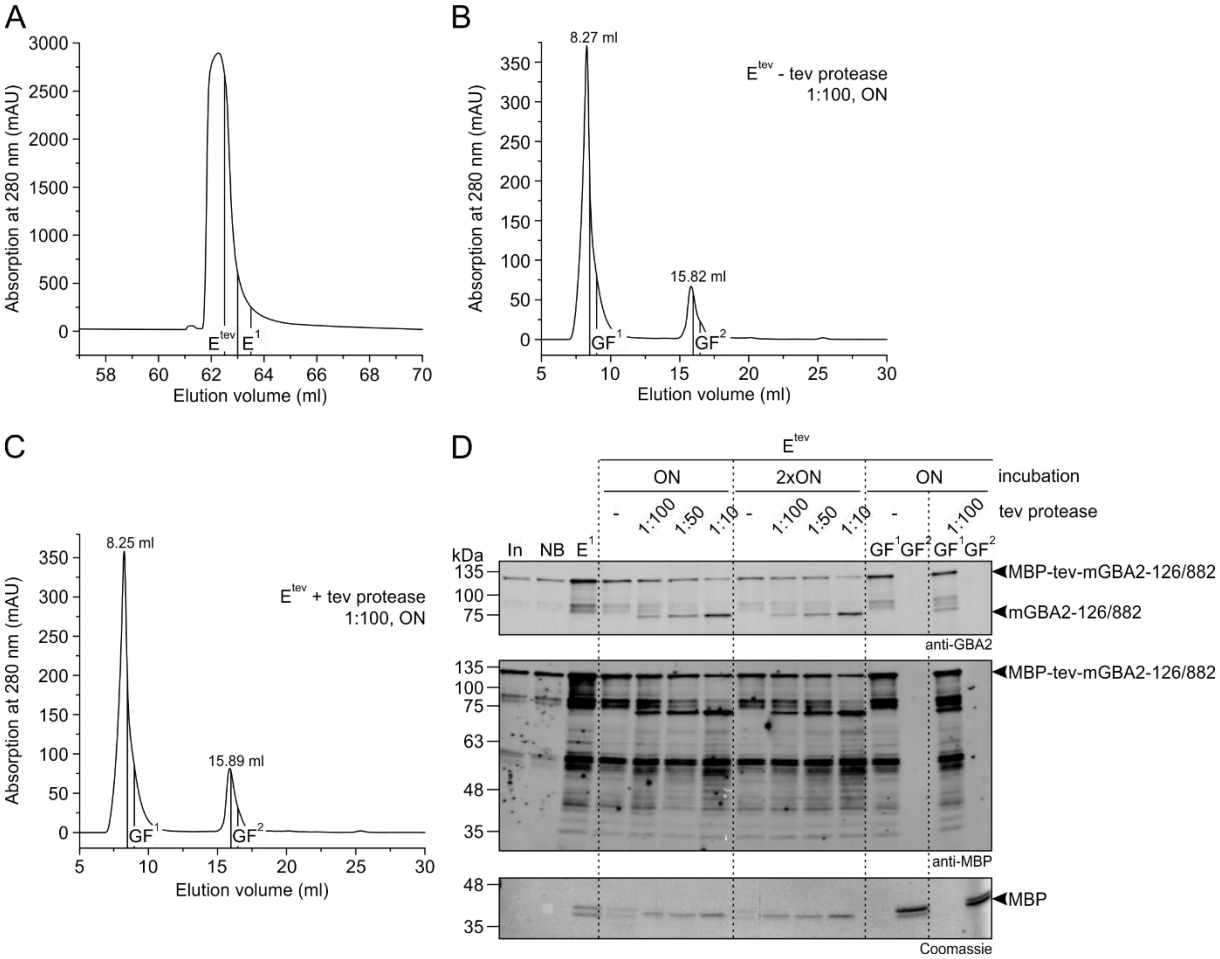

Figure 23: Optimization of tev cleavage of MBP-tev-mGBA2-126/882. A) Purification of MBP-tev-mGBA2-126/882 by an MBPTrap™ and **B)** size-exclusion chromatography performed before (- tev protease) and **C)** after incubation of purified MBP-tev-mGBA2 (fraction: E^{tev}) with tev protease overnight. 100 µl eluate (E^{tev}) containing 710 µg MBP-tev-mGBA2-126/882 protein was incubated without (- tev protease) or with 7.1 µg (= 1:100) tev protease (+ tev protease) in a total volume of 250 µl. 180 µl sample after incubation was subjected to the column; 750 µl elution fractions were collected as GF^1 and GF^2. mAU: milli arbitrary units. **D)** Western blot analysis of purified MBP-tev-mGBA2-126/882 before (E^1; -) and after incubation with different amounts of tev protease overnight (E^{tev} ON) or for 48 h (E^{tev} 2x ON) at 4°C: 37.5 µl eluate (E^{tev}) containing 266 µg MBP-tev-mGBA2-126/882 protein was incubated without (-) or with 2.66 µg (= 1:100), 5.32 µg (= 1:50), or 26.6 µg (= 1:10) tev protease in a total volume of 60 µl. Samples collected during MBPTrap™ from **A)** were loaded as input (In, 1:700), non-bound (NB, 1:700), and eluate (E^1: 1:170), and during size-exclusion chromatography from **B)** and **C)** were loaded as GF^1 (1:450) and GF^2 (1:450). 10 µl diluted sample was loaded per lane. MBP-tev-mGBA2-126/882 and mGBA2-126/882 was detected using a MBP- and/or GBA2-specific antibody; after blotting Coomassie staining of the SDS-gel was performed.

3.4.6 MBP-tev-mGBA2-126/882 is not active

Crystallization of recombinant proteins in principle can also be performed using the MBP-fusion protein. However, a protein tag might disturb proper protein folding and impair protein function. Also, according to my previous results, demonstrating that mGBA2 mutants lacking N- or C-terminal amino acids were inactive (see 3.2), I hypothesize that the MBP-tev-mGBA2-126/882 protein is not active. I expressed wild-type mGBA2-His (mGBA2) and MBP-tev-mGBA2-126/882 in *E.coli* (see 2.11.5.2) and analyzed the protein expression by Western blot analysis (**Figure 24 A**). At 37°C, most of the protein was present in the membrane fraction (**Figure 24 A**). However, when performing an activity assay using hypotonic lysates from bacteria,

expressing mGBA2 or MBP-tev-mGBA2-126/882 for 3 h at 37°C, mGBA2 was active, but not MBP-tev-mGBA2-126/882 (**Figure 24 B**). Expression of MBP-tev-mGBA2-126/882 was also performed at 18°C overnight, which leads to an increased expression with maximized solubility of the protein, but did not result in protein activity (**Figure 24 B**).

Nonetheless, crystallization of inactive mGBA2 would allow to predict the ligand-free open conformation of the enzyme. Moreover, by studying mGBA2-126/882, one could test whether the amino acids 1-125 and 883-918 are required for substrate binding. In addition, attempts could be made to solubilize and re-fold the inactive mGBA2 protein *in vitro* using guanidine-HCl or urea and by adjusting the ionic strength, pH, or temperature of the buffer, respectively (Clark, 1998; Lilie et al., 1998). All experiments would shed light on the structural properties of GBA2 in different conformational states, supplementary to the structure modelled *in silico* (see 3.3) (Charoenwattanasatien et al., 2016).

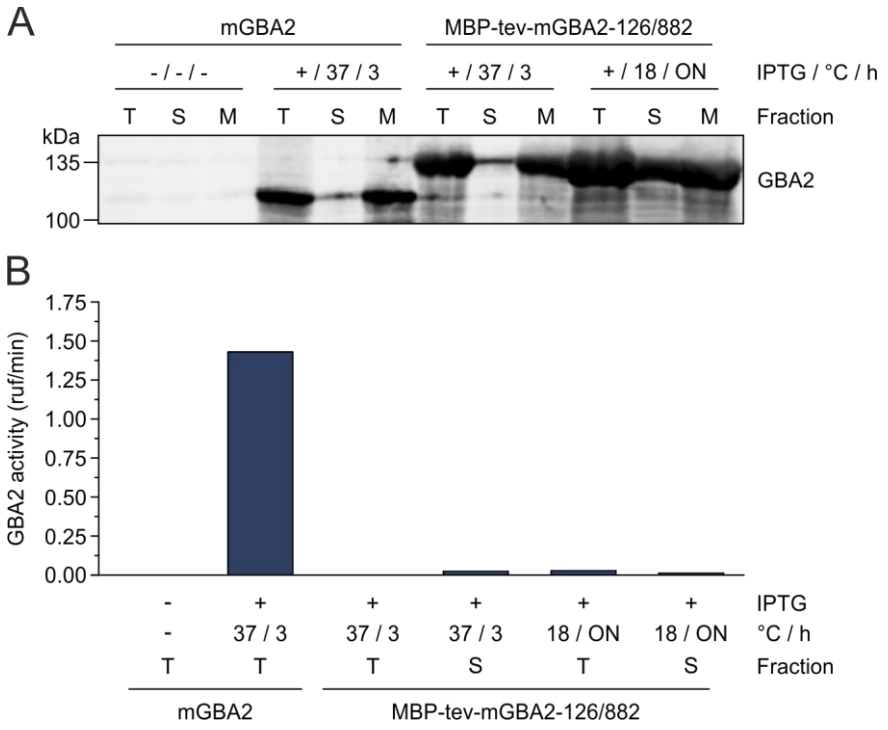

Figure 24: Expression and activity of recombinant MBP-tev-mGBA2-126/882. A) Western blot analysis of hypotonic lysates prepared from *E.coli* expressing wild-type mGBA2-His (mGBA2) or MBP-tev-mGBA2-126/882 after induction with IPTG (+) and incubation at 37°C for 3 h or at 18°C overnight (ON). A non-induced sample from *E.coli* transformed with wild-type mGBA2-His was loaded as a negative control. 7.5 µl sample was loaded per lane. GBA2 was detected using a GBA2-specific antibody. **B)** Analysis of the GBA2 activity of recombinant GBA2 before (-) and after (+) addition of IPTG and incubated at 37°C for 3 h or at 18°C overnight (ON). **A)** and **B)** The total (T), soluble (S) or insoluble membrane fraction (M) was loaded to localize GBA2 expression and activity to the different lysates fractions. IPTG: Isopropyl β-D-1-thiogalactopyranoside; rfu/min: relative fluorescence units per minute.

3.5 GBA2 interaction studies

Several glucosidases from different glycoside hydrolase families form oligomers to be active. Both bacterial and fungal glucosidases were identified to crystallize in a two- or three-domain structure and form dimers or tetramers to be active (Aleshin et al., 2003; Gudmundsson et al., 2016). Moreover, archaeal β-glucosidases of the GH1 family were shown to function as a tetramer (Aguilar et al., 1997; Kado et al., 2011). Since GBA2 tended to aggregate during purification, I wondered whether it also forms oligomers and performed co-immunoprecipitation and cross-linking experiments.

Protein interaction was studied in lysates of CHO cells expressing mGBA2-Flag and mGBA2-HA protein. The construct encoding wild-type mGBA2-Flag was generated as follows: The open reading frame of mouse GBA2 (NM_172692) was amplified from cDNA using primers containing restriction sites and a Kozak sequence in front of the start codon (**Table 4**, 2.4.1). The sequence encoding a Flag tag was added by PCR at the 3'-end. The PCR product was subcloned into pcDNA6/V5-HisA and its sequence was verified. Wild-type and mutant mGBA2-HA constructs were generated as described before (3.1.1).

3.5.1 Co-immunoprecipitation

For co-immunoprecipitation, magnetic beads coated with the anti-Flag antibody were incubated with protein lysates of CHO cells expressing Flag- and HA-tagged mGBA2. Using this assay, I addressed the following questions: 1.) Does wild-type mGBA2-Flag bind to the anti-Flag magnetic beads?, 2.) Do mGBA2-HA and mGBA2-Flag interact, meaning the proteins co-immunoprecipitate?, 3.) Is the binding specific, or does any other HA-tagged protein co-immunoprecipitate?, and 4.) Is the interaction disrupted by mutations in GBA2?

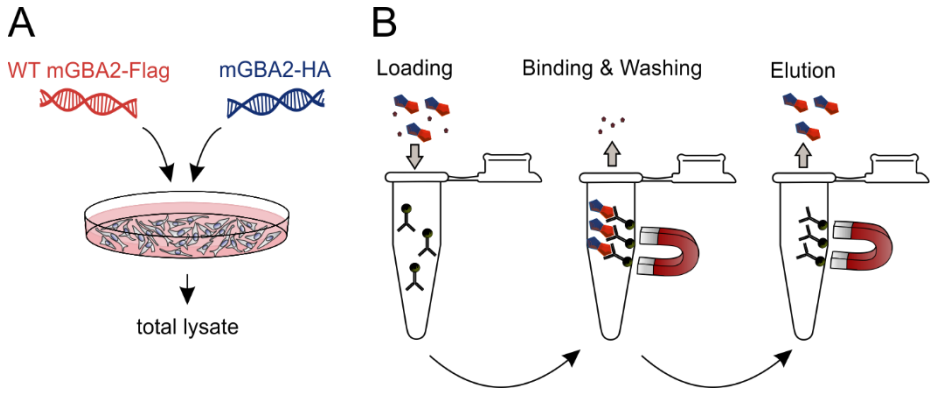

Figure 25: Co-immunoprecipitation of GBA2 using anti-Flag magnetic beads. A) Co-expression of wild-type (WT) mGBA2-Flag with mGBA2-HA in CHO cells. Total lysates were prepared and loaded on the equilibrated beads and **B)** incubated overnight end-over-end. Beads were then washed and bound proteins eluted in 1 M glycine at pH 3.0.

3.5.1.1 Does mGBA2-Flag bind to anti-Flag magnetic beads?

A prerequisite for the use of anti-Flag magnetic beads to study GBA2 interaction is, that mGBA2-Flag quantitatively binds the antibody attached to the beads. Thus, different buffer conditions were tested for antibody-protein binding. According to the manufacturer's protocol (Sigma), the pH of the protein lysate should be in the range of pH 7 to pH 8, the salt concentration (NaCl or KCl) should be 150 mM or higher, and either TritonX-100 or CHAPS can be used as a to detergent to minimize unspecific binding of proteins to the resin. Thus, I used a "normal" lysis buffer containing 10 mM Tris, 150 mM NaCl, 0.5 mM EDTA, and 1% Triton X-100, but increased the NaCl concentration to 500 mM in a buffer referred to as "high NaCl" or reduced the NaCl concentration to 10 mM in a "low NaCl" buffer. Moreover, I tested a buffer without EDTA ("w/o EDTA") and one that contained CHAPS instead of TritonX-100 at the same concentration ("CHAPS"). The corresponding washing buffers contained a reduced Triton X-100 or CHAPS concentration of 0.2%. In all tested conditions, mGBA2-Flag quantitatively bound to the antibody column and no protein was present in the non-bound and final wash sample (**Figure 26**). Thus, the normal lysis buffer was used in subsequent immunoprecipitation experiments.

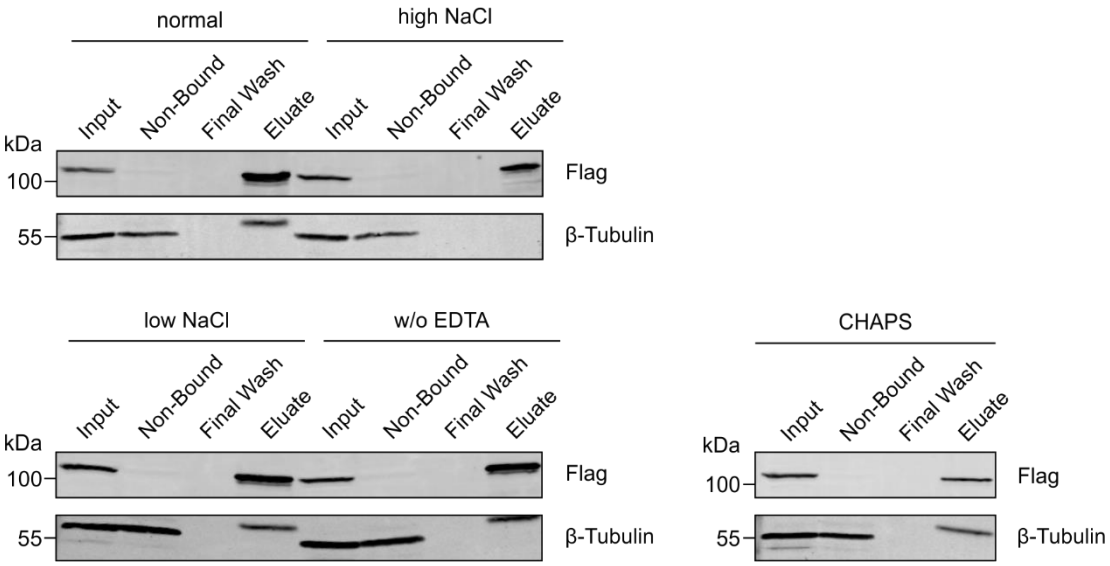

Figure 26: Immunoprecipitation of mGBA2-Flag using different buffer conditions. Different buffers were used to lyse CHO cells expressing mGBA2-Flag. The normal buffer contained 10 mM Tris, 150 mM NaCl, 0.5 mM EDTA, 1% Triton X-100, whereas NaCl was increased to 500 mM (high NaCl), reduced to 10 mM (low NaCl), EDTA was excluded (w/o EDTA), or TritonX-100 was exchanged by CHAPS in the same concentrations. The corresponding washing buffers contained reduced Triton X-100 concentration (0.2%). Western blot analysis of the different fractions was performed and 16.67 µl protein lysate was loaded as Input, 37.5 µl supernatant after incubation of the lysate on the beads was loaded as Non-Bound, 37.5 µl supernatant after washing the beads with 300 µl washing buffer was loaded as Final Wash, 37.5 µl supernatant was loaded after elution in 100 µl 1 M glycine pH 3.0 and neutralization in 16.67 µl 1 M Tris/HCl pH 8.0. mGBA2-Flag was detected using a Flag-specific antibody. β-Tubulin served as a loading control.

3.5.1.2 Test for specificity

A prerequisite to study GBA2 interaction by co-immunoprecipitation is that only mGBA2-Flag and not mGBA2-HA binds to the anti-Flag magnetic beads. Unspecific binding of protein to the agarose matrix therefore needs to be prevented. Including a pre-clearing step on underivatized agarose beads ensures that any protein interacting with the agarose is removed from the lysate.

I first tested whether mGBA2-Flag or mGBA2-HA bind to underivatized agarose beads. Western blot analysis revealed that mGBA2-Flag does not bind to the agarose beads, it was only present in the input and non-bound and at low levels in the initial washing fraction (**Figure 27 A**). Also, mGBA2-HA was also only present in the input, but not in the eluate when performing precipitation experiments on underivatized agarose matrix, anti-Flag magnetic beads (FlagTrap), or anti-Flag magnetic beads after pre-clearing on underivatized agarose (**Figure 27 B**). Thus, the latter approach including a pre-clearing step was utilized to perform co-immunoprecipitation experiments of mGBA2-Flag and mGBA2-HA.

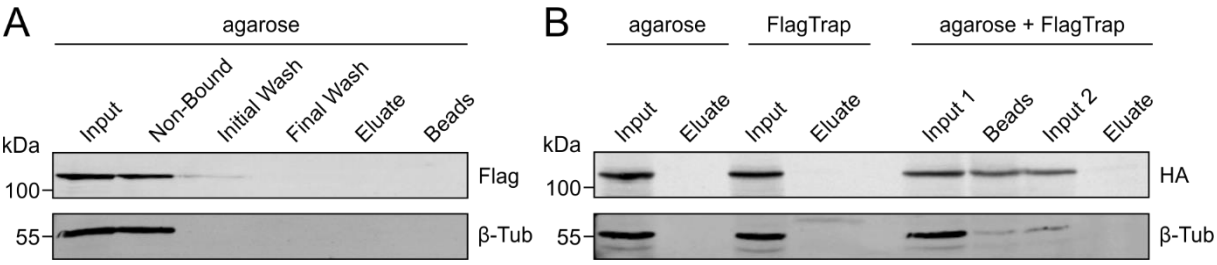

Figure 27: Control precipitation experiments performed with mGBA2-HA and mGBA2-Flag. Western blot analysis of different fractions collected during **A)** precipitation of mGBA2-Flag incubated on empty agarose beads, and **B)** precipitation and immunoprecipitation of mGBA2-HA incubated on empty agarose beads (agarose), anti-Flag magnetic beads (FlagTrap), or anti-Flag magnetic beads after pre-clearing on empty agarose matrix (agarose + FlagTrap). **A) and B)** For co-immunoprecipitation total lysates of transfected cells were prepared; 250 µg total protein was loaded in a total volume of 500 µl on equilibrated agarose or anti-Flag magnetic beads (50 µl bead slurry of a 50% suspension in storage buffer was used). For Western blot analysis, 16.67 µl protein lysate was loaded as Input, 25 µl agarose matrix resuspended in 30 µl 1x SDS sample buffer was loaded (Beads), 37.5 µl supernatant after incubation of the lysate on the beads was loaded as Non-Bound, 37.5 µl supernatant after washing the beads with 300 µl washing buffer was loaded as Initial and Final Wash, 37.5 µl supernatant was loaded after elution in 100 µl 1 M glycine pH 3.0 and neutralization in 16.67 µl 1 M Tris/HCl pH 8.0. Beads: agarose matrix after incubation with the protein lysate; Input 1: protein lysate loaded on underivatized agarose matrix as a pre-clearing step; Input 2: protein lysate loaded on anti-Flag magnetic beads after pre-clearing on agarose; Input: protein lysate loaded on empty agarose matrix or anti-Flag magnetic beads. mGBA2-Flag and mGBA2-HA were detected using Flag- and HA-specific antibodies, respectively. β-Tubulin (β-Tub) served as a loading control.

3.5.1.3 Co-immunoprecipitation of mGBA2-Flag and mGBA2-HA

Using the optimized protocol, I performed co-immunoprecipitation of mGBA2-Flag and mGBA2-HA. Indeed, mGBA2 interacted with mGBA2-Flag and was detected in the elution fraction using an HA-specific antibody indicating a protein-protein interaction (**Figure 28**).

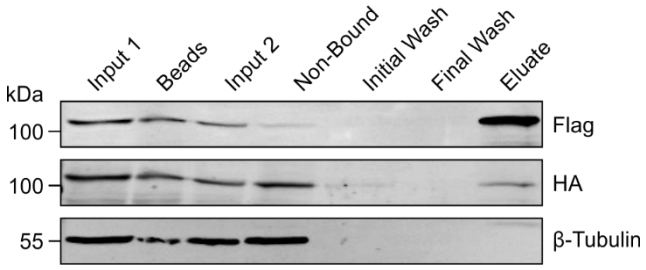

Figure 28: Pre-incubation on underivatized agarose matrix needed for specific co-immunoprecipitation. Western blot analysis of the different fractions collected during co-immunoprecipitation of mGBA2-HA with mGBA2-Flag performed using anti-Flag magnetic beads after-pre-clearing on underivatized agarose beads. For co-immunoprecipitation total lysates of transfected cells were prepared; 250 µg total protein was loaded in a total volume of 500 µl on equilibrated agarose or anti-Flag magnetic beads (50 µl bead slurry of a 50% suspension in storage buffer was used). 16.67 µl protein lysate was loaded as Input, 37.5 µl supernatant after incubation of the lysate on the beads was loaded as Non-Bound, 37.5 µl supernatant after washing the beads with 300 µl washing buffer was loaded as Initial and Final Wash, 37.5 µl supernatant was loaded after elution in 100 µl 1 M glycine pH 3.0 and neutralization in 16.67 µl 1 M Tris/HCl pH 8.0. Beads: agarose matrix after incubation with the protein lysate; Input 1: protein lysate loaded on underivatized agarose matrix as a pre-clearing step; Input 2: protein lysate loaded on anti-Flag magnetic beads after pre-clearing on agarose. mGBA2-Flag and mGBA2-HA was detected using Flag- and HA-specific antibodies, respectively. β-Tubulin served as a loading control.

3.5.1.4 Independent HA-tagged control protein

To verify that the interaction of mGBA2 proteins was not dependent on the HA tag, I performed a co-immunoprecipitation using an independent HA-tagged protein, the bacterial photoactivated adenylyl cyclase of the soil bacterium *Beggiatoa sp.* (bPAC-HA). Similar to the previous experiment, a pre-clearing step was included to ensure that the lysate loaded on the magnetic beads (Input 2) is free of any protein interacting with the agarose resin itself. Western blot analysis indicated that bPAC-HA is found at high levels in the non-bound, but not in the elution fraction (**Figure 29**). Thus, the interaction of mGBA2-Flag and mGBA2-HA is GBA2-specific.

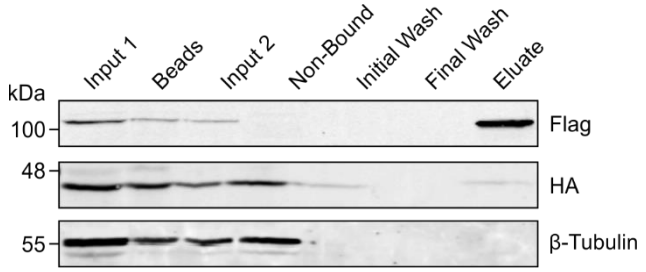

Figure 29: bPAC-HA does not interact with mGBA2-Flag. Western blot analysis of the different fractions collected during co-immunoprecipitation of bPAC-HA with mGBA2-Flag performed using anti-Flag magnetic beads after-pre-clearing on underivatized agarose beads. For co-immunoprecipitation total lysates of transfected cells were prepared; 16.67 µl protein lysate was loaded as Input, 37.5 µl supernatant after incubation of the lysate on the beads was loaded as Non-Bound, 37.5 µl supernatant after washing the beads with 300 µl washing buffer was loaded as Initial and Final Wash, 37.5 µl supernatant was loaded after elution in 100 µl 1 M glycine pH 3.0 and neutralization in 16.67 µl 1 M Tris/HCl pH 8.0. Beads: agarose matrix after incubation with the protein lysate; Input 1: protein lysate loaded on underivatized agarose matrix as a pre-clearing step; Input 2: protein lysate loaded on anti-Flag magnetic beads after pre-clearing on agarose. mGBA2-Flag and bPAC-HA were detected using Flag- and HA-specific antibodies, respectively. β-Tubulin served as a loading control.

3.5.1.5 Co-immunoprecipitation of mutant and wild-type mGBA2

Next, I tested whether missense or nonsense mutations in GBA2 impair GBA2-GBA2 interaction. Co-immunoprecipitation was performed according to the optimized protocol (3.5.1.1, 3.5.1.3) with lysates of cells expressing wild-type mGBA2-Flag and mutant mGBA2-HA and compared to control cells co-expressing wild-type mGBA2-Flag and -HA. Western blot analysis revealed that in all experiments, wild-type mGBA2-Flag quantitatively bound to the anti-Flag magnetic beads and mutant mGBA2-HA co-precipitated in the eluate (**Figure 30 A, B**). Thus, neither amino-substitution nor C-terminal truncation of GBA2 affect protein-protein interaction.

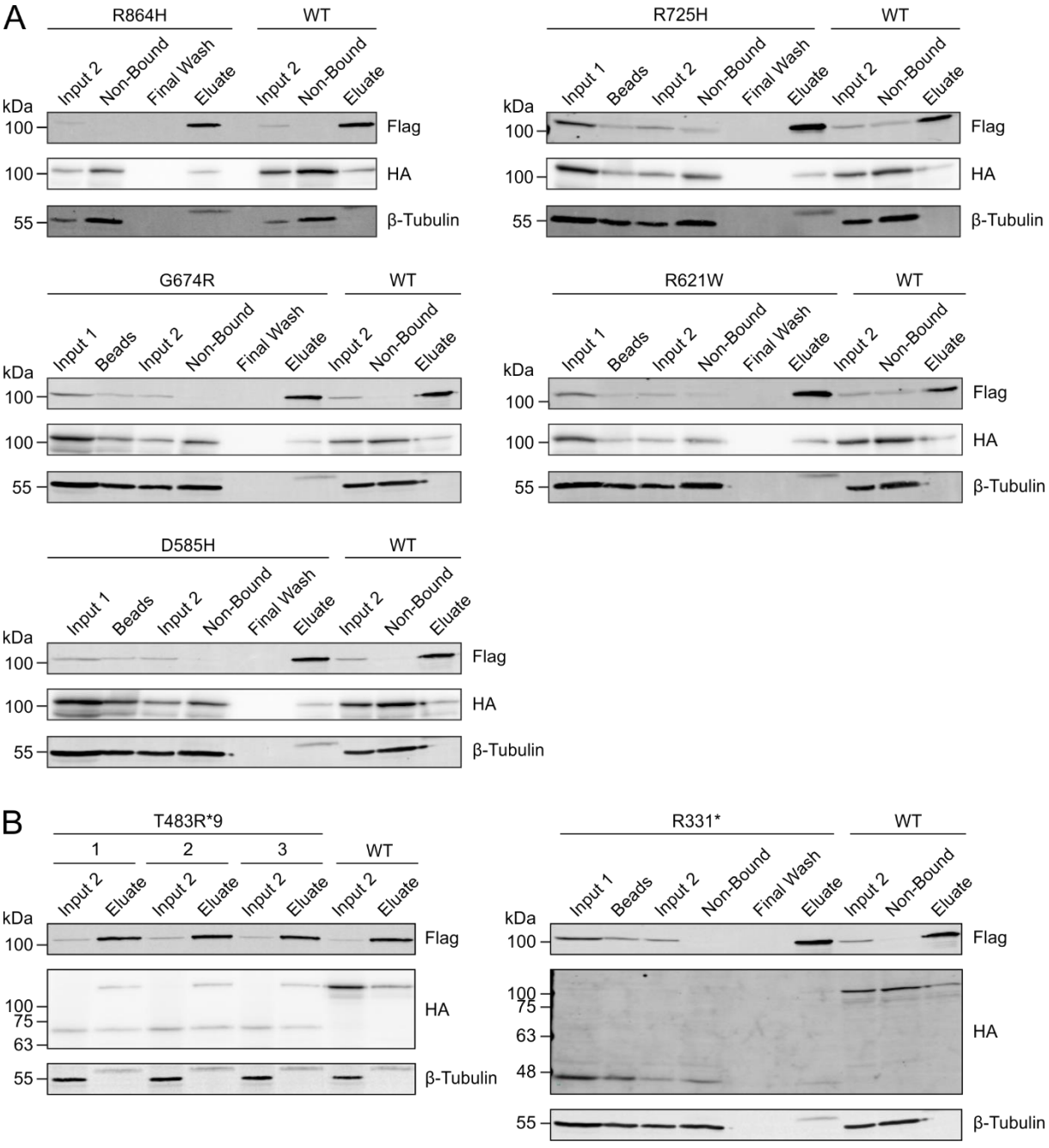

Figure 30: GBA2 mutations do not impair GBA2-GBA2 interaction. A) Western blot analysis of the different fractions collected during co-immunoprecipitation of the missense mutations mGBA2-R864H-HA, -R725H-HA, -G674R-HA, -R621W-HA, or -D585H-HA with mGBA2-Flag performed using anti-Flag magnetic beads after-pre-clearing on underivatized agarose beads. **B)** Western blot analysis of the different fractions collected during co-immunoprecipitation of the nonsense mutations mGBA2-T483R*9-HA and -R331*-HA with mGBA2-Flag performed using anti-Flag magnetic beads after-pre-clearing on underivatized agarose beads. **A)** and **B)** For co-immunoprecipitation total lysates of transfected cells were prepared; A control experiment with mGBA2-Flag and mGBA2-HA was performed in parallel (WT); 16.67 µl protein lysate was loaded as Input, 37.5 µl supernatant after incubation of the lysate on the beads was loaded as Non-Bound, 37.5 µl supernatant after washing the beads with 300 µl washing buffer was loaded as Final Wash, 37.5 µl supernatant was loaded after elution in 100 µl 1 M glycine pH 3.0 and neutralization in 16.67 µl 1 M Tris/HCl pH 8.0. Beads: agarose matrix after incubation with the protein lysate; Input 1: protein lysate loaded on underivatized agarose matrix as a pre-clearing step; Input 2: protein lysate loaded on anti-Flag magnetic beads after pre-clearing on agarose. mGBA2-Flag and mGBA2-HA were detected using Flag- and HA-specific antibodies, respectively. β-Tubulin served as a loading control.

3.5.2 Chemical cross-linking

The co-immunoprecipitation approach demonstrated that GBA2 proteins interact. To identify the oligomeric structure of GBA2 protein complexes, I performed chemical cross-linking using the homo-bifunctional disuccinimicyl suberate (DSS) with a linker arm length of 11.4 Å. With *N*-hydroxysuccinimid (NHS) groups at both ends, DSS reacts with primary amines in proteins, forming an amide bond (**Figure 31**). This reaction occurs at pH 7-9 in aqueous solution and can be quenched by addition of Tris-(hydroxymethyl)-aminomethane (Tris).

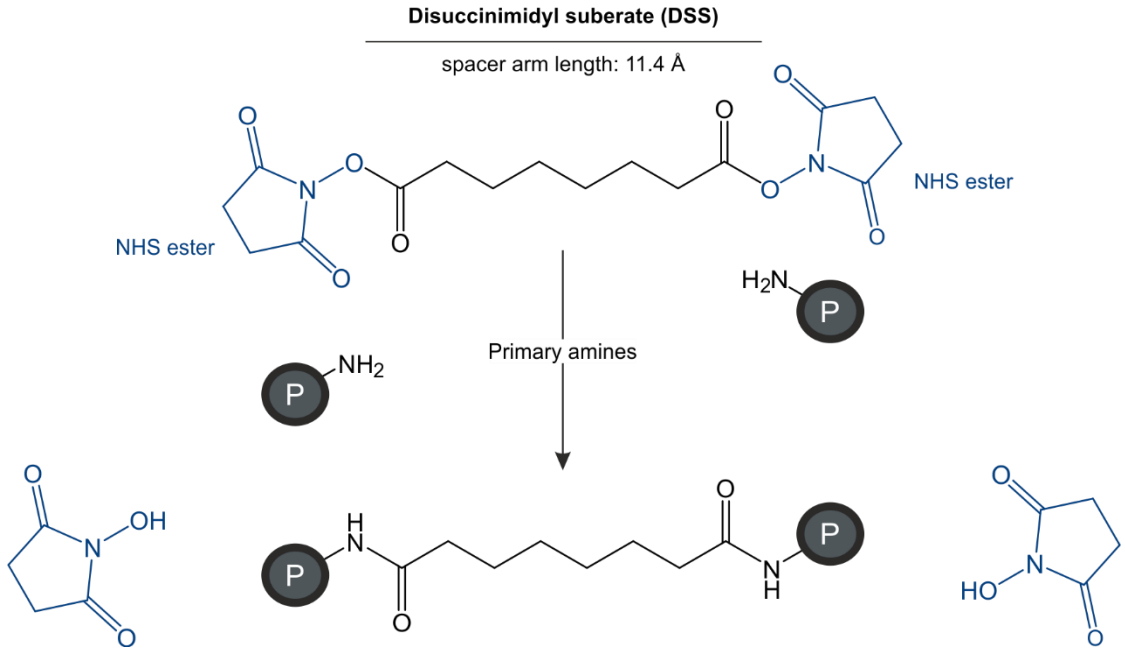

Figure 31: Chemical cross-linking of proteins using disuccinimidyl suberate (DSS). The *N*-hydroxysuccinimid (NHS) groups linked to the suberate backbone by ester bonds react with primary amines at the N terminus of proteins (P) to form a stable amide bond. This reaction occurs at pH 7-9 in aqueous solution and can be quenched by addition of Tris-(hydroxymethyl)-aminomethane.

3.5.2.1 Optimizing cross-linking conditions

I first tested cross-linking of mGBA2 proteins under conditions used for activity measurements in our β-glucosidase assay (10 mM HEPES at pH 7.4) for 20 min at 4°C at different DSS concentrations (0.77 mM, 1.48 mM, 2.14 mM, and 2.76 mM; **Figure 32 A**). To be able to detect protein aggregates, I also blotted the stacking gel for Western blot analysis. My results show that 0.77 mM DSS was sufficient to cross-link mGBA2-Flag and mGBA2-HA (O*) without causing protein aggregation (A*), whereas higher DSS concentrations did not improve cross-linking, but tend to promote aggregate formation (**Figure 32 A**). Incubation with DSS for 2 h resulted in optimal oligomer formation (O*) with no prominent aggregation of mGBA2 (A*) (**Figure 32 B**). Thus, for further cross-linking experiments, 0.77 mM DSS was used and the reaction was performed for 2 h at 4°C.

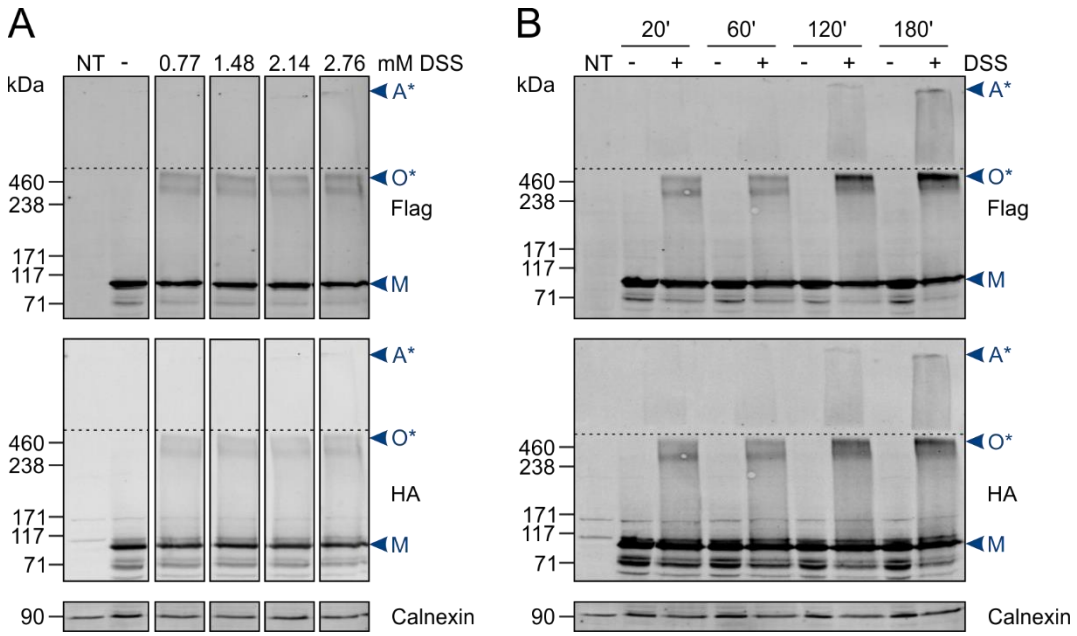

Figure 32: Cross-linking efficiency of mGBA2 using different DSS concentrations and incubation times. Protein lysates of CHO cells co-expressing mGBA2-Flag and mGBA2-HA were prepared and different **A)** DSS concentrations (for 20 min at 4°C) and **B)** incubation times (at 4°C) were tested. Reaction was stopped by addition of Tris-(hydroxymethyl)-aminomethane (Tris) pH 7.5 (final concentration: 0.22 M) and 40 µg protein was loaded for Western blot analysis. mGBA2-Flag and mGBA2-HA was detected using a Flag- or HA-specific antibody, respectively. Calnexin served as a loading control. M: GBA2 monomer, O*: cross-linked oligomer, A*: aggregated protein. Dotted line indicates border of stacking (top) and separating (bottom) gel.

To analyze whether modifying the buffer composition improves the yield of cross-linked GBA2, I compared buffer containing 25 mM HEPES and 100 mM NaCl (pH 7.4; buffer 2) to the normal buffer (10 mM HEPES at pH 7.4; buffer 1) and incubated the samples at room temperature for 20 min or at 4°C for 2 h with or without boiling the final SDS sample before loading on the gel. Cross-linking at room temperature for 20 min and at 4°C for 2 h generated oligomerized mGBA2-Flag > 245 kDa (O*; **Figure 33 A and B**). Moreover, boiled and non-boiled samples were similar (**Figure 33 A and B**). However, cross-linking at room-temperature resulted in

protein aggregation (A*) at both buffer conditions (**Figure 33 A**). At 4°C, aggregates were only present in samples lysed in NaCl-containing buffer 2, whereas in 10 mM HEPES alone (buffer 1), no mGBA2 aggregates were formed (**Figure 33 B**).

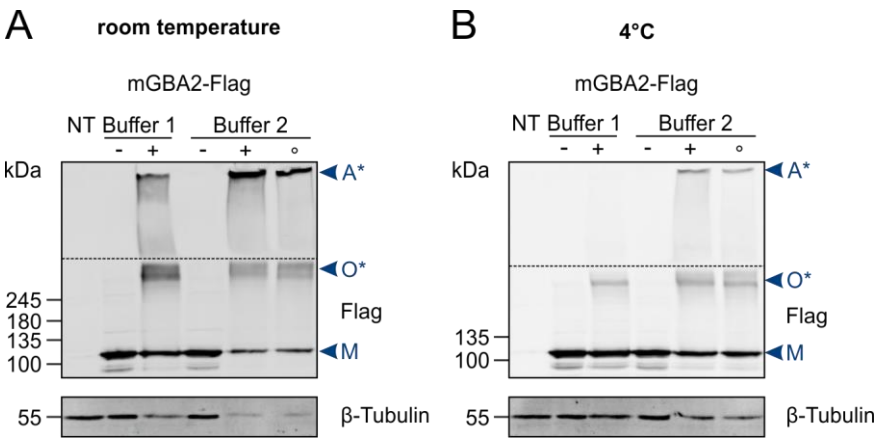

Figure 33: Cross-linking efficiency of mGBA2 at different temperatures and buffer conditions. Western blot analyses of CHO cells expressing mGBA2-Flag lysed in buffer 1 (10 mM HEPES, pH 7.4) or buffer 2 (25 mM HEPES, 100 mM NaCl, pH 7.4) before (-) and after cross-linking with 0.77 mM DSS (+). Incubation with DSS was performed at room temperature for 20 min **(A)** or 4°C for 2 h **(B)**. Reaction was stopped by addition of Tris-(hydroxymethyl)-aminomethane (Tris) pH 7.5 (final concentration: 0.22 M) and 40 µg protein was loaded for Western blot analysis. Samples indicated with ° were boiled at 95°C for 5 min before loading on the gel. mGBA2-Flag was detected using a Flag-specific antibody. β-Tubulin served as a loading control. Dotted line indicates border of stacking (top) and separating (bottom) gel. M: GBA2 monomer, O*: cross-linked oligomer, A*: aggregated protein.

3.5.2.2 Cross-linking of mutant mGBA2

To test whether disease-associated GBA2 mutations affect protein oligomerization, I performed cross-linking experiments using the different HA-tagged mGBA2 mutants. Western blot analysis demonstrated that the GBA2 mutants R864H, R725H, G674R, R621W, and D585H formed protein oligomers that resemble the wild-type mGBA2 oligomers (between 238-460 kDa; **Figure 34 A**). Moreover, detailed analysis of the oligomer/monomer ratio upon addition of DSS (+) revealed no difference in mutant and wild-type (WT) oligomer formation (**Figure 34 B**; parts of the experiments have been performed by Dominik Dittmann).

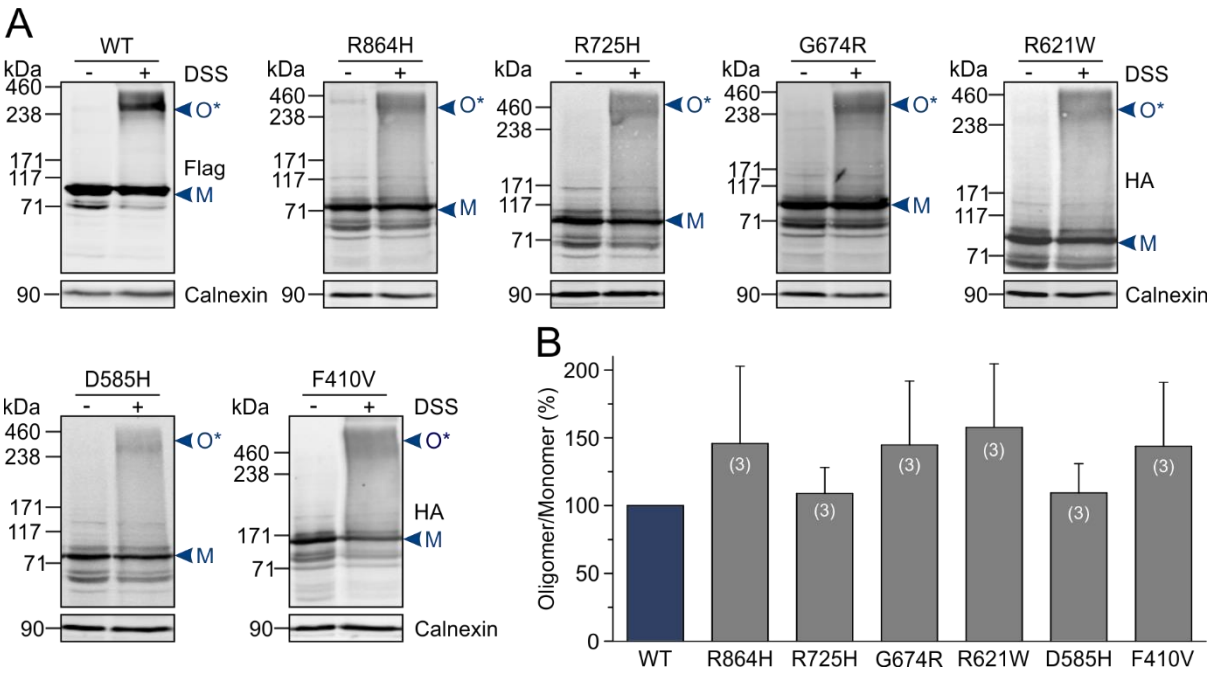

Figure 34: Chemical cross-linking of wild-type and mGBA2 missense mutations. A) Western blot analysis of hypotonic lysates from CHO cells expressing wild-type Flag-tagged or mutant HA-tagged mGBA2 before (-) and after cross-linking with 0.77 mM DSS. Reaction was stopped by addition of Tris-(hydroxymethyl)-aminomethane (Tris) pH 7.5 (final concentration: 0.22 M) and 40 µg protein was loaded for Western blot analysis. GBA2 was detected using a HA-specific antibody. Calnexin served as a loading control. **B)** Quantitative analysis of oligomer/monomer formation (%) upon DSS cross-linking of mutant mGBA2 compared to wild-type mGBA2. Columns represent values + SD. Statistical analysis was performed using one-sample t-test (n numbers are indicated). M: GBA2 monomer, O*: cross-linked oligomer. Parts of the experiments have been performed by Dominik Dittmann.

Similarly, we analyzed if the truncated mGBA2 mutants T483R*9 and R331* form oligomers by chemical cross-linking (experiments performed by Dominik Dittmann). Since the size of the T483R*9 (55 kDa) and R331* (37 kDa) mutant differs from that of the wild-type protein (103 kDa), homo- or hetero-oligomers can be distinguished by Western blot analysis. The experiments revealed that T483R*9 and R331* exhibit impaired oligomerization compared to wild-type mGBA2 (WT) (**Figure 35 A**; O*/M ratio). Hetero-oligomers of mutant and wild-type protein were not observed (**Figure 35 B**) and oligomerization of wild-type mGBA2-Flag was not affected by the mutants (**Figure 35 D**; O*/M ratio WT-Flag). This result is different from the outcome of the co-immunoprecipitation experiments, where wild-type mGBA2 also interacted with the mGBA2 mutants T483R*9 and R331* (**Figure 30**). One explanation for this experimental discrepancy might be the different buffers, total lysis buffer for co-immunoprecipitation and hypotonic lysis buffer that were used for chemical cross-linking and co-immunoprecipitation, which might favor or abolish protein-protein interaction. For example, NaCl, which is present in the lysis buffer used for co-immunoprecipitation, impaired cross-linking and caused excessive protein aggregation.

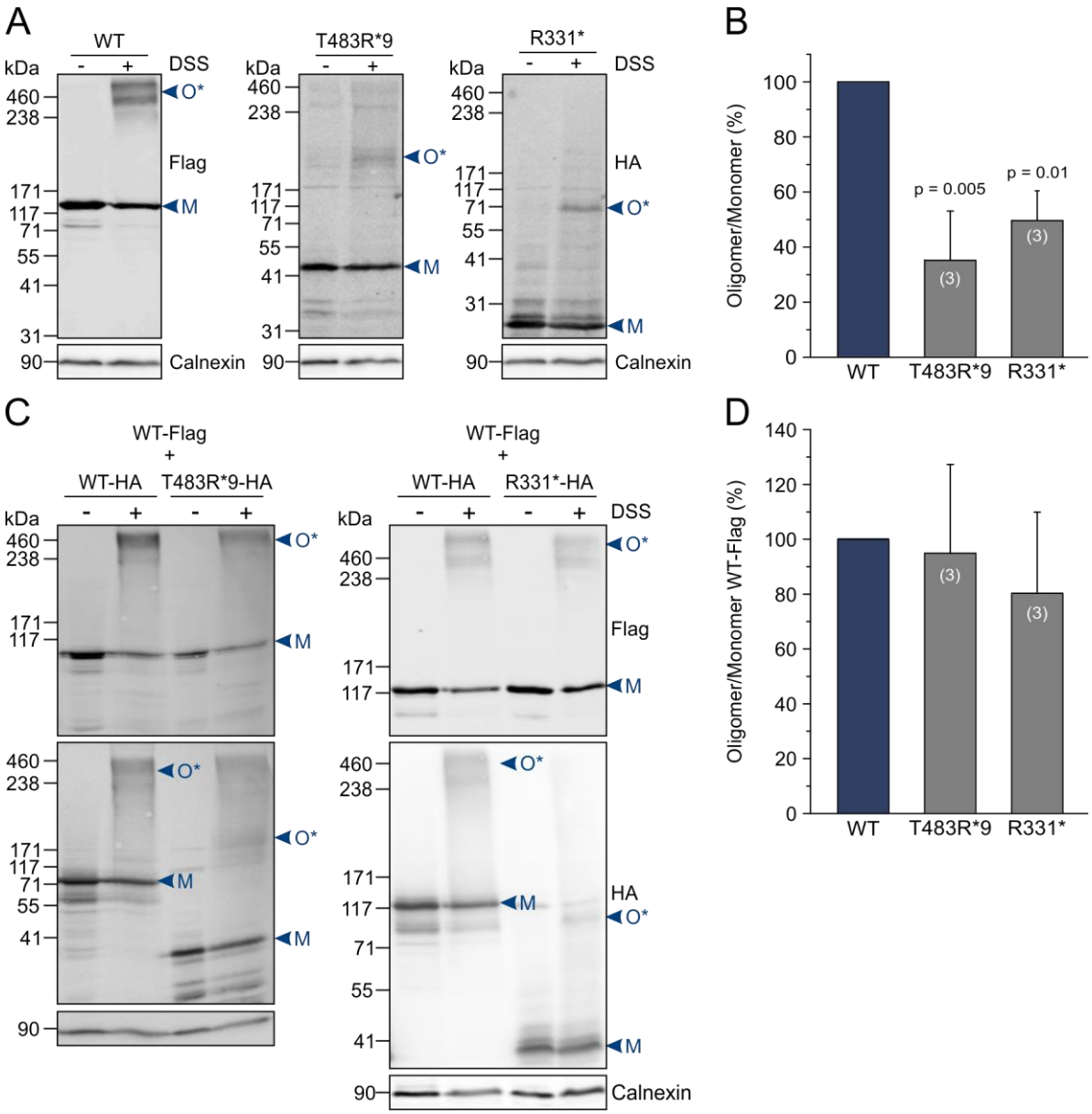

Figure 35: Chemical cross-linking of wild-type and mGBA2 nonsense mutations. A) Western blot analysis of hypotonic lysates from CHO cells expressing wild-type mGBA2-Flag or mutant mGBA2-HA before (-) and after cross-linking with 0.77 mM DSS. Reaction was stopped by addition of Tris-(hydroxymethyl)-aminomethane (Tris) pH 7.5 (final concentration: 0.22 mM) and 40 µg protein was loaded for Western blot analysis. mGBA2-Flag and mGBA2-HA was detected using a Flag- and HA-specific antibody, respectively. Calnexin served as a loading control. **B)** Quantification of oligomer/monomer formation (O*/M ratio in %) upon DSS cross-linking of mGBA2-T483R*9-HA (T483R*9) or mGBA2-R331*-HA (R331*) compared to wild-type mGBA2-HA (WT; set to 100%). **C)** Western blot analysis of hypotonic lysates from CHO cells expressing wild-type mGBA2-Flag and wild-type mGBA2-HA or wild-type mGBA2-Flag and mutant mGBA2-HA before (-) and after cross-linking with 0.66 mM DSS. Reaction was stopped by addition of Tris-(hydroxymethyl)-aminomethane (Tris) pH 7.5 (final concentration: 0.22 mM) and 40 µg protein was loaded for Western blot analysis. GBA2 was detected using a HA-specific antibody. Calnexin served as a loading control. **D)** Quantification of oligomer/monomer formation of wild-type mGBA2-Flag (O*/M ratio in %) upon DSS cross-linking of wild-type mGBA2-Flag in the presence of wild-type mGBA2-HA (WT; set to 100%), mGBA2-T483R*-HA (T483R*9), or mGBA2-R331*-HA (R331*). **B)** and **D)** Columns represent mean values + SD. Statistical analysis was performed using one-sample t-test (n numbers and p values are indicated). M: GBA2 monomer, O*: cross-linked oligomer. Experiments were performed by Dominik Dittmann.

3.5.3 GBA2 activity interaction studies

To analyze whether mutant GBA2 protein affects the activity of wild-type GBA2, I performed the β-glucosidase activity assay using lysates of cells that express both proteins. However, a prerequisite for this assay is that wild-type and mutant GBA2 are expressed in stoichiometric amounts. To this end, we generated plasmids, encoding the wild-type Flag-tagged GBA2 and mutant HA-tagged GBA2, either connected by a linker or a 2A peptide (cloning performed by Dr. Wolfgang Bönigk; see 2.4.1.2).

3.5.3.1 Cloning of the GBA2-2A and -linker constructs

The open reading frame of mouse GBA2 (NM_172692) was amplified from cDNA using primers containing restriction sites and a Kozak sequence in front of the start codon (**Table 4**). The sequence encoding a HA- or Flag-tag was added by PCR at the 3'-end. PCR products were subcloned into pcDNA3.1(+) and their sequence was verified. These mGBA2 constructs were used as a template to generate constructs, coding for a Flag-tagged mGBA2 and the coding sequence for the 2A peptide derived from the Foot-and-Mouth picornavirus (VKQTLNFDLLKLAGDVESNPGP) followed by mGBA2-HA. Addition of the 2A peptide flanked by a PPGSG- and GSG-linker to the Flag-tagged mGBA2 was performed in a sequential manner (**Table 4**). The final chimeric product was amplified in a recombinant PCR, subcloned into pcDNA3.1(+), and verified by sequencing.

Using the 2A peptide constructs, mGBA2-Flag and mGBA2-HA can be expressed at equimolar ratios through a mechanism called *ribosomal skipping* (de Felipe et al., 2003; Donnelly et al., 2001). 2A peptide encoding sequences are found in viruses of the *Picornaviridae*, *Iflaviridae*, *Tetraviridae*, *Dicistroviridae*, and *Reoviridae* family (Luke et al., 2008). Their genome is composed of a single open reading frame (ORF). However, the 2A peptide allows translation of multiple proteins for instance needed for capsid formation and replication (Collis et al., 1992; Li et al., 2001; Molla et al., 1993). The majority of the 2A peptides from the different virus species share the conserved amino-acid sequence GDVEXNPGP at the C terminus (Luke et al., 2008), and introducing a GSG linker upstream of the 2A peptide was shown to improve "cleavage" efficiency in different expression systems (Chng et al., 2015; Wang et al., 2015; Yang et al., 2008). Thus, for the mGBA2 2A constructs, we also flanked the 2A peptide with a PPGSG- and GSG-linker.

We compared the 2A-approach to a linker-approach with mGBA2-Flag and mGBA2-HA, expressed as a single polypeptide, but separated by a linker (N terminus of rat CNCA2, aa 3-67). EcoRI and an XbaI restriction sites following the linker sequence allow to introduce wild-type or mutant mGBA2-HA at the C terminus.

3.5.3.2 Activity of mutant and wild-type mGBA2-2A and -linker chimera

Expression of the different 2A peptide and linker constructs of mGBA2 in CHO cells was analyzed by Western blot and their GBA2 activity was determined in the β-glucosidase activity assay. Besides the 2A peptide and linker constructs expressing both mGBA2-Flag and mGBA2-HA, I also tested the single constructs for mGBA2-2A and mGBA2-linker expression (**Figure 36 A**). My results demonstrate that addition of the 2A peptide or linker to the mGBA2-Flag protein significantly reduced GBA2 activity compared to cells expressing mGBA2-Flag (F) (**Figure 36 B**). mGBA2-Flag-2A (F^{2A}) and mGBA2-Flag-linker (F^{link}) only revealed an activity of 30.0 ± 5.7 % and 10.5 ± 4.2 % relative to control mGBA2-Flag, respectively (F^{2A}: $p = 0.0022$; F^{link}: $p = 0.00074$). Furthermore, the double constructs mGBA2-Flag-2A-mGBA2-HA ($F^{2A}H$) and mGBA2-Flag-linker-mGBA2-HA ($F^{link}H$) revealed an activity of 62.2 ± 10.2 % and 51.2 ± 14.1 %, respectively, compared to CHO cells co-expressing mGBA2-Flag and mGBA2-HA (F+H) (**Figure 36 B**; $F^{2A}H$: $p = 0.023$; $F^{link}H$: $p = 0.027$). Thus, also the GBA2 activity of the double construct is diminished by introducing a linker and – to a lesser extent – a 2A peptide. Overall, the linker and protein fusion might interfere with protein folding, whereas the 2A peptide-mediated “cleavage” results in two separate GBA2 proteins that can correctly fold into their tertiary structure to be active. Thus, the 2A-approach was chosen for further studies.

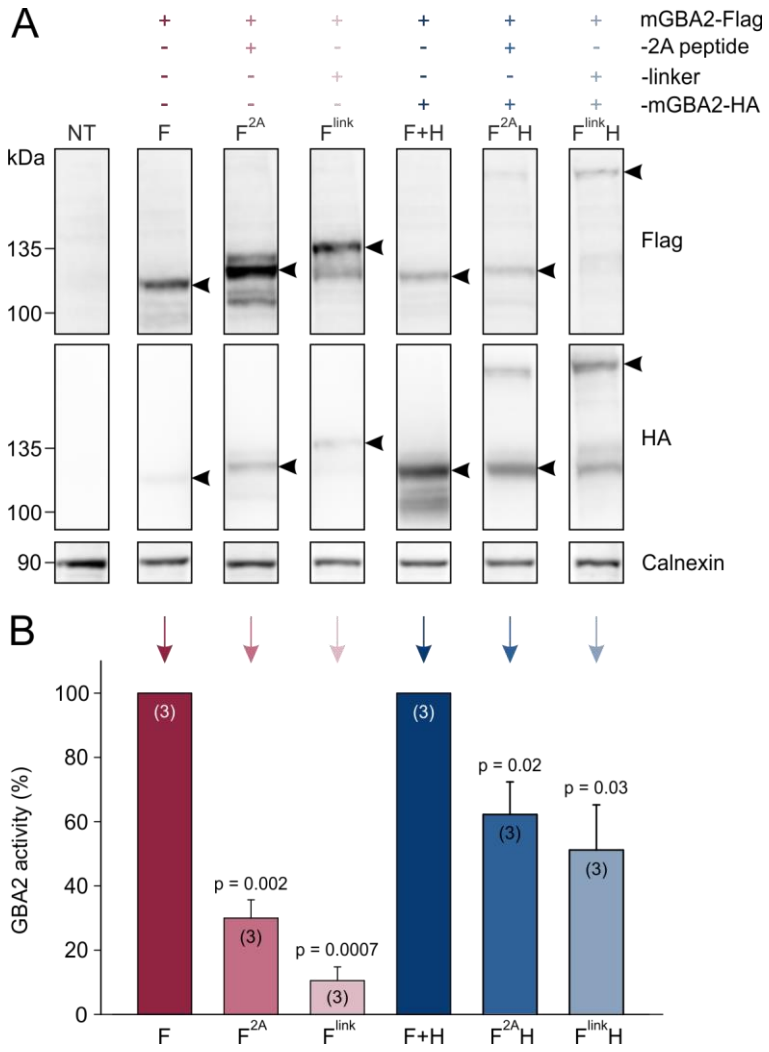

Figure 36: GBA2 expression and activity of mGBA2 2A peptide and linker constructs. A) Western blot analysis of hypotonic lysates from CHO cells expressing 2A peptide and linker constructs generated for the stoichiometric expression of mGBA2-Flag and mGBA2-HA. 35 µg protein was loaded per lane. mGBA2-Flag and mGBA2-HA was detected using a Flag- and HA-specific antibody, respectively. Calnexin served as a loading control. Representative blot for n = 3 experiments. **B)** GBA2 activity in hypotonic lysates from CHO cells expressing the different mGBA2-2A and -linker constructs (normalized to their expression in the corresponding Western blot). Columns represent mean values + SD. Statistical analysis was performed using one-sample t-test (n numbers and p values are indicated). F: mGBA2-Flag, F^{2A}: mGBA2-Flag-2A, F^{link}: mGBA2-Flag-linker, F+H: mGBA2-Flag + mGBA2-HA, $F^{2A}H$: mGBA2-Flag-2A-mGBA2-HA, $F^{link}H$: mGBA2-Flag-linker-mGBA2-HA.

To test whether the presence of mutant GBA2 affects the activity of wild-type GBA2, I expressed the 2A peptide-based constructs encoding both wild-type mGBA2-Flag and mutant mGBA2-HA in CHO cells (WT-2A-mt). As controls, constructs encoding only WT mGBA2 (WT-2A-WT) or mutant mGBA2 (mt-2A-mt) were chosen. Western blot analysis revealed that the constructs for the amino-acid substitutions R864H, R725H, G674R, R621W, D585H and the truncated variants T483R*9 and R331* were expressed in CHO cells (**Figure 37 A, B**).

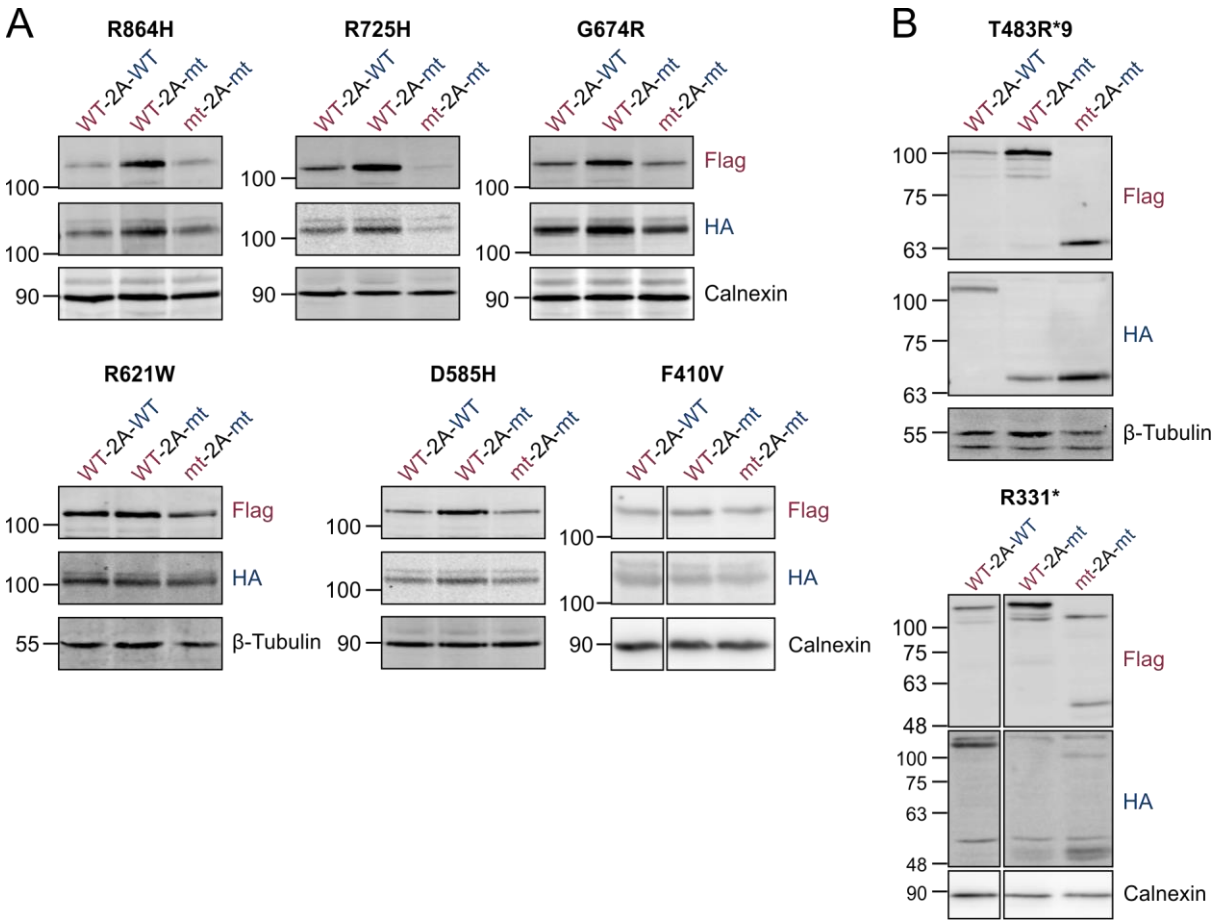

Figure 37: GBA2 expression of the wild-type and mutant mGBA2 2A peptide constructs. Western blot analysis of hypotonic lysates from CHO cells expressing wild-type mGBA2-Flag and wild-type mGBA2-HA (WT-2A-WT), wild-type mGBA2-Flag and mutant mGBA2-HA (WT-2A-mt), or mutant mGBA2-Flag and mutant mGBA2- HA (mt-2A-mt). **A)** Analysis of the missense mGBA2 mutants R864H, R725H, G674R, R621W, D585H, and F410V in WT-2A-mt and mt-2A-mt-transfected CHO cells compared to the WT-2A-WT control. **B)** Analysis of the nonsense mGBA2 mutants T483R*9 and R331* in WT-2A-mt and mt-2A-mt-transfected CHO cells compared to the WT-2A-WT control. mGBA2-Flag and mGBA2-HA was detected using a Flag- and HA-specific antibody, respectively. 20 µg protein was loaded per lane. Calnexin or β-Tubulin served as a loading control.

Next, GBA2 activity in hypotonic lysates of the transfected cells was measured and normalized to the protein expression determined by Western blot. Compared to the WT-2A-WT control (set to 100%), the wild-type GBA2 activity in cells expressing WT-2A-mt would account for 50% because only half the amount of wild-type GBA2 is expressed. If there is a dominant-negative effect, GBA2 activity in WT-2A-mt-expressing cells would account for significantly less than 50% activity compared to WT-2A-WT. However, for none of the missense mutations R864H, G674R, R621W, D585H, F410V or nonsense mutations T483R*9 and R331*, a dominant-negative effect was seen as the activity in the WT-2A-mt condition resembled an activity of about 50% (**Figure 38**).

Since the R725H mutant showed residual GBA2 activity of 30.28 ± 9.32% compared to wild-type mGBA2 (**Figure 14**), this activity would add up on the wild-type GBA2 activity in cells transfected with the WT-2A-R725H construct, accounting for about 80% activity (50% WT + 30% R725H) compared to WT-2A-WT. If the R725H variant exhibits a dominant-negative

effect, the activity of wild-type GBA2 would be diminished, resulting in significantly less than 80% activity in WT-2A-R725H-expressing cells, but at least resembling 30% residual activity of the R725H mutant. Similar to my results obtained before (see 3.1.4), the R725H mutant revealed a residual activity of 51.71 ± 13.08% when expressing the WT-2A-R725H construct in CHO cells (**Figure 38**). However, no dominant-negative effect for the R725H was observed, as the WT-2A-R725H revealed an activity of 78.02 ± 14.05 % compared to WT-2A-WT (**Figure 38**).

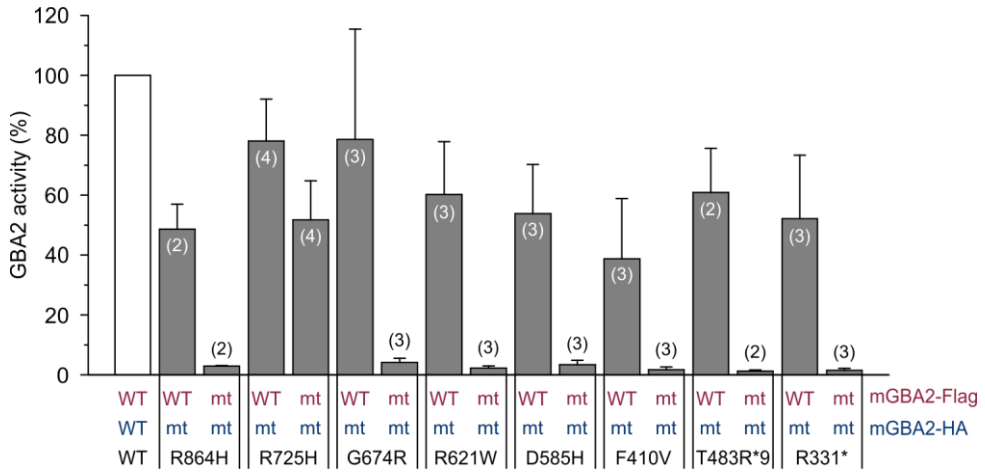

Figure 38: Mutant mGBA2 has no dominant negative effect on wild-type mGBA2 activity. Analysis of the GBA2 activity in hypotonic lysates from CHO cells expressing wild-type mGBA2-Flag (WT) and wild-type mGBA2-HA (WT) or mutant mGBA2-HA (mt) using the 2A peptide approach. In addition, cells solely expressing the mutant mGBA2 protein were studied. More precisely, the GBA2 activity (%) in cells expressing the wild-type mGBA2-Flag 2A mutant mGBA2-HA and mutant mGBA2-Flag 2A mutant mGBA2-HA compared to the control (wild-type mGBA2-Flag 2A wild-type mGBA2-HA) are plotted. The activity was normalized to the expression of the constructs determined by Western blot analysis. Columns represent mean values + SD (n numbers are indicated). WT: wild-type; mt: mutant. Parts of the experiments have been performed by Dominik Dittmann.

3.6 Genetic ablation of GBA2 expression in mice

ARCA, HSP, and MSLS patients carrying mutations in GBA2 suffer from neurological symptoms with morphological and functional defects in the central nervous system (Citterio et al., 2014; Hammer et al., 2013; Haugarvoll et al., 2017; Martin et al., 2013; Sultana et al., 2015; Votsi et al., 2014). I could show that all disease-associated mutations – besides R725H – cause a complete loss of function of GBA2 (see **Figure 14 B**). Hence, human patients carrying the GBA2 mutations in a homozygous state are most likely devoid of GBA2 activity. So far, only one study analyzed GBA2 activity in lymphoblasts or leukocytes isolated from three patients carrying the R630W mutation, demonstrating that, in fact, these patients do not display GBA2 activity, at least in the experimental set-up used (Martin et al., 2013). However, how loss of GBA2 might cause motor dysfunctions remains elusive.

In my PhD thesis, I used mice as a model system to unravel the role of GBA2 in locomotion *in vivo*. Two global GBA2-knockout mouse lines GBA2-KO (Yildiz et al., 2006) and GBA2-EUCOMM (Gba2$^{tm1a(EUCOMM)Wtsi}$) were included in this project, which are referred to as KO and

KO^{EU}, respectively (**Figure 39 A, B**). The GBA2-KO mouse line has been generated and intensively studied by Yildiz and colleagues (Yildiz et al., 2006). The main phenotype of these mice is globozoospermia (Yildiz et al., 2006). We could show that male mice lacking GBA2 are subfertile due to accumulation of GlcCer, which alters the actin cytoskeleton dynamics and cause a malformation of the sperm head (Raju et al., 2015). This phenotype was observed in both KO (Raju et al., 2015) and KO^{EU} mice (Dr. Diana N. Raju, unpublished data). The KO^{EU} line bears conditional potential: exon 2 and 3 of the *Gba2* gene are flanked by recognition sites for the Cre recombinase (*loxP* sites) (**Figure 39 B**). Mating these mice with transgenic mice expressing the Cre recombinase in a tissue-specific manner generates tissue-specific GBA2-knockout mice. Neurological symptoms as seen in human patients carrying GBA2 mutations can arouse from defects in the nervous system and/or muscle. Thus, studying neuron- and muscle-specific GBA2-knockout mice will allow to deduce if loss of the enzyme in either neurons or muscle underlies the development of motor dysfunction. First, KO^{EU} were crossed with Flp deleter mice (Flp deleter +/flp) to eliminate the FRT-flanked *lacZ* cassette, resulting in the floxed *GBA2* allele (**Figure 39 B**). GBA2 flox/flox; Flp deleter +/+ mice were mated with Synapsin (Syn)-Cre or Myogenic factor 5 (Myf5)-Cre mice to generate GBA2 flox/flox; Flp deleter +/+; Synapsin-Cre Cre/+ and Myf5-Cre Cre/+; Flp deleter +/+; GBA2 flox/flox offspring, respectively (**Figure 39 B, C**). The Cre recombinase in these offspring is expressed under the Syn or Myf5 promotor, resulting in a loss of GBA2 expression in neurons and skeletal muscle, respectively.

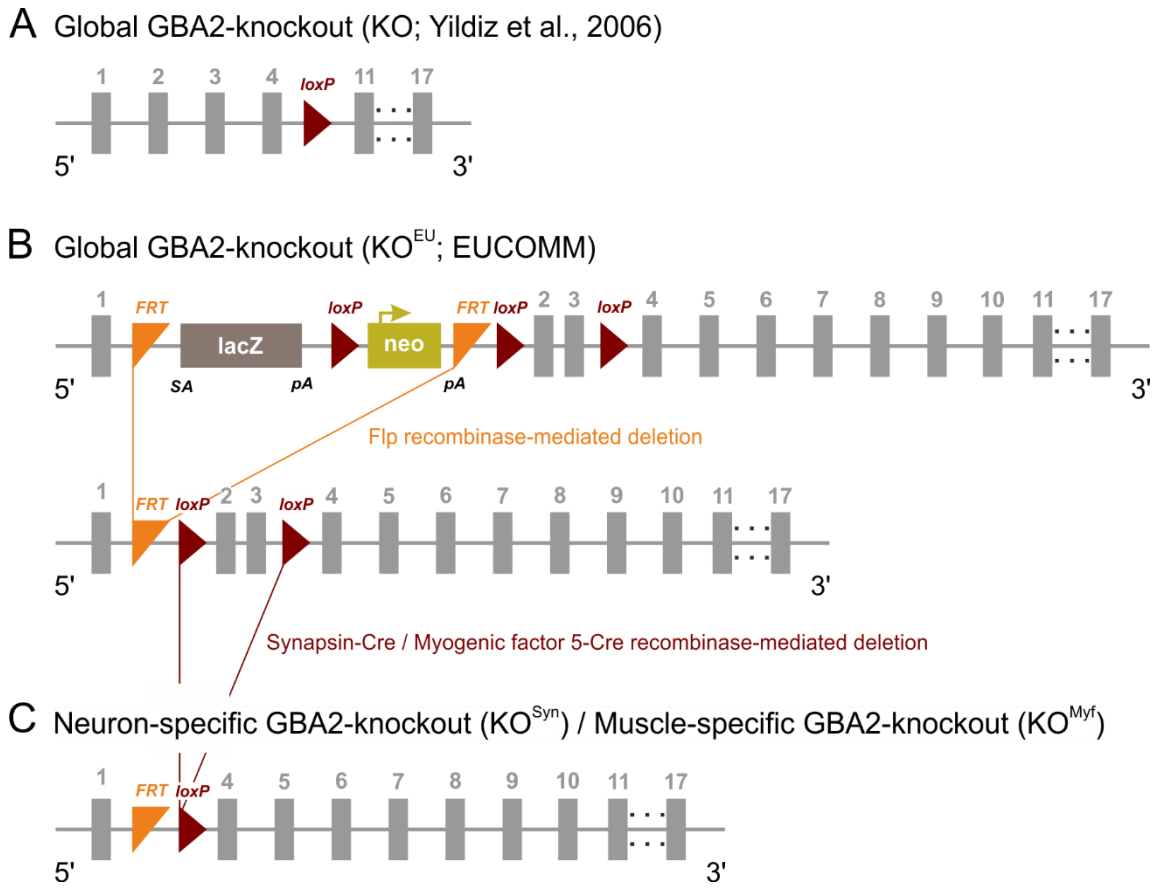

Figure 39: Targeting strategy to generate global and tissue-specific GBA2-knockout mouse lines. A) GBA2-knockout mice (KO; Yildiz et al., 2006) lack exon 5 to 10. Exon deletion results in non-sense *Gba2* mRNA decay and, thereby, in a loss of GBA2. **B)** GBA2-knockout mice (EUCOMM; KO^{EU}) contain an FRT-flanked *lacZ* cassette introduced into the region spanning exon 1 to 4. Thereby, the *lacZ* gene encoding the β-glucosidase is expressed under the control of the *Gba2* promotor, whereas the *Gba2* gene is not expressed. KO^{EU} mice are mated with Flp deleter mice (Flp deleter +/flp) to eliminate the FRT-flanked *lacZ* cassette, resulting in the floxed GBA2 allele. **C)** GBA2 flox/flox; Flp deleter +/+ mice were mated with Synapsin (Syn)-Cre recombinase or Myogenic factor 5 (Myf5)-Cre recombinase mice to delete exon 2 and 3 of the *Gba2* gene. Neo: cassette coding for the neomycin phosphotransferase inducing neomycin resistance for positive selection; loxP: 34 bp DNA sequence, recognition site for Cre recombinase; FRT: recognition site for Flp-mediated excision; pA: polyadenylation site; SA: splice acceptor site. Image modified from International Mouse Phenotype Consortium: Allele Map of $Gba2^{tm1a(EUCOMM)Wtsi}$.

In GBA2-KO mice, GlcCer mainly accumulates in the testis, brain, and liver where GBA2 expression is highest (Yildiz et al., 2006). However, GBA2-KO mice do not show organ enlargement and a reduction in life span (Yildiz et al., 2006). Apart from the fertility defect in male mice, no gross phenotype has been observed. In particular, no neurological symptoms have been documented so far, which are commonly observed in lipid storage disorders (Bellettato and Scarpa, 2010). Thus, I performed a phenotypical characterization of the KO mice with particular focus on neurological defects. First, I determined their body and brain weight (female, 33 ± 2 weeks). A reduced body weight is suggestive for growth retardation (Lang and Legates, 1969; Sun et al., 2004) and a reduced brain weight could indicate atrophy (Shimada et al., 1992). However, neither body weight nor brain weight was altered in the KO mice (body weight: WT: 25.78 ± 3.08 g *versus* KO: 27.40 ± 4.95 g; brain weight: WT: 446.95 ± 14.32 mg *versus* KO: 444.00 ±15.29 mg; **Figure 40 A, B**). The morphology of GBA2-KO brains

was also not different to wild-type mice with a similar size of the hemispheres and no differences in the cerebellar lobes were observed (**Figure 40 C**). The results for KO^{EU} mice (female, 33 ± 3 weeks) were similar: body and brain weight was not different in WT and KO^{EU} (body weight: WT: 26.66 ± 3.55 g *versus* KO^{EU}: 26.55 ± 3.25 g; brain weight: WT: 436.73 ± 17.24 mg *versus* KO^{EU}: 432.00 ± 17.94 mg; **Figure 40 D, E**). Similarly, brain morphology was not different between WT and KO^{EU} mice (**Figure 40 F**).

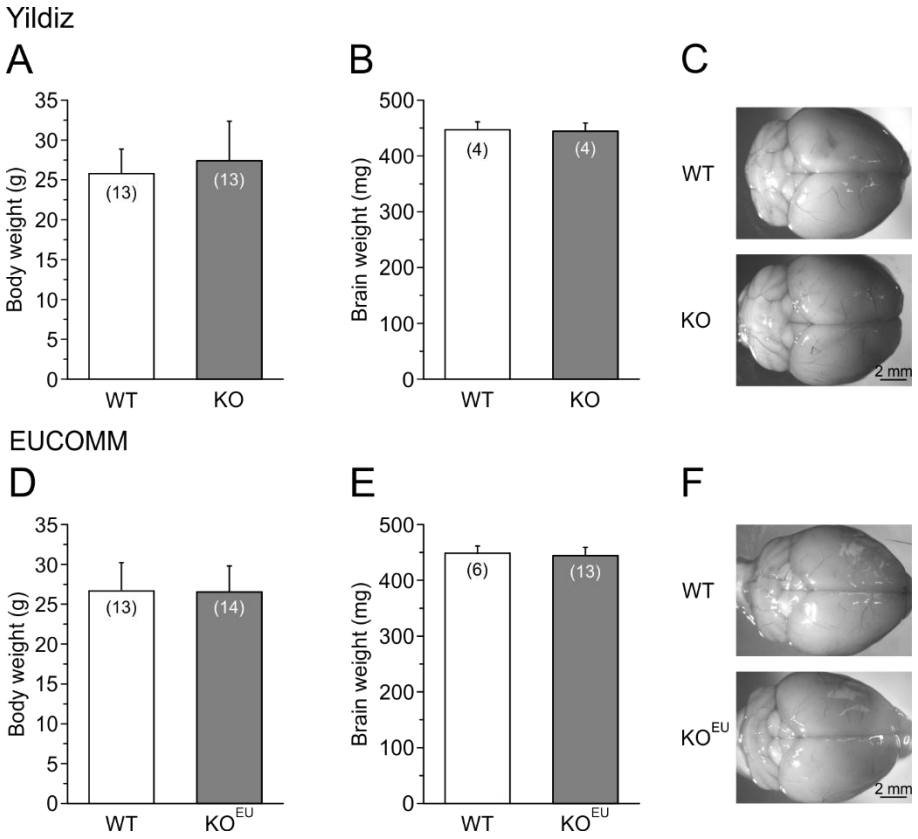

Figure 40: Body and brain weight of wild-type and GBA2-knockout mice. A) Body (g) and **B)** brain weight (mg) of adult (female, 33 ± 2 weeks) wild-type (WT) and GBA2-knockout (KO) mice from the mouse line generated by Yildiz et al. (2006). **D)** Body (g) and **E)** brain weight (mg) of adult (female, 33 ± 3 weeks) wild-type (WT) and GBA2-knockout (KO^{EU}) mice. Columns represent mean values + SD. Statistical analysis was performed using one-way ANOVA (n numbers are indicated). Representative images of **C)** adult wild-type (WT; female, 31 weeks) and GBA2-knockout (KO; female, 31 weeks) brain and **F)** adult wild-type (WT; female, 30 weeks) and GBA2-knockout (KO^{EU}; female, 28 weeks) brain are depicted. Scale bars are indicated.

Neuron-specific loss of GBA2 also did not result in major morphological differences: Body weight and brain weight, and the macroscopic brain morphology was not different between genotypes (body weight: WT: 28.78 ± 5.31 g *versus* KO^{Syn}: 25.75 ± 3.93 g; brain weight: WT: 466.13 ± 11.55 mg v*ersus* KO^{Syn}: 461.86 ± 19.22 mg; female, 33 ± 2 weeks; **Figure 41 A-C**). Loss of GBA2 activity in skeletal muscle did not affect body (WT: 26.67 ± 2.96 g *versus* KO^{Myf}: 27.21 ± 2.67 g) or brain weights (WT: 443.36 ± 31.85 mg *versus* KO^{Myf}: 469.77 ± 16.35 mg), and overall brain morphology appeared similar in KO^{Myf} and WT control mice (female, 34 ± 3 weeks; **Figure 41 D-F**).

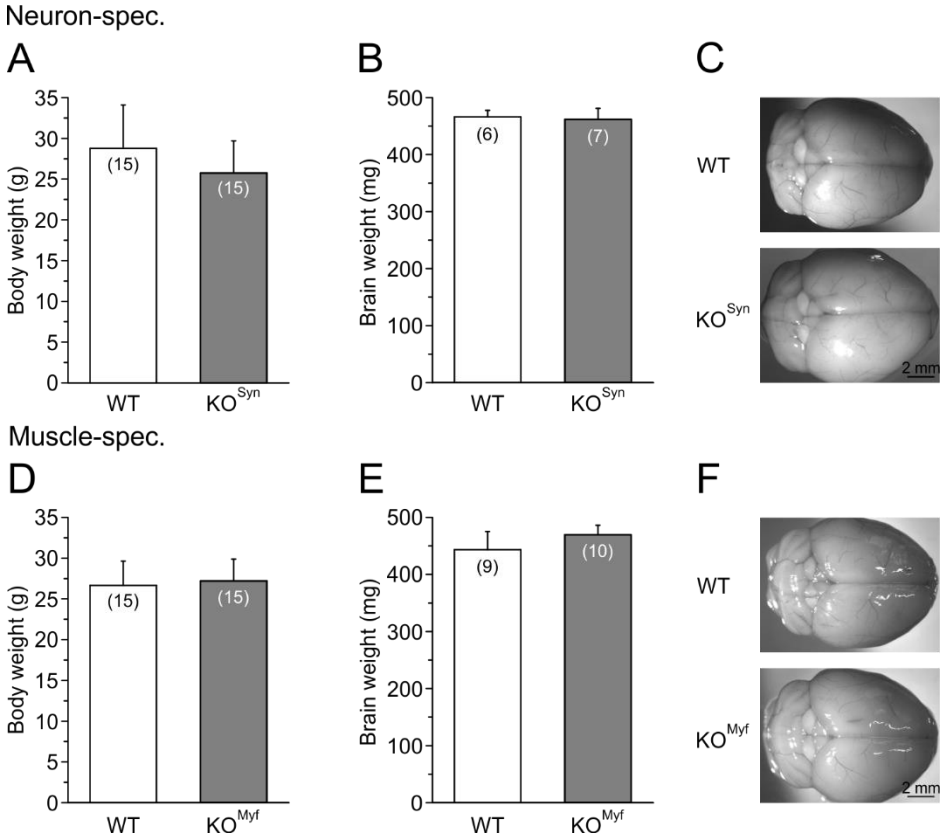

Figure 41: Body and brain weight of wild-type and tissue-specific GBA2-knockout mice. A) Body (g) and **B)** brain weight (mg) of adult (female, 33 ± 2 weeks) wild-type (WT) and neuron-specific GBA2-knockout (KO^{Syn}) mice. **D)** Body (g) and **E)** brain weight (mg) of adult (female, 34 ± 3 weeks) wild-type (WT) and muscle-specific GBA2-knockout (KO^{Myf}) mice. Columns represent mean values + SD. Statistical analysis was performed using one-way ANOVA (n numbers are indicated). Representative images of **C)** adult wild-type (WT; female, 33 weeks) and neuron-specific GBA2-knockout (KO^{Syn}; female, 32 weeks) brain and **F)** adult wild-type (WT; female, 31 weeks) and muscle-specific GBA2-knockout (KO^{Myf}; female, 31 weeks) brain are depicted. Scale bars are indicated.

3.7 Expression and activity of GBA2 in the central nervous system

Glycosphingolipids are important structural and functional constituents of the central nervous system (CNS) in mammals (Cuzner and Davison, 1968; Ngamukote et al., 2007; Thudichum et al., 1884). GlcCer is the main precursor for all these lipids; thus, GlcCer metabolism needs to be tightly regulated. Dysregulation of GlcCer homeostasis due to loss of GBA2 might lead to severe defects in the central nervous system. Thus, I analyzed the expression and activity of GBA2 in the brain, in particular in neurons, in comparison to other tissues.

3.7.1.1 Brain

Western blot analysis indicated that GBA2 is expressed in the brain of WT, but not KO animals (**Figure 42 A**). Similarly, GBA2 activity was only detected in brain lysates from WT, but not from KO/KO^{EU} mice (**Figure 42 B**). Interestingly, GBA1 activity was not altered in KO/KO^{EU} mice (**Figure 42 C**).

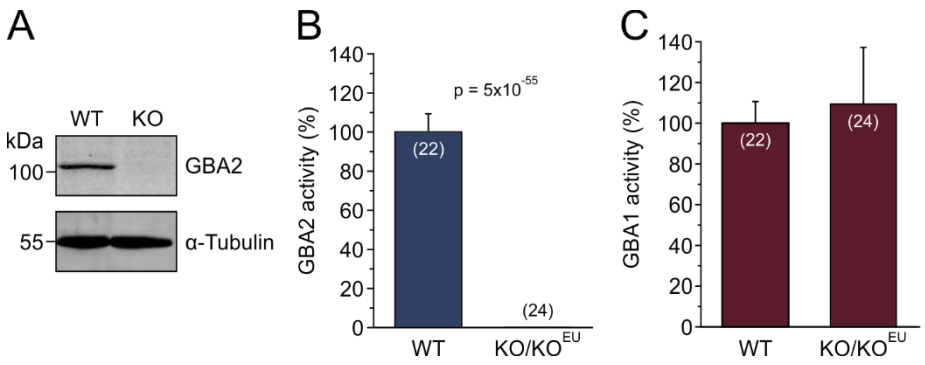

Figure 42: GBA2 expression and activity in brain of wild-type and global GBA2-knockout mice. A) Western blot analysis of GBA2 in brain from an adult (31 weeks) wild-type (WT) and global GBA2-knockout (KO) mouse. GBA2 was detected using a GBA2-specific antibody. α-Tubulin served as a loading control. 90 µg protein was loaded per lane. Analysis of **B)** GBA2 activity and **C)** GBA1 activity in hypotonic lysates of brain from adult (35 ± 9 weeks) wild-type (WT) and global GBA2-knockout (KO, KO^{EU}) mice. Columns represent mean values + SD. Statistical analysis was performed using one-sample t-test (n numbers and p values are indicated).

Ablating GBA2 only in neurons will reveal if neurons or other cell types account for the GBA2 expression and activity in the central nervous system. Thus, I analyzed the expression and activity of GBA2 in the brain and spinal cord of WT and KO^{Syn} mice and compared it to skeletal muscle, liver, spleen, and testis. Indeed, the expression of GBA2 is significantly decreased in the brain and spinal cord of KO^{Syn} mice, indicating that neurons exhibit high GBA2 expression levels (**Figure 43**).

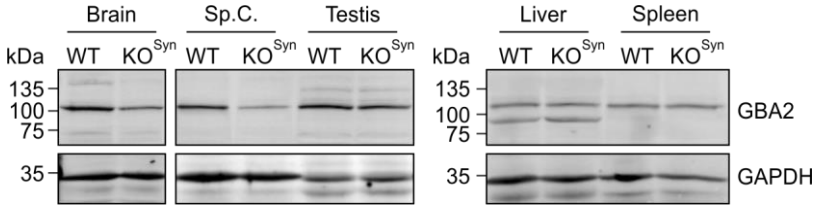

Figure 43: GBA2 expression in different tissues of wild-type and neuron-specific GBA2-knockout mice. Western blot analysis of GBA2 in hypotonic lysates of brain, spinal cord (Sp.C.), testis, liver, and spleen from an adult wild-type (WT; 28 weeks) and neuron-specific GBA2-knockout (KO^{Syn}; 23 weeks) mouse. GBA2 was detected using a GBA2-specific antibody. GADPH served as a loading control. 60 µg protein was loaded per lane.

To verify whether also GBA2 activity is reduced in brain and spinal cord, I analyzed the activity in hypotonic lysates of brain, spinal cord, testis, skeletal muscle, liver, and spleen. Indeed, GBA2 activity was only diminished in brain (WT: 8.76 ± 2.97 rfu/min *versus* KO^{Syn}: 3.14 ± 0.76 rfu/min; p = 0.033) and spinal cord (WT: 6.66 ± 2.55 rfu/min *versus* KO^{Syn}: 1.26 ± 0.44 rfu/min; p = 0.023), but remained unchanged in testis, skeletal muscle, liver, and spleen of the KO^{Syn} mouse compared to the WT control (**Figure 44 A**). In general, GBA2 activity in brain (WT: 8.76 ± 2.97 rfu/min) and spinal cord (6.66 ± 2.55 rfu/min) was the highest, followed by testis with 5.99 ± 2.31 rfu/min (WT). GBA2 activity levels in liver and spleen were rather low compared to the central nervous tissue with 1.66 ± 0.43 rfu/min and 1.57 ± 0.85 rfu/min in WT, respectively (**Figure 44 A**). In skeletal muscle, GBA2 activity was even lower accounting for 0.14 ± 0.09 rfu/min in WT (**Figure 44 B**).

This data also indicates that the activity of GBA2 in other cell types than neurons in the brain and spinal cord does not majorly contribute to the total GBA2 activity in these tissues. The residual activity levels in KO^{Syn} brain and spinal cord only accounted for 3.14 ± 0.76 rfu/min compared to 8.76 ± 2.97 rfu/min in WT brain and 1.26 ± 0.44 rfu/min compared to 6.66 ± 2.55 rfu/min in WT spinal cord, respectively (**Figure 44 A**). Of note, GBA1 activity remained unchanged in brain and spinal cord of KO^{Syn} mice (**Figure 44 C**). Overall, the variation in GBA1 activity was not as high as for GBA2 between the different tissues: Spinal cord, testis, and liver from WT mice displayed similar activities with 1.10 ± 0.16 rfu/min, 1.30 ± 0.32 rfu/min, 1.28 ± 0.47 rfu/min, respectively, whereas brain and spleen revealed slightly lower GBA1 activities of 0.82 ± 0.18 rfu/min and 0.86 ± 0.11 rfu/min, respectively. Similar to the GBA2 activity, skeletal muscle appeared to have the lowest GBA1 activity (0.30 ± 0.05 rfu/min; **Figure 44 C, D**).

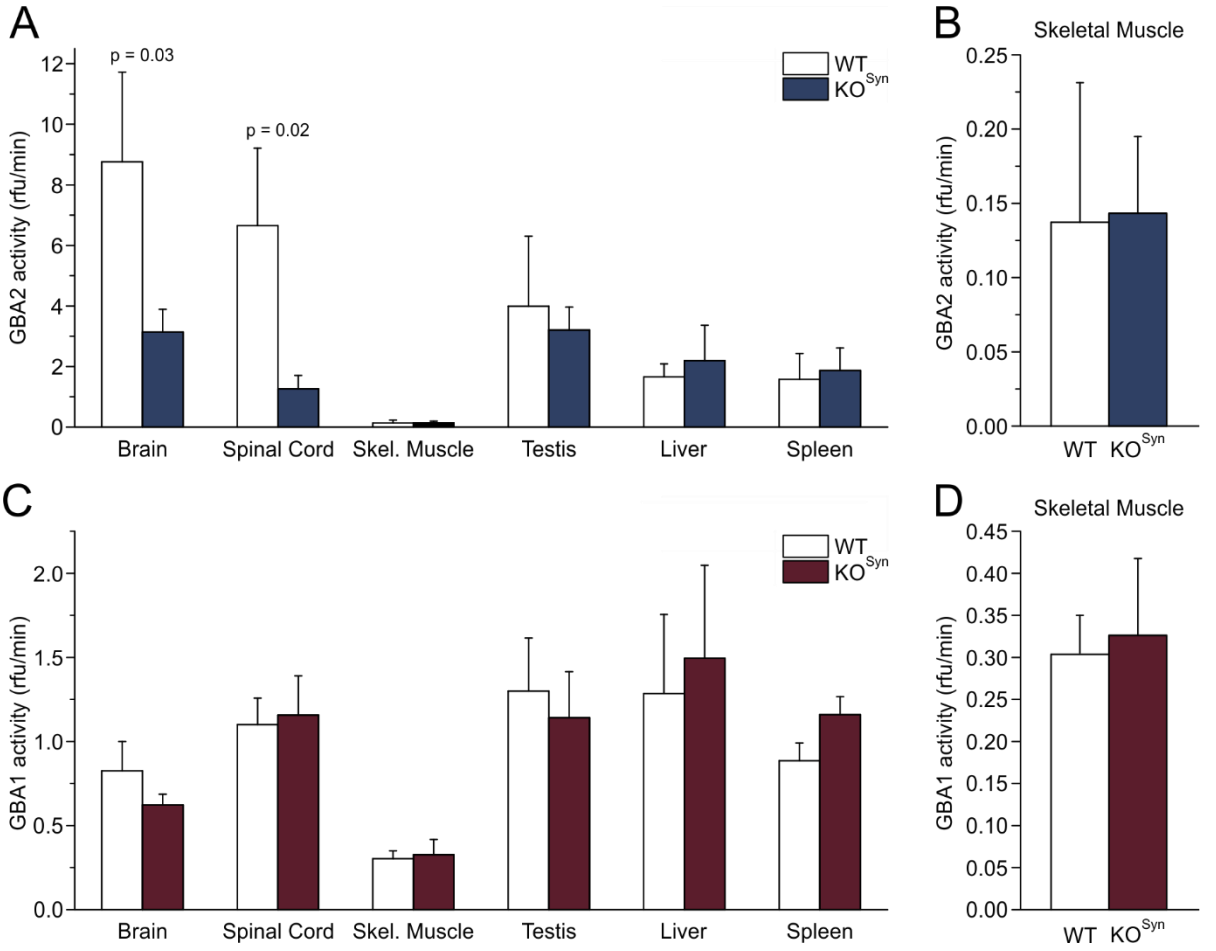

Figure 44: GBA2 and GBA1 activity in different tissues of wild-type and neuron-specific GBA2-knockout mice. Analysis of **A)** GBA2 and **C)** GBA1 activity in hypotonic lysates of brain, spinal cord, skeletal muscle (Skel. Muscle), testis, liver, and spleen from adult (26 ± 7 weeks) wild-type (WT) and neuron-specific GBA2-knockout (KO^{Syn}) mice. 10.79 ± 1.41 µg protein was used in the β-glucosidase activity assay. **B)** and **D)** show activities in the skeletal muscle separately. Columns represent mean values + SD. Statistical analysis was performed using one-way ANOVA (p values are indicated). n = 3 for all tissues besides testis and spleen (n = 2). rfu/min: relative fluorescence units per minute.

To determine the expression pattern of GBA2 in the brain, I performed immunohistochemical stainings. However, the application of GBA2-specific antibodies for immunohistochemical analysis of brain sections was not successful (data not shown). Thus, I made use of the KO^{EU} mouse line, which contains a *lacZ* cassette that expresses the β-galactosidase under the control of the GBA2 promotor (see **Figure 39**).

X-gal staining of coronal brain sections from WT and KO^{EU} mice revealed β-galactosidase expression in the brain stem and the cerebellum (**Figure 45**). I tested two different X-gal concentrations, namely 0.01% and 0.05%, and both concentrations were sufficient to detect activity of β-galactosidase specifically in the KO^{EU} brain, whereas no β-galactosidase activity was observed in brain sections from WT mice (**Figure 45**).

Fixation of the tissue with glutaraldehyde results in high background staining. Thus, glutaraldehyde fixation is not suitable for immunofluorescent stainings since it produces high auto-fluorescence (Collins and Goldsmith, 1981). However, this characteristic can also be used to detect myelinated regions in the nervous tissue (Christensen et al., 2014): The white matter in the brain reveals high background staining (brown) because it is enriched in myelin sheaths, whereas the grey matter containing unmyelinated neurons remains unstained (beige) (**Figure 45**). In the cerebellum, the granular layer (light brown) and the molecular layer (beige) in the lobules can be nicely distinguished.

In the brain stem, β-galactosidase activity was high in the region adjacent to the fourth ventricle and in the lobules of the cerebellum (**Figure 45**). Microscopic analysis revealed that the Purkinje cell layer surrounding the granular layer (light brown) showed the highest β-galactosidase activity. Only a few cells were labeled in the molecular (beige) and granular layer (light brown) and no staining was observed in the white matter (dark brown) in the center of the granular layer (light brown). Thus, GBA2 seems to be highly expressed in Purkinje cells, but also in a few cells in the molecular and granular layer.

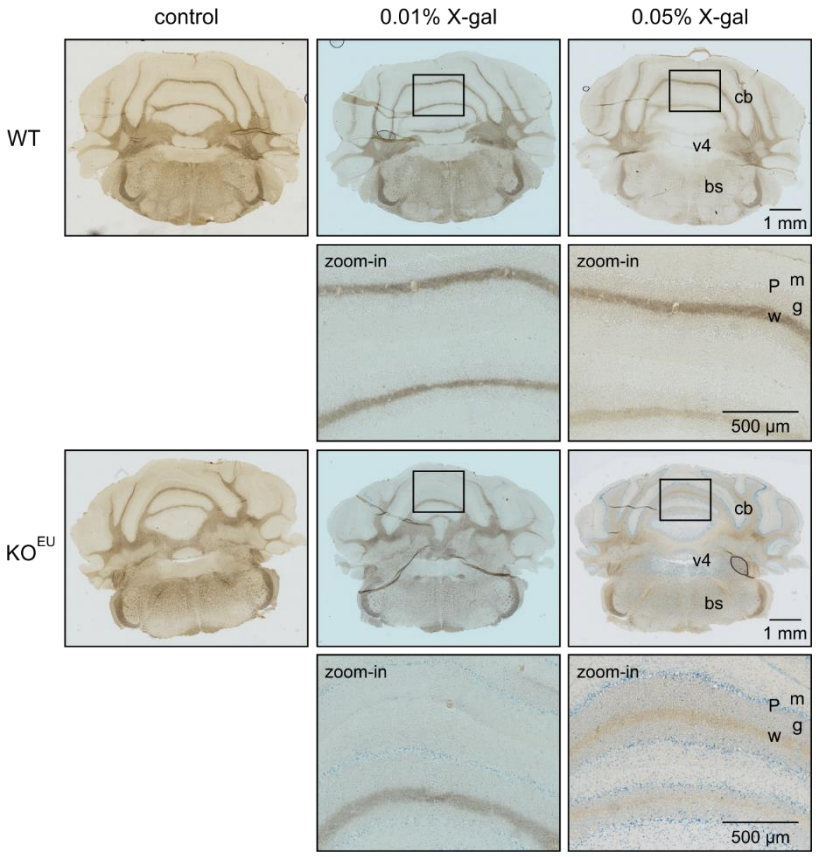

Figure 45: β-Galactosidase expression in wild-type and global GBA2-knockout (KO^{EU}) brain. X-gal staining on coronal brain sections of an adult wild-type (WT; 19 weeks) and global GBA2-knockout (KO^{EU}; 23 weeks) mouse expressing the *lacZ* reporter cassette under the GBA2 promotor. 0.01% and 0.05% X-gal was used as a substrate for β-galactosidase. Regions of the cerebellum were zoomed-in to indicate the predominant β-galactosidase expression in the Purkinje cell layer in KO^{EU} mice. Scale bars are indicated. cb: cerebellum, v4: fourth ventricle, bs: brain stem; m: molecular layer, P: Purkinje cell layer, g: granular layer, w: white matter.

3.7.1.2 Spinal Cord

Patients with *GBA2* mutations suffering from ARCA, HSP, or MSLS majorly display atrophy in different brain regions such as the cerebrum, cerebellum, or corpus callosum (Citterio et al., 2014; Hammer et al., 2013; Haugarvoll et al., 2017; Martin et al., 2013; Votsi et al., 2014). The diagnosis has been predominantly made according to the performance in different physical tasks or in reflex tests. However, these studies convey little information about the spinal cord that might also be affected. Thus, I also analyzed the expression and activity of GBA2 in murine spinal cord.

GBA2 is expressed in the spinal cord of WT, but not KO mice (**Figure 46 A**). In line with this finding, GBA2 activity was detected in WT, but not in KO/KO^{EU} spinal cord protein lysates (**Figure 46 B**), and GBA1 activity remained unchanged in the absence of GBA2 (**Figure 46 C**).

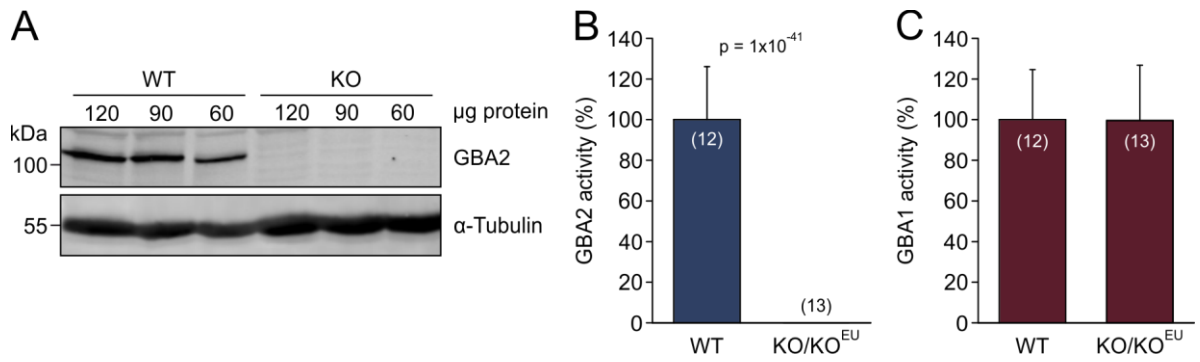

Figure 46: GBA2 expression and activity in spinal cord of wild-type and global GBA2-knockout mice. A) Western blot analysis of GBA2 in hypotonic lysates of spinal cord from an adult wild-type (WT; 19 weeks) and global GBA2-knockout (KO; 21 weeks) mouse. GBA2 was detected using a GBA2-specific antibody. α-Tubulin served as a loading control. 120 µg, 90 µg, or 65 µg protein was loaded per lane. Modified from Woeste, Master thesis, 2015. Analysis of **B)** GBA2 activity and **C)** GBA1 activity in hypotonic lysates of spinal cord from adult (45 ± 12 weeks) wild-type (WT) and global GBA2-knockout (KO, KO^{EU}) mice. Columns represent mean values + SD. Statistical analysis was performed using one-sample t-test (n numbers and p values are indicated).

X-gal staining of spinal cord sections from WT and KO^{EU} mice revealed that β-galactosidase, and, thereby GBA2, is predominantly expressed in the grey matter (**Figure 47**).

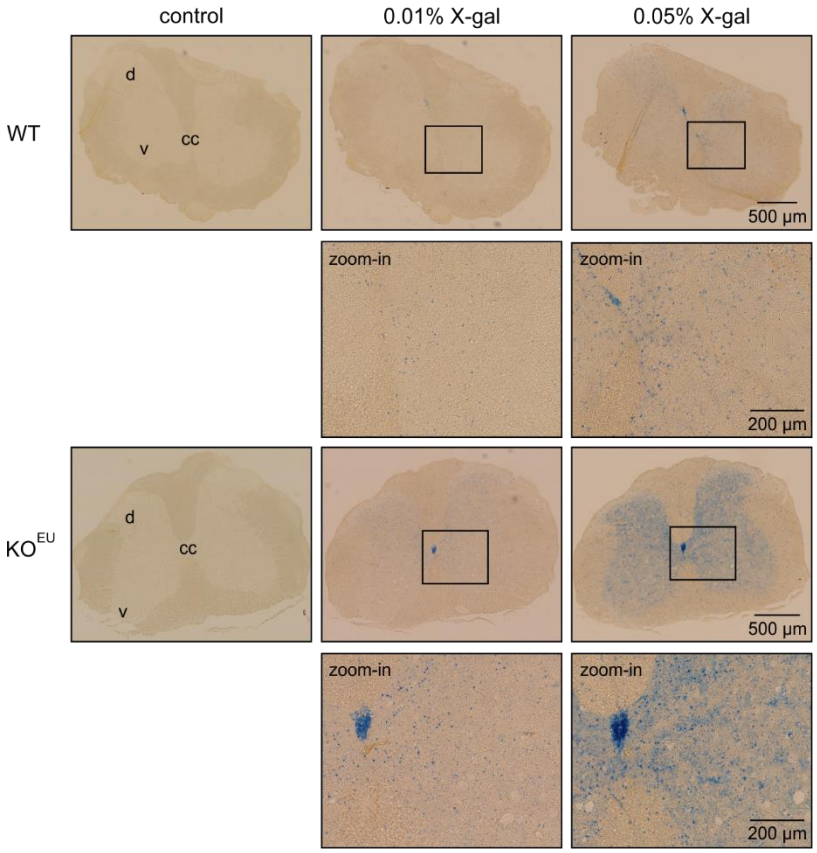

Figure 47: β-Galactosidase expression in wild-type and global GBA2-knockout (KO^{EU}) spinal cord. X-gal staining on transverse sections (16 µm) of the cervical spinal cord of an adult wild-type (WT; 28 weeks) and global GBA2-knockout (KO^{EU}; 31 weeks) mouse expressing the *lacZ* reporter cassette under the GBA2 promotor. 0.01% and 0.05% X-gal was used as a substrate for the β-galactosidase. Regions of the spinal cord were zoomed-in to indicate the predominant β-galactosidase expression in the grey matter in KO^{EU} mice. Scale bars are indicated. cc: central canal, D: dorsal horn of the grey matter, v: ventral horn of the grey matter.

3.7.1.3 Cerebellum

Human patients carrying mutations in the *GBA2* gene suffer from ataxia and show defects in the cerebellum, which controls in motor coordination. Thus, I studied this brain region in more detail. The cerebellum of early postnatal mice (P8) was dissected (in collaboration with Prof. Dr. Frank Bradke; Dr. Sina Stern, DZNE, Bonn) and I analyzed GBA2 expression and activity. My results show that, indeed, GBA2 is expressed in WT, but not in KO^{EU} cerebellum (**Figure 48 A**). This is in line with my data obtained by X-gal staining of coronal brain sections, including the cerebellum (see **Figure 45**). Moreover, GBA2 activity is only detectable in the WT, but not in KO/KO^{EU} cerebellum (**Figure 48 B**).

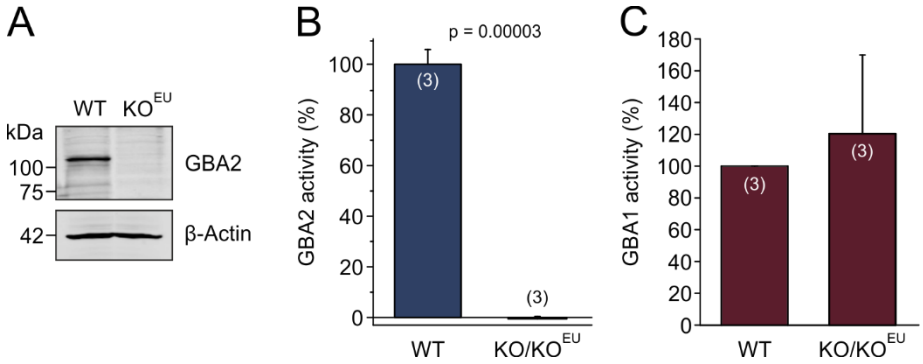

Figure 48: GBA2 expression and activity in cerebellum of P8 wild-type and global GBA2-knockout mice. A) Western blot analysis of GBA2 in hypotonic lysates of cerebellum from a P8 wild-type (WT) and global GBA2-knockout (KO^{EU}) mouse. GBA2 was detected using a GBA2-specific antibody. β-Actin served as a loading control. 35 µg protein was loaded per lane. Analysis of **B)** GBA2 activity and **C)** GBA1 activity in hypotonic lysates of cerebellum from P8 wild-type (WT) and global GBA2-knockout (KO; KO^{EU}) mice. Columns represent mean values + SD. Statistical analysis was performed using one-way ANOVA (n numbers and p values are indicated).

Cerebellar neurons were isolated from P8-P9 mice and GBA2 expression and activity was analyzed. GBA2 is expressed and active in cerebellar neurons (**Figure 49 A, B**). However, the GBA2 activity was not completely abolished by addition of 8.3 µM NB-DNJ and accounted for the residual 0.26 ± 0.30 rfu/min in KO cerebellar lysates (**Figure 49 B**). This activity represents GBA1, which shows residual activity at pH 6 (**Figure 13**).

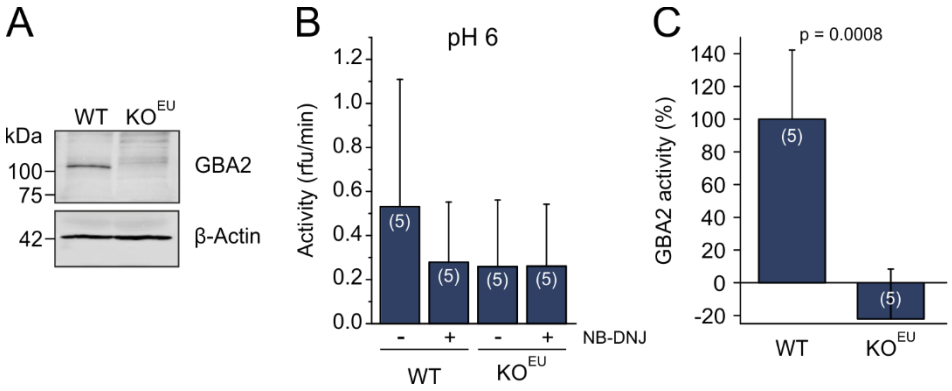

Figure 49: GBA2 expression and activity in cerebellar neurons of P8 wild-type and global GBA2-knockout mice. A) Western blot analysis of GBA2 in hypotonic lysates of cerebellar neurons from a P8 wild-type (WT) and global GBA2-knockout (KO^{EU}) mouse. GBA2 was detected using a GBA2-specific antibody. β-Actin served as a

loading control. 60 µg protein was loaded per lane. **B)** Analysis of GBA2 activity and in cerebellar neurons of P8-9 wild-type (WT) and global GBA2-knockout (KO^{EU}) mice measured in the absence (-) or presence (+) of the GBA2 inhibitor NB-DNJ. **C)** GBA2 activity represented in **B)** defined as the NB-DNJ-blockable activity compared to WT (in %). Cerebellar neurons were isolated by Dr. Sina Stern, DZNE (Bonn). Columns represent mean values + SD. Statistical analysis was performed using one-way ANOVA in **(A)** or one-sample t-test in **(B)** (n numbers and p values are indicated). rfu/min: relative fluorescence units per minute. NB-DNJ: *N*-butyl-deoxynojirimycin.

In addition, I analyzed the expression of GBA2 on a cellular level by determining the β-galactosidase activity in cerebellar neurons from P9 WT and KO^{EU} mice. Using 0.01% and 0.05% X-gal as a substrate, I could detect β-galactosidase activity in isolated KO^{EU} neurons (**Figure 50**). No cleavage of X-gal, thus, no β-galactosidase activity, was observed in the WT neurons.

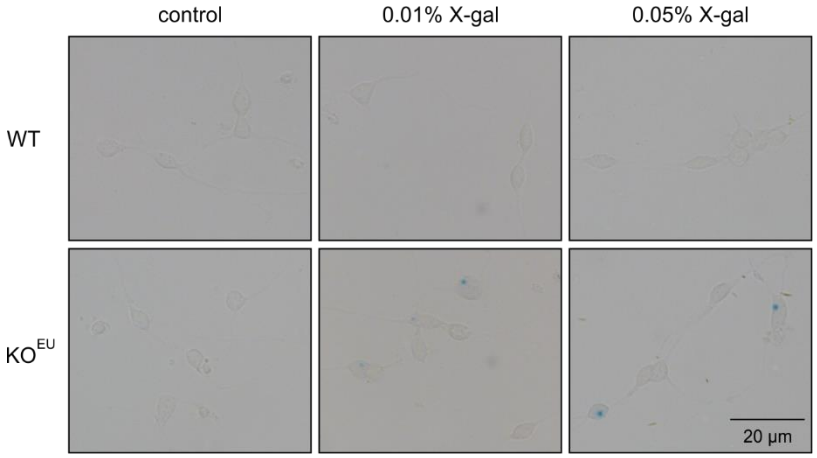

Figure 50: β-Galactosidase expression in wild-type and global GBA2-knockout (KO^{EU}) cerebellar neurons. X-gal staining performed on cerebellar neurons of P9 wild-type (WT) or GBA2 lacZ/lacZ mice (KO^{EU}) expressing the *lacZ* reporter cassette under the *GBA2* promotor. 0.01% or 0.05% X-gal was used as a substrate for β-galactosidase. Cerebellar neurons were isolated by Dr. Sina Stern, DZNE (Bonn). Scale bar is indicated.

3.7.1.3.1 Cerebellar morphology in GBA2-KO mice

Patients with *GBA2* mutations suffering from ARCA, HSP, or MSLS often showed atrophy in the cerebellum (Citterio et al., 2014; Hammer et al., 2013; Haugarvoll et al., 2017; Martin et al., 2013; Votsi et al., 2014). Thus, I studied the morphology of the cerebellum by performing histochemical staining of cerebella from P18 and adult WT and KO mice.

I prepared sections of the lateral hemispheres (left/right), also termed the *cerebrocerebellum*, and the median vermis, which aligned by the intermediate hemispheres comprises the *spinocerebellum* (**Figure 51 A**) (Chambers and Sprague, 1955). As their names indicate, cerebrocerebellum and spinocerebellum receive input from the cerebral cortex and spinal cord, respectively. At the base of the cerebellum, adjacent to the brain stem, the *vestibulocerebellum*, comprising flocculus and nodulus, is located (**Figure 51 A**) (Voogd et al., 1996). The two structures are separated from the large cerebro- and spinocerebellum by the posterior fissure and constitute the flocculonodular lobe (Voogd et al., 1996). Moreover,

cerebro-, spino-, and vestibulocerebellum are further segmented into lobules, which, in the vermis, account for ten tightly folded areas (lobules I-X; **Figure 51 B**) (Larsell, 1952; 1958). Input and output signals of the cerebellum are integrated in the deep nuclei in the center of the cerebellum (Gould, 1979). These deep nuclei are subdivided into dentate nuclei, emboliform and globose nuclei, and fastigial nuclei, which are connected with the GABAergic Purkinje cells of the lateral hemispheres, the intermediate hemispheres, and the vermis, respectively (Gould, 1979). The somata of the Purkinje cells are organized in a defined layer within the cerebellar cortex. Their large dendrites together with basket and stellate cells in the molecular layer and the Golgi and granule cells in the granular layer form a complex signaling network (Palay and Chan-Palay, 1974; Ramón y Cajal et al., 1909).

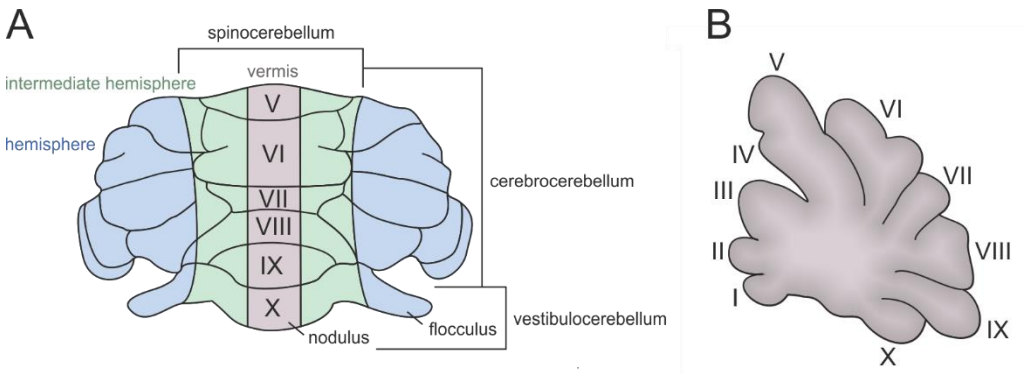

Figure 51: Morphology of the cerebellum. A) Illustration of the murine cerebellum with the median vermis (grey), the intermediate hemispheres (green), and the lateral hemispheres (blue). Vermis and intermediate hemispheres comprise the spinocerebellum, whereas the lateral hemispheres are termed cerebrocerebellum. The posterior vestibulocerebellum is subdivided into nodulus and flocculus. Cerebellar lobules V-X are indicated. **B)** Sagittal section of the vermis with the cerebellar lobules I-X.

Defects in any of the cells in the cerebellum could lead to impaired motor coordination, however, in ataxic mouse models, mainly the Purkinje cells are affected (Heckroth et al., 1989; Landis, 1973; Mullen et al., 1976; Norman et al., 1995). Nissl staining of WT and KO^{EU} cerebellum revealed that there is no morphological defect in the vermis and right hemisphere in P18 mice: their overall morphology of the distinct lobules was similar with no prominent atrophy of the cerebellum (**Figure 52 A**). The Purkinje cell layer, containing the cell bodies of the Purkinje cells, also did not show any overt differences in morphology. In adult KO^{EU} mice (11 weeks), gross cerebellar morphology also remained unaffected (**Figure 52 B**). Microscopic study of the Purkinje cells indicated similar shaped and aligned somata in WT and KO^{EU} (**Figure 52 B**: zoom-in regions).

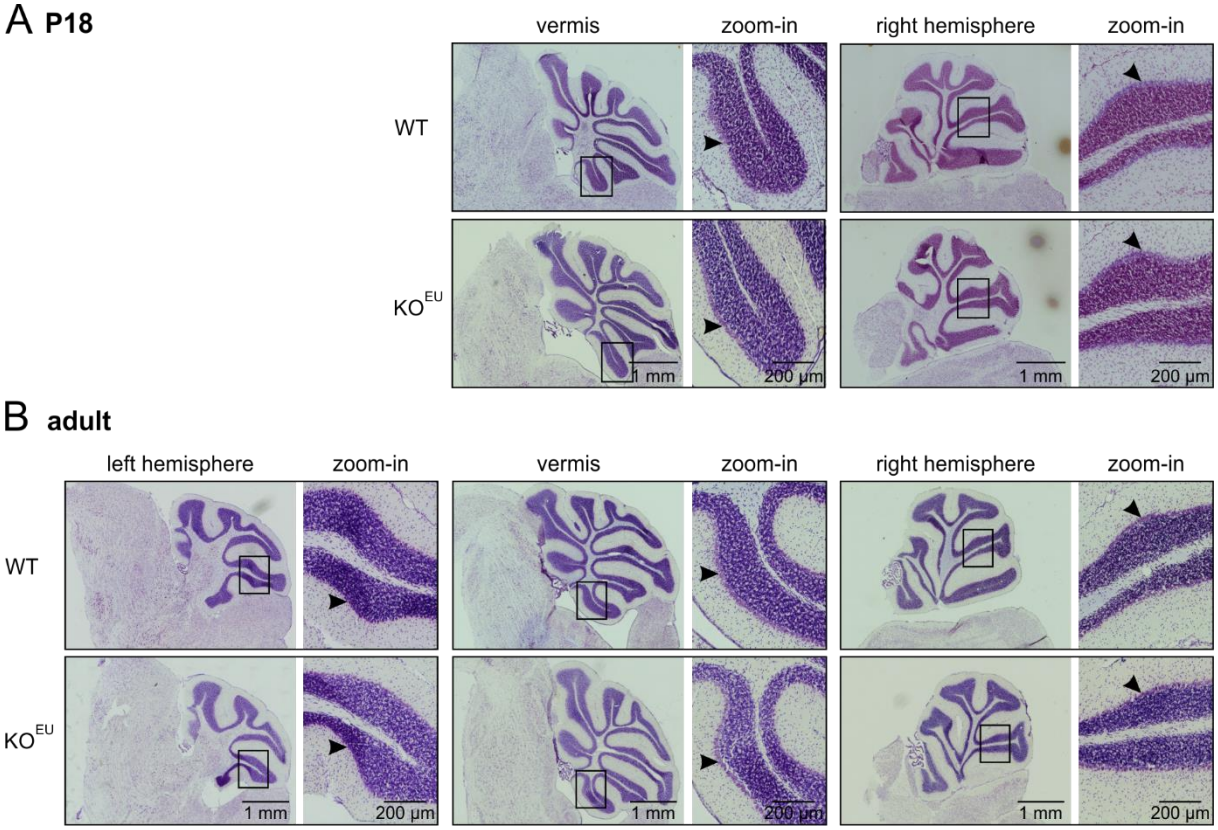

Figure 52: Histological analysis of the cerebellum of GBA2-knockout mice. The cerebellum of **A)** P18 and **B)** adult (11 weeks) wild-type (WT) and GBA2-knockout (KO^{EU}) cerebellum was stained with cresyl violet. Sagittal sections (16 µm) of the left hemisphere, vermis, and right hemisphere are depicted. Scale bars are indicated. Regions of interest were zoomed-in showing no changes in the Purkinje cell layer in KO^{EU} compared to WT mice.

3.8 Expression and activity of GBA2 in skeletal muscle

Not only the central nervous system, also the musculoskeletal system plays an important role in locomotion. Loss of GBA2 could also impair motor function on a muscular level. A prerequisite is that GBA2 is expressed in this tissue. I first performed a Western blot analysis of skeletal muscle from WT and KO mice. Detergent-based (total) lysis with 1% TritonX-100 yielded slightly higher GBA2 levels compared to a physical disruption (sonication) in hypotonic (hypo) buffer without detergent (compare 65 µg protein load for hypotonic and total lysis; **Figure 53 A**). To ensure that low GBA2 expression levels are not due to insufficient cell lysis or protein extraction, I confirmed the presence of the muscle-specific protein desmin. Overall, GBA2 is expressed in the skeletal muscle only at low levels in WT and completely absent in the KO (**Figure 53 A**). A β-glucosidase activity assay indicated that GBA2 activity is solely present in WT skeletal muscle and completely absent in the KO/KO^{EU} (**Figure 53 B**). GBA1 activity was unaffected by the loss of GBA2 similar to my findings in brain and spinal cord (**Figure 53 B**; see also **Figure 42 B** and **Figure 46 B**).

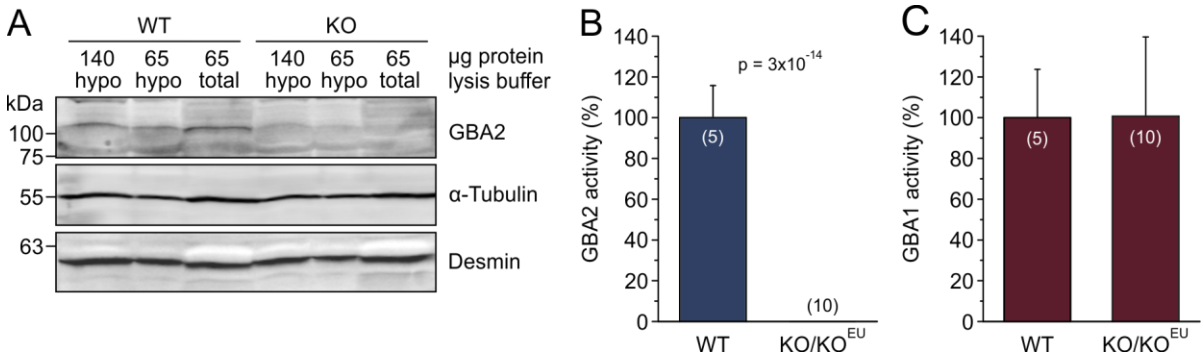

Figure 53: GBA2 expression and activity in skeletal muscle of wild-type and global GBA2-knockout mice. A) Western blot analysis of GBA2 in lysates of skeletal muscle from an adult wild-type (WT; 35 weeks) and global GBA2-knockout (KO; 36 weeks) mouse. The tissue was homogenized either in hypotonic buffer (hypo; 10 mM HEPES, 0.5 mM EDTA) or total lysis buffer (total; 10 mM Tris/HCl pH 7.6, 140 mM NaCl, 1 mM EDTA, 1% (v/v) TritonX-100) and different protein amounts were loaded (140 µg or 65 µg). GBA2 was stained using a GBA2-specific antibody. α-Tubulin served as a loading control. Desmin was used as a control to validate that the muscle extraction and lysis worked properly. Modified from Woeste, Master thesis, 2015. **B)** GBA2 and **C)** GBA1 activity in hypotonic lysates of skeletal muscle from adult (51 ± 13 weeks) wild-type (WT) and global GBA2-knockout (KO, KO^{EU}) mice. Columns represent mean values + SD. Statistical analysis was performed using one-sample t-test (n numbers and p values are indicated).

Ablating GBA2 specifically in skeletal muscle, will reveal whether the loss of GBA2 in skeletal muscle impairs motor function. Thus, I analyzed the expression and activity of GBA2 in skeletal muscle of WT and KO^{Myf} mice. Expression of Cre recombinase under the control of Myf5, a transcriptional activator involved in myogenesis and muscle differentiation (Braun et al., 1989; Braun et al., 1990), allows skeletal-muscle specific gene deletion (see also 3.6). GBA2 expression levels in skeletal muscle were not detectable using GBA2-specific antibodies (**Figure 54**).

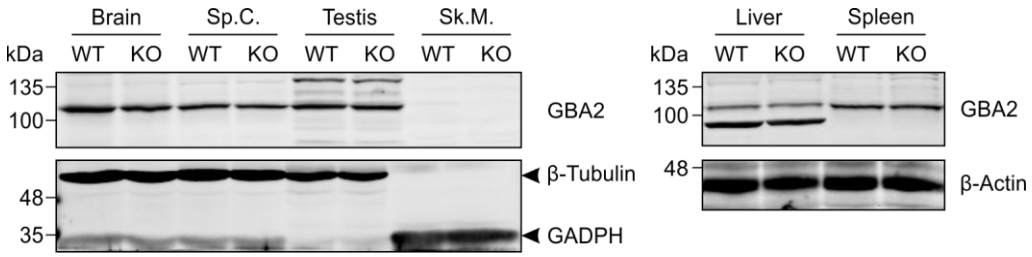

Figure 54: GBA2 expression in different tissues of wild-type and muscle-specific GBA2-knockout mice. Western blot analysis of GBA2 in hypotonic lysates of brain, spinal cord (Sp.C.), testis, skeletal muscle (Sk.M.), liver, and spleen from an adult (18 weeks) wild-type (WT) and muscle-specific GBA2-knockout (KO^{Myf}) mouse. GBA2 was detected using a GBA2-specific antibody. GADPH, β-Tubulin, and β-Actin served as a loading control. 60 µg protein was loaded per lane.

Thus, I tested whether I can distinguish WT and KO mice using the β-glucosidase activity assay. Compared to other tissues, GBA2 activity was low in the skeletal muscle with 0.17 ± 0.09 rfu/min (**Figure 55 A, B**). However, GBA2 activity was decreased in skeletal muscle of KO^{Myf} mice (0.05 ± 0.05 rfu/min), whereas the activity was unaltered in WT and KO^{Myf} brain (8.03 ± 1.95 rfu/min *versus* 8.77 ± 4.01 rfu/min), spinal cord (4.66 ± 1.26 rfu/min *versus* 3.65 ± 0.89 rfu/min), testis (5.89 ± 2.32 rfu/min *versus* 5.68 ± 2.36 rfu/min), liver (1.48 ± 0.65 rfu/min

versus 1.43 ± 0.70 rfu/min), and spleen (1.51 ± 0.76 rfu/min *versus* 1.74 ± 0.96 rfu/min) (**Figure 55 A, B**). Also, GBA1 activity remained unchanged in skeletal muscle from KO^{Myf} mice (**Figure 55 C, D**; WT: 0.27 ± 0.03 rfu/min *versus* KO^{Myf}: 0.30 ± 0.03 rfu/min). Altogether, regarding the low activity levels determined in skeletal muscle, both GBA1 and GBA2 might not play a major role in this tissue.

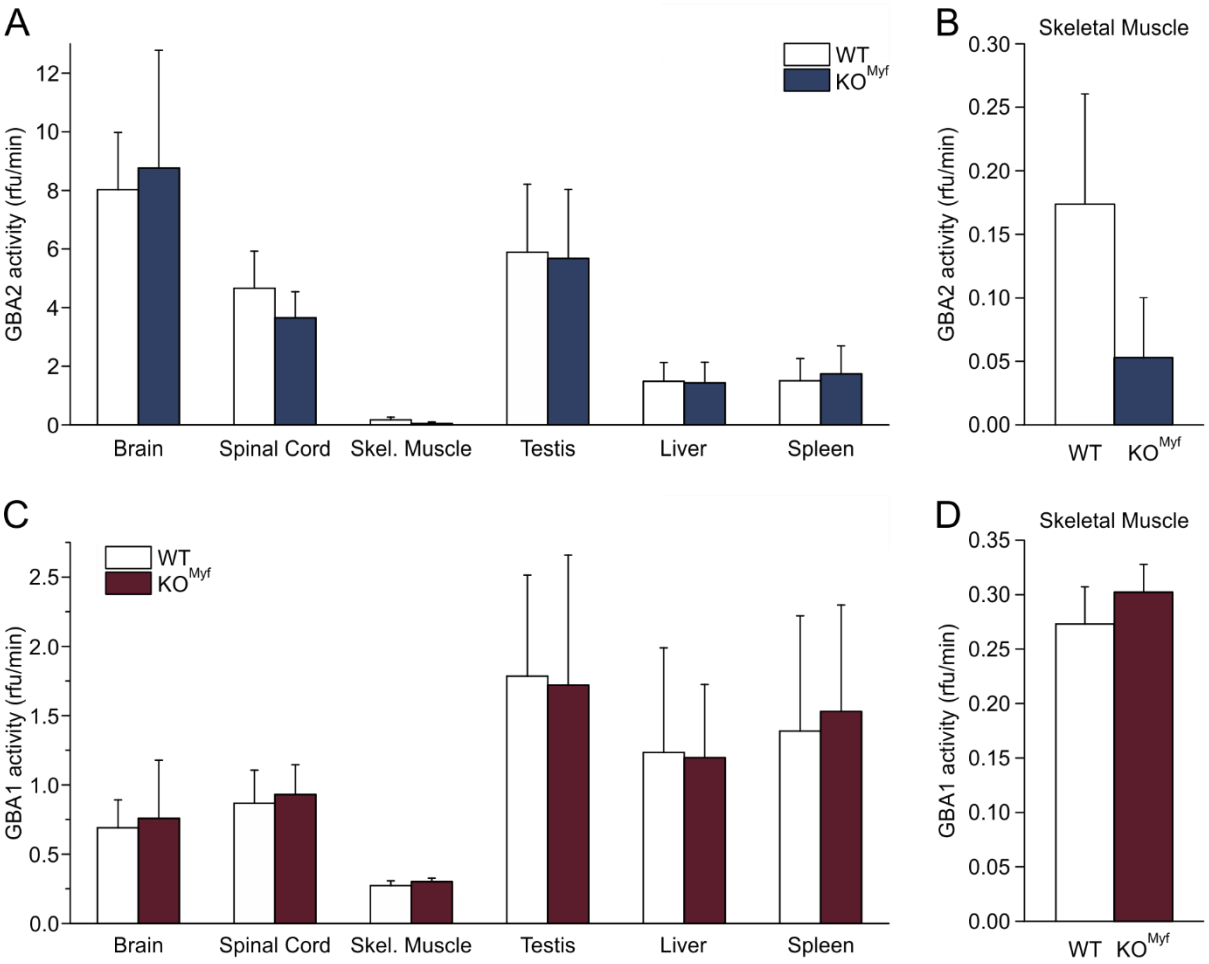

Figure 55: GBA2 and GBA1 activity in different tissues of wild-type and muscle-specific GBA2-knockout mice. Analysis of **A)** GBA2 and **C)** GBA1 activity in hypotonic lysates of brain, spinal cord, skeletal muscle (Skel. Muscle), testis, liver, and spleen from adult (23 ± 6 weeks) wild-type (WT) and muscle-specific GBA2-knockout (KO^{Myf}). 12.55 ± 2.19 µg protein was used in the β-glucosidase activity assay. **B)** and **D)** show activities in the skeletal muscle separately. Columns represent mean values + SD. Statistical analysis was performed using one-way-ANOVA. n = 3 for all tissues besides testis and spleen (n = 2). rfu/min: relative fluorescence units per minute.

3.9 GlcCer accumulates in the cerebellum in GBA2-KO mice

Loss of GBA2 leads to an accumulation of GlcCer (Raju et al., 2015; Yildiz et al., 2006). Testis and sperm from KO mice displayed increased levels of C18, C20, C22, and C24 GlcCer (Raju et al., 2015). In collaboration with the lab of Prof. Dr. Peter Dörmann (IMBIO, Bonn), we performed mass spectrometry and measured the content of neutral total and main lipid species in the cerebellum of WT and KO mice lysed in hypotonic buffer. Furthermore, we determined ganglioside levels using thin layer chromatography (TLC; experiments performed in the lab of

Prof. Dr. Roger Sandhoff, DKFZ, Heidelberg). Since GlcCer accumulation potentially increases with age, lipidomic analysis in the cerebellum of early postnatal (P10) and adult mice (10-13 weeks) was performed.

In the cerebellum of P10 mice, the total lipid content of ceramide (Cer), hexosylceramides (HexCer), sphingomyelin (SM), and long-chain bases (LCBs) was not different in WT and KO mice (**Figure 56 A**). However, detailed analysis of the most abundant HexCer species demonstrated that C18 GlcCer were highly increased in the KO cerebellum (WT: 0.23 ± 0.08 ng/mg protein *versus* KO: 0.40 ± 0.05 ng/mg protein; **Figure 56 B**).

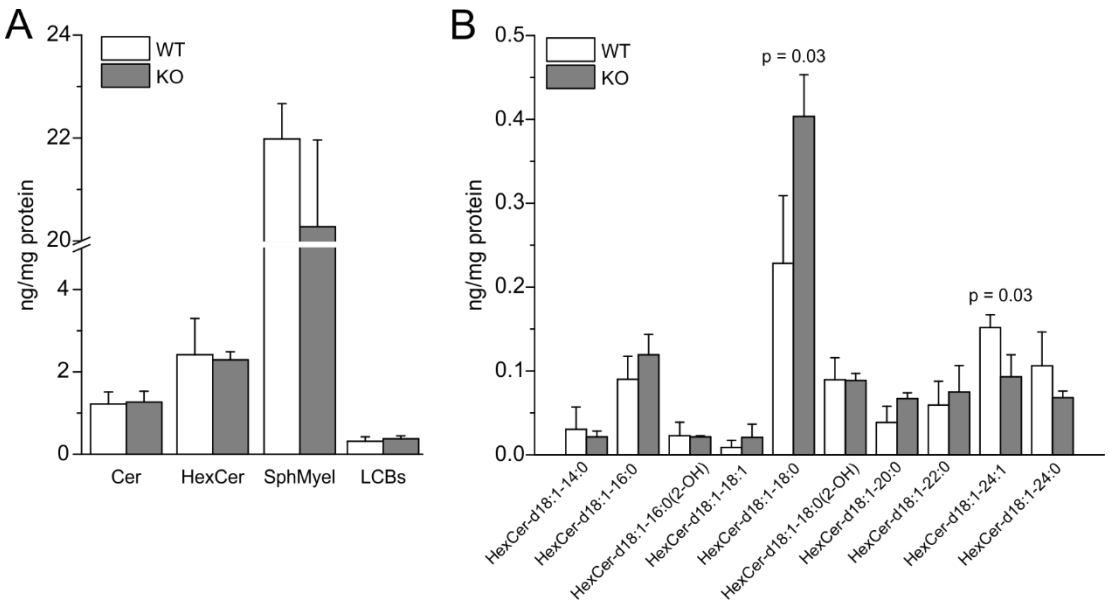

Figure 56: Mass spectrometry of lipid species in cerebellum of P10 wild-type and global GBA2-knockout mice. A) Quantitative analysis of neutral sphingolipids in the cerebellum of P10 wild-type (WT) and global GBA2-knockout (KO) mice. Hypotonic lysates of the cerebellum were prepared and ceramides (Cer), hexosylceramides (HexCer), sphingomyelin (SphMyel), and long-chain bases (LCBs) were studied (ng/mg protein). **B)** Quantitative analysis of the most abundant HexCer, classified according to their acyl chain-length, in the cerebellum of P10 wild-type (WT) and GBA2-knockout (KO) mice. Columns represent mean values + SD (n = 3). Statistical analysis was performed using one-way ANOVA (p values are indicated).

Thin layer chromatography revealed only a slight increase in GM3, GD3, GD1b, and GT1b in KO cerebellum (**Figure 57 C**). GM2 and fucosylated GM1a (fucGM1a) was barely detectable in any of the samples. Thus, mainly GlcCer accumulates in the cerebellum in GBA2-KO mice, whereas complex glycosphingolipids are barely affected.

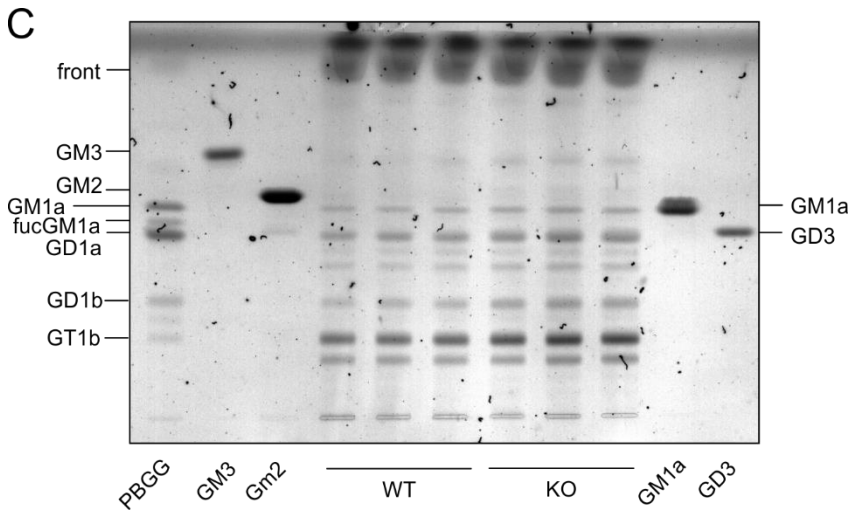

Figure 57: Thin layer chromatography (TLC) of lipid species in cerebellum of adult wild-type and global GBA2-knockout mice. TLC of gangliosides derived from GlcCer in cerebellum from adult (10-13 weeks) wild-type (WT) and global GBA2-knockout (KO) mice**.** 1 mg protein was loaded per lane. Acidic lipids isolated from hypotonic lysates of the cerebellum were separated by HP-TLC with the solvent chloroform:methanol:0.2% aqueous $CaCl_2$ (45:45:10) and stained for glycolipids with orcinol reagent. Control samples included porcine brain gangliosides (PBGG), and the gangliosides GM3, GM2, GM1a, and GD3. fucGM1a: Fucosyl-GM1a.

3.10 Analysis of small Rho GTPases

In previous studies, we could show that GlcCer accumulation alters the stacking of the plasma membrane (Raju et al., 2015) and dynamics of the actin cytoskeleton. We hypothesized that this is due to changes in the activity of small Rho GTPases. Filopodia formation is controlled by the Rho GTPases Cdc42, whereas lamellipodia formation is controlled by Rac1 (Hall, 1998; Nobes and Hall, 1995; Ridley et al., 1992). Cdc42 and Rac1 are active in a GTP-bound state at the plasma membrane (Boivin and Beliveau, 1995; Fleming et al., 1996). Changing the lipid homeostasis, resulting in an altered lipid composition of the membrane might affect their recruitment to the plasma membrane and, thereby, their activity. Thus, we performed a Rho GTPase activity assay to determine the activity of Cdc42 and Rac1 in lysates of wild-type WT WT and KO murine dermal fibroblasts. In fact, levels of active Rac1 were significantly increased in KO compared to WT cells (**Figure 58 A**).

Small Rho GTPases have been proposed to be associated with detergent-resistant membranes (Moissoglu and Schwartz, 2014), rich in glycopshingolipids and cholesterol (Hooper, 1999). Accumulation of GlcCer might affect localization of Rac1 and Cdc42 in these membrane domains. We isolated detergent-resistant membrane (DRM) fractions from murine dermal fibroblasts of WT and KO mice by ultracentrifugation in a density gradient (Dr. Diana N. Raju, unpublished data). Detergent-resistant membrane (top) fractions are rich in caveolin-1, a membrane protein, which can bind cholesterol, whereas the ER protein calnexin is enriched in detergent-sensitive (bottom) membranes. Indeed, Rac1 localization was shifted to the DRM fraction in KO compared to WT fibroblasts (**Figure 58 B**).

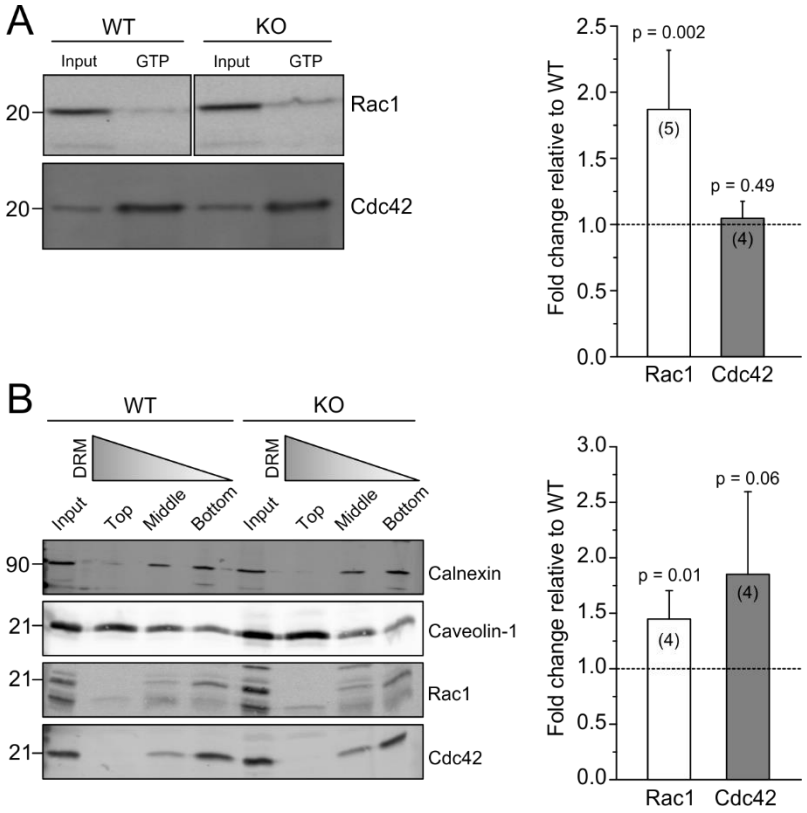

Figure 58: Analysis of small Rho GTPases in dermal fibroblasts of wild-type and global GBA2-knockout mice. A) Activity of the Rho GTPases Rac1 and Cdc42 in wild-type (WT) and global GBA2-knockout (KO) murine dermal fibroblasts. Left: Active, GTP-bound Rac1 and Cdc42 was affinity purified using GST-tagged PAK-PBD protein and subjected to Western blot analysis; 10 µg cell lysate was loaded as input. Right: Quantification of activated Rac1 and Cdc42 in KO fibroblasts. Rac1-GTP and Cdc42-GTP expression was normalized to the input and expressed as fold change relative to WT. **B)** Western blot analysis of Rac1 and Cdc42 at detergent-resistant membranes (DRM; represented in grey triangle). Left: DRM were isolated from wild-type (WT) and global GBA2-knockout (KO) fibroblasts by ultracentrifugation in a density gradient. Rac1 and Cdc-42 in top, middle, and bottom fractions were detected using a Rac1- and Cdc42-specific antibody, respectively. Calnexin and caveolin-1 served as a non-DRM and DRM marker, respectively. Right: Rac1 and Cdc42 expression in the middle fraction was normalized to the input and represented as fold change relative to WT. Columns represent mean values + SD. Statistical analysis was performed using one-way ANOVA (n numbers and p values are indicated). Experiments were performed by Dr. Diana N. Raju (unpublished data).

To test whether loss of GBA2 in neurons also changes the activity of Rac1, I performed initial experiments to establish a protocol for DRM isolation from cerebellum and spinal cord lysates. Separation of detergent-resistant and detergent-sensitive membranes, following the protocol previously used for fibroblasts, could also be applied to cerebellum and spinal cord. Western blot analysis with different protein amounts loaded as input and the different DRM fractions was performed: The ER-marker calnexin was present at high levels in the detergent-sensitive membrane fraction, but completely absent in the detergent-resistant membrane fraction (**Figure 59**). In contrast, caveolin-1 was detected at high levels in the detergent-resistant membrane fraction in spinal cord lysates (**Figure 59**). However, no caveolin-1 was present in the membrane fractions isolated from the cerebellum. Thus, DRM isolation from the cerebellum needs to be further optimized. However, Cdc42 and Rac1 were found in the detergent-sensitive membrane fraction of both tissues (**Figure 59**). Based on these experiments, future studies

can be performed to determine the levels of Rac1 and Cdc42 in the cerebellum and spinal cord of WT and KO mice.

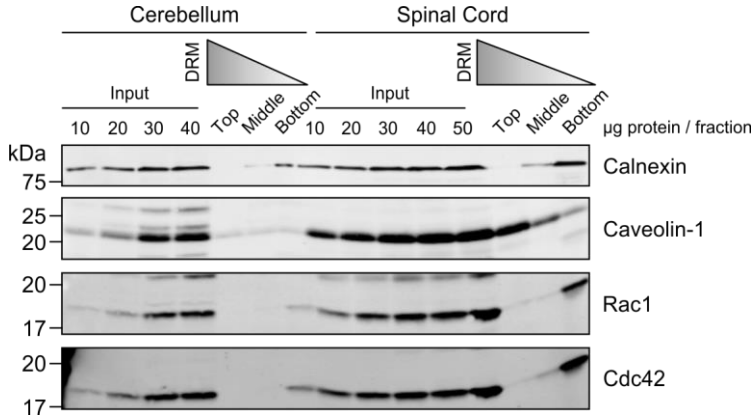

Figure 59: Analysis of small Rho GTPases in murine cerebellum and spinal cord. Western blot analysis of Rac1 and Cdc42 at detergent-resistant membranes (DRM; represented in grey triangle). DRM were isolated from cerebellum and spinal cord of P7 and adult (32 weeks) wild-type mice, respectively, by ultracentrifugation in a density gradient. Rac1 and Cdc-42 in top, middle, and bottom fractions were detected using a Rac1- and Cdc42-specific antibody. Calnexin and caveolin-1 served as a non-DRM and DRM marker, respectively. 10-50 µg protein was loaded per lane. 15 µl of the top, middle, and bottom fractions was loaded per lane.

3.11 Pharmacological inhibition of GBA2 by iminosugars

Most commercially available blockers for α- and β-glucosidases are derivatives of nojirimycin (NJ), an iminosugar with structural similarity to D-glucose, which competes with the enzyme's natural substrate for binding (Asano, 2003). These iminosugars lack an O-glycosidic bond that is attacked by the glucosidases, but rather contain an endocyclic nitrogen (Paulsen and Todt, 1968). *N*-butyl-deoxynojirimycin (NB-DNJ) is used as an inhibitor for GBA2 (**Figure 60**, **2**) and has also been established in our β-glucosidase activity assay (Körschen et al., 2013). The IC_{50} values in this assay for NB-DNJ are 20.9 ± 1.3 nM, 18.2 ± 0.3 nM, and 19.2 ± 0.4 nM in hypotonic lysates of murine liver, brain, and testis, respectively (Körschen et al., 2013). However, NB-DNJ also inhibits the glucosylceramide synthase (IC_{50}: ~50 µM; *in vitro*) and is used for the treatment of Gaucher type 1 patients (Miglustat®, Zavesca) to ameliorate GlcCer accumulation (Aerts et al., 2006; Platt et al., 1994).

A more specific blocker for GBA2 is AMP-DNM (**Figure 60**, **3**), which inhibits GBA2 in the nanomolar range (IC_{50}: 0.3-1.7 nM; *in vitro*) and has a lower affinity for GBA1 and GlcCer synthase, indicated by an IC_{50} of 200 µM (*in vitro*) and 25 nM (*in vitro*)/150 µM (*in vivo*), respectively (Overkleeft et al., 1998; Wennekes et al., 2010). Moreover, AMP-DNM has been successfully used *in vivo* in mice and rats and decreased GlcCer levels in various tissues (Aerts et al., 2007; Wennekes et al., 2010).

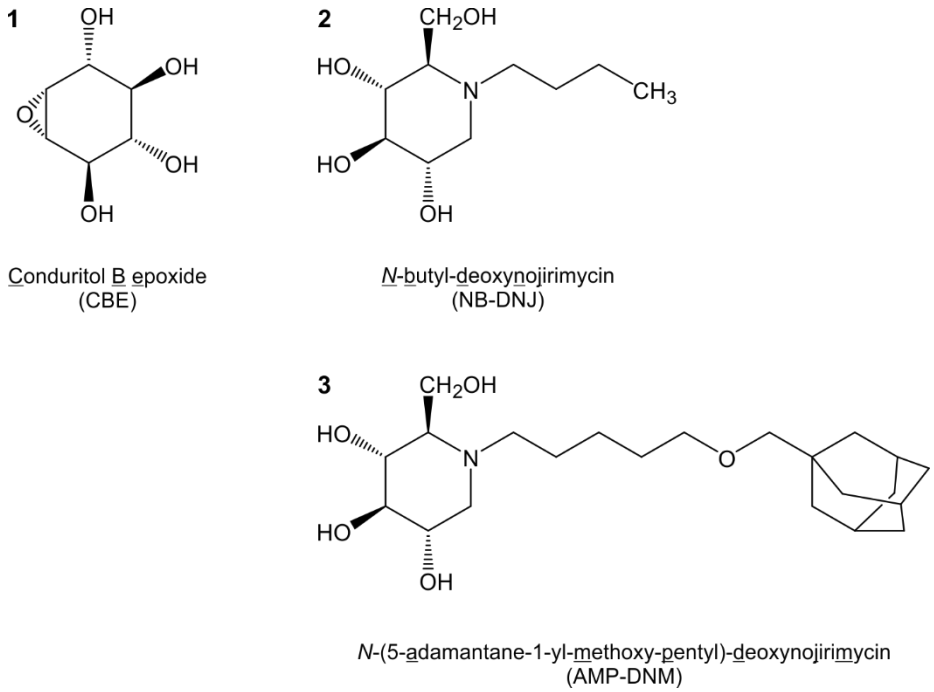

Figure 60: Iminosugar-based inhibitors of β-glucosidases. Structures of **1)** the GBA1 inihibitor conduritol B epoxide (CBE) and the GBA2 inhibitors **2)** *N*-butyldeoxynojirimycin (NB-DNJ) and **3)** *N*-(5-adamantane-1-yl-methoxy-pentyl)-deoxynojirimycin (AMP-DNM).

3.11.1 Dose-response relationship of AMP-DNM and GBA2

To apply AMP-DNM in my experiments, I first determined at which AMP-DNM concentration GBA2, but not GBA1, is inhibited. I performed the β-glucosidase activity assay at different AMP-DNM concentrations and monitored GBA1 and GBA2 activity at pH 4 and pH 6, respectively. The following tissues and cell types were used: 1.) GBA2 expressed in bacteria, 2.) murine dermal fibroblasts, 3.) murine brain lysates, and 4.) murine cerebellar neurons.

E.coli of the BL21 Codon Plus (DE3) RIPL strain were transformed with the plasmid pET21 mGBA2-His and the protein expression was induced by addition of 1 mM IPTG at an OD_{600} of 0.5 (see 2.11.5.2). Expression was performed for 3 h at 37°C. Cells were pelleted and lysed in hypotonic buffer upon sonication, and subjected to a β-glucosidase activity assay, testing different concentrations from 0.0083 pM up to 25 µM of AMP-DNM. After induction of protein expression, GBA2 but not GBA1 activity was detected (**Figure 61 A**). For the dose-response analysis, GBA2 activity was defined as the NB-DNJ-blockable activity at pH 6 (**Figure 13**). I measured GBA2 activity at different AMP-DNM concentrations and determined an IC_{50} of 1.73 ± 0.46 pM, which is even lower than the IC_{50} of 0.3-1.7 nM determined in previous studies (Overkleeft et al., 1998).

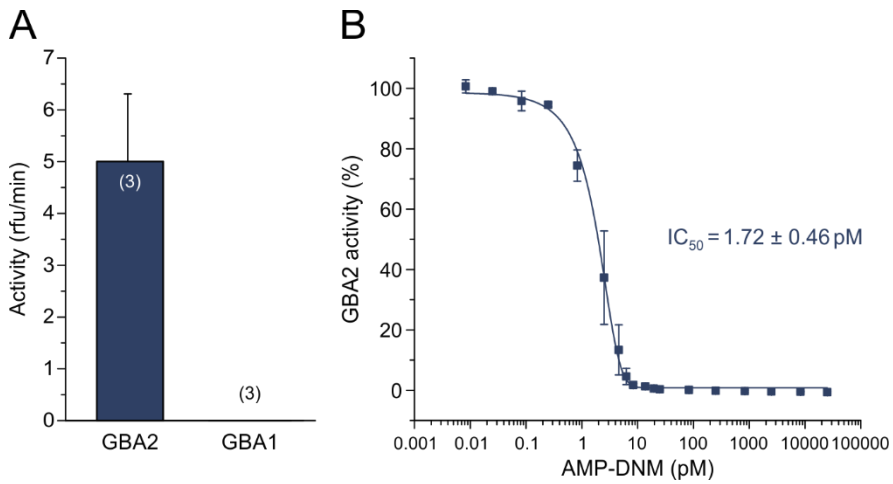

Figure 61: Dose-response relationship of recombinant GBA2 to AMP-DNM. A) Activity of GBA2 and GBA1 in hypotonic lysates of *E.coli* showing no endogenous GBA1 activity, but overexpression of GBA2 after transformation with the pET21 mGBA2-His plasmid and induction of the expression using Isopropyl-β-D-thiogalactopyranoside (IPTG). Column represent mean values + SD. Statistical analysis was performed using one-way ANOVA (n numbers are indicated). rfu/min: relative fluorescent units per minute. **B)** Dose-response relationship of recombinant GBA2 in hypotonic bacterial lysates to AMP-DNM. Data was normalized to a non-treated control and plotted as an average of three independent experiments ± SD. The IC_{50} (1.72 ± 0.46 pM) was determined using sigmoidal curve fitting in Origin Pro.

Similarly, I performed experiments using hypotonic protein lysates from murine dermal fibroblasts to determine the effect of AMP-DNM on the endogenous GBA2 and GBA1 activity. The total GBA1 activity in WT cells was higher than the GBA2 activity (**Figure 62 A, B**). KO cells displayed residual activity at pH 6, which was not inhibited by NB-DNJ (**Figure 62 A**), which is supposed to be residual GBA1 activity at pH 6. At pH 4, only GBA1 activity was detected (**Figure 62 B**).

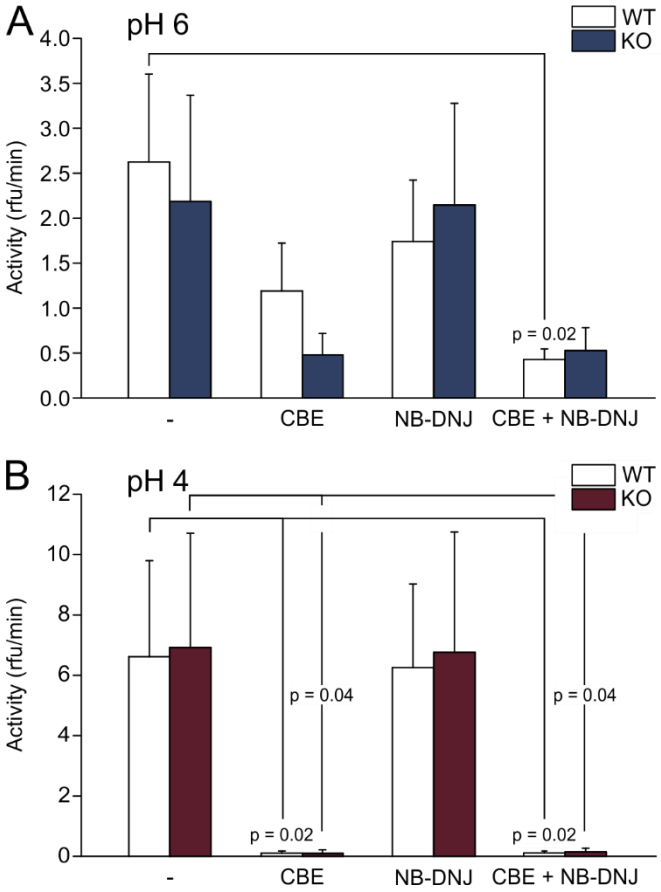

Figure 62: β-Glucosidase activities at pH 6 and pH 4 in murine dermal fibroblasts. Analysis of the β-glucosidase activity in hypotonic lysates of adult (26 ± 7 weeks) wild-type (WT) and GBA2-knockout (KO) murine dermal fibroblasts at **A)** pH 6 and **B)** pH 4 in the absence (-) or presence of CBE and/or NB-DNJ. 8.59 ± 0.36 µg total protein was used in the assays. Columns represent mean values + SD. Statistical analysis was performed using one-way ANOVA (n = 3). rfu/min: relative fluorescent units per minute.

The dose-response curve for AMP-DNM at pH 6 exhibited a biphasic shape (**Figure 63 A**). Most likely, the first phase of inhibition at low picomolar concentrations of AMP-DNM refers to inhibition of GBA2 activity (see also **Figure 61**), whereas the second phase at higher AMP-DNJ concentrations is most likely inhibition of GBA1 activity at pH 6 (**Figure 63 A**). Plotting the data for the AMP-DNM concentrations from 0.0083 pM to 4.58 pM shows that GBA2 is inhibited by lower inhibitor concentrations that do not affect GBA1 activity (**Figure 63 B**). However, IC_{50} values could not be determined from this data.

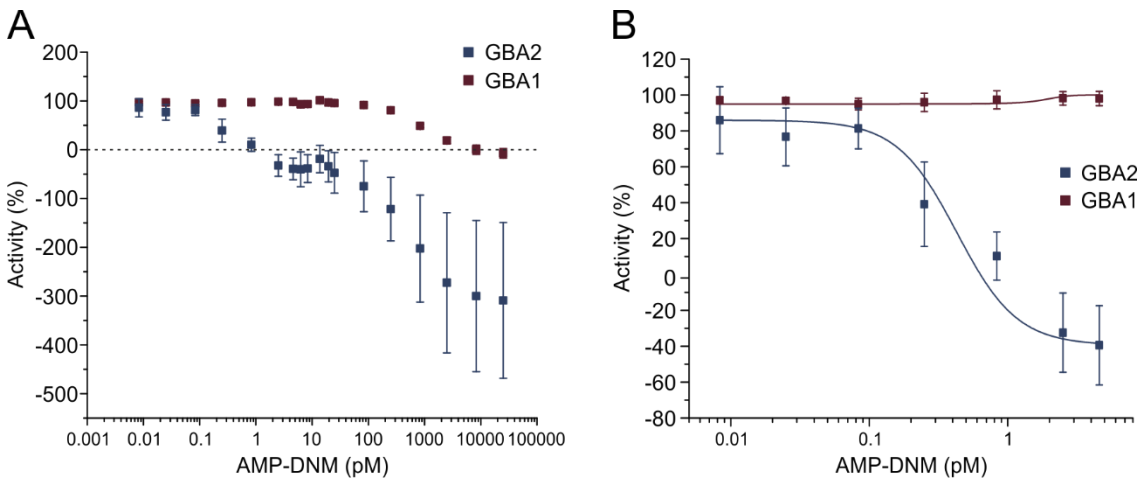

Figure 63: Dose-response relationship of GBA2 and GBA1 in murine dermal fibroblasts to AMP-DNM. A) Dose-response relationship of GBA2 and GBA1 in hypotonic lysates of adult (27 ± 2 weeks) wild-type murine dermal fibroblasts to AMP-DNM. Data was normalized to a non-treated control and plotted as an average of three independent experiments ± SD. **B)** First 7 data points including 0.0083 pM to 4.58 pM AMP-DNM from **A)** plotted, showing that AMP-DNM inhibits GBA2 in the low picomolar range, whereas GBA1 activity is unaffected at these concentrations.

In hypotonic lysates of murine brain, residual activities of GBA2 at pH 4 and GBA1 at pH 6 are rather low, and the enzymatic activities are clearly distinguishable. Also in brain lysates, GBA2 activity was inhibited at low picomolar AMP-DNM concentrations (IC_{50}: 4.78 ± 0.40 pM; **Figure 64**), whereas GBA1 was inhibited at higher AMP-DNM concentrations of about 100 pM (**Figure 64**).

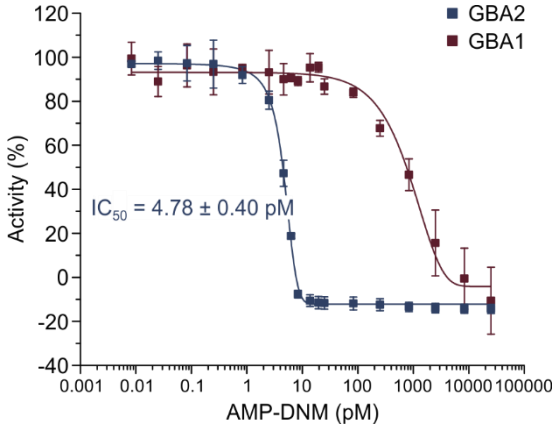

Figure 64: Dose-response relationship of GBA2 and GBA1 in murine brain to AMP-DNM. Dose-response relationship of GBA2 and GBA1 in hypotonic brain lysates from adult (37 ± 6 weeks) wild-type mice to AMP-DNM. Data was normalized to a non-treated control and plotted as an average of three independent experiments ± SD. The IC_{50} of 4.78 ± 0.40 pM (GBA2) was determined using sigmoidal curve fitting in Origin Pro. The IC_{50} for GBA1 could not be determined due to lacking data points at higher AMP-DNM concentrations.

I validated whether 25 pM AMP-DNM inhibits GBA2 activity in protein lysates from cerebellar neurons (in collaboration with Prof. Dr. Frank Bradke; Dr. Sina Stern, DZNE, Bonn). Indeed, 25 pM AMP-DNM abolished GBA2 activity without affecting GBA1 activity (**Figure 65 A, B**). Next, isolated cerebellar neurons were treated with 30 pM AMP-DNM for 48 h and the effect

on GBA2 and GBA1 activity was determined. Also under these conditions, GBA2 activity was significantly diminished (p = 0.005; **Figure 65 C**), whereas GBA1 activity remained unchanged (**Figure 65 D**). Thus, a AMP-DNM concentration of 25 pM to 30 pM was used in subsequent experiments.

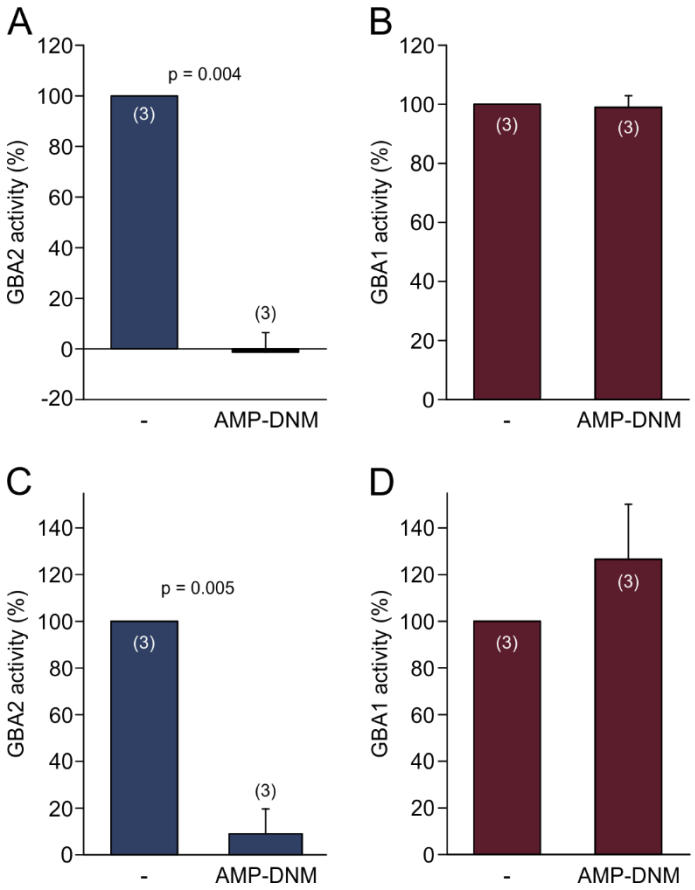

Figure 65: Inhibition of GBA2 activity by AMP-DNM in cerebellar neurons. Analysis of the **A)** GBA2 activity and **B)** GBA1 activity in hypotonic lysates of cerebellar neurons in the absence (-) and presence of 25 pM AMP-DNM. Analysis of the **C)** GBA2 activity and **D)** GBA1 activity in cultured cerebellar neurons left untreated (-) or treated with 30 pM AMP-DNM for 48 h. Cerebellar neurons were isolated at P7-8 from wild-type mice by Dr. Sina Stern, DZNE (Bonn). Columns represent mean values + SD. Statistical analysis was performed using one-sample t-test (n numbers and p values are indicated).

3.12 Loss of GBA2 affects cytoskeletal dynamics

Previous studies in our lab showed that the loss of GBA2 causes accumulation of GlcCer, which in turn alters the cytoskeletal dynamics (Raju et al., 2015). This was true for both sperm cells and mouse dermal fibroblasts. When fibroblasts were seeded on CYTOO chips that force cells to grow on a certain shape, KO fibroblasts failed to follow this shape and exhibited extended actin protrusions, namely filopodia and lamellipodia (**Figure 66 A**). Both the number of cells, which developed filopodia and lamellipodia, as well as the average number of lamellipodia per cell was significantly increased in KO fibroblasts (**Figure 66 B, C**).

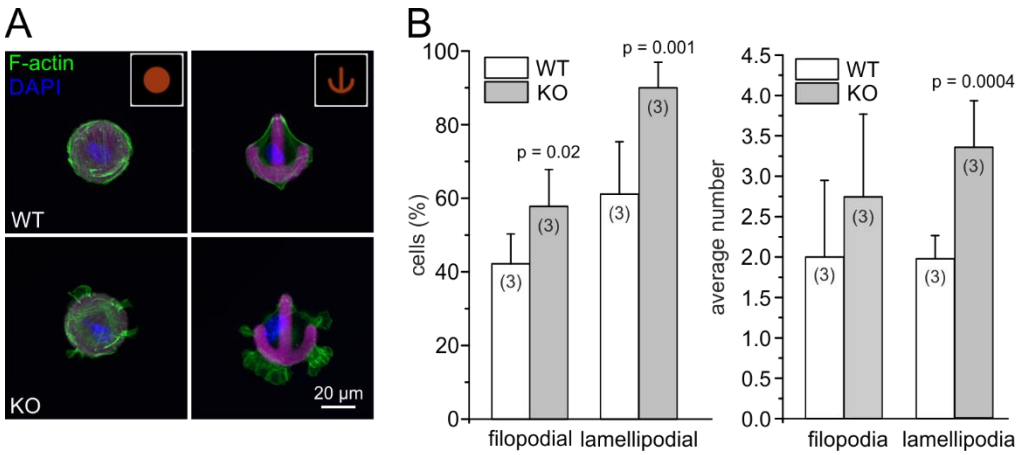

Figure 66: Analysis of the actin cytoskeleton in murine dermal fibroblasts of global GBA2-knockout. A) Representative images of adult wild-type (WT) and global GBA2-knockout (KO) murine dermal fibroblasts that were seeded on CYTOO chips with fluorescently-labeled fibronectin patterns (purple). F-actin and nuclei were stained using Alexa Fluor Phalloidin 488 (green) and DAPI (blue), respectively. Scale bar is indicated. **B)** Quantitative analysis of the F-actin structures stained in **(A)**. The number of cells containing filopodia and lamellipodia (left) and the average number of filopodia and lamellipodia per cell (right) were determined. Column represent mean values + SD. Statistical analysis was performed using one-way ANOVA (n numbers and p values are indicated). Modified from Raju et al., 2015.

3.13 Neurite outgrowth of cerebellar neurons

Neurite outgrowth highly depends on cytoskeletal dynamics (Buck and Zheng, 2002; Dent and Gertler, 2003; Letourneau et al., 1987). Thus, we wondered whether loss of GBA2 also affects the cytoskeleton in these cells. Martin and colleagues could show that genetic ablation of the GBA2 orthologue in zebrafish leads to impaired motor neuron outgrowth (Martin et al., 2013). Loss of GBA2 might therefore affect neurite outgrowth, leading to defects in motor coordination. Thus, we set out to study neurite outgrowth in cerebellar neurons that lack GBA2 activity.

3.13.1 Pharmacological blocking of GBA2

In a first set of experiments, we treated WT cerebellar neurons with either 5 µM NB-DNJ or 30 pM AMP-DNM, which completely blocks GBA2 activity, but has not effect on GBA1 (see **Figure 65**). In collaboration with the lab of Prof. Dr. Frank Bradke, we studied the actin cytoskeleton in these cells using Rhodamine-conjugated Phalloidin (experiments performed by Dr. Sina Stern; **Figure 67 A, B**). Neurite length was significantly reduced when GBA2 was blocked by either NB-DNJ or AMP-DNM (**Figure 67 C, D**). Compared to control cells, NB-DNJ-treated cells were 22.48 ± 14.41 % shorter than control neurons, and AMP-DNM-treated neurons were even shorter with 45.80 ± 8.02 % than control cells.

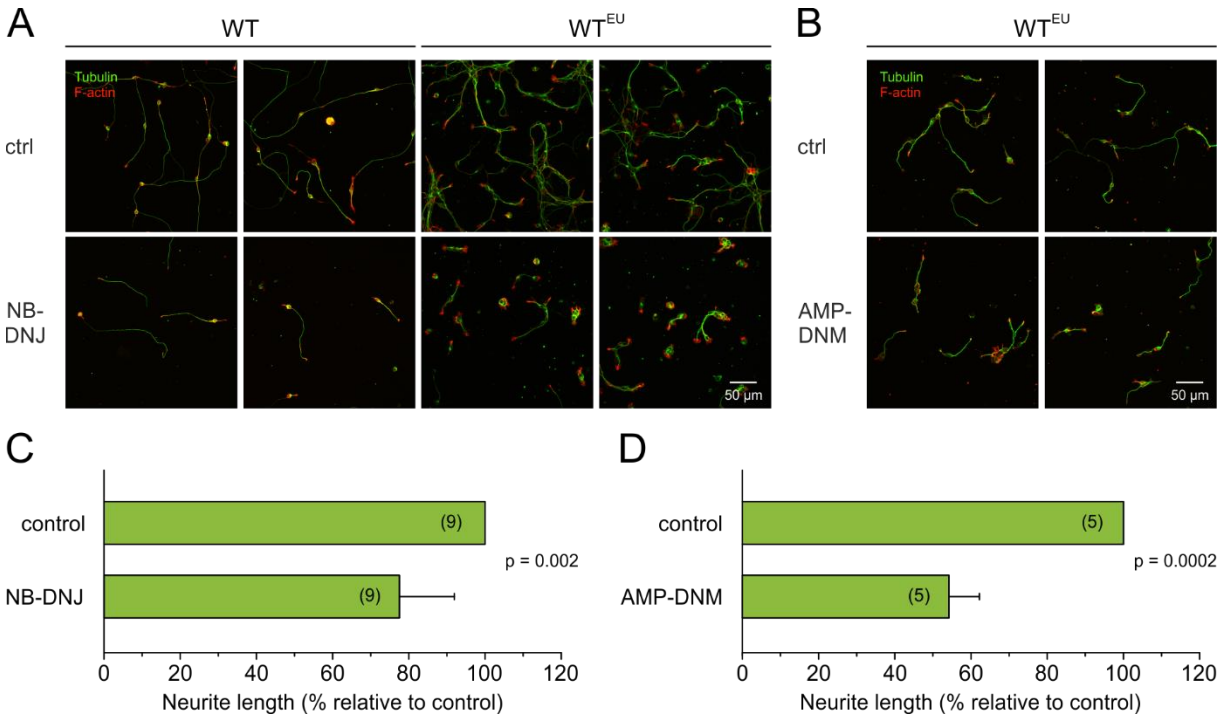

Figure 67: Neurite outgrowth is diminished upon GBA2 inhibition. Representative images of **A)** P7-9 wild-type (WT, WT^{EU}) cerebellar neurons left untreated (ctrl) or treated with 5 µM NB-DNJ for 48 h, **B)** P6 wild-type (WT^{EU}) cerebellar neurons left untreated (control) or treated with 30 pM AMP-DNM for 48 h and stained for microtubules and F-actin using an anti-neuronal β-Tubulin antibody and Rhodamine-conjugated Phalloidin, respectively. Quantitative analysis of the neurite length of **C)** NB-DNJ-treated wild-type (WT, WT^{EU}) cerebellar neurons as depicted in **(A)** and **D)** AMP-DNM-treated wild-type (WT^{EU}) cerebellar neurons as depicted in **(B)** compared to the untreated neurons (control). Columns represent mean values + SD. Statistical analysis was performed using one-sample t-test (n numbers and p values are indicated). Experiments were performed by Dr. Sina Stern.

3.13.2 Genetic ablation of GBA2

Similar experiments were performed using neurons isolated from the cerebellum of WT and KO mice from the two different global GBA2-KO lines. However, in both KO and KO^{EU} cerebellar neurons, no difference in neurite length was observed compared to WT controls (**Figure 68 A, B**).

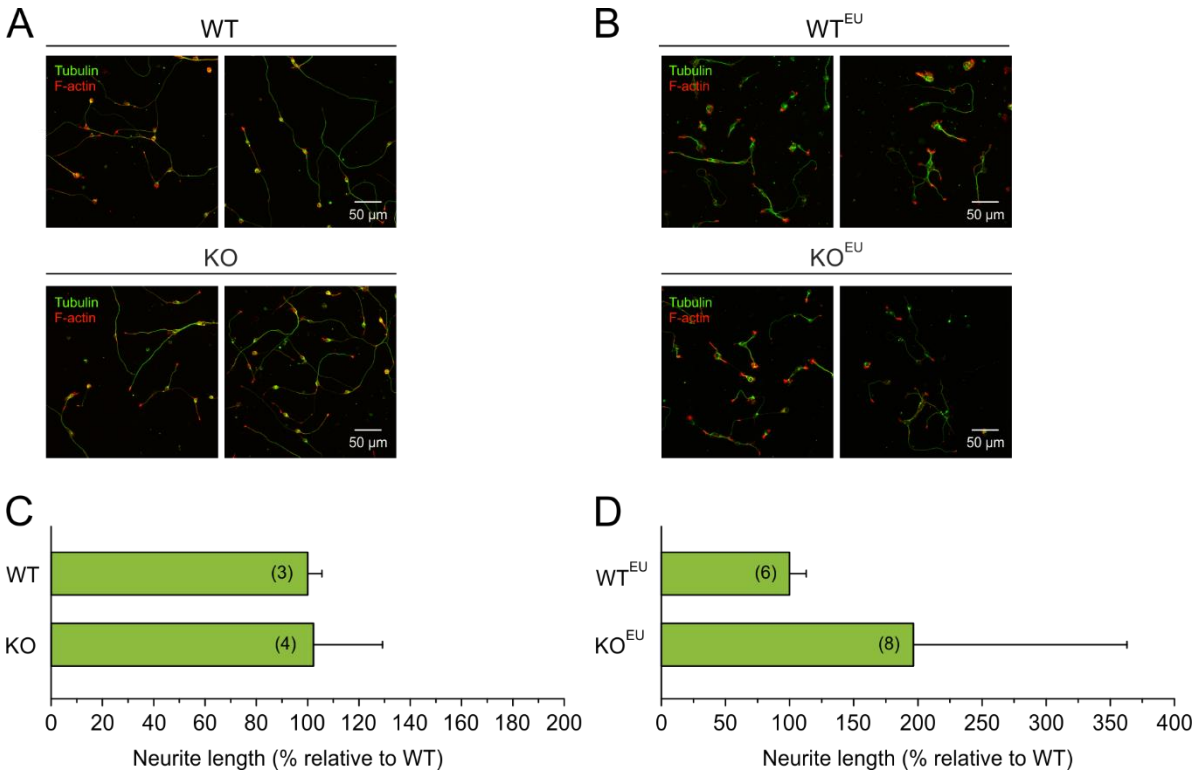

Figure 68: Neurite outgrowth of wild-type and GBA2-KO cerebellar neurons. Representative images of **A)** P8 wild-type (WT) and GBA2-knockout (KO) cerebellar neurons, **B)** P7-9 wild-type (WT^{EU}) and GBA2-knockout (KO^{EU}) cerebellar neurons stained for microtubules and F-actin using an anti-neuronal β-Tubulin antibody and Rhodamine-conjugated Phalloidin, respectively. Quantitative analysis of the neurite length of **C)** GBA2-knockout (KO) cerebellar neurons as depicted in **(A)** and **D)** GBA2-knockout (KO^{EU}) cerebellar neurons as depicted in **(B)** compared to the respective wild-type controls (WT/WT^{EU}). Columns represent mean values + SD. Statistical analysis was performed using one-sample t-test (n numbers are indicated). Experiments were performed by Dr. Sina Stern.

3.14 Behavior studies

3.14.1 Behavior abnormalities in GBA2-KO mice

To analyze whether GBA2-KO mice display locomotor dysfunction, I performed different behavioral experiments (based on initial experiments implemented in Woeste, Master thesis, 2015). Even when observing GBA2-KO mice in a cage in their normal environment, some KO mice exhibited behavior abnormalities (**Table 37**). Three KO^{EU} and one KO mouse suffered from seizures with uncontrolled muscle contraction when they were handled during cage transfer. Moreover, these mice also displayed cramped front paws, squeaking, excessive jumping, and falling over during fur cleaning. The seizures were always followed by an apathetic behavior, leaving the animals in a limp and dazed condition. Two KO mice were barely moving in their cage and showed abnormal gait with wide-spread hind limbs (Woeste, Master thesis, 2015). Due to the severe seizures and motor defects, potentially causing pain, the mice were sacrificed.

Table 37: Behavior abnormalities in GBA2-knockout mice

Genotype		Line	Sex	Age (weeks)	Symptoms
KO^{EU}	GBA2 lacZ/lacZ	GBA2-EUCOMM	♀	29	Seizures: when taking cage out of rack, muscle contraction, postictal: apathetic, limp, dazed
KO^{EU}	GBA2 lacZ/lacZ	GBA2-EUCOMM	♀	29	Seizures: muscle contraction, foam in front of mouth, postictal: apathetic, limp, dazed
KO	GBA2 -/- ; GBA1 flox/flox; Amh-Cre Cre/+; Cre deleter ?/?	Amh-Cre/Cre deleter (CD)/GBA1/GBA2-KO	♀	30	Seizures: squeaking, front paws cramped; mouth wide open, excessive jumping around in cage, falls over during fur cleaning, postictal: apathetic, limp, dazed
KO^{EU}	GBA2 lacZ/lacZ	GBA2-EUCOMM	♂	42	Seizures during transfer in new cage
KO	GBA2 -/-	GBA2-KO	♀	54	Wide-spread hind limbs during walking, barely moving
KO	GBA2 -/-	GBA2-KO	♀	48	Wide-spread hind limbs during walking, barely moving
het^{EU}	GBA2 lacZ/+	GBA2-EUCOMM	♀	27	died

3.14.2 Muscle strength

Besides a disturbed gait and motor coordination defects, head tremor (Hammer et al., 2013), lower and/or upper limb spasticity (Citterio et al., 2014; Hammer et al., 2013; Haugarvoll et al., 2017; Martin et al., 2013; Votsi et al., 2014), and muscle weakness in the limbs (Citterio et al., 2014; Martin et al., 2013) was observed in patients with *GBA2* mutations. Thus, I performed a weight test (see 2.13.1) using global and neuron- and muscle-specific GBA2-knockout mice

(females, 29 ± 2 weeks) and compared their forepaw muscle strength to the corresponding WT animals (Deacon, 2013).

The relative muscle strength was significantly reduced in KO mice (**Figure 69 B**, WT: 9.4 ± 2.5 rsu *versus* KO: 6.9 ± 2.9 rsu). However, no significant difference was observed for the KO^{EU}, which obtained a muscle strength of 9.1 ± 2.7 rsu comparable to WT mice with 7.7 ± 1.8 rsu. Also, muscle strength of the neuron- and muscle-specific KO mice, KO^{Syn} and KO^{Myf}, respectively, was unaltered (**Figure 69 C-E**; WT: 8.3 ± 1.9 rsu *versus* KO^{Syn}: 7.6 ± 1.7 rsu; WT: 7.8 ± 1.7 rsu *versus* KO^{Myf}: 8.0 ± 1.5 rsu).

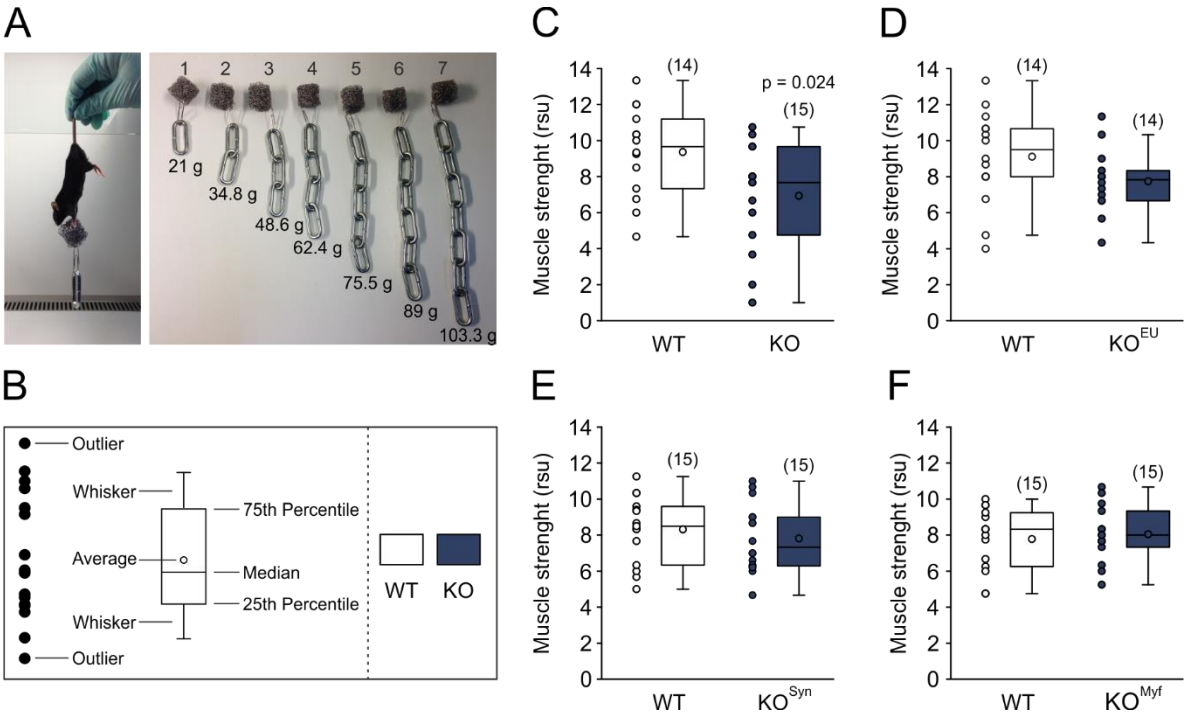

Figure 69: Muscle strength of global and tissue-specific GBA2-knockout mice. A) A weight test was performed by letting the mice grasp steel chain with a weight of 1) 21 g, 2) 34.8 g, 3) 48.6 g, 4) 62.4 g, 5) 75.7 g, 6) 89 g, 7) 103.3 g. Modified from Woeste, Master thesis, 2015. **B)** Illustration of box plots used for data presentation with the box portion including the average (circle), median (horizontal line), 25th and 75th percentile (lower and upper horizontal line), and the whisker (vertical lines). Data is plotted as dots next to the box, including the outliers. The forepaw muscle strength (in rsu) was determined from the time the mice could lift the different weights and is depicted in **C)** for GBA2-KO, **D)** for GBA2-EUCOMM, **E)** for neuron-specific GBA2-KO, and **F)** for muscle-specific GBA2-KO mice. Statistical analysis was performed using one-way ANOVA (n numbers and p values are indicated). rsu: relative muscle strength unit.

3.14.3 Gait and locomotion

To analyze the gait, I used the CatWalk™ XT system (Noldus Information Technologies, Netherlands) and determined several gait parameters of wild-type and GBA2-knockout mice (females, 32 ± 2 weeks). The CatWalk™ XT system is a video-based technique, which visualizes placement of the mouse paws, while freely walking on a glass-plate (see 2.13.2). High sensitivity of the CatWalk™ system is ensured since placement of the paws is detected by fluorescent light scattering, which is recorded with a high-speed color camera. Both static

and dynamics parameters can then be determined using the corresponding computer software (CatWalk™ XT 9.0 and 10.6).

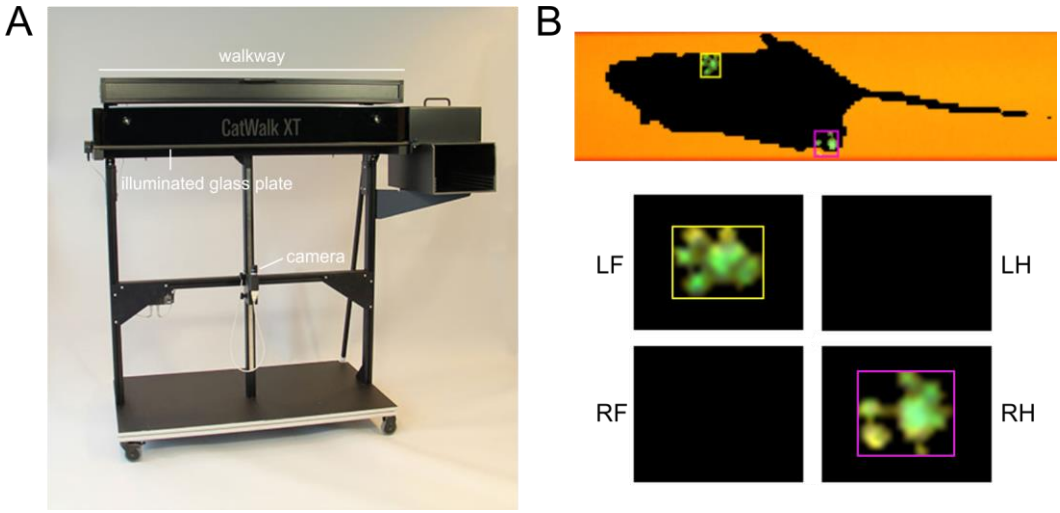

Figure 70: CatWalk™ setup used for gait analysis. A) Illustration of the CatWalk™ with its walkway, comprising the illuminated glass plate and the camera positioned below. Image modified from: Noldus Information Technology – Discover CatWalk XT; https://www.noldus.com/files/u64/catwalk-overview.jpg. **B)** Classification of the paws using the CatWalk™ software for gait analysis. RF: right front; RH: right hind; LF: left front; LH: left hind.

The most basic static parameters are stand and swing phase, which comprise one step cycle of a paw (**Figure 71**). Simultaneous placement of different paws can be easily recognized by overlapping stand phases of the paws.

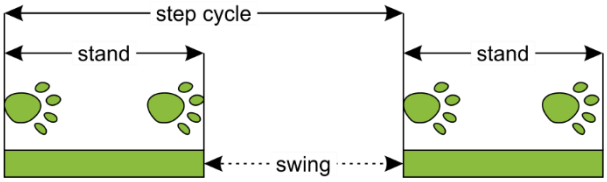

Figure 71: Step cycle of a paw during walking. One step cycle of a paw includes a stand phase, in which the paw is placed on the walkway, and the corresponding swing phase, in which the paw is lifted.

Locomotor dysfunction in mice is often accompanied by an altered duration of the swing phase, as observed in Parkinson's disease (Amende et al., 2005), ataxia (Hoogland et al., 2015), and HSP mouse models (Connell et al., 2016). When testing KO, KO^{EU}, KO^{Syn}, and KO^{Myf} mice compared to the corresponding WT controls, the swing duration of the right front in KO^{EU} and KO^{Syn} mice was altered (**Figure 72 B, C**). However, no difference was observed in KO and KO^{Myf} mice (**Figure 72 A, D**).

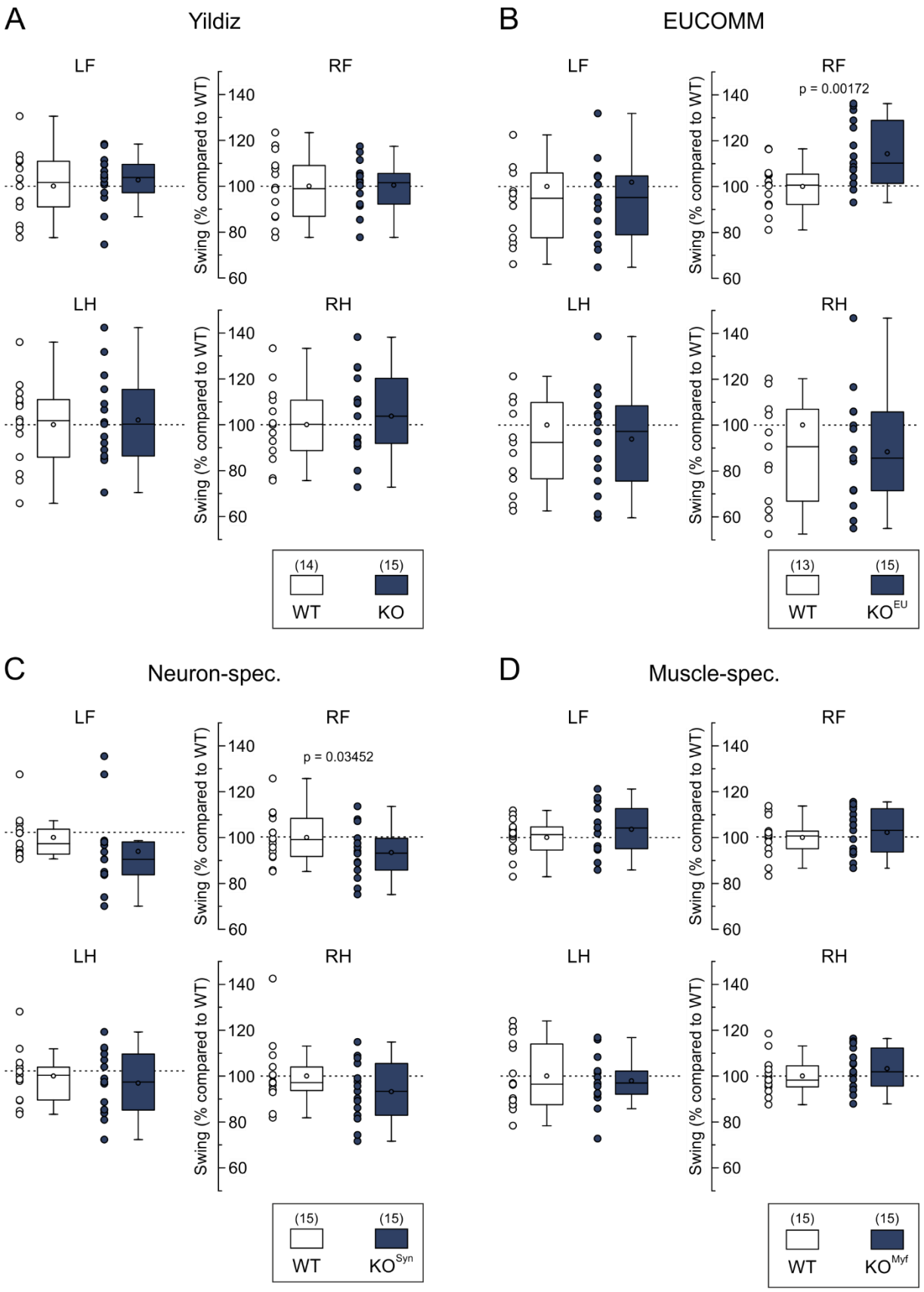

Figure 72: Analysis of the paw swing phase in wild-type and GBA2-knockout mice. Gait analysis using the CatWalk^{TM} was used to determine the swing phase of the different paws in **A)** global GBA2-knockout (KO) (Yildiz), **B)** global GBA2-knockout (KO^{EU}; GBA2-EUCOMM), **C)** neuron-specific GBA2-knockout (KO^{Syn}; Neuron-spec.), and **D)** muscle-specific GBA2-knockout (KO^{Myf}; Muscle-spec.) compared to the respective wild-type (WT) mice (plotted as % compared to WT). Statistical analysis was performed using one-sample t-test (n numbers and p values are indicated). RF: right front; RH: right hind; LF: left front; LH: left hind.

In contrast to humans, mice – as quadrupedal animals – can use several paw combinations during walking (**Figure 73**). Combinations of right front (RF) and left hind (LH) or left front (LF) and right hind (RH) paw are referred to as a *diagonal paw pair*. In contrast, *ipsilateral paw pairs* describe either RF-RH or LF-LH combinations, whereas *girdle paw pairs* include the lateral paws RF-LF or RH-LH.

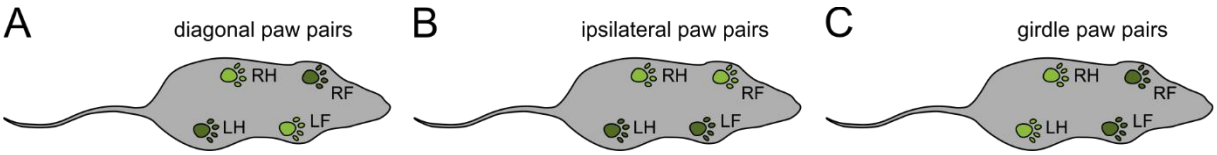

Figure 73: Different paw pairs for quadrupedal animals. Mice - as quadrupedal animals - utilize different combinations of paws during walking: **A)** diagonal (RF-LH; LF-RH), **B)** ipsilateral (RF-RH, LF-LH), and **C)** girdle (RF-LF, RH-LH) paw pairs. RF: right front; RH: right hind; LF: left front; LH: left hind.

For the girdle pairs, the Base of Support (BOS) is determined by the CatWalk™ software, which describes the distance between the front or the hind paws (in cm). A common phenotype seen in mice suffering from locomotor dysfunction to compensate coordination defects is a wide-based gait, which is reflected by an increased BOS, in particular of the hind paws (Barez-Lopez et al., 2014; Hamers et al., 2006). However, the BOS of the front and hind paws was unaffected in the global, as well as neuron- and muscle-specific GBA2-knockout mice (**Figure 74**).

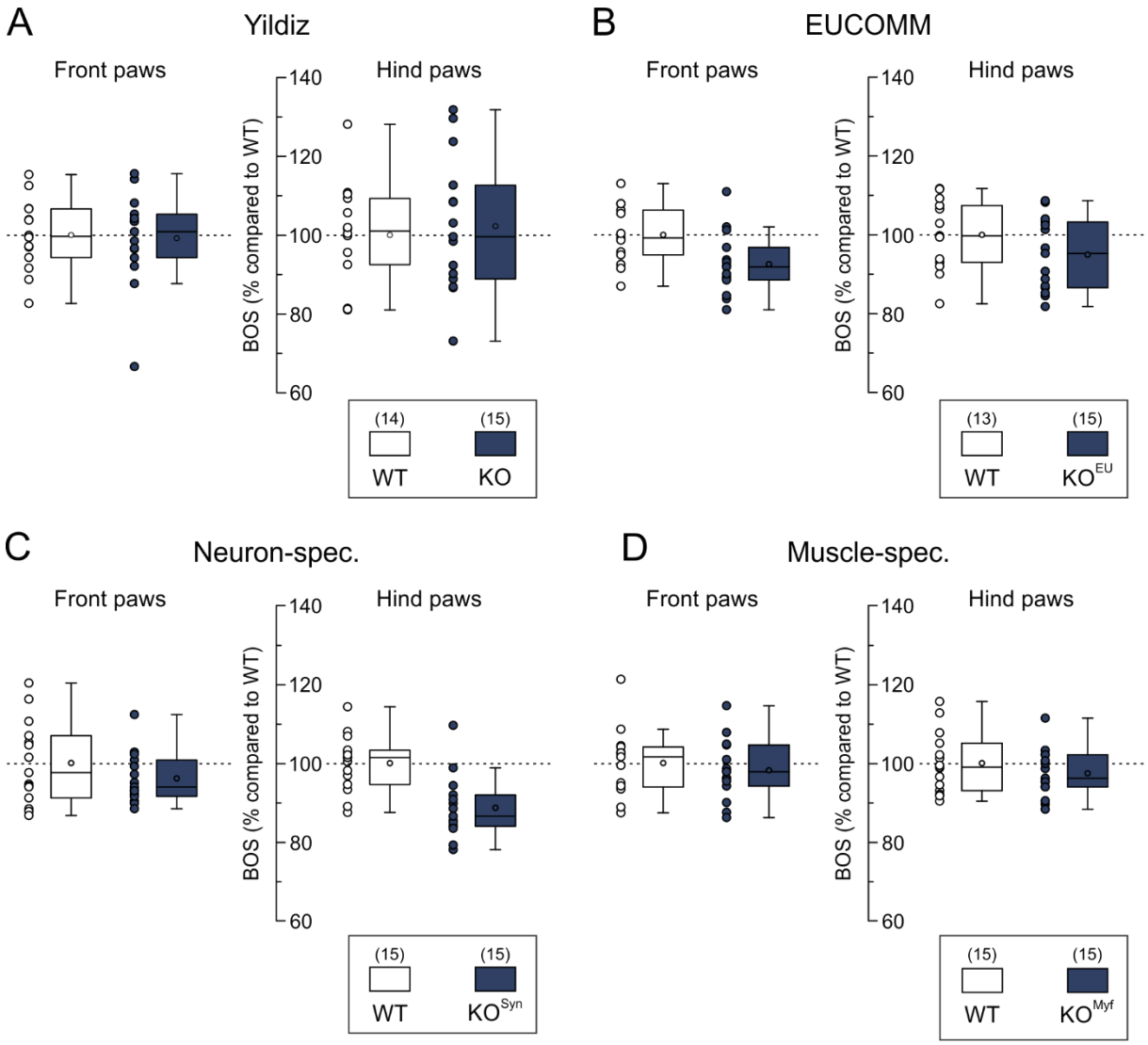

Figure 74: Base of Support of the front and hind paws in wild-type and GBA2-knockout mice. Analysis of the Base of Support (BOS) of the front and hindpaws of **A)** global GBA2-knockout (KO) (Yildiz), **B)** global GBA2-knockout (KO^{EU}; GBA2-EUCOMM), **C)** neuron-specific GBA2-knockout (KO^{Syn}; Neuron-spec.), and **D)** muscle-specific GBA2-knockout (KO^{Myf}; Muscle-spec.) compared to the respective wild-type (WT) mice (plotted as % compared to WT). Statistical analysis was performed using one-sample t-test (n numbers are indicated).

In addition, I analyzed the step sequence in WT and GBA2-KO mice used during walking. These step sequences are assigned according to the consecutive placement of the paws, following either an alternating (ipsilateral-girdle), a cruciate (girdle-diagonal), or rotating (ipsilateral-girdle) pattern that are subdivided into AA (RF-RH-LF-LH) and AB (LF-RH-RF-LH), CA (RF-LF-RH-LH) and CB (LF-RF-LH-RH), and RA (RF-LF-LH-RH) and RB (LF-RF-RH-LH), respectively (**Figure 75**). The AB step sequence pattern is normally preferred by rodents, whereas the rotating step sequence is barely seen (Cheng et al., 1997; Neumann et al., 2009).

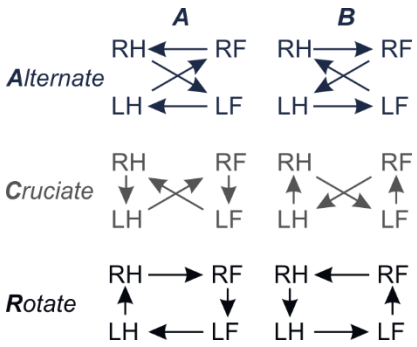

Figure 75: Step sequences during gait utilized by quadrupedal animals. Alternating paw placement following an ipsilateral-girdle pattern in the AA (RF-RH-LF-LH) and AB (LF-RH-RF-LH) step sequence, cruciate paw placement following an girdle-diagonal pattern in the CA (RF-LF-RH-LH) and CB (LF-RF-LH-RH) step sequence, and rotating paw placement following an ipsilateral-girdle pattern in the RA (RF-LF-LH-RH) and RB (LF-RF-RH-LH) step sequence. RF: right front; RH: right hind; LF: left front; LH: left hind.

My results show that KO mice exhibited increased usage of the AA step sequence (WT: 1.19% *versus* KO: 8.97%, p = 0.015), whereas the AB step sequence was not used as frequently (WT: 82.22% *versus* KO: 51.98%, p = 0.0034; **Figure 76 A**). In line with these findings, the cruciate step sequence is more often observed in KO mice. KO^{EU}, KO^{Syn}, and KO^{Myf} as well as the corresponding WT control mice revealed predominant usage of the AA step sequence (**Figure 76 B-D**). However, no difference in the step sequence were found in these GBA2-knockout lines.

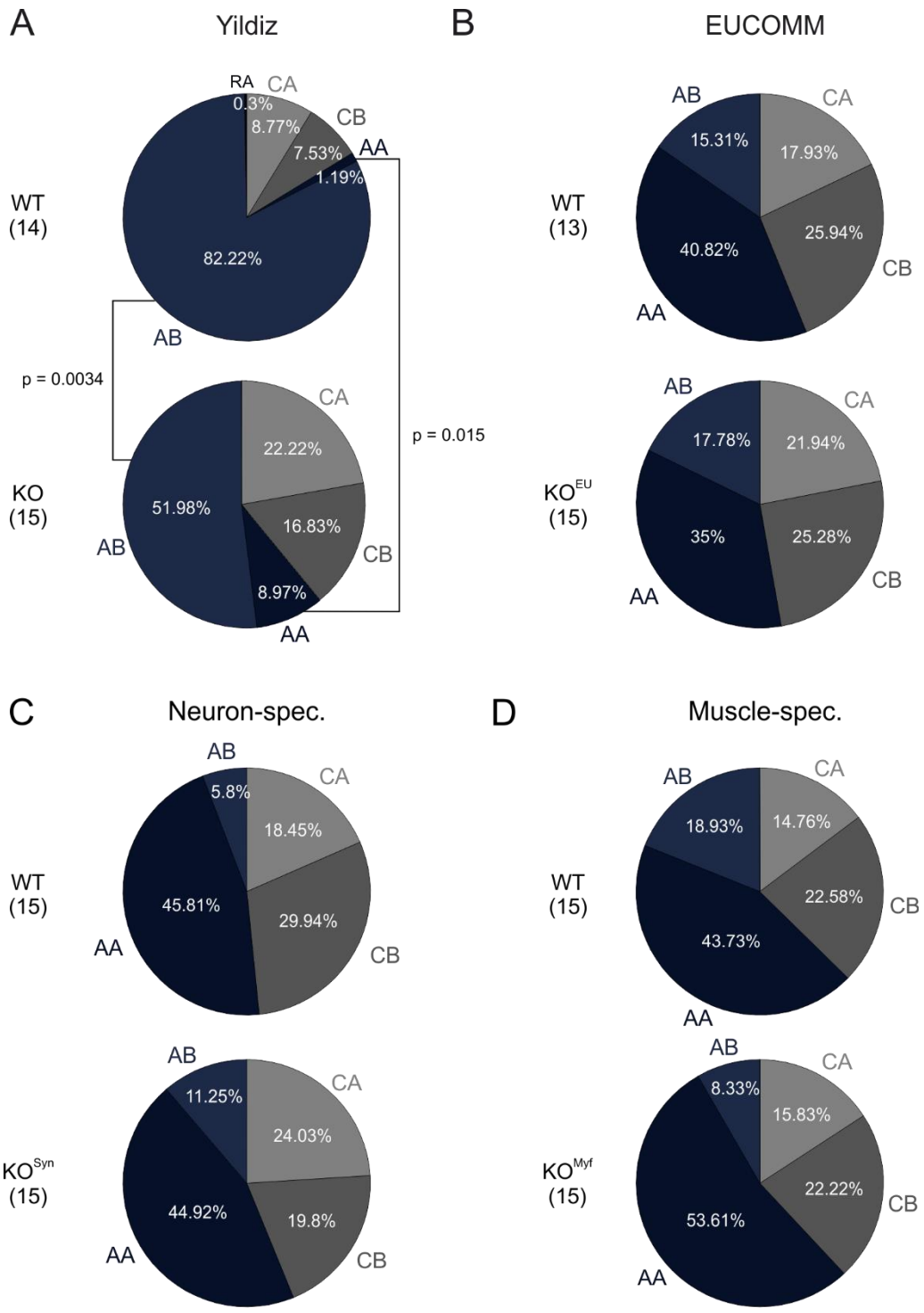

Figure 76: Analysis of the step sequence in wild-type and GBA2-knockout mice. Step sequence during walking of **A)** global GBA2-knockout (KO) (Yildiz), **B)** global GBA2-knockout (KO^{EU}; GBA2-EUCOMM), **C)** neuron-specific GBA2-knockout (KO^{Syn}; Neuron-spec.), and **D)** muscle-specific GBA2-knockout (KO^{Myf}; Muscle-spec.) compared to the respective wild-type (WT) mice. Statistical analysis was performed using one-way ANOVA (n numbers and p values are indicated). RF: right front; RH: right hind; LF: left front; LH: left hind.

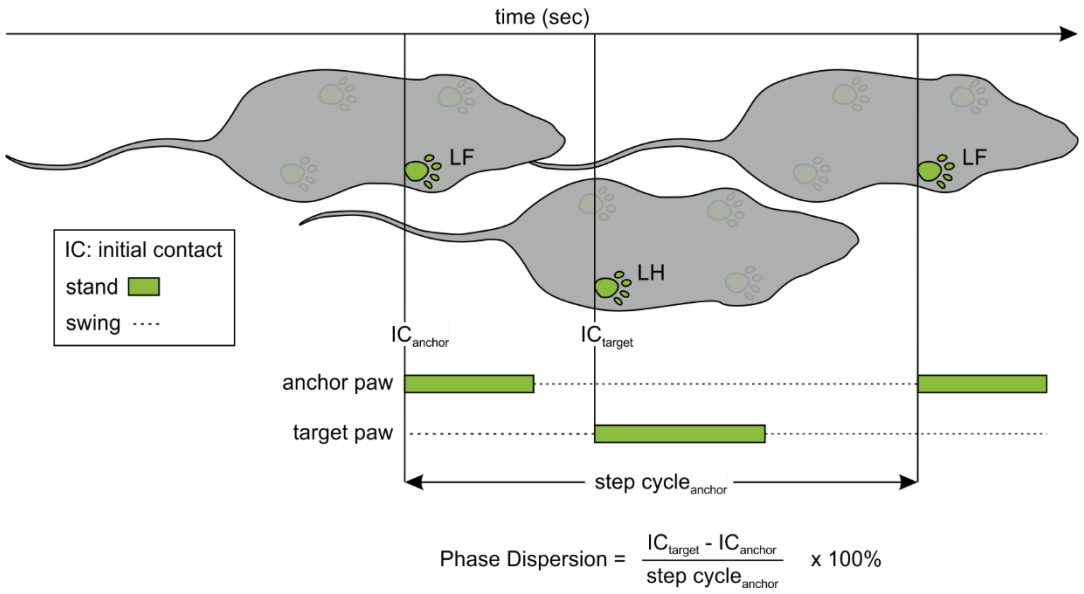

Figure 77: Phase Dispersion determined by the CatWalk™ gait analysis. Inter-paw coordination is represented by the Phase Dispersion (in %) displaying the temporal relation between the placement of different paws. The Phase Dispersion can be calculated for the different paw pairs: diagonal (RF-LH, LF-RH), ipsilateral (RF-RH, LF-LH), and girdle (LF-RF, LH-RH). RF: right front; RH: right hind; LF: left front; LH: left hind.

As a measure for inter-paw coordination, the Phase Dispersion can be determined according to Kloos and colleagues (Kloos et al., 2005). The Phase Dispersion is calculated for the different paw pairs and describes the placement (initial contact) of a target paw – following placement of an anchor paw – relative to the step cycle duration of the anchor paw (**Figure 77**). Opposing paw combinations (e.g. RF_{anchor}-RH_{target} and RH_{anchor}-RF_{target}) are correlated. Thus, the CatWalk™ software depicts the Phase Dispersion for diagonal and ipsilateral paw pairs with the front paws as the anchor, and for girdle paw pairs with the left paws as the anchor. A value of 50% means that the target paw was placed in the middle of the step cycle of the anchor paw. If the stand phase of the target paw exceeds the step cycle duration of the anchor, the Phase Dispersion is calculated in relation to the next placement of the anchor paw, resulting in a negative value. In general, Phase Dispersion can range from -50 to 75%. However, performing circular statistics (Cstat in the CatWalk™ software), the Phase Dispersion is more precisely assigned according to the phase lag of the paws and then ranges from 0 to 100%. A value of 0%, typical for diagonal paw pairs, reflects simultaneous placement of the anchor and target paw, whereas a value of 50% indicates perfect alternation of the paws, as normally seen for girdle paw pairs. Translating the Cstat values of the Phase Dispersion to angles, data can be plotted in a circular scatter plot, where a value of 25% equals 90°, 50% equals 180°, 75% equals 270°, and 100% equals 360° (**Figure 78**). The phase dispersions for diagonal, ipsilateral, and girdle paw pairs in all tested KO mice revealed a higher variation compared to the respective WT controls (**Figure 78**). Thus, mice lacking GBA2 seem to exhibit slightly altered inter-paw coordination.

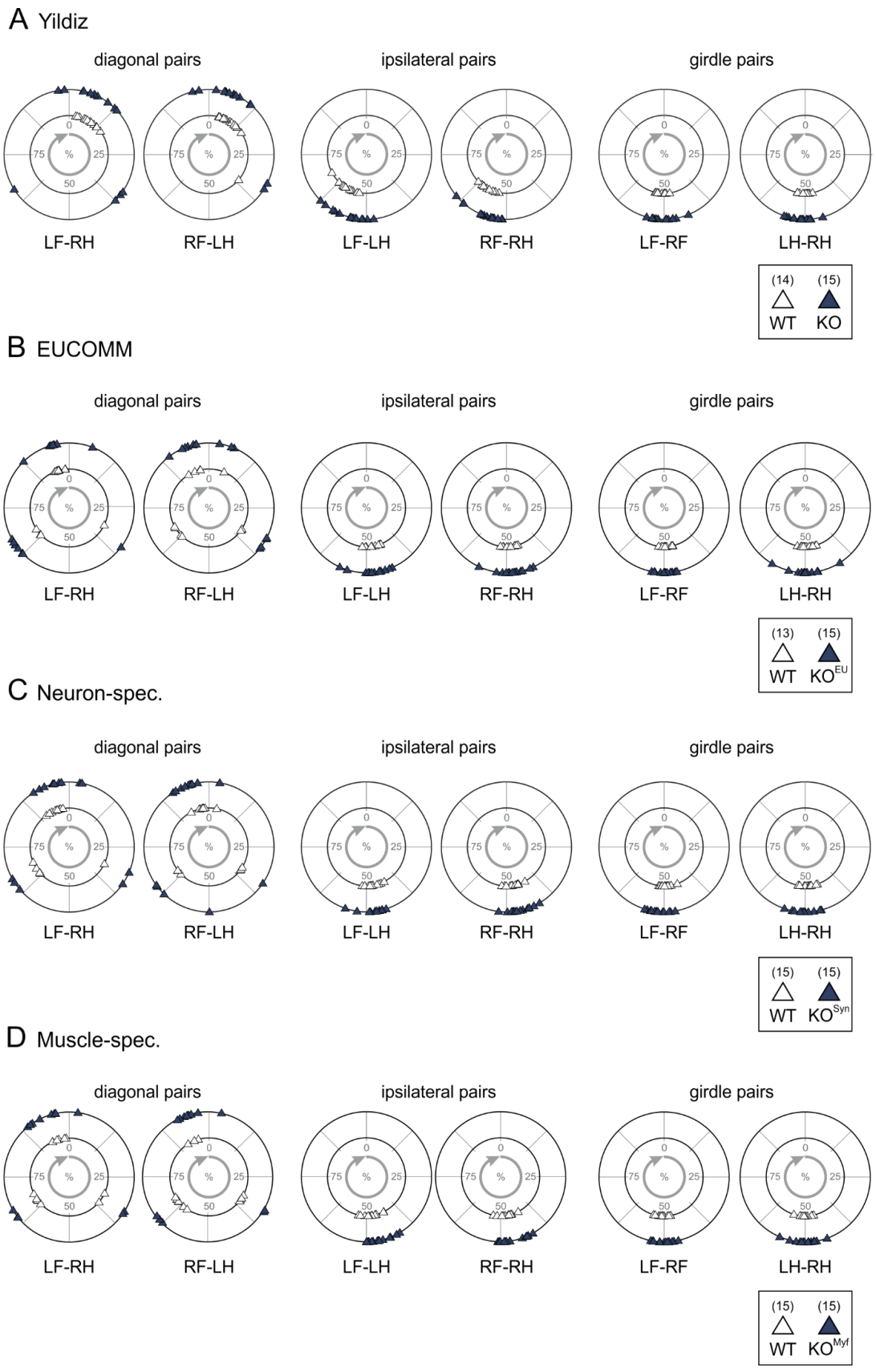

Figure 78: Analysis of the Phase Dispersion of the different paw pairs in wild-type and GBA2-knockout mice. Circular dot blots representing the Phase Dispersion (Cstat values) ranging from 0 to 100% of the different paw pairs (diagonal: RF-LH, LF-RH; ipsilateral: RF-RH, LF-LH; girdle: LF-RF, LH-RH) of **A)** global GBA2-knockout (KO) (Yildiz), **B)** global GBA2-knockout (KO^{EU}; GBA2-EUCOMM), **C)** neuron-specific GBA2-knockout (KO^{Syn}; Neuron-spec.), and **D)** muscle-specific GBA2-knockout (KO^{Myf}; Muscle-spec.) compared to the respective wild-type (WT) mice. Statistical analysis was performed using one-way ANOVA (n numbers are indicated). RF: right front; RH: right hind; LF: left front; LH: left hind.

4 Discussion

In my thesis, I have demonstrated that the catalytic activity of GBA2 is encoded in the protein's tertiary structure, including the N-terminal domain, linker region, and C-terminal domain. Single mutations in GBA2, which have been identified in human patients suffering from ARCA, HSP, and MSLS, cause a loss of function of the enzyme, one exception being the R725H (mGBA2) mutation. GBA2 proteins interact and form oligomers, a characteristic that is potentially important for its function. A phenotypic discrepancy between humans carrying GBA2 mutations and mice lacking GBA2 points towards species-dependent differences in GBA2-regulated metabolism of GlcCer and its metabolites in the CNS. My study demonstrates a pivotal role of mammalian GBA2 in neurite outgrowth of dissociated cerebellar neurons and, thus, provides a first idea of the mechanism underlying ataxia and spasticity in ARCA, HSP, and MSLS patients carrying mutations in GBA2.

4.1 Structural and functional analysis of GBA2

All mGBA2 mutants, besides R725H, are devoid of GBA2 activity (see 3.1.4), which is in line with other studies, which have already analyzed the activity of some of these mutants (Sultana et al., 2015). To date, only for the hGBA2 R630W mutant (R621W in mGBA2), GBA2 activity has been analyzed in samples from human patients: lymphoblasts and leukocytes, isolated from three patients that are homozygous for the R630W mutation, were devoid of GBA2 activity (Martin et al., 2013). It needs to be investigated in future studies whether also the patients carrying the other missense or nonsense GBA2 mutations are devoid of GBA2 activity and whether patients homozygous for the R734H mutant display residual GBA2 activity. If loss of GBA2 activity results in locomotor dysfunction, patients homozygous for R734H might exhibit milder clinical symptoms. However, this mutation has been identified in ARCA patients, which are homozygous for R734H mutant, but also for the D594H mutation (Votsi et al., 2014). Thus, the contribution of the R734H mutation to disease pathology is impossible to decipher.

According to the homology modelling of hGBA2 based on the structure of the bacterial β-glucosidase *Tx*GH116, R734, in contrast to the other mutated amino acids does not face the catalytic site (see 3.3), but is rather located at the protein surface. Here, it might control association of GBA2 with the membrane, which has also been shown for arginines in other membrane-associated proteins (Bentham et al., 2006; Patel et al., 2017). The positively charged arginine interacts with negatively charged phosphate groups of lipids and can form extensive hydrogen bonds (Kooijman et al., 2007; Li et al., 2013). In addition, lysine residues are known to be involved in anchoring proteins to the membrane. For instance, membrane association of saposin C, a regulator of liposomal membrane fusion, is mediated by lysine residues at the N terminus that interact with phospholipids (Liu et al., 2005). Mutating these residues to uncharged alanine or negatively charged glutamic acid resulted in loss of fusion

activity, whereas mutating these residues to arginine only led to partial loss of activity (Liu et al., 2005). Thus, charged arginine or lysine residues in GBA2 might have a similar function in mediating membrane association.

In our homology model, G683 also points towards the protein surface (see 3.3), but others have proposed that G683 is crucial for proper assembly of the acid/base and sugar-binding region in the catalytic cleft (Charoenwattanasatien et al., 2016). This study proposes D677 and E527 in hGBA2 being the acid/base and nucleophile, respectively, needed for the double-displacement reaction to cleave GlcCer to glucose and ceramide (Charoenwattanasatien et al., 2016). In contrast, D594 and R873 face the catalytic cleft and might be involved in hydrogen-bond formation with the substrate (Charoenwattanasatien et al., 2016). The amino acid R630 is thought to be important for overall protein stability (Charoenwattanasatien et al., 2016), and, according to our model, F419V and M510V align to the linker region preceding the C-terminal domain. Such a C-terminal linker region, extending the catalytic site, is also present in the fungal β-glucosidase *Re*Cel3A, which assembles in a tetrameric complex (Gudmundsson et al., 2016). The three-domain monomers also harbour a second linker region, connecting the N-terminal domain and the middle sandwich domain. The two-domain glucoamylase *t*GA of the *Thermoanaerobacterium thermosaccharolyticum* from the GH15 family resembles a similar domain architecture as GBA2 with an N-terminal domain, predominantly containing β-sheets, a linker region, and a C-terminal $(\alpha/\alpha)_6$ barrel domain (Aleshin et al., 2003). Thus, mutating any of the aforementioned amino acids might impair proper assembly of the catalytic site with the acid/base and nucleophile, and sugar binding or stability of GBA2, comprised of the N-terminal, linker, and C-terminal domain.

In contrast to the C-terminal catalytic domain, which is predominantly assembled by α-helices, the N-terminal domain predominantly contains β-sheets (see 3.3) (Charoenwattanasatien et al., 2016). Since deletion of parts of the N-terminal domain resulted in complete loss of function of GBA2, this region – besides the catalytic domain – is also crucial for enzyme function. Moreover, GBA2 activity is known to be highly dependent on the presence of phospholipids (Matern et al., 1997) and loses its activity upon membrane solubilisation (Boot et al., 2007) or in the absence of membranes (Körschen et al., 2013).

I could show that GBA2 similar to other bacterial, archaeal, or fungal β-glucosidases, forms oligomers (Aguilar et al., 1997; Aleshin et al., 2003; Gudmundsson et al., 2016; Kado et al., 2011; McAndrew et al., 2013). Co-immunoprecipitation and chemical cross-linking demonstrated that GBA2 proteins interact and form oligomers. Loss of the C-terminal domain, as seen for the nonsense mutations T483R*9 and R331*, did not destroy interaction with the wild-type mGBA2 protein, when analyzed by co-immunoprecipitation (see 3.5.1.5). However, oligomer formation of GBA2 analyzed by chemical cross-linking was dependent on the

presence of the C-terminal domain: Loss of the C-terminal domain in the T483R*9 and R331* mutant impaired oligomer formation of mutant proteins and also hetero-oligomers with wild-type mGBA2 protein were not formed (see 3.5.2.2). Moreover, the presence of T483R*9 and R331* did not affect oligomerization of wild-type GBA2. In line with these results, β-glucosidase activity in cells expressing both wild-type and mutant GBA2 did not reveal a dominant-negative effect of any of the GBA2 mutant on wild-type GBA2 activity (see 3.5.3.2). One explanation for the discrepancy in the co-immunoprecipitation and cross-linking approach for mGBA2 T483R*9 and R331* might be that the experiments were performed in different buffers. Interaction studies of GBA2 proteins analyzed by co-immunoprecipitation were performed in detergent-containing buffer in the presence of 150 mM NaCl. Under these buffer conditions, GBA2 protein interaction was preserved. In contrast, upon cross-linking in detergent-free buffer in the absence of NaCl, oligomer formation of mGBA2 T483R*9 and R331* was not stable. Thus, the two approaches were influenced by the different buffer conditions and/or potentially targeted different interaction sites between the proteins.

Dimerization of the glucoamylase *t*GA of the *Thermoanaerobacterium thermosaccharolyticum* is thought to be promoted or stabilized by membrane lipids (Aleshin et al., 2003). Thus, GBA2 oligomerization could also be dependent on the presence of lipids. One approach to answer whether GBA2 oligomerization depends on lipids would be to cross-link GBA2 in the presence and absence of liposomes. Moreover, it remains unclear whether the cross-linked product is a GBA2-GBA2 oligomer or whether GBA2 complexed with (a) different protein(s). Our previous studies demonstrated that wild-type mGBA2, expressed in *E.coli* in the absence of other mammalian proteins, which might function as an interaction partner, is active (Schonauer et al., 2017). However, the oligomerization state of GBA2 under these conditions is not known. Further studies are needed to analyze if oligomerization is required for GBA2 activity by performing activity measurements of purified non-cross-linked and cross-linked GBA2. According to structural analysis of other β-glucosidases that form oligomers, also GBA2 activity seems to rely on complex formation: The β-glucosidase JMB19063, expressed by thermophilic microorganisms present in compost and belonging to the GH3 family, is only active upon dimerization: two monomers in an opposing orientation provide two distinct residues in their C-terminal domains, which are needed for substrate binding (McAndrew et al., 2013).

4.2 Role of GBA2 in the CNS

The present study shows that GBA2 is highly expressed and active in the murine CNS, but barely in skeletal muscle (see 3.7, 3.8). A previous study could also show that GBA2 expression in the brain is higher compared to lung, kidney, heart, and spleen in mice (Yildiz et

al., 2006). Thus, GlcCer metabolism, controlled by GBA2, seems to play a pivotal role in the CNS.

4.2.1 Neurons: major site of GBA2 expression and activity in the CNS

In a previous study, we have shown that hippocampal neurons, but not astrocytes express GBA2 (Körschen et al., 2013). My study revealed that GBA2 activity in brain and spinal cord is primarily attributable to its activity in neurons, rather to other cell types residing in the tissue (see 3.7.1.1). In particular, GBA2 is expressed and active in murine cerebellar neurons (see 3.7.1.3).

Sphingolipid synthesis is crucial for axonal growth in neurons: In cells treated with an inhibitor for ceramide synthase (fumonisin B1), axon growth was impaired at stage 3 during neuronal development after 2-3 days in culture (Harel and Futerman, 1993). This was also shown for dendritic growth in Purkinje cells upon ceramide synthase inhibition (Furuya et al., 1995). Impaired *de novo* synthesis of ceramide resulted in decreased gangliosides levels (Furuya et al., 1995; Harel and Futerman, 1993). Not the lack of ceramide itself, but rather of its glycosylated metabolite GlcCer, as the glycosphingolipid precursor, underlies this axon outgrowth defect: In the presence of fumonisin B1, a ceramide derivative, which is glycosylated to GlcCer, ameliorated the axon outgrowth defect, whereas a ceramide derivative, which cannot be glycosylated to GlcCer, failed to do so (Furuya et al., 1995; Harel and Futerman, 1993; Schwarz and Futerman, 1997). Also, inhibition of GBA2-mediated degradation of GlcCer affected neurite outgrowth: Pharmacological inhibition of GBA2 activity by NB-DNJ in cerebellar neurons resulted in significantly shorter neurites (see 3.13). GBA2 expression increases during neuronal differentiation (Aureli et al., 2012), implicating that the enzyme plays an important role in the CNS already during development.

We have previously shown in sperm and fibroblasts isolated from GBA2-KO mice that actin polymerization is augmented in GBA2-knockout murine dermal fibroblasts, indicated by an increased number of actin protrusions, filopodia and lamellipodia, in cells seeded on CYTOO chips (Raju et al., 2015). These actin structures also play a pivotal role in neurite outgrowth. Filopodia formation is regulated by Cdc42, whereas lamellipodia formation is regulated by Rac1 (Hall, 1998). Both Cdc42 and Rac1 belong to a class of mammalian small Rho GTPases, which bind guanine nucleotides and regulate actin dynamics (Ridley, 2006). In a guanosine 5′-diphosphate (GDP)-bound state, the Rho GTPases reside in the cytosol, where there are complexed with a guanine dissociation inhibitor (GDIs) and are inactive (Garcia-Mata et al., 2011). Guanine-nucleotide exchange factors (GEFs) promote the exchange from GDP to guanosine-5'-triphosphate (GTP), needed for activation of the protein (Bos et al., 2007). When GTPase activating proteins (GAPs) bind to the Rho GTPases, hydrolysis of GTP to GDP is induced (Bos et al., 2007). The majority of the Rho GTPases is post-translationally prenylated

(Roberts et al., 2008), which allows incorporation into the plasma membrane. Here, the Rho GTPases fulfill their function by activating several proteins for actin polymerization. Activated Cdc42 can bind to the (neural) Wiskott-Aldrich syndrome protein (N)-WASP (Carlier et al., 1999) and activated Rac1 can bind to N-WASP and the WASP family Verprolin-homologous protein (WAVE) (Suetsugu et al., 2006; Tomasevic et al., 2007), thereby activating the actin-related protein (Arp)2/3 complex. The Arp2/3 complex promotes actin polymerization as a nucleation factor (Mullins et al., 1998). Rac1 binds to phosphatidic acid (PA) and phosphatidylinositol-(3,4,5)-trisphosphate (PIP_3) in the membrane and has recently been shown to cluster in PA- and PIP_3-enriched membrane areas (Maxwell et al., 2018). The presence of phosphatidylinositol-(4,5)-bisphosphate (PIP_2) enhances actin polymerization by the Arp2/3 complex upon induction by Cdc42 or Rac1 via N-WASP (Tomasevic et al., 2007). By binding to the p21-activated kinase (PAK), Rac1 and Cdc42 induce phosphorylation and activation of the Lin-11/Isl-1/Mec-3 (LIM) kinases (Edwards et al., 1999; Manser et al., 1994), which inactivate cofilin and thereby promote actin polymerization (Arber et al., 1998). Our previous studies demonstrated that the lipid organization of the plasma membranes shifts to a more ordered state upon loss of GBA2 in fibroblasts, and hypothesized that this affects Rac1 and Cdc42 activity, which are active in a GTP-bound state at the plasma membrane (Raju et al., 2015). Accumulation of GlcCer and complex glycosphingolipids might affect Rac1 and Cdc42 recruitment to the plasma membrane and, thereby, their activity.

Besides the actin cytoskeleton, also microtubules promote elongation of neurites and their formation might be disturbed by a lipid accumulation (Ferreira et al., 1989). The ganglioside GM1 was shown to alter association of microtubule-associated protein (MAP)-2 to microtubules in fibroblasts, inducing its association with the actin cytoskeleton (Colella et al., 2000). Furthermore, the myelin-associated protein (MAG), an inhibitor of neurite outgrowth that can bind the gangliosides GD1a and GT1b (Vyas et al., 2002), affects microtubule formation: *In vitro* in the presence of MAG, rat cerebellar neurons exhibited impaired microtubule assembly (Mimura et al., 2006). MAG activates the small Rho GTPase RhoA, which promotes collapse of the growth cone in neurons, thereby inhibiting neuronal outgrowth (Yamashita et al., 2002). Thus, not only actin dynamics, but also microtubule dynamics are potentially impaired by a glycosphingolipid accumulation. As we have previously shown in fibroblasts, loss of GBA2 enhanced microtubules persistence (Raju et al., 2015). However, whether the impaired neurite outgrowth in cerebellar neurons, lacking GBA2 activity due to pharmacological inhibition, was caused by defects in the actin cytoskeleton or microtubules needs to be elucidated. Strikingly, genetic ablation of GBA2 did not affect neurite outgrowth and might also explain the mild phenotype of GBA2-knockout mice compared to human patients with GBA2 mutations.

4.2.2 Species-specific functions of GBA2 in the brain

In contrast to the ARCA, HSP, and MSLS patients, carrying mutations in *GBA2*, genetic ablation of GBA2 in mice did not affect cerebellar morphology or induce severe motor dysfunction (see 3.7.1.3.13.14), albeit GlcCer (C18) accumulated in the cerebellum (see 3.9). However, there was no strong accumulation of complex glycosphingolipids in the cerebellum (see 3.9). Whether GlcCer or more complex glycosphingolipids accumulate in the CNS of ARCA, HSP, and MSLS patients carrying *GBA2* mutations is not known. A more pronounced accumulation of GlcCer and its complex metabolites might have caused the severe clinical phenotype in humans compared to mice. Human patients suffer from severe spastic and ataxic symptoms with an onset in childhood or early adulthood (7 ± 5 years), often accompanied by peripheral neuropathy, axonal damage, demyelination, and atrophy in the corpus callosum, cerebrum and/or cerebellum (Citterio et al., 2014; Hammer et al., 2013; Haugarvoll et al., 2017; Martin et al., 2013; Votsi et al., 2014). In contrast, global and neuron- and muscle-specific GBA2-knockout mice only revealed mild alterations in muscle strength and gait. The brain weight was not altered upon genetic ablation of GBA2 in mice, in line with the study of Yildiz and colleagues (Yildiz et al., 2006), and no morphological defects in the cerebellum, including the Purkinje cells, were observed (see 3.7.1.3.1). However, a few GBA2-knockout mice exhibited an extremely wide-based gait or suffered from severe seizures, indicating that there is a high phenotypic variation (see 3.14.1). Martin and colleagues, who studied the role of GBA2 in zebrafish, reported that only 12.5% of the larvae, lacking the *GBA2* orthologue after knock down by antisense morpholino oligonucleotides, displayed an abnormal tail morphology (curly tail) (Martin et al., 2013). However, the majority of the larvae did not show this phenotype. In a locomotion test, solely 24% of the knock-down animals, lacking the curly tail phenotype, exhibited motor defects (Martin et al., 2013). Analysis of axon morphology demonstrated that only 20% of the axons displayed an abnormal morphology, whereas such a defect was only seen in 2% of the axons in control zebrafish ($p < 0.00001$) (Martin et al., 2013). Thus, also in GBA2-knockout zebrafish, the phenotypic variation is high.

How can this variation be explained on a molecular level? An explanation could be that individual mice accumulate different amounts of GlcCer, which result in a moderate or mild phenotype. Such a correlation between the level of accumulated glycosphingolipid and the severity of the phenotype is seen in human patients suffering from Fabry disease. Mutations in the *GLA* gene coding for α-galactosidase A, leading to complete or partial loss of the enzyme's activity, result in a moderate or severe accumulation of Gb3 and cause a moderate or severe disease form, respectively: Serum levels of deacylated Gb3 in blood plasma was the highest in patients suffering from the classic, severe form of the disease, whereas lowest plasma deacylated Gb3 levels were present in patients suffering from the late-onset, milder form of the disease (Nowak et al., 2018).

An explanation for the overall mild phenotype in GBA2-knockout mice would be that compensatory mechanisms might prevent severe neurological manifestation by loss of GBA2. A cross-talk of GBA2 and GBA1 is observed in the Gaucher disease background: Fibroblasts from Gaucher patients, suffering from a loss of GBA1, and GBA1-deficient human fibroblast-like cell lines exhibit a decrease in GBA2 activity, whereas GBA2 mRNA and expression levels remained unchanged (Schonauer et al., 2017). A similar effect was seen upon pharmacological inhibition of GBA1 by CBE in human fibroblasts and mice (Schonauer et al., 2017). However, *vice versa*, loss of GBA2 activity did not affect GBA1 activity (Schonauer et al., 2017), a result that was also resembled in my study: No increase in GBA1 activity upon loss of GBA2 was detected in spinal cord, cerebellum, brain, skeletal muscle, and dermal fibroblasts from GBA2-knockout mice compared to wild-type mice (see 3.7, 3.8). Also, AMP-DNM treatment of cerebellar neurons, completely inhibiting GBA2 activity, did not result in increased GBA1 activity (see 3.11.1). In line with my finding, in lymphoblasts isolated from a patient carrying the R630W mutation, GBA1 activity remained unchanged (Martin et al., 2013). Thus, GBA1 does not compensates for the loss of GBA2. Another enzyme that might compensate for the loss of GBA2 is the GlcCer synthase. Both enzymes reside at the cytoplasmic side of the *cis* Golgi (Körschen et al., 2013; Schweizer et al., 1994), and loss of either enzyme might directly influence the activity of the other. An accumulation of GlcCer in the absence of GBA2 might induce an inhibition of GlcCer synthase activity, ameliorating GlcCer accumulation. One could envision that GlcCer levels only increase up to a certain point, without reaching a critical level to drive neurological defects. However, why such an effect might solely occur in the CNS remains elusive.

Of note, GBA2 also exerts a transglucosylation activity and can transfer a glucose moiety from GlcCer to cholesterol, or *vice versa* deglycosylate glucosylcholesterol (GlcChol), transferring the glucose moiety to ceramide (Akiyama et al., 2011; Marques et al., 2016). In mice, GlcChol is highly abundant in the brain, sciatic nerve, and lung (Marques et al., 2016). Loss of GBA2 is accompanied by a decrease in GlcChol levels, as observed in murine dermal fibroblasts, testis (Dr. Diana N. Raju, unpublished data), thymus, liver, and blood plasma (Marques et al., 2016). Upon glycosylation, cholesterol relocalizes from ordered to less ordered membrane domains (Halling et al., 2008). Thus, not only GlcCer and GlcChol metabolism is strongly linked, but also the function of these lipid metabolites might be intertwined on the level of lipid rafts. In a GBA2-deficient condition, in which glycosylation of cholesterol is diminished, cholesterol might still localize to more ordered membrane domains, promoting the effect of accumulated GlcCer on membrane stacking. However, whether GlcChol levels also decrease in the brain upon loss of GBA2 is not known. Moreover, the cellular function of GlcChol is still unclear. Since GlcChol is more water-soluble than cholesterol, a potential role of GlcChol as an ATP-independent transport metabolite of cholesterol was suggested (Marques et al., 2016). Interestingly, a

glycosylated sterol (sitosterol) from cycads was shown to be toxic to neurons *in vivo* in mice and *in vitro* (Ly et al., 2007). However, whether GlcChol in mammals also exerts a neurotoxic function and whether a decrease in GlcChol ameliorates neuronal damage needs to be elucidated.

In a mouse model of autosomal-recessive HSP, which lacks paraplegin due to a loss-of-function mutation in the *Spg7* gene, minor defects in motor coordination were observed at 4 month of age, axonal swelling occurred at 8 month, abnormal gait at 17 month, severe axonal degeneration at 12 month, and axon degeneration in the corticospinal tract at 29 month of age (Ferreirinha et al., 2004). Thus, symptoms – in contrast to human HSP patients – developed slowly, and only became severe in mice older than 17 month. Also, lack of GM3 synthase, impairing the synthesis of complex glycosphingolipids downstream of LacCer, has been associated with an epileptic syndrome in humans (Simpson et al., 2004) but not in mice (Proia, 2004; Yamashita et al., 2003). Thus, several mouse models of neurological disorders develop symptoms only at later stages compared to humans or solely suffer from mild CNS defects, indicating that compensatory mechanisms also occur in other lipid disorders in mice. The phenotypical discrepancy between human and mouse might underlie species-specific differences in the lipidome. In comparison to other mammalian species, humans display the largest lipidomic difference in the brain compared to non-neural tissues, whereas mice reveal the smallest difference, as demonstrated in a lipidomic study of the brain cortex, kidney, and skeletal muscle of humans, primates (chimpanzee, macaque), and mice (Bozek et al., 2015). Comparing the lipid species of different tissues in humans to 31 mammalian species of rodents, primates, and bats revealed that the lipid composition of the brain cortex, heart, and kidney significantly differed from that of the tissues in the other species (Khrameeva et al., 2018). Given the high lipid complexity and the evolutionary distinct lipid composition of the human brain compared to other mammalian species, no effective compensatory mechanisms might have evolved to prevent neurological defects caused by impaired glycosphingolipid metabolism.

In mouse models of the lipid storage disorders Sandhoff disease, characterized by an accumulation of GM2, and Niemann-Pick type C (NPC) disease, the iminosugar NB-DNJ or Genz-529468 was administered to ameliorate glycosphingolipid accumulation (Ashe et al., 2011; Nietupski et al., 2012). Strikingly, in both studies, an accumulation of GlcCer in the CNS was observed, indicating that the used drugs not only inhibited GlcCer synthase, but also GBA2 (Ashe et al., 2011; Nietupski et al., 2012). In the Sandhoff and NPC disease background, NB-DNJ or Genz-529468 treatment was shown to improve neuropathic symptoms and prolong lifespan in mice (Ashe et al., 2011; Nietupski et al., 2012). However, NB-DNJ (Miglustat®,

Zavesca) administration in patients suffering from the neuronopathic form of Gaucher disease did not ameliorate their symptoms (Schiffmann et al., 2008). In contrast, non-neuronopathic Gaucher and NPC patients positively responded to treatment with three dosages of 100 mg or 200 mg Miglustat® (Zavesca) per day, respectively, as their GlcCer levels and liver and spleen enlargement was reduced (Aerts et al., 2006) and disease progression was slowed down (EMA: European public assessment report Miglustat® - Zavesca, 2009). However, the treatment is often accompanied by side effects such as peripheral neuropathy, ataxia, amnesia, paresthesia, hypoesthesia, dizziness, headache, or muscle weakness and cramps (EMA: European public assessment report Miglustat® - Zavesca, 2009). Thus, detailed analyses of other neuronopathic and non-neuronopathic lipid storage diseases with respect to GBA2 activity and function will help to refine the enzyme's role – also in the CNS – in relation to other glycosphingolipid synthases or hydrolases.

4.2.3 AMP-DNM – a potent GBA2 inhibitor applicable *in vivo*

My study shows that GBA2 can be inhibited by picomolar concentrations of AMP-DNM (IC_{50}: 1.7-4.8 pM) that do not affect GBA1 activity (see 3.11.1). AMP-DNM can also be used to inhibit GBA2 *in vivo* in rodents: A 2-week oral administration of 25 mg/kg AMP-DNM per day, yielding a constant plasma concentration of 108 nM AMP-DNM, significantly reduced GlcCer levels in liver and skeletal muscle in 6-week-old C57Bl/6J and obese (ob/ob) mice (Aerts et al., 2007). According to the IC_{50} values determined in previous studies, this concentration of AMP-DNM present in the plasma would induce inhibition of GBA2 (IC_{50}: 0.3-1.7 nM; *in vitro*), but not affect GBA1 (IC_{50}: 200 µM; *in vitro*) or GlcCer synthase activity (IC_{50}: 150 µM; *in vivo*) (Aerts et al., 2007; Wennekes et al., 2010). Another study reported a significant reduction of GlcCer in blood plasma and liver of 7-week-old obese (ob/ob) mice after 4-week oral administration of 100 mg/kg AMP-DNM per day (Wennekes et al., 2010). However, oral uptake of AMP-DNM also has an inhibitory effect on intestinal glucosidases, thereby affecting assimilation of carbohydrates and lowering blood glucose and insulin levels (Aerts et al., 2007; Wennekes et al., 2010). In summary, administration of AMP-DNM would also allow to study the effect on brain function upon loss of GBA2 activity. In line with the studies already performed in this thesis, loss of GBA2 could be induced at specific time points during development, which would prevent compensation by other mechanisms. Alternatively, an inducible GBA2-knockout mouse model could be generated, e.g. by utilizing the tetracycline-inducible transgenic approach. Introduction of a tetracycline-responsive promotor element (TRE) would allow to control the expression of GBA2 by tetracycline. In the Tet-Off expression system, the tetracycline-controlled transactivator protein (tTA) binds to the TRE and activates transcription (Saunders, 2011). Administration of tetracycline to these transgenic mice prevents binding of tTA to the TRE, thereby, inactivating transcription (Saunders, 2011).

5 References

Aerts, J. M., Hollak, C. E., Boot, R. G., Groener, J. E. & Maas, M. (2006). "Substrate reduction therapy of glycosphingolipid storage disorders". *J Inherit Metab Dis* **29**, p. 449-456

Aerts, J. M., Ottenhoff, R., Powlson, A. S., Grefhorst, A., van Eijk, M., Dubbelhuis, P. F., Aten, J., Kuipers, F., Serlie, M. J., Wennekes, T., Sethi, J. K., O'Rahilly, S. & Overkleeft, H. S. (2007). "Pharmacological inhibition of glucosylceramide synthase enhances insulin sensitivity". *Diabetes* **56**, p. 1341-1349

Aguilar, C. F., Sanderson, I., Moracci, M., Ciaramella, M., Nucci, R., Rossi, M. & Pearl, L. H. (1997). "Crystal structure of the beta-glycosidase from the hyperthermophilic archeon Sulfolobus solfataricus: resilience as a key factor in thermostability". *J Mol Biol* **271**, p. 789-802

Akiyama, H., Sasaki, N., Hanazawa, S., Gotoh, M., Kobayashi, S., Hirabayashi, Y. & Murakami-Murofushi, K. (2011). "Novel sterol glucosyltransferase in the animal tissue and cultured cells: evidence that glucosylceramide as glucose donor". *Biochim Biophys Acta* **1811**, p. 314-322

Aleshin, A. E., Feng, P. H., Honzatko, R. B. & Reilly, P. J. (2003). "Crystal structure and evolution of a prokaryotic glucoamylase". *J Mol Biol* **327**, p. 61-73

Ali, M. R., Cheng, K. H. & Huang, J. Y. (2007). "Assess the nature of cholesterol-lipid interactions through the chemical potential of cholesterol in phosphatidylcholine bilayers". *Proc Natl Acad Sci U S A* **104**, p. 5372-5377

Amende, I., Kale, A., McCue, S., Glazier, S., Morgan, J. P. & Hampton, T. G. (2005). "Gait dynamics in mouse models of Parkinson's disease and Huntington's disease". *J Neuroeng Rehabil* **2**, p. 20

Arber, S., Barbayannis, F. A., Hanser, H., Schneider, C., Stanyon, C. A., Bernard, O. & Caroni, P. (1998). "Regulation of actin dynamics through phosphorylation of cofilin by LIM-kinase". *Nature* **393**, p. 805-809

Asano, N. (2003). "Naturally occurring iminosugars and related compounds: structure, distribution, and biological activity". *Curr Top Med Chem* **3**, p. 471-484

Ashe, K. M., Bangari, D., Li, L., Cabrera-Salazar, M. A., Bercury, S. D., Nietupski, J. B., Cooper, C. G., Aerts, J. M., Lee, E. R., Copeland, D. P., Cheng, S. H., Scheule, R. K. & Marshall, J. (2011). "Iminosugar-based inhibitors of glucosylceramide synthase increase brain glycosphingolipids and survival in a mouse model of Sandhoff disease". *PLoS One* **6**, p. e21758

Aureli, M., Gritti, A., Bassi, R., Loberto, N., Ricca, A., Chigorno, V., Prinetti, A. & Sonnino, S. (2012). "Plasma membrane-associated glycohydrolases along differentiation of murine neural stem cells". *Neurochem Res* **37**, p. 1344-1354

Barez-Lopez, S., Bosch-Garcia, D., Gomez-Andres, D., Pulido-Valdeolivas, I., Montero-Pedrazuela, A., Obregon, M. J. & Guadano-Ferraz, A. (2014). "Abnormal Motor Phenotype at Adult Stages in Mice Lacking Type 2 Deiodinase". *PLoS One* **9**

Barlow, D. J. & Thornton, J. M. (1983). "Ion-pairs in proteins". *J Mol Biol* **168**, p. 867-885

Basu, S., Kaufman, B. & Roseman, S. (1968). "Enzymatic synthesis of ceramide-glucose and ceramide-lactose by glycosyltransferases from embryonic chicken brain". *J Biol Chem* **243**, p. 5802-5804

Bellettato, C. M. & Scarpa, M. (2010). "Pathophysiology of neuropathic lysosomal storage disorders". *J Inherit Metab Dis* **33**, p. 347-362

Bentham, M., Mazaleyrat, S. & Harris, M. (2006). "Role of myristoylation and N-terminal basic residues in membrane association of the human immunodeficiency virus type 1 Nef protein". *J Gen Virol* **87**, p. 563-571

Berent, B. L. & Radin, N. S. (1981). "beta-Glucosidase activator protein from bovine spleen ("coglucosidase")". *Arch Biochem Biophys* **208**, p. 248-260

Berg-Fussman, A., Grace, M. E., Ioannou, Y. & Grabowski, G. A. (1993). "Human acid beta-glucosidase. N-glycosylation site occupancy and the effect of glycosylation on enzymatic activity". *J Biol Chem* **268**, p. 14861-14866

Bergmann, J. E. & Grabowski, G. A. (1989). "Posttranslational processing of human lysosomal acid beta-glucosidase: a continuum of defects in Gaucher disease type 1 and type 2 fibroblasts". *Am J Hum Genet* **44**, p. 741-750

Bethani, I., Skanland, S. S., Dikic, I. & Acker-Palmer, A. (2010). "Spatial organization of transmembrane receptor signalling". *EMBO J* **29**, p. 2677-2688

Birnboim, H. C. & Doly, J. (1979). "A rapid alkaline extraction procedure for screening recombinant plasmid DNA". *Nucleic Acids Res* **7**, p. 1513-1523

Blanz, J. & Saftig, P. (2016). "Parkinson's disease: acid-glucocerebrosidase activity and alpha-synuclein clearance". *J Neurochem* **139 Suppl 1**, p. 198-215

Bloch, K. (1992). "Sterol molecule: structure, biosynthesis, and function". *Steroids* **57**, p. 378-383

Boivin, D. & Beliveau, R. (1995). "Subcellular distribution and membrane association of Rho-related small GTP-binding proteins in kidney cortex". *Am J Physiol* **269**, p. F180-189

Boot, R. G., Verhoek, M., Donker-Koopman, W., Strijland, A., van Marle, J., Overkleeft, H. S., Wennekes, T. & Aerts, J. M. (2007). "Identification of the non-lysosomal glucosylceramidase as beta-glucosidase 2". *J Biol Chem* **282**, p. 1305-1312

Borders, C. L., Jr., Broadwater, J. A., Bekeny, P. A., Salmon, J. E., Lee, A. S., Eldridge, A. M. & Pett, V. B. (1994). "A structural role for arginine in proteins: multiple hydrogen bonds to backbone carbonyl oxygens". *Protein Sci* **3**, p. 541-548

Bos, J. L., Rehmann, H. & Wittinghofer, A. (2007). "GEFs and GAPs: critical elements in the control of small G proteins". *Cell* **129**, p. 865-877

Bozek, K., Wei, Y., Yan, Z., Liu, X., Xiong, J., Sugimoto, M., Tomita, M., Paabo, S., Sherwood, C. C., Hof, P. R., Ely, J. J., Li, Y., Steinhauser, D., Willmitzer, L., Giavalisco, P. & Khaitovich, P. (2015). "Organization and evolution of brain lipidome revealed by large-scale analysis of human, chimpanzee, macaque, and mouse tissues". *Neuron* **85**, p. 695-702

Brade, L., Vielhaber, G., Heinz, E. & Brade, H. (2000). "In vitro characterization of anti-glucosylceramide rabbit antisera". *Glycobiology* **10**, p. 629-636

Bradford, M. M. (1976). "A rapid and sensitive method for the quantitation of microgram quantities of protein utilizing the principle of protein-dye binding". *Anal Biochem* **72**, p. 248-254

Brady, R. O., Barton, N. W. & Grabowski, G. A. (1993). "The role of neurogenetics in Gaucher disease". *Arch Neurol* **50**, p. 1212-1224

Braun, T., Buschhausen-Denker, G., Bober, E., Tannich, E. & Arnold, H. H. (1989). "A novel human muscle factor related to but distinct from MyoD1 induces myogenic conversion in 10T1/2 fibroblasts". *EMBO J* **8**, p. 701-709

Braun, T., Winter, B., Bober, E. & Arnold, H. H. (1990). "Transcriptional activation domain of the muscle-specific gene-regulatory protein myf5". *Nature* **346**, p. 663-665

Breydo, L., Wu, J. W. & Uversky, V. N. (2012). "Alpha-synuclein misfolding and Parkinson's disease". *Biochim Biophys Acta* **1822**, p. 261-285

Brocca, P. & Sonnino, S. (1997). "Dynamics and spatial organization of surface gangliosides". *Trends in Glycoscience and Glycotechnology* **9**, p. 433-445

Brown, D. A. & Rose, J. K. (1992). "Sorting of GPI-anchored proteins to glycolipid-enriched membrane subdomains during transport to the apical cell surface". *Cell* **68**, p. 533-544

Buck, K. B. & Zheng, J. Q. (2002). "Growth cone turning induced by direct local modification of microtubule dynamics". *J Neurosci* **22**, p. 9358-9367

Carlier, M. F., Ducruix, A. & Pantaloni, D. (1999). "Signalling to actin: the Cdc42-N-WASP-Arp2/3 connection". *Chem Biol* **6**, p. R235-240

Chakrabandhu, K., Huault, S., Garmy, N., Fantini, J., Stebe, E., Mailfert, S., Marguet, D. & Hueber, A. O. (2008). "The extracellular glycosphingolipid-binding motif of Fas defines its internalization route, mode and outcome of signals upon activation by ligand". *Cell Death Differ* **15**, p. 1824-1837

Chalat, M., Menon, I., Turan, Z. & Menon, A. K. (2012). "Reconstitution of glucosylceramide flip-flop across endoplasmic reticulum: implications for mechanism of glycosphingolipid biosynthesis". *J Biol Chem* **287**, p. 15523-15532

Chambers, W. W. & Sprague, J. M. (1955). "Functional localization in the cerebellum. I. Organization in longitudinal cortico-nuclear zones and their contribution to the control of posture, both extrapyramidal and pyramidal". *Journal of Comparative Neurology* **103**, p. 105-129

Charoenwattanasatien, R., Pengthaisong, S., Breen, I., Mutoh, R., Sansenya, S., Hua, Y., Tankrathok, A., Wu, L., Songsiriritthigul, C., Tanaka, H., Williams, S. J., Davies, G. J., Kurisu, G. & Cairns, J. R. (2016). "Bacterial beta-Glucosidase Reveals the Structural and Functional Basis of Genetic Defects in Human Glucocerebrosidase 2 (GBA2)". *ACS Chem Biol* **11**, p. 1891-1900

Cheng, H., Almstrom, S., Gimenez-Llort, L., Chang, R., Ove Ogren, S., Hoffer, B. & Olson, L. (1997). "Gait analysis of adult paraplegic rats after spinal cord repair". *Exp Neurol* **148**, p. 544-557

Chng, J., Wang, T., Nian, R., Lau, A., Hoi, K. M., Ho, S. C., Gagnon, P., Bi, X. & Yang, Y. (2015). "Cleavage efficient 2A peptides for high level monoclonal antibody expression in CHO cells". *MAbs* **7**, p. 403-412

Christensen, P. C., Brideau, C., Poon, K. W., Doring, A., Yong, V. W. & Stys, P. K. (2014). "High-resolution fluorescence microscopy of myelin without exogenous probes". *Neuroimage* **87**, p. 42-54

Citterio, A., Arnoldi, A., Panzeri, E., D'Angelo, M. G., Filosto, M., Dilena, R., Arrigoni, F., Castelli, M., Maghini, C., Germiniasi, C., Menni, F., Martinuzzi, A., Bresolin, N. & Bassi, M. T. (2014). "Mutations in CYP2U1, DDHD2 and GBA2 genes are rare causes of complicated forms of hereditary spastic paraparesis". *J Neurol* **261**, p. 373-381

Clark, E. D. B. (1998). "Refolding of recombinant proteins". *Curr Opin Biotechnol* **9**, p. 157-163

Colella, R., Lu, C., Hodges, B., Wilkey, D. W. & Roisen, F. J. (2000). "GM1 enhances the association of neuron-specific MAP2 with actin in MAP2-transfected 3T3 cells". *Brain Res Dev Brain Res* **121**, p. 1-9

Collins, J. S. & Goldsmith, T. H. (1981). "Spectral properties of fluorescence induced by glutaraldehyde fixation". *J Histochem Cytochem* **29**, p. 411-414

Collis, P. S., O'Donnell, B. J., Barton, D. J., Rogers, J. A. & Flanegan, J. B. (1992). "Replication of poliovirus RNA and subgenomic RNA transcripts in transfected cells". *J Virol* **66**, p. 6480-6488

Connell, J. W., Allison, R. & Reid, E. (2016). "Quantitative Gait Analysis Using a Motorized Treadmill System Sensitively Detects Motor Abnormalities in Mice Expressing ATPase Defective Spastin". *PLoS One* **11**, p. e0152413

Cooper, R. A. (1978). "Influence of increased membrane cholesterol on membrane fluidity and cell function in human red blood cells". *J Supramol Struct* **8**, p. 413-430

Cox, T. M. (2001). "Gaucher disease: understanding the molecular pathogenesis of sphingolipidoses". *J Inherit Metab Dis* **24 Suppl 2**, p. 106-121; discussion 187-108

Cuzner, M. L. & Davison, A. N. (1968). "The lipid composition of rat brain myelin and subcellular fractions during development". *Biochem J* **106**, p. 29-34

D'Angelo, G., Polishchuk, E., Di Tullio, G., Santoro, M., Di Campli, A., Godi, A., West, G., Bielawski, J., Chuang, C. C., van der Spoel, A. C., Platt, F. M., Hannun, Y. A., Polishchuk, R., Mattjus, P. & De Matteis, M. A. (2007). "Glycosphingolipid synthesis requires FAPP2 transfer of glucosylceramide". *Nature* **449**, p. 62-67

de Felipe, P., Hughes, L. E., Ryan, M. D. & Brown, J. D. (2003). "Co-translational, intraribosomal cleavage of polypeptides by the foot-and-mouth disease virus 2A peptide". *J Biol Chem* **278**, p. 11441-11448

Deacon, R. M. (2013). "Measuring the strength of mice". *J Vis Exp* **76 (2610)**

Delorme, C., Brussow, H., Sidoti, J., Roche, N., Karlsson, K. A., Neeser, J. R. & Teneberg, S. (2001). "Glycosphingolipid binding specificities of rotavirus: identification of a sialic acid-binding epitope". *J Virol* **75**, p. 2276-2287

Dent, E. W. & Gertler, F. B. (2003). "Cytoskeletal dynamics and transport in growth cone motility and axon guidance". *Neuron* **40**, p. 209-227

Donnelly, M. L., Luke, G., Mehrotra, A., Li, X., Hughes, L. E., Gani, D. & Ryan, M. D. (2001). "Analysis of the aphthovirus 2A/2B polyprotein 'cleavage' mechanism indicates not a proteolytic reaction, but a novel translational effect: a putative ribosomal 'skip'". *J Gen Virol* **82**, p. 1013-1025

Edwards, D. C., Sanders, L. C., Bokoch, G. M. & Gill, G. N. (1999). "Activation of LIM-kinase by Pak1 couples Rac/Cdc42 GTPase signalling to actin cytoskeletal dynamics". *Nat Cell Biol* **1**, p. 253-259

EMA. Zavesca: EPAR Product Information - Summary of Product Characteristics (Marketing Authorization Number: EU/02/238/001; Actelion Registration Ltd, UK). (2009).

Ferreira, A., Busciglio, J. & Caceres, A. (1989). "Microtubule Formation and Neurite Growth in Cerebellar Macroneurons Which Develop Invitro - Evidence for the Involvement of the Microtubule-Associated Proteins, Map-1a, Hmw-Map2 and Tau". *Developmental Brain Research* **49**, p. 215-228

Ferreirinha, F., Quattrini, A., Pirozzi, M., Valsecchi, V., Dina, G., Broccoli, V., Auricchio, A., Piemonte, F., Tozzi, G., Gaeta, L., Casari, G., Ballabio, A. & Rugarli, E. I. (2004). "Axonal degeneration in paraplegin-deficient mice is associated with abnormal mitochondria and impairment of axonal transport". *J Clin Invest* **113**, p. 231-242

Filocamo, M. & Morrone, A. (2011). "Lysosomal storage disorders: molecular basis and laboratory testing". *Hum Genomics* **5**, p. 156-169

Finn, R. D., Attwood, T. K., Babbitt, P. C., Bateman, A., Bork, P., Bridge, A. J., Chang, H. Y., Dosztanyi, Z., El-Gebali, S., Fraser, M., Gough, J., Haft, D., Holliday, G. L., Huang, H., Huang, X., Letunic, I., Lopez, R., Lu, S., Marchler-Bauer, A., Mi, H., Mistry, J., Natale, D. A., Necci, M., Nuka, G., Orengo, C. A., Park, Y., Pesseat, S., Piovesan, D., Potter, S. C., Rawlings, N. D., Redaschi, N., Richardson, L., Rivoire, C., Sangrador-Vegas, A., Sigrist, C., Sillitoe, I., Smithers, B., Squizzato, S., Sutton, G., Thanki, N., Thomas, P. D., Tosatto, S. C., Wu, C. H., Xenarios, I., Yeh, L. S., Young, S. Y. & Mitchell, A. L. (2017). "InterPro in 2017-beyond protein family and domain annotations". *Nucleic Acids Res* **45**, p. D190-D199

Fitch, C. A., Platzer, G., Okon, M., Garcia-Moreno, B. E. & McIntosh, L. P. (2015). "Arginine: Its pKa value revisited". *Protein Sci* **24**, p. 752-761

Fleming, I. N., Elliott, C. M. & Exton, J. H. (1996). "Differential translocation of rho family GTPases by lysophosphatidic acid, endothelin-1, and platelet-derived growth factor". *J Biol Chem* **271**, p. 33067-33073

Fox, J. D. & Waugh, D. S. (2003). "Maltose-binding protein as a solubility enhancer". *Methods Mol Biol* **205**, p. 99-117

Fujita, H., Saeki, M., Yasunaga, K., Ueda, T., Imoto, T. & Himeno, M. (1999). "In vitro binding study of adaptor protein complex (AP-1) to lysosomal targeting motif (LI-motif)". *Biochem Biophys Res Commun* **255**, p. 54-58

Furst, W. & Sandhoff, K. (1992). "Activator proteins and topology of lysosomal sphingolipid catabolism". *Biochim Biophys Acta* **1126**, p. 1-16

Furuya, S., Ono, K. & Hirabayashi, Y. (1995). "Sphingolipid biosynthesis is necessary for dendrite growth and survival of cerebellar Purkinje cells in culture". *J Neurochem* **65**, p. 1551-1561

Futerman, A. H., Stieger, B., Hubbard, A. L. & Pagano, R. E. (1990). "Sphingomyelin synthesis in rat liver occurs predominantly at the cis and medial cisternae of the Golgi apparatus". *J Biol Chem* **265**, p. 8650-8657

Futerman, A. H. & Pagano, R. E. (1991). "Determination of the intracellular sites and topology of glucosylceramide synthesis in rat liver". *Biochem J* **280 (Pt 2)**, p. 295-302

Garcia-Mata, R., Boulter, E. & Burridge, K. (2011). "The 'invisible hand': regulation of RHO GTPases by RHOGDIs". *Nat Rev Mol Cell Biol* **12**, p. 493-504

Geeraert, L., Mannaerts, G. P. & van Veldhoven, P. P. (1997). "Conversion of dihydroceramide into ceramide: involvement of a desaturase". *Biochem J* **327 (Pt 1)**, p. 125-132

Gillard, B. K., Clement, R. G. & Marcus, D. M. (1998). "Variations among cell lines in the synthesis of sphingolipids in de novo and recycling pathways". *Glycobiology* **8**, p. 885-890

Ginkel, C., Hartmann, D., vom Dorp, K., Zlomuzica, A., Farwanah, H., Eckhardt, M., Sandhoff, R., Degen, J., Rabionet, M., Dere, E., Dormann, P., Sandhoff, K. & Willecke, K. (2012). "Ablation of neuronal ceramide synthase 1 in mice decreases ganglioside levels and expression of myelin-associated glycoprotein in oligodendrocytes". *J Biol Chem* **287**, p. 41888-41902

Gould, B. B. (1979). "The organization of afferents to the cerebellar cortex in the cat: projections from the deep cerebellar nuclei". *Journal of Comparative Neurology* **184**, p. 27-42

Grabe, M. & Oster, G. (2001). "Regulation of organelle acidity". *J Gen Physiol* **117**, p. 329-344

Grabowski, G. A., Osiecki-Newman, K., Dinur, T., Fabbro, D., Legler, G., Gatt, S. & Desnick, R. J. (1986). "Human acid beta-glucosidase. Use of conduritol B epoxide derivatives to investigate the catalytically active normal and Gaucher disease enzymes". *J Biol Chem* **261**, p. 8263-8269

Grace, M. E., Newman, K. M., Scheinker, V., Berg-Fussman, A. & Grabowski, G. A. (1994). "Analysis of human acid beta-glucosidase by site-directed mutagenesis and heterologous expression". *J Biol Chem* **269**, p. 2283-2291

Graf, L., Jancso, A., Szilagyi, L., Hegyi, G., Pinter, K., Narayszabo, G., Hepp, J., Medzihradszky, K. & Rutter, W. J. (1988). "Electrostatic Complementarity within the Substrate-Binding Pocket of Trypsin". *Proc Natl Acad Sci U S A* **85**, p. 4961-4965

Gudmundsson, M., Hansson, H., Karkehabadi, S., Larsson, A., Stals, I., Kim, S., Sunux, S., Fujdala, M., Larenas, E., Kaper, T. & Sandgren, M. (2016). "Structural and functional studies of the glycoside hydrolase family 3 beta-glucosidase Cel3A from the moderately thermophilic fungus Rasamsonia emersonii". *Acta Crystallogr D Struct Biol* **72**, p. 860-870

Hall, A. (1998). "Rho GTPases and the actin cytoskeleton". *Science* **279**, p. 509-514

Halling, K. K., Ramstedt, B. & Slotte, J. P. (2008). "Glycosylation induces shifts in the lateral distribution of cholesterol from ordered towards less ordered domains". *Biochim Biophys Acta* **1778**, p. 1100-1111

Hamers, F. P., Koopmans, G. C. & Joosten, E. A. (2006). "CatWalk-assisted gait analysis in the assessment of spinal cord injury". *J Neurotrauma* **23**, p. 537-548

Hammer, M. B., Eleuch-Fayache, G., Schottlaender, L. V., Nehdi, H., Gibbs, J. R., Arepalli, S. K., Chong, S. B., Hernandez, D. G., Sailer, A., Liu, G., Mistry, P. K., Cai, H., Shrader, G., Sassi, C., Bouhlal, Y., Houlden, H., Hentati, F., Amouri, R. & Singleton, A. B. (2013). "Mutations in GBA2 cause autosomal-recessive cerebellar ataxia with spasticity". *Am J Hum Genet* **92**, p. 245-251

Hanada, K., Kumagai, K., Yasuda, S., Miura, Y., Kawano, M., Fukasawa, M. & Nishijima, M. (2003). "Molecular machinery for non-vesicular trafficking of ceramide". *Nature* **426**, p. 803-809

Harel, R. & Futerman, A. H. (1993). "Inhibition of sphingolipid synthesis affects axonal outgrowth in cultured hippocampal neurons". *J Biol Chem* **268**, p. 14476-14481

Harms, M. J., Schlessman, J. L., Sue, G. R. & Garcia-Moreno, B. (2011). "Arginine residues at internal positions in a protein are always charged". *Proc Natl Acad Sci U S A* **108**, p. 18954-18959

Haugarvoll, K., Johansson, S., Rodriguez, C. E., Boman, H., Haukanes, B. I., Bruland, O., Roque, F., Jonassen, I., Blomqvist, M., Telstad, W., Mansson, J. E., Knappskog, P. M. & Bindoff, L. A. (2017). "GBA2 Mutations Cause a Marinesco-Sjogren-Like Syndrome: Genetic and Biochemical Studies". *PLoS One* **12**, p. e0169309

Heckroth, J. A., Goldowitz, D. & Eisenman, L. M. (1989). "Purkinje-Cell Reduction in the Reeler Mutant Mouse - a Quantitative Immunohistochemical Study". *Journal of Comparative Neurology* **279**, p. 546-555

Hildebrand, J. & Hauser, G. (1969). "Biosynthesis of Lactosylceramide and Triglycosylceramide by Galactosyltransferases from Rat Spleen". *Journal of Biological Chemistry* **244**, p. 5170-+

Ho, M. W., O'Brien, J. S., Radin, N. S. & Erickson, J. S. (1973). "Glucocerebrosidase: reconstitution of activity from macromolecular components". *Biochem J* **131**, p. 173-176

Hoffman, L. M., Amsterdam, D. & Schneck, L. (1976). "GM2 ganglioside in fetal Tay-Sachs disease brain cultures: a model system for the disease". *Brain Res* **111**, p. 109-117

Hoffmann, B. & Mayatepek, E. (2005). "Neurological manifestations in lysosomal storage disorders - from pathology to first therapeutic possibilities". *Neuropediatrics* **36**, p. 285-289

Holub, B. J. & Kuksis, A. (1978). "Metabolism of molecular species of diacylglycerophospholipids". *Adv Lipid Res* **16**, p. 1-125

Hoogland, T. M., De Gruijl, J. R., Witter, L., Canto, C. B. & De Zeeuw, C. I. (2015). "Role of Synchronous Activation of Cerebellar Purkinje Cell Ensembles in Multi-joint Movement Control". *Curr Biol* **25**, p. 1157-1165

Hooper, N. M. (1999). "Detergent-insoluble glycosphingolipid/cholesterol-rich membrane domains, lipid rafts and caveolae (review)". *Mol Membr Biol* **16**, p. 145-156

Huang, J. Q., Trasler, J. M., Igdoura, S., Michaud, J., Hanal, N. & Gravel, R. A. (1997). "Apoptotic cell death in mouse models of GM2 gangliosidosis and observations on human Tay-Sachs and Sandhoff diseases". *Hum Mol Genet* **6**, p. 1879-1885

Ilangumaran, S. & Hoessli, D. C. (1998). "Effects of cholesterol depletion by cyclodextrin on the sphingolipid microdomains of the plasma membrane". *Biochem J* **335 (Pt 2)**, p. 433-440

Isom, D. G., Castaneda, C. A., Cannon, B. R. & Garcia-Moreno, B. (2011). "Large shifts in pKa values of lysine residues buried inside a protein". *Proc Natl Acad Sci U S A* **108**, p. 5260-5265

Jacewicz, M., Clausen, H., Nudelman, E., Donohuerolfe, A. & Keusch, G. T. (1986). "Pathogenesis of Shigella Diarrhea .11. Isolation of a Shigella Toxin-Binding Glycolipid from Rabbit Jejunum and Hela-Cells and Its Identification as Globotriaosylceramide". *Journal of Experimental Medicine* **163**, p. 1391-1404

Kado, Y., Inoue, T. & Ishikawa, K. (2011). "Structure of hyperthermophilic beta-glucosidase from Pyrococcus furiosus". *Acta Crystallogr Sect F Struct Biol Cryst Commun* **67**, p. 1473-1479

Kapust, R. B. & Waugh, D. S. (1999). "Escherichia coli maltose-binding protein is uncommonly effective at promoting the solubility of polypeptides to which it is fused". *Protein Sci* **8**, p. 1668-1674

Khrameeva, E., Kurochkin, I., Bozek, K., Giavalisco, P. & Khaitovich, P. (2018). "Lipidome evolution in mammalian tissues". *Mol Biol Evol*

Klenk, E. (1951). "[Contribution to the concept of gangliosides]". *Hoppe Seylers Z Physiol Chem* **288**, p. 216-220

Kloos, A. D., Fisher, L. C., Detloff, M. R., Hassenzahl, D. L. & Basso, D. M. (2005). "Stepwise motor and all-or-none sensory recovery is associated with nonlinear sparing after incremental spinal cord injury in rats". *Exp Neurol* **191**, p. 251-265

Kolodny, E. H., Brady, R. O. & Volk, B. W. (1969). "Demonstration of an alteration of ganglioside metabolism in Tay-Sachs disease". *Biochem Biophys Res Commun* **37**, p. 526-531

Kolter, T. & Sandhoff, K. (2010). "Lysosomal degradation of membrane lipids". *Febs Letters* **584**, p. 1700-1712

Kooijman, E. E., Tieleman, D. P., Testerink, C., Munnik, T., Rijkers, D. T. S., Burger, K. N. J. & de Kruijff, B. (2007). "An electrostatic/hydrogen bond switch as the basis for the specific interaction of phosphatidic acid with proteins". *Journal of Biological Chemistry* **282**, p. 11356-11364

Körschen, H. G., Yildiz, Y., Raju, D. N., Schonauer, S., Bonigk, W., Jansen, V., Kremmer, E., Kaupp, U. B. & Wachten, D. (2013). "The non-lysosomal beta-glucosidase GBA2 is a non-integral membrane-associated protein at the endoplasmic reticulum (ER) and Golgi". *J Biol Chem* **288**, p. 3381-3393

Kuziemko, G. M., Stroh, M. & Stevens, R. C. (1996). "Cholera toxin binding affinity and specificity for gangliosides determined by surface plasmon resonance". *Biochemistry* **35**, p. 6375-6384

Laemmli, U. K. (1970). "Cleavage of structural proteins during the assembly of the head of bacteriophage T4". *Nature* **227**, p. 680-685

Landis, S. C. (1973). "Ultrastructural changes in the mitochondria of cerebellar Purkinje cells of nervous mutant mice". *J Cell Biol* **57**, p. 782-797

Lang, B. J. & Legates, J. E. (1969). "Rate, composition and efficiency of growth in mice selected for large and small body weight". *Theor Appl Genet* **39**, p. 306-314

Lannert, H., Bunning, C., Jeckel, D. & Wieland, F. T. (1994). "Lactosylceramide Is Synthesized in the Lumen of the Golgi-Apparatus". *Febs Letters* **342**, p. 91-96

Larsell, O. (1952). "The morphogenesis and adult pattern of the lobules and fissures of the cerebellum of the white rat". *Journal of Comparative Neurology* **97**, p. 281-356

Larsell, O. (1958). "Lobules of the Mammalian and Human Cerebellum". *Anatomical Record* **130**, p. 329-330

Letourneau, P. C., Shattuck, T. A. & Ressler, A. H. (1987). ""Pull" and "push" in neurite elongation: observations on the effects of different concentrations of cytochalasin B and taxol". *Cell Motil Cytoskeleton* **8**, p. 193-209

Levental, I., Lingwood, D., Grzybek, M., Coskun, U. & Simons, K. (2010). "Palmitoylation regulates raft affinity for the majority of integral raft proteins". *Proc Natl Acad Sci U S A* **107**, p. 22050-22054

Levy, M. & Futerman, A. H. (2010). "Mammalian ceramide synthases". *IUBMB Life* **62**, p. 347-356

Li, L., Vorobyov, I. & Allen, T. W. (2013). "The different interactions of lysine and arginine side chains with lipid membranes". *J Phys Chem B* **117**, p. 11906-11920

Li, X. Y., Lu, H. H., Mueller, S. & Wimmer, E. (2001). "The C-terminal residues of poliovirus proteinase 2A(pro) are critical for viral RNA replication but not for cis- or trans-proteolytic cleavage". *Journal of General Virology* **82**, p. 397-408

Lichtenberg, D., Goni, F. M. & Heerklotz, H. (2005). "Detergent-resistant membranes should not be identified with membrane rafts". *Trends in Biochemical Sciences* **30**, p. 430-436

Lilie, H., Schwarz, E. & Rudolph, R. (1998). "Advances in refolding of proteins produced in E. coli". *Curr Opin Biotechnol* **9**, p. 497-501

Lingwood, D. & Simons, K. (2007). "Detergent resistance as a tool in membrane research". *Nat Protoc* **2**, p. 2159-2165

Liu, A., Wenzel, N. & Qi, X. (2005). "Role of lysine residues in membrane anchoring of saposin C". *Arch Biochem Biophys* **443**, p. 101-112

Luke, G. A., de Felipe, P., Lukashev, A., Kallioinen, S. E., Bruno, E. A. & Ryan, M. D. (2008). "Occurrence, function and evolutionary origins of '2A-like' sequences in virus genomes". *J Gen Virol* **89**, p. 1036-1042

Ly, P. T., Singh, S. & Shaw, C. A. (2007). "Novel environmental toxins: steryl glycosides as a potential etiological factor for age-related neurodegenerative diseases". *J Neurosci Res* **85**, p. 231-237

Mandel, M. & Higa, A. (1970). "Calcium-dependent bacteriophage DNA infection". *J Mol Biol* **53**, p. 159-162

Mandon, E. C., Ehses, I., Rother, J., van Echten, G. & Sandhoff, K. (1992). "Subcellular localization and membrane topology of serine palmitoyltransferase, 3-dehydrosphinganine reductase, and sphinganine N-acyltransferase in mouse liver". *J Biol Chem* **267**, p. 11144-11148

Manser, E., Leung, T., Salihuddin, H., Zhao, Z. S. & Lim, L. (1994). "A brain serine/threonine protein kinase activated by Cdc42 and Rac1". *Nature* **367**, p. 40-46

Marques, A. R., Mirzaian, M., Akiyama, H., Wisse, P., Ferraz, M. J., Gaspar, P., Ghauharali-van der Vlugt, K., Meijer, R., Giraldo, P., Alfonso, P., Irun, P., Dahl, M., Karlsson, S., Pavlova, E. V., Cox, T. M., Scheij, S., Verhoek, M., Ottenhoff, R., van Roomen, C. P., Pannu, N. S., van Eijk, M., Dekker, N., Boot, R. G., Overkleeft, H. S., Blommaart, E., Hirabayashi, Y. & Aerts, J. M. (2016). "Glucosylated cholesterol in mammalian cells and tissues: formation and degradation by multiple cellular beta-glucosidases". *J Lipid Res* **57**, p. 451-463

Martin, E., Schule, R., Smets, K., Rastetter, A., Boukhris, A., Loureiro, J. L., Gonzalez, M. A., Mundwiller, E., Deconinck, T., Wessner, M., Jornea, L., Oteyza, A. C., Durr, A., Martin, J. J., Schols, L., Mhiri, C., Lamari, F., Zuchner, S., De Jonghe, P., Kabashi, E., Brice, A. & Stevanin, G. (2013). "Loss of function of glucocerebrosidase GBA2 is responsible for motor neuron defects in hereditary spastic paraplegia". *Am J Hum Genet* **92**, p. 238-244

Matern, H., Gartzen, R. & Matern, S. (1992). "Beta-Glucosidase Activity Towards a Bile-Acid Glucoside in Human Liver". *Febs Letters* **314**, p. 183-186

Matern, H., Heinemann, H., Legler, G. & Matern, S. (1997). "Purification and characterization of a microsomal bile acid beta-glucosidase from human liver". *J Biol Chem* **272**, p. 11261-11267

Matern, H., Boermans, H., Lottspeich, F. & Matern, S. (2001). "Molecular cloning and expression of human bile acid beta-glucosidase". *J Biol Chem* **276**, p. 37929-37933

Maxfield, F. R. & Yamashiro, D. J. (1987). "Endosome acidification and the pathways of receptor-mediated endocytosis". *Adv Exp Med Biol* **225**, p. 189-198

Maxwell, K. N., Zhou, Y. & Hancock, J. F. (2018). "Rac1 nanoscale organization on the plasma membrane is driven by lipid binding specificity encoded in the membrane anchor". *Mol Cell Biol*

McAndrew, R. P., Park, J. I., Heins, R. A., Reindl, W., Friedland, G. D., D'Haeseleer, P., Northen, T., Sale, K. L., Simmons, B. A. & Adams, P. D. (2013). "From soil to structure, a novel dimeric beta-glucosidase belonging to glycoside hydrolase family 3 isolated from compost using metagenomic analysis". *J Biol Chem* **288**, p. 14985-14992

Migdalska-Richards, A. & Schapira, A. H. V. (2016). "The relationship between glucocerebrosidase mutations and Parkinson disease". *J Neurochem* **139**, p. 77-90

Mimura, F., Yamagishi, S., Arimura, N., Fujitani, M., Kubo, T., Kaibuchi, K. & Yamashita, T. (2006). "Myelin-associated glycoprotein inhibits microtubule assembly by a Rho-kinase-dependent mechanism". *J Biol Chem* **281**, p. 15970-15979

Moissoglu, K. & Schwartz, M. A. (2014). "Spatial and temporal control of Rho GTPase functions". *Cell Logist* **4**, p. e943618

Molla, A., Paul, A. V., Schmid, M., Jang, S. K. & Wimmer, E. (1993). "Studies on dicistronic polioviruses implicate viral proteinase 2Apro in RNA replication". *Virology* **196**, p. 739-747

Morell, P. & Radin, N. S. (1969). "Synthesis of cerebroside by brain from uridine diphosphate galactose and ceramide containing hydroxy fatty acid". *Biochemistry* **8**, p. 506-512

Mullen, R. J., Eicher, E. M. & Sidman, R. L. (1976). "Purkinje cell degeneration, a new neurological mutation in the mouse". *Proc Natl Acad Sci U S A* **73**, p. 208-212

Mullins, R. D., Heuser, J. A. & Pollard, T. D. (1998). "The interaction of Arp2/3 complex with actin: nucleation, high affinity pointed end capping, and formation of branching networks of filaments". *Proc Natl Acad Sci U S A* **95**, p. 6181-6186

Neumann, M., Wang, Y., Kim, S., Hong, S. M., Jeng, L., Bilgen, M. & Liu, J. (2009). "Assessing gait impairment following experimental traumatic brain injury in mice". *J Neurosci Methods* **176**, p. 34-44

Ngamukote, S., Yanagisawa, M., Ariga, T., Ando, S. & Yu, R. K. (2007). "Developmental changes of glycosphingolipids and expression of glycogenes in mouse brains". *J Neurochem* **103**, p. 2327-2341

Nietupski, J. B., Pacheco, J. J., Chuang, W. L., Maratea, K., Li, L., Foley, J., Ashe, K. M., Cooper, C. G., Aerts, J. M., Copeland, D. P., Scheule, R. K., Cheng, S. H. & Marshall, J. (2012). "Iminosugar-based inhibitors of glucosylceramide synthase prolong survival but paradoxically increase brain glucosylceramide levels in Niemann-Pick C mice". *Mol Genet Metab* **105**, p. 621-628

Nobes, C. D. & Hall, A. (1995). "Rho, Rac and Cdc42 Gtpases - Regulators of Actin Structures, Cell-Adhesion and Motility". *Biochemical Society Transactions* **23**, p. 456-459

Norman, D. J., Feng, L., Cheng, S. S., Gubbay, J., Chan, E. & Heintz, N. (1995). "The Lurcher Gene Induces Apoptotic Death in Cerebellar Purkinje-Cells". *Development* **121**, p. 1183-1193

Nowak, A., Mechtler, T. P., Hornemann, T., Gawinecka, J., Theswet, E., Hilz, M. J. & Kasper, D. C. (2018). "Genotype, phenotype and disease severity reflected by serum LysoGb3 levels in patients with Fabry disease". *Mol Genet Metab* **123**, p. 148-153

Okazaki, T., Bell, R. M. & Hannun, Y. A. (1989). "Sphingomyelin turnover induced by vitamin D3 in HL-60 cells. Role in cell differentiation". *J Biol Chem* **264**, p. 19076-19080

Overkleeft, H. S., Renkema, G. H., Neele, J., Vianello, P., Hung, I. O., Strijland, A., van der Burg, A. M., Koomen, G. J., Pandit, U. K. & Aerts, J. M. (1998). "Generation of specific deoxynojirimycin-type inhibitors of the non-lysosomal glucosylceramidase". *J Biol Chem* **273**, p. 26522-26527

Palay, S. L. & Chan-Palay, V. (1974). *Cerebellar cortex : cytology and organization*. (Springer)

Patel, A., Williams-Perez, S., Peyton, N., Reicks, A., Buzick, J., Farley, J., Shirar, S. & Ellerbroek, S. M. (2017). "Arg188 drives RhoC membrane binding". *Small GTPases* **8**, p. 114-121

Paulsen, H. & Todt, K. (1968). "Cyclic monosaccharides having nitrogen of sulfur in the ring". *Adv Carbohydr Chem Biochem* **23**, p. 115-232

Pennelli, N., Scaravilli, F. & Zacchello, F. (1969). "The morphogenesis of Gaucher cells investigated by electron microscopy". *Blood* **34**, p. 331-347

Platt, F. M., Neises, G. R., Dwek, R. A. & Butters, T. D. (1994). "N-butyldeoxynojirimycin is a novel inhibitor of glycolipid biosynthesis". *J Biol Chem* **269**, p. 8362-8365

Platt, F. M., Reinkensmeier, G., Dwek, R. A. & Butters, T. D. (1997). "Extensive glycosphingolipid depletion in the liver and lymphoid organs of mice treated with N-butyldeoxynojirimycin". *J Biol Chem* **272**, p. 19365-19372

Platt, F. M., Boland, B. & van der Spoel, A. C. (2012). "The cell biology of disease: lysosomal storage disorders: the cellular impact of lysosomal dysfunction". *J Cell Biol* **199**, p. 723-734

Proia, R. L. (2004). "Gangliosides help stabilize the brain". *Nat Genet* **36**, p. 1147-1148

Pryor, P. R. & Luzio, J. P. (2009). "Delivery of endocytosed membrane proteins to the lysosome". *Biochim Biophys Acta* **1793**, p. 615-624

Raffy, S. & Teissie, J. (1999). "Control of lipid membrane stability by cholesterol content". *Biophys J* **76**, p. 2072-2080

Raju, D., Schonauer, S., Hamzeh, H., Flynn, K. C., Bradke, F., Vom Dorp, K., Dormann, P., Yildiz, Y., Trotschel, C., Poetsch, A., Breiden, B., Sandhoff, K., Korschen, H. G. & Wachten, D. (2015). "Accumulation of glucosylceramide in the absence of the beta-glucosidase GBA2 alters cytoskeletal dynamics". *PLoS Genet* **11**, p. e1005063

Ramón y Cajal, S., London County Council & Azoulay, L. (1909). *Histologie du système nerveux de l'homme & des vertébrés*. (A. Maloine)

Reczek, D., Schwake, M., Schroder, J., Hughes, H., Blanz, J., Jin, X., Brondyk, W., Van Patten, S., Edmunds, T. & Saftig, P. (2007). "LIMP-2 is a receptor for lysosomal mannose-6-phosphate-independent targeting of beta-glucocerebrosidase". *Cell* **131**, p. 770-783

Rice, P., Longden, I. & Bleasby, A. (2000). "EMBOSS: the European Molecular Biology Open Software Suite". *Trends Genet* **16**, p. 276-277

Ridley, A. J., Paterson, H. F., Johnston, C. L., Diekmann, D. & Hall, A. (1992). "The small GTP-binding protein rac regulates growth factor-induced membrane ruffling". *Cell* **70**, p. 401-410

Ridley, A. J. (2006). "Rho GTPases and actin dynamics in membrane protrusions and vesicle trafficking". *Trends Cell Biol* **16**, p. 522-529

Roberts, P. J., Mitin, N., Keller, P. J., Chenette, E. J., Madigan, J. P., Currin, R. O., Cox, A. D., Wilson, O., Kirschmeier, P. & Der, C. J. (2008). "Rho Family GTPase modification and

dependence on CAAX motif-signaled posttranslational modification". *J Biol Chem* **283**, p. 25150-25163

Rohrbach, M. & Clarke, J. T. (2007). "Treatment of lysosomal storage disorders : progress with enzyme replacement therapy". *Drugs* **67**, p. 2697-2716

Rother, J., van Echten, G., Schwarzmann, G. & Sandhoff, K. (1992). "Biosynthesis of sphingolipids: dihydroceramide and not sphinganine is desaturated by cultured cells". *Biochem Biophys Res Commun* **189**, p. 14-20

Samsonov, A. V., Mihalyov, I. & Cohen, F. S. (2001). "Characterization of cholesterol-sphingomyelin domains and their dynamics in bilayer membranes". *Biophys J* **81**, p. 1486-1500

Sargiacomo, M., Sudol, M., Tang, Z. & Lisanti, M. P. (1993). "Signal transducing molecules and glycosyl-phosphatidylinositol-linked proteins form a caveolin-rich insoluble complex in MDCK cells". *J Cell Biol* **122**, p. 789-807

Saunders, T. L. (2011). "Inducible transgenic mouse models". *Methods Mol Biol* **693**, p. 103-115

Scherer, M., Leuthauser-Jaschinski, K., Ecker, J., Schmitz, G. & Liebisch, G. (2010). "A rapid and quantitative LC-MS/MS method to profile sphingolipids". *J Lipid Res* **51**, p. 2001-2011

Schiffmann, R., Fitzgibbon, E. J., Harris, C., DeVile, C., Davies, E. H., Abel, L., van Schaik, I. N., Benko, W., Timmons, M., Ries, M. & Vellodi, A. (2008). "Randomized, controlled trial of miglustat in Gaucher's disease type 3". *Ann Neurol* **64**, p. 514-522

Schonauer, S., Korschen, H. G., Penno, A., Rennhack, A., Breiden, B., Sandhoff, K., Gutbrod, K., Dormann, P., Raju, D. N., Haberkant, P., Gerl, M. J., Brugger, B., Zigdon, H., Vardi, A., Futerman, A. H., Thiele, C. & Wachten, D. (2017). "Identification of a feedback loop involving beta-glucosidase 2 and its product sphingosine sheds light on the molecular mechanisms in Gaucher disease". *J Biol Chem* **292**, p. 6177-6189

Schulte, S. & Stoffel, W. (1993). "Ceramide Udpgalactosyltransferase from Myelinating Rat-Brain - Purification, Cloning, and Expression". *Proc Natl Acad Sci U S A* **90**, p. 10265-10269

Schwarz, A. & Futerman, A. H. (1997). "Distinct roles for ceramide and glucosylceramide at different stages of neuronal growth". *J Neurosci* **17**, p. 2929-2938

Schwarzmann, G. & Sandhoff, K. (1990). "Metabolism and intracellular transport of glycosphingolipids". *Biochemistry* **29**, p. 10865-10871

Schweizer, A., Clausen, H., Van Meer, G. & Hauri, H. P. (1994). "Localization of O-Glycan Initiation, Sphingomyelin Synthesis, and Glucosylceramide Synthesis in Vero Cells with Respect to the Endoplasmic Reticulum-Golgi Intermediate Compartment". *Journal of Biological Chemistry* **269**, p. 4035-4041

Scriver, C. R. (1995). *The metabolic and molecular bases of inherited disease*. 7th ed edn, (McGraw-Hill, Health Professions Division)

Sheets, E. D., Holowka, D. & Baird, B. (1999). "Critical role for cholesterol in Lyn-mediated tyrosine phosphorylation of Fc epsilon RI and their association with detergent-resistant membranes". *Journal of Cell Biology* **145**, p. 877-887

Shimada, A., Ohta, A., Akiguchi, I. & Takeda, T. (1992). "Inbred SAM-P/10 as a mouse model of spontaneous, inherited brain atrophy". *J Neuropathol Exp Neurol* **51**, p. 440-450

Sidransky, E. & Lopez, G. (2012). "The link between the GBA gene and parkinsonism". *Lancet Neurology* **11**, p. 986-998

Simons, K. & van Meer, G. (1988). "Lipid sorting in epithelial cells". *Biochemistry* **27**, p. 6197-6202

Simons, K. & Ikonen, E. (1997). "Functional rafts in cell membranes". *Nature* **387**, p. 569-572

Simons, K. & Toomre, D. (2000). "Lipid rafts and signal transduction". *Nat Rev Mol Cell Biol* **1**, p. 31-39

Simpson, M. A., Cross, H., Proukakis, C., Priestman, D. A., Neville, D. C., Reinkensmeier, G., Wang, H., Wiznitzer, M., Gurtz, K., Verganelaki, A., Pryde, A., Patton, M. A., Dwek, R. A., Butters, T. D., Platt, F. M. & Crosby, A. H. (2004). "Infantile-onset symptomatic epilepsy syndrome caused by a homozygous loss-of-function mutation of GM3 synthase". *Nat Genet* **36**, p. 1225-1229

Slotte, J. P. (1999). "Sphingomyelin-cholesterol interactions in biological and model membranes". *Chem Phys Lipids* **102**, p. 13-27

Sprong, H., Kruithof, B., Leijendekker, R., Slot, J. W., van Meer, G. & van der Sluijs, P. (1998). "UDP-galactose:ceramide galactosyltransferase is a class I integral membrane protein of the endoplasmic reticulum". *J Biol Chem* **273**, p. 25880-25888

Stoffel, W., LeKim, D. & Sticht, G. (1968). "Metabolism of sphingosine bases. 8. Distribution, isolation and properties of D-3-oxosphinganine reductase. Stereospecificity of the NADPH-dependent reaction of 3-oxodihydrospingosine (2-amino-1-hydroxyoctadecane-3-one)". *Hoppe Seylers Z Physiol Chem* **349**, p. 1637-1644

Stults, C. L., Sweeley, C. C. & Macher, B. A. (1989). "Glycosphingolipids: structure, biological source, and properties". *Methods Enzymol* **179**, p. 167-214

Suetsugu, S., Kurisu, S., Oikawa, T., Yamazaki, D., Oda, A. & Takenawa, T. (2006). "Optimization of WAVE2 complex-induced actin polymerization by membrane-bound IRSp53, PIP(3), and Rac". *J Cell Biol* **173**, p. 571-585

Sugiki, T., Takeuchi, K., Yamaji, T., Takano, T., Tokunaga, Y., Kumagai, K., Hanada, K., Takahashi, H. & Shimada, I. (2012). "Structural basis for the Golgi association by the pleckstrin homology domain of the ceramide trafficking protein (CERT)". *J Biol Chem* **287**, p. 33706-33718

Sultana, S., Reichbauer, J., Schule, R., Mochel, F., Synofzik, M. & van der Spoel, A. C. (2015). "Lack of enzyme activity in GBA2 mutants associated with hereditary spastic paraplegia/cerebellar ataxia (SPG46)". *Biochem Biophys Res Commun* **465**, p. 35-40

Sun, L. Q., Lee, D. W., Zhang, Q., Xiao, W., Raabe, E. H., Meeker, A., Miao, D., Huso, D. L. & Arceci, R. J. (2004). "Growth retardation and premature aging phenotypes in mice with disruption of the SNF2-like gene, PASG". *Genes Dev* **18**, p. 1035-1046

Suzuki, K. (2003). "Globoid cell leukodystrophy (Krabbe's disease): update". *J Child Neurol* **18**, p. 595-603

Svennerholm, L. (1956). "Composition of gangliosides from human brain". *Nature* **177**, p. 524-525

Svennerholm, L. (1963). "Chromatographic Separation of Human Brain Gangliosides". *J Neurochem* **10**, p. 613-623

Svennerholm, L. (1980). "Ganglioside designation". *Adv Exp Med Biol* **125**, p. 11

Tagami, S., Inokuchi Ji, J., Kabayama, K., Yoshimura, H., Kitamura, F., Uemura, S., Ogawa, C., Ishii, A., Saito, M., Ohtsuka, Y., Sakaue, S. & Igarashi, Y. (2002). "Ganglioside GM3 participates in the pathological conditions of insulin resistance". *J Biol Chem* **277**, p. 3085-3092

Takizawa, M., Nomura, T., Wakisaka, E., Yoshizuka, N., Aoki, J., Arai, H., Inoue, K., Hattori, M. & Matsuo, N. (1999). "cDNA cloning and expression of human lactosylceramide synthase". *Biochim Biophys Acta* **1438**, p. 301-304

Taube, S., Jiang, M. X. & Wobus, C. E. (2010). "Glycosphingolipids as Receptors for Non-Enveloped Viruses". *Viruses-Basel* **2**, p. 1011-1049

Tettamanti, G., Bassi, R., Viani, P. & Riboni, L. (2003). "Salvage pathways in glycosphingolipid metabolism". *Biochimie* **85**, p. 423-437

Thudichum, J. L. W., Simon, J., Thudichum, J. L. W. & St. Thomas's Hospital. Medical School Library (1884). *A treatise on the chemical constitution of the brain*. (Baillière, Tindall and Cox)

Tomasevic, N., Jia, Z., Russell, A., Fujii, T., Hartman, J. J., Clancy, S., Wang, M., Beraud, C., Wood, K. W. & Sakowicz, R. (2007). "Differential regulation of WASP and N-WASP by Cdc42, Rac1, Nck, and PI(4,5)P2". *Biochemistry* **46**, p. 3494-3502

van der Spoel, A. C., Jeyakumar, M., Butters, T. D., Charlton, H. M., Moore, H. D., Dwek, R. A. & Platt, F. M. (2002). "Reversible infertility in male mice after oral administration of alkylated imino sugars: a nonhormonal approach to male contraception". *Proc Natl Acad Sci U S A* **99**, p. 17173-17178

van Meer, G., Voelker, D. R. & Feigenson, G. W. (2008). "Membrane lipids: where they are and how they behave". *Nat Rev Mol Cell Biol* **9**, p. 112-124

van Weely, S., Brandsma, M., Strijland, A., Tager, J. M. & Aerts, J. M. (1993). "Demonstration of the existence of a second, non-lysosomal glucocerebrosidase that is not deficient in Gaucher disease". *Biochim Biophys Acta* **1181**, p. 55-62

Voogd, J., Gerrits, N. M. & Ruigrok, T. J. (1996). "Organization of the vestibulocerebellum". *Ann N Y Acad Sci* **781**, p. 553-579

Votsi, C., Zamba-Papanicolaou, E., Middleton, L. T., Pantzaris, M. & Christodoulou, K. (2014). "A novel GBA2 gene missense mutation in spastic ataxia". *Ann Hum Genet* **78**, p. 13-22

Vyas, A. A., Patel, H. V., Fromholt, S. E., Heffer-Lauc, M., Vyas, K. A., Dang, J. Y., Schachner, M. & Schnaar, R. L. (2002). "Gangliosides are functional nerve cell ligands for myelin-

associated glycoprotein (MAG), an inhibitor of nerve regeneration". *Proc Natl Acad Sci U S A* **99**, p. 8412-8417

Wade, R. C., Gabdoulline, R. R., Ludemann, S. K. & Lounnas, V. (1998). "Electrostatic steering and ionic tethering in enzyme-ligand binding: insights from simulations". *Proc Natl Acad Sci U S A* **95**, p. 5942-5949

Wang, T. Y., Leventis, R. & Silvius, J. R. (2001). "Partitioning of lipidated peptide sequences into liquid-ordered lipid domains in model and biological membranes". *Biochemistry* **40**, p. 13031-13040

Wang, Y., Wang, F., Wang, R., Zhao, P. & Xia, Q. (2015). "2A self-cleaving peptide-based multi-gene expression system in the silkworm Bombyx mori". *Sci Rep* **5**, p. 16273

Wennekes, T., Meijer, A. J., Groen, A. K., Boot, R. G., Groener, J. E., van Eijk, M., Ottenhoff, R., Bijl, N., Ghauharali, K., Song, H., O'Shea, T. J., Liu, H., Yew, N., Copeland, D., van den Berg, R. J., van der Marel, G. A., Overkleeft, H. S. & Aerts, J. M. (2010). "Dual-action lipophilic iminosugar improves glycemic control in obese rodents by reduction of visceral glycosphingolipids and buffering of carbohydrate assimilation". *J Med Chem* **53**, p. 689-698

Woeste, M. A. (2015). "Analyzing the role of GBA2 in locomotor dysfunction [Master thesis]". *Rheinische Friedrich-Wilhelms-Universität Bonn*

Woeste, M. A. & Wachten, D. (2017). "The Enigmatic Role of GBA2 in Controlling Locomotor Function". *Front Mol Neurosci* **10**, p. 386

Yamashita, T., Higuchi, H. & Tohyama, M. (2002). "The p75 receptor transduces the signal from myelin-associated glycoprotein to Rho". *J Cell Biol* **157**, p. 565-570

Yamashita, T., Hashiramoto, A., Haluzik, M., Mizukami, H., Beck, S., Norton, A., Kono, M., Tsuji, S., Daniotti, J. L., Werth, N., Sandhoff, R., Sandhoff, K. & Proia, R. L. (2003). "Enhanced insulin sensitivity in mice lacking ganglioside GM3". *Proc Natl Acad Sci U S A* **100**, p. 3445-3449

Yang, S., Cohen, C. J., Peng, P. D., Zhao, Y., Cassard, L., Yu, Z., Zheng, Z., Jones, S., Restifo, N. P., Rosenberg, S. A. & Morgan, R. A. (2008). "Development of optimal bicistronic lentiviral vectors facilitates high-level TCR gene expression and robust tumor cell recognition". *Gene Ther* **15**, p. 1411-1423

Yildiz, Y., Matern, H., Thompson, B., Allegood, J. C., Warren, R. L., Ramirez, D. M., Hammer, R. E., Hamra, F. K., Matern, S. & Russell, D. W. (2006). "Mutation of beta-glucosidase 2 causes glycolipid storage disease and impaired male fertility". *J Clin Invest* **116**, p. 2985-2994

Yu, R. K., Macala, L. J., Taki, T., Weinfield, H. M. & Yu, F. S. (1988). "Developmental changes in ganglioside composition and synthesis in embryonic rat brain". *J Neurochem* **50**, p. 1825-1829

Zachos, C., Blanz, J., Saftig, P. & Schwake, M. (2012). "A critical histidine residue within LIMP-2 mediates pH sensitive binding to its ligand beta-glucocerebrosidase". *Traffic* **13**, p. 1113-1123

Zunke, F., Andresen, L., Wesseler, S., Groth, J., Arnold, P., Rothaug, M., Mazzulli, J. R., Krainc, D., Blanz, J., Saftig, P. & Schwake, M. (2016). "Characterization of the complex

formed by beta-glucocerebrosidase and the lysosomal integral membrane protein type-2". *Proc Natl Acad Sci U S A* **113**, p. 3791-3796

Zurita, A. R., Maccioni, H. J. & Daniotti, J. L. (2001). "Modulation of epidermal growth factor receptor phosphorylation by endogenously expressed gangliosides". *Biochem J* **355**, p. 465-472

6 Appendix

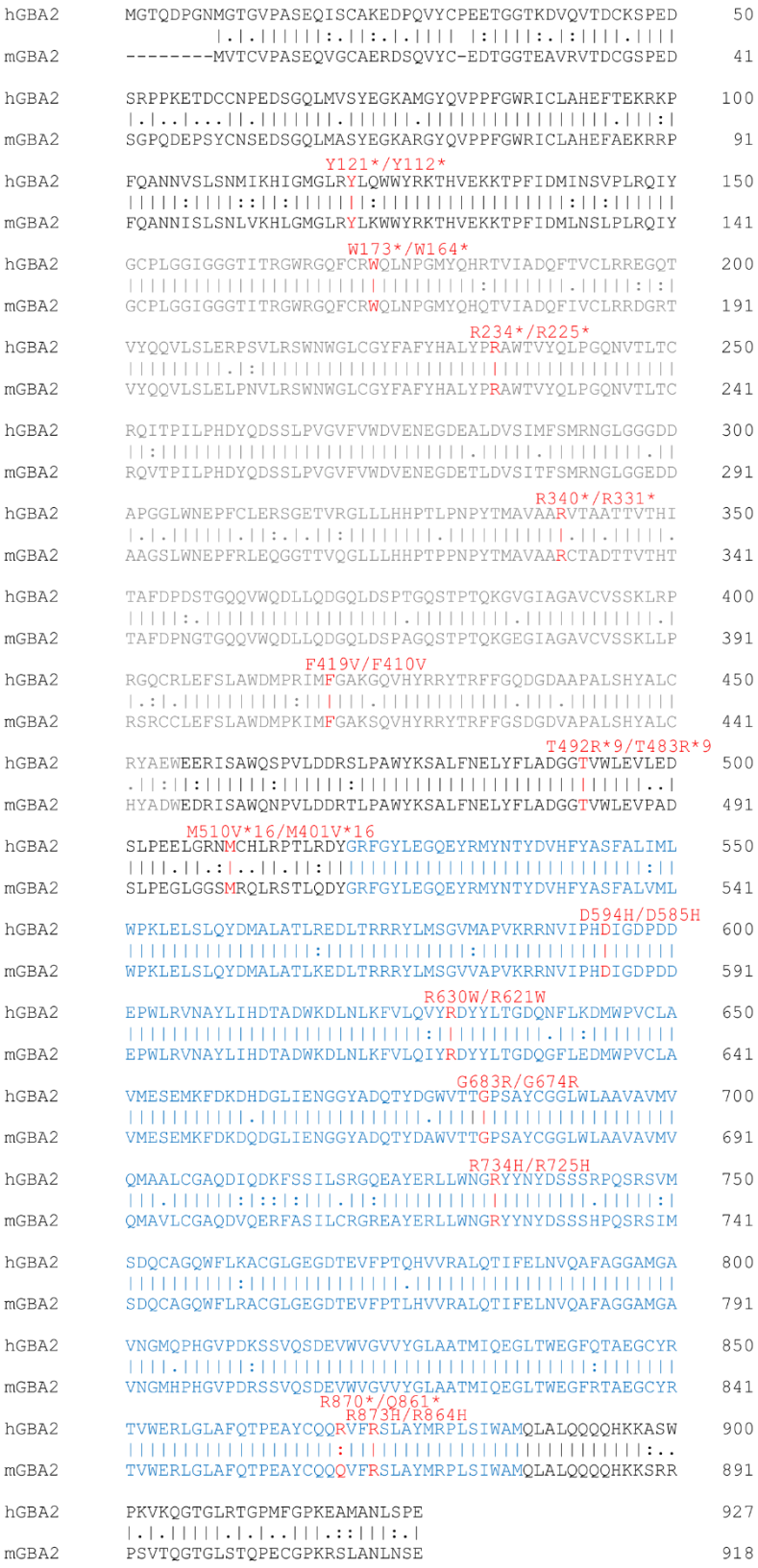

Figure 79: Amino-acid sequence alignment of hGBA2 and mGBA2. Mutated amino acids in hGBA2, which have been identified in human patients suffering from autosomal-recessive ataxia (ARCA), hereditary spastic paraplegia (HSP), and Marinesco-Sjögren-like syndrome (MSLS), and in mGBA2 are depicted (red). Conserved amino acids are referred to as "I", strongly similar properties as ":", and weakly similar properties as "." (EMBL-EBI – EMBOSS Needle Tool, Rice et al., 2000). The N-terminal domain (hGBA2: aa151-aa455) and the predicted catalytic glucosylceramidase domain (hGBA2: aa521-aa886) are indicated in grey and blue, respectively. The functional domains were assigned according to InterPro (Finn et al., 2017).

Table 38: Primer sequences.

Internal primer #	Sequence (5’ to 3’)
C0609	TCTTCTAGATTAGGCGTAGTCGGGCACGTCGTAGGGG
C0895	GCATGTACAACACATACGATGTCCA
C0896	GTGCTGGCTCACTGAGCTGGA
C0897	CCAGTCAGCAGTATCATGAATCAA
C1054	ACAGAATTCCACCATGGTAACCTGCGTCCCGGCC
C1055	CATCATCCGGATCCCCAATGTCATG
C1056	CATGACATTGGGGATCCGGATGATG
C1061	ATATATATACATATGGTAACCTGCGTCCCGGCC
C1067	ATCTGCACTGTTCAATGAACTGTAC
C1216	TGATGATGGTGATGGTGATGCTCTGAATTGAGGTTTGCCAGCG
C1217	TGTCTCGAGCTAATGGTGATGGTGATGATGGTGATGGTGATGCTC
C1997	GACACCTACTCAGACAATGCGATGC
C2062	TAGTCGGGCACGTCGTAGGGGTACCTCAAGCCCATACCGAGG
C2063	TAGTCGGGCACGTCGTAGGGGTAACGACAGAACTGGCCTCTCC
C2064	TAGTCGGGCACGTCGTAGGGGTAGGGATAGAGGGCGTGGTAG
C2065	TAGTCGGGCACGTCGTAGGGGTATGCAGCCACAGCCATGGTG
C2066	CAGGTAATAGTCCCAATAAATTTGCAATAC
C2067	GTATTGCAAATTTATTGGGACTATTACCTG
C2068	GGCCAGGGAGTGGAACACTTGTTG
C2069	CAACAAGTGTTCCACTCCCTGGCC
C2070	GCTGCTGCCGGCCACGCTGTGCCTGCCTCCATCGGCCAGGAAG
C2071	TAGTCGGGCACGTCGTAGGGGTAGCTGCTGCCGGCCACGCTGTG
C2152	TCGTGGTATCGTTATGCGCC
C2153	CTGCTCCAGTTCAAGGTCCC
C2154	ATCACGACGCGCTGTATC

Internal primer #	Sequence (5’ to 3’)
C2155	ACATCGGGCAAATAATATCG
C2436	ATCATCATCATCTTTATAATCCTCTGAATTGAGGTTTGCCAGCGATC
C2440	CAGGTAATAGTCCTTATAAATTTGCAATAC
C2441	GTATTGCAAATTTATAAGGACTATTACCTG
C2442	CAGGTAATAGTCCTGATAAATTTGCAATAC
C2443	GTATTGCAAATTTATCAGGACTATTACCTG
C2444	GTAGGCCAGGGATTTGAACACTTGTTGC
C2445	GTAGGCCAGGGATTTGAACACTTGTTGC
C2446	GTAGGCCAGGGATTTGAACACTTGTTGC
C2447	GTAGGCCAGGGATTTGAACACTTGTTGC
C2473	GGATCCCCAATGTGATGAGGGATGACG
C2474	CGTCATCCCTCATCACATTGGGGATCC
C2475	GTAAGCACTGGGGCGTGTGGTGACCCATG
C2476	CATGGGTCACCACACGCCCCAGTGCTTAC
C2477	GTAGTTGTAATAGTGTCCGTTCCACAG
C2478	CTGTGGAACGGACACTATTACAACTAC
C2609	CCAGAATTCCACCATGCACTATGCAGACTGGGAGGACAG
C2610	TACGAATTCCACCATGGGGCGATTTGGCTATCTTGAAGG
C2663	AAAGAATTCCACCATGACCCCTTTCATCGACATGCTCAATTC
C2664	AAAGAATTCCACCATGCCCCTGAGACAGATCTATGGTTGTC
C2665	GTAGTCGGGCACGTCGTAGGGGTATTGCAGGGCCAGCTGCATGGCC
C2793	CGCGGATCCACCCCTTTCATCGACATGCTCAATTCTCTAC
C2794	CTCATCATCCGGATCTCCAATGTCATGAG
C2795	CTCATGACATTGGAGATCCGGATGATGAG
C2796	GCTGAATTCATTGCAGGGCCAGCTGCATGGCCCAGATG

Internal primer #	Sequence (5’ to 3’)
C3462	GGTAAGCTTCCACCATGGTAACCTGCGTCCCGG
C3463	GTCTCTCATAAGCCTCTCGGCCTCGGC
C3464	GCCGAGGCCGAGAGGCTTATGAGAGAC
C3476	CACTCCACTTCCAGGTGGCTTATCATCATCATCTTTATAATCCTCTG
C3477	GGTCAAAATTCAAAGTCTGTTTCACTCCACTTCCAGGTGGCTTATC
C3478	GTCTCCTGCCAACTTGAGAAGGTCAAAATTCAAAGTCTGTTTCACTC
C3479	GGGCCCGGGGTTGGACTCCACGTCTCCTGCCAACTTGAGAAGGTC
C3480	GTGGAATTCCCTCCACTTCCGGGCCCGGGGTTGGACTCCACG
C3635	GGCTTTTAGCTCCAACCATGATCTTAGG
C3636	CCTAAGATCATGGTTGGAGCTAAAAGCC
C3802	ATCATCATCATCTTTATAATCACGACAGAACTGGCCTCTCCAGCC
C3803	CACTCCACTTCCAGGTGGCTTATCATCATCATCTTTATAATCACGACAG
C3804	ATCATCATCATCTTTATAATCTGCAGCCACAGCCATGGTGTAGGG
C3805	CACTCCACTTCCAGGTGGCTTATCATCATCATCTTTATAATCTGCAGCC
C3866	CTTATCATCATCATCTTTATAATCGGGATAGAGGGCGTGGTAGAAAGC
C3867	CACTCCACTTCCAGGTGGCTTATCATCATCATCTTTATAATCGGG

Danksagung

Diese Arbeit wurde am Forschungszentrum caesar in der Forschungsgruppe „Molekulare Physiologie“, die seit April 2017 dem Institut für angeborene Immunität als Forschungsgruppe „Biophysical Imaging“ angegliedert ist, angefertigt.

An dieser Stelle möchte ich für die Unterstützung und Zusammenarbeit danken:

- Prof. Dr. Dagmar Wachten, die mir die Möglichkeit gegeben hat an diesem spannenden Projekt über meine Masterarbeit hinaus zu forschen. Danke für Deine unaufhaltsame Unterstützung in jeglicher Phase meiner Promotion.
- Prof. Dr. Christoph Thiele, für seine Beteiligung als Zweitgutachter in der Prüfungskommission.
- Prof. Dr. Frank Bradke, für die gute Zusammenarbeit zur Analyse des Neuritenwachstums und seine Beteiligung als dritter, fachnaher Gutachter in der Prüfungskommission.
- Prof. Dr. Anton Bovier, für seine Beteiligung als vierter, fachfremder Gutachter in der Prüfungskommission.
- Dr. Sina Stern, für ihr riesiges Engagement und die ständige Bereitschaft dieses Projekt durch ihr Know-how zur Neuronenisolation tatkräftig zu unterstützen und maßgeblich voranzutreiben. Vielen Dank, dass Du für jegliche Fragen offen warst und diesem gesamten Projekt eine so große Bereicherung warst!
- Dr. Heike Endepols, für die gute Zusammenarbeit, die das Fortführen der Verhaltensexperimente ermöglicht hat, und dies in sehr herzlicher Atmosphäre.
- Dr. Wolfgang Bönigk, für seine Hilfe bei der molekularbiologischen Arbeit. Danke, dass du für das Klonieren der GBA2-Konstrukte immer gerne Zeit eingeräumt hast.
- Dr. Heinze Körschen, für das Beantworten zahlreicher GBA2-bezogenen Fragen und Lösen so manch eines labortechnischen Problems.
- Dr. Diana N. Raju, for her support, especially in the last month of my lab work and beyond. Thanks for all the fruitful scientific and non-scientific discussions and the great time (especially during long working hours)!
- Dr. Thomas Berger und Elena Grahn, für das Einbringen ihrer Elektrophysiologie-Expertise in die weiteren Versuche dieses Projektes.
- Jens-Henning Krause, für seine Hilfe in der Zellkultur und bei der Fortführung von Experimenten in meiner Abwesenheit; ein Hoch auf dein wahnsinniges (Labor-) organisatorisches Talent und deine Auffassungsgabe, dadurch hast du mir ungemein geholfen!

- Isabel Lux, Dana Herborn und Mona Völker, für ihre Unterstützung bei der Präparation der Mäuse sowie allen Tierstall-Angelegenheiten.
- Dominik Dittmann, für die tatkräftige Unterstützung zur Finalisierung der Interaktionsstudien während meiner Schreibphase.
- Jessica Hierer, für ihre Unterstützung in der Zellkultur, ganz besonders wenn mal wieder mehr Bakterien als Zellen gewachsen waren.
- Dr. Sophie Schonauer, für die Einarbeitung in GBA2-relevante Arbeitsabläufe im Labor und ihre Unterstützung, besonders in der Anfangsphase meines Projekts.
- Allen Mitgliedern der AG Wachten, insbesondere meinen Mitdoktoranden Melanie Balbach, Fabian Kaiser, Christina Vianden und Jan-Niklas Hansen für die tolle Arbeitsatmosphäre und den immer gewissen Rückhalt in vielerlei Hinsicht!

Vielen Dank an das Bonner Forum Biomedizin, das ImmunoSensation Cluster und das Bonner Graduiertenzentrum für die zahlreichen interessanten Vorlesungen, Seminare und Workshops, an denen ich teilnehmen durfte, sowie die finanzielle Förderung durch Reisestipendien.

Ein ganz besonderer Dank gilt meinem Freund, meiner Familie und meinen Freunden, die mich immer unterstützt haben, ob aus der Ferne oder vor Ort, ob in alltäglichen oder außergewöhnlichen Belangen. Ihr habt mir wahnsinnig viel Kraft gegeben und immer an mich und mein Schaffen geglaubt!